Atmospheric Pressure Plasma Treatment of Complex Interfaces

by

Kseniia Konina

A dissertation submitted in partial fulfillment
of the requirements for the degree of
Doctor of Philosophy
(Nuclear Engineering and Radiological Sciences)
in the University of Michigan
2024

Doctoral Committee:

Professor Mark J. Kushner, Chair
Associate Professor Scott D. Baalrud
Professor John E. Foster
Associate Professor Louise Willingale

Kseniia Konina

kseniiak@umich.edu

ORCID iD: 0000-0001-8933-1399

Dedication

This dissertation is dedicated to all those who have helped along the way.

Acknowledgements

I would like to express my deepest gratitude to Professor Mark Kushner for his exceptional dedication to teaching and mentoring, both personally and professionally. His continuous support has been crucial to the realization of this work, and his guidance has been invaluable in shaping my academic and personal growth. The continuous funding support maintained by Professor Kushner had a critical impact on the thesis, publications, and conference presentations.

I extend my gratitude to the past and current group members: Dr. Amanda Lietz, Dr. Juliusz Kruszelnicki, Dr. Florian Krüger, Dr. Chenhui Qu, Dr. Shuo Huang, Dr. Xifeng Wang, Dr. Sanjana Kerketta, Dr. Astrid Raisanen, Dr. Scott Doyle, Dr. Jordyn Polito, Dr. Mackenzie Meyer, Dr. Eve Lanham, Dr. Tugba Piskin, Evan Litch, Yifan Gui, Jisu Jeon, Yeon Geun Yook, Chenyao Huang, and Dr. Tiago Dias, for their collaboration and support. Special gratitude is dedicated to Julia Falkovitch-Khain for her continuous help.

Several studies in this thesis have been done in collaboration with experimental groups. I thank Sai Raskar and Professor Igor Adamovich, Dr. Joshua Morsell and Professor Steven Shannon for their collaborative effort and experimental expertise that enhanced the results presented and grew my knowledge in the field of atmospheric pressure plasmas.

Prior to joining Professor Kushner's group, I worked in the field of low-temperature plasmas under the supervision of Professor Boris Potapkin and Dr. Maxim Deminsky. My gratitude is dedicated to them for teaching me plasma chemistry and physics and sharing with me their knowledge and wisdom. I also thank Professor Natalia Babaeva for her helpful mentorship.

I thank Dr. Yulia Polynskaya and Dr. Alexander Lebedev for enhancing my knowledge in research and science.

Finally, I express my appreciation to my family and friends whose unwavering moral support has sustained me through the challenges of this journey. Your belief in me has been my greatest strength.

Table of Contents

Dedication ii

Acknowledgements iii

List of Figures ix

Abstract xvii

Chapter 1 Introduction 1

1.1 Basic Phenomena in Plasmas 3

1.2 Phenomenon of Breakdown in Gases 6

1.3 Electron Energy Distribution Functions and Electron Temperature 8

1.4 Reduced Electric Field 9

1.5 Streamer Phenomenon and Bulk Ionization Waves 10

1.6 Surface Ionization Waves 11

1.7 Atmospheric Pressure Plasma Jets (APPJs) 12

1.8 Surface Dielectric Barrier Discharges (SDBDs) 13

1.9 Gas Phase Plasma-Chemistry 15

1.10 Plasma Liquid Interactions 17

1.11 Chemical Interaction of Plasmas with Interfaces 19

1.12 Atmospheric Pressure Plasmas and Complex Surfaces 21

1.13 Role of Modeling in Studying Atmospheric Pressure Plasmas 22

1.14 Motivation 23

1.15 Scope of the Dissertation 24

1.16 References 26

Chapter 2 Model Description 33
2.1 Geometry and Mesh 38
2.2 Plasma Module 39
2.3 Poisson's Equation and Continuity Equation for Charged Species 40
2.4 Numerical Methods 42
2.5 Neutral Transport 43
2.6 Boltzmann's Equation 43
2.7 Electron Energy Balance Equation 44
2.8 Photon Transport Module 45
2.9 Plasma Chemistry Module 46
2.10 Liquid Module 47
2.11 Fluid Mechanics Module and Neutral Transport 49
2.12 Surface Kinetic Module 50
2.13 References 52
Chapter 3 Atmospheric Pressure Plasma Treatment of Porous Dielectrics 53
3.1 Introduction 54
3.2 Description of the model 60
3.3 Surface Ionization Waves Propagating across the Flat Interface 61
3.4 Surface Ionization Waves Propagating across the Porous Dielectric 64
3.5 Concluding Remarks 73
3.6 References 75
Chapter 4 Atmospheric Pressure Plasma Treatment of Wet Microchannels: Optimal Surface-to-Volume Ratio 78
4.1 Introduction 79
4.2 Description of the Model 81
4.3 Surface Ionization Wave Interacting With Microchannels 83

4.3.1 Hydrophobicity: Shape of Meniscus 89
4.3.2 Width of Channels 92
4.4 Concluding Remarks 95
4.5 References 97
Chapter 5 Atmospheric Pressure Plasma Treatment of Microchannels: Formation of Reverse Ionization Waves 100
5.1 Introduction 101
5.2 Description of the Model 103
5.3 Description of the Experiment 106
5.4 Atmospheric Pressure Plasma Jet Interacting with Dry Microchannels 108
5.5 Atmospheric Pressure Plasma Jet Interacting with Wet Microchannels 123
5.6 Concluding Remarks 128
5.7 References 130
Chapter 6 Atmospheric Pressure Plasma Treatment of Skin: Penetration into Hair Follicles 133
6.1 Introduction 135
6.2 Description of the Model 138
6.3 APPJ Interactions with Skin and Follicles 142
6.3.1 Orientation and Location of the Hair Follicle 150
6.3.2 Fluxes and Densities in the Afterglow 154
6.3.3 Fat Layer Thickness 157
6.3.4 Skin Properties 159
6.4 Concluding Remarks 162
6.5 References 165
Chapter 7 Atmospheric Pressure Plasma Jet Treatment of Polypropylene Step Barriers 169
7.1 Introduction 171
7.2 Description of the Model and Experiment 174

7.2.1 Description of the Model 174
7.2.2 Description of the Experiment 176
7.3 Propagation of SIWs on Dielectric Interfaces 177
7.3.1 Propagation of SIWs on Flat Surfaces 177
7.3.2 SIWs interaction with Dielectric Steps: Direction of the Barriers 180
7.3.3 SIWs interaction with Dielectric Steps: Polarity of the Source 183
7.3.4 SIWs interaction with Dielectric Steps: Height of Barriers 185
7.3.5 SIWs interaction with Dielectric Steps: Dielectric Permittivity of the Barrier 186
7.3.6 SIWs interaction with Dielectric Steps: Shape of the Barriers 188
7.4 Analysis of Fluxes of Species 189
7.5 Polypropylene Modification on the Step Barrier 192
7.6 Concluding Remarks 194
7.7 References 196
Chapter 8 Summary and Future Work 199
8.1 Summary 199
8.2 Future Work 203
8.3 References 206

List of Figures

Figure 1.1. Classification of different plasmas by electron temperatures and densities [8]. 4

Figure 1.2. Avalanche initiation process in a discharge system [20]..... 6

Figure 1.3. Classical Paschen's curves for different gases [28]. 7

Figure 1.4. Maxwellian, Druyvesteyn, and Boltzmann distribution functions [31]. 8

Figure 1.5. Energy loss fraction for different processes in air-hydrogen plasma as a function of reduced electric field [33]. 9

Figure 1.6. Mechanism of propagation of streamers that are a) cathode directed, b) anode directed [41]. 11

Figure 1.7. Schematic image of an atmospheric pressure plasma helium jet with two powered ring electrodes (left); experimental photograph of this device applied to human tissue [60]..... 13

Figure 1.8. Schematic image of the surface dielectric barrier discharge in top view (top-left); experimental photograph of top view (top-right); side view of surface dielectric barrier discharge (bottom view) [71]..... 14

Figure 1.9. Rate coefficients for elementary processes in hydrogen-air plasma presented as a function of gas temperature [33]..... 15

Figure 1.10. Cross-section graphical data presented for electron impact of N_2O molecule as a function electron energy [75]..... 17

Figure 1.11. Mechanism of species in plasma influencing a simple flat liquid interface [76]. 19

Figure 1.12. Schematic image of atmospheric pressure plasma interacting with a polymer surface: a) prior to surface modification, b) after surface modification [81]..... 21

Figure 2.1. Scheme of work of nonPDPSIM. 33

Figure 2.2. Time evolution of plasma computed in nonPDPSIM for an APPJ incident onto modeled human skin: a) electron impact ionization source, b) electron density. 34

Figure 2.3. Fluid flow of helium produced by APPJ applied on modeled human skin computed in nonPDPSIM. 35

Figure 2.4. Example of the numerical domain corresponding to a setup of SDBD. a) Full numerical domain, b) full map of nodes, c) enlarged geometry microfeature, d) map of nodes in enlarged microfeature. 36

Figure 2.5. Schematic image of a section of the mesh and a constructed finite volume cell. 39

Figure 3.1. The geometry of the model. (a) the entire scheme of the reactor, (b) a full numerical mesh, (c) a zoomed-in image of pore on the top of the dielectric surface, (d) a computational mesh of an enlarged image of the pore. 59

Figure 3.2. Properties of a negative SIW propagating across a flat dielectric surface with relative permittivity $\varepsilon_r = 4$. a) Electron density, b) electron impact ionization source, c) electron temperature, d) electric field and e) photoionization source. The range of values in the image are noted in the frame, with the number of decades for log-plots. Maximal values of the parameters are identified in the figure. 61

Figure 3.3. Propagation of a negative SIW across a surface with cut pores with diameter 285 having different depths of the pores, Δh. a) $\Delta h = 0$ μm (flat), b) 50 μm, c) 150 μm and d) 250 μm. Electron density (maximum 5×10^{13} cm^{-3}, 2-decade log scale) is shown in the left column at 16.5 ns after the SIW crosses the 3 cut pores. Electron impact ionization source (maximum 5×10^{22} $cm^{-3}s^{-1}$, 3 decade log scale) is shown in the right column for the first (left-most) pore when the SIW arrives at 11.5 ns. 63

Figure 3.4. Plasma properties for the negative SIW arriving at the first, left-most cut-pore (diameter 285 μm) having depth $\Delta h = 250$ μm at times of a) 11.0 ns, b) 11.5 ns, c) 12.5 ns and d) 13.5 ns. The columns (left to right) show electron density, electron impact ionization source and E/N. The range of values for each quantity (and number of decades for log-plots) are shown at the top of each column..... 66

Figure 3.5. Plasma properties for the negative SIW arriving at the first, left-most buried pore (diameter 285 μm) having an opening to the plasma of 25 μm at times of a) 10.0 ns, b) 10.7 ns, c) 12.2 ns and d) 13.5 ns. The columns (left to right) show electron density, photo-ionization source and electron impact ionization source. The range of values for each quantity (4-decade log scale) are shown at the top of each column. Values in the bulk plasma on top of the surface may be saturated for the range of values in the image. The range of values was chosen to emphasize the in-pore properties. 67

Figure 3.6. Plasma properties for the positive SIW arriving at the first, left-most buried pore (diameter 285 μm) having an opening to the plasma of 25 μm at times of a) 9.3 ns, b) 9.4 ns, c) 9.6 ns and d) 10.0 ns. The columns (left to right) show electron density, photo-ionization source and electron impact ionization source. The range of values for each quantity and number of decades for these log plots are shown at the top of each column. Values in the bulk plasma on top of the surface may be saturated for the range of values in the image. The range of values was chosen to emphasize the in-pore properties. 69

Figure 3.7. Plasma properties for the negative SIW arriving at the first, left-most buried pore (diameter 285 μm) having an opening to the plasma of 4 μm at times of a) 10.0 ns, b) 10.6 ns,

c) 12.6 ns and d) 16.6 ns. The columns (left to right) show electron density, photo-ionization source and electron impact ionization source. The number of decades for these log plots are shown at the top of each column. The maximum values for each image are shown in the frame. Values in the bulk plasma on top of the surface may be saturated for the range of values in the image. The range of values was chosen to emphasize the in-pore properties. 71

Figure 3.8. Plasma properties for the positive SIW arriving at the first, left-most buried pore (diameter 285 μm) having an opening to the plasma of 4 μm at times of a) 9.3 ns, b) 9.5 ns, c) 10.4 ns and d) 13.0 ns. The columns (left to right) show electron density, photoionization source and electron impact ionization source. The number of decades for these log plots are shown at the top of each column. The maximum values for each image are shown in the frame. Values in the bulk plasma on top of the surface may be saturated for the range of values in the image. The range of values was chosen to emphasize the in-pore properties. 73

Figure 4.1. Schematic image of the geometry domain. a) Full image of the 2D geometry, b) zoomed-in image of the array of channels, c) zoomed-in periodic channel structure with dimensions. 81

Figure 4.2. Base case: evolution of the SIW on the array of wet microchannels generated by a negative polarity pulse of -30kV. a) Electron density evolution, b) electron impact ionization source, c) reduced electric field. 83

Figure 4.3. Base case: evolution of the SIW on the array of wet microchannels (neutral substrate) generated by a positive polarity pulse of 30kV. a) Electron density evolution, b) electron impact ionization source, c) reduced electric field. 85

Figure 4.4. Fluence of photons to the water surface over 14 ns. 86

Figure 4.5. Evolution of electron density when the SIW travels across the array of channels with water having different meniscus shapes. a) Hydrophilic substrate, b) neutral substrate, c) hydrophobic substrate. 87

Figure 4.6. Fluence of photons over the water interface for different meniscus shapes..... 88

Figure 4.7. Mechanism of precharge of the following channels and the right-most edge of the treated channel for three meniscus shapes. a) Photoionization source, b) electron density. 89

Figure 4.8. OH_{aq} and e_{eq} formed on the water surface at 13 ns. 90

Figure 4.9. Electron density evolution following the propagation of SIWs for three different lengths of channels..... 92

Figure 4.10. Fluences of photons and electrons onto the liquid surface for three widths of channels..... 93

Figure 4.11. OH_{aq} concentration on the interface of liquids in three different widths of channels at 15 ns. 94

Figure 5.1. Schematic of the computational geometry. a) Full computational domain, b) computational mesh, c) enlargement showing chain of microchannels (dotted domain in previous images), and d) enlargement of individual channels. 103

Figure 5.2. The stabilized fluid flow field with flow streamlines prior to application of the voltage pulse. The streamline are labeled with speeds (cm/s). a) Argon and b) N_2 flow with enlargement near the channels. 104

Figure 5.3. Schematic of the experiment. a) APPJ over the grooved substrate sitting in a bath of deionized water. b) Cross section showing the incident laser beam. 106

Figure 5.4. Ionization wave propagation through the tube and onto the channeled substrate. a) Electron impact ionization source ($cm^{-3}s^{-1}$) and b) electron density (cm^{-3}). Images are plotted on a 3-decade log scale with maximum values indicated for every characteristic. 107

Figure 5.5. Surface ionization wave propagation across a chain of microchannels for the base case. a) S_e – electron impact ionization source ($cm^{-3}s^{-1}$, 3-decade log scale). b) [e] – electron density (cm^{-3}, 3-decade log scale). c) E/N – reduced electric field (Td, linear scale). Maximum values or the range of values are noted in the images. 109

Figure 5.6. Plasma properties demonstrating reverse (positive) ionization wave. a) S_e – electron impact ionization source ($cm^{-3}s^{-1}$) and [e] – electron density ($cm^{-3}s^{-1}$). The "N" and "P" labels indicate a negative or positive ionization wave. Images are plotted on a 3-decade log scale with maximum values indicated. 110

Figure 5.7. Comparison of (left) simulated electron density for applied voltage of -18 kV with (right) ICCD imaging for the plasma jet propagating along dry microchannels. The ICCD imaging frames were chosen for times that showed similar structure as the simulations. These images have been enhanced emphasize regions of weak emission. 112

Figure 5.8. Comparison of electric fields on the top of ridges of the channels numbered according to the schematic. a) Simulation and b) EFISH measurements. 113

Figure 5.9. Electron density during surface ionization wave propagation across a chain of microchannels for different voltages for otherwise the base case conditions. a) -20 kV, b) -22.5 kV and c) -25 kV. The time for the image is noted in each frame. The horizontally aligned images are for the same propagation distance. The shaded times indicate images at approximately the same time. Densities are plotted on a 3-decade log scale with the maximum value noted. 115

Figure 5.10. Electron density during SIW propagation across a chain of microchannels for different permittivity of the substrate for otherwise the base case conditions. a) $\varepsilon_r = 2$, b) $\varepsilon_r = 6$ and c) $\varepsilon_r = 20$. The time for the image is noted in each frame. The horizontally aligned images are for the approximately the same propagation distance. The shaded times indicate images at approximately the same time. Densities are plotted on a 3-decade log scale with the maximum value noted. 117

Figure 5.11. Electron density during SIW propagation across a chain of microchannels for different conductivities, σ, and dielectric relaxation times, τ, of the substrate for otherwise the base case conditions. a) $\sigma = 0$, b) $\sigma = 2 \times 10^{-4}$ S/cm, $\tau = 2.7$ ns, and c) $\sigma = 1 \times 10^{-3}$ S/cm, $\tau = 0.53$ ns. The time for the image is noted in each frame. The horizontally aligned images are for the approximately the same propagation distance of the SIW. The shaded times indicate when the propagation of the SIW stalls. Densities are plotted on a 3-decade log scale with the maximum value noted. 118

Figure 5.12. Electron density during surface ionization wave propagation across a chain of microchannels for different heights of the powered electrode above the substrate. The electrode position above the electrode is d. The gap between the substrate and bottom of the nozzle is h. a) d = 7.5 mm, h = 0.8 mm, b) d = 8.4 mm, h = 1.7 cm and c) d = 9.0 mm, h = 2.3 mm. Densities are plotted on a 3-decade log scale with the maximum value noted. 121

Figure 5.13. Surface ionization wave propagating across a chain of wet microchannels. a) S_e – electron impact ionization source ($cm^{-3}s^{-1}$, 3-decade log scale). b) [e] – electron density (cm^{-3},3-decade log scale). c) E/N – reduced electric field (Td, linear scale). The maximum value or range of values are indicated. 123

Figure 5.14. Plasma properties centered on water filled channel 6. Simulated a) electron impact ionization source and b) electron density. The time for the horizontally aligned images are indicated in the first column. The properties are shown in a 3-decade log scale with maximum indicated. c) ICCD images chosen at times to align with the simulations. The ICCD images have been enhanced to show dim detail. 124

Figure 5.15. Comparison of (left) simulated electron density for applied voltage of -18 kV and (right) ICCD imaging for the Ar plasma jet propagating over water filled microchannels. 127

Figure 6.1. Trichrome histology of porcine skin with multiple follicles. a) Typical follicle shows an example of the space that surrounds a prominent central hair shaft. b) Multiple follicles with attached sebaceous glands. Some follicles lack a hair shaft. 136

Figure 6.2. Computational domain. a) Schematic of the system which is symmetric across the right boundary. b) Numerical mesh. 138

Figure 6.3. Schematic image of the hair follicle and surrounding tissue. 139

Figure 6.4. The stabilized concentration of helium flow at before the plasma pulse is generated with velocity streamlines. The streamline labels are speeds (cm/s). 141

Figure 6.5. Plasma properties during propagation of the ionization wave onto the skin in the vicinity of the follicle. a) Electron impact ionization source and b) electron density. Images are plotted on a 3-decade logscale with the maximum value noted for each frame. 142

Figure 6.6. Propagation of plasma into hair follicles for the base case for times t = 51.7–52.4 ns. (a) E/N before plasma entry into the follicle (linear), (b) electron density (log-scale), (c) electron density (log-scale) and (d) E/N (linear). The logscale images are plotted over 3 decades. Maximum values are noted for each frame. 144

Figure 6.7. Deeper propagation of plasma into hair follicles for the base case for t = 90-115 ns. a) Electron density (logscale), b) electron impact ionization source (log-scale), c) E/N (linear) and d) electron temperature. The log-scale images are plotted over 3 decades. Maximum values are noted for each frame. 146

Figure 6.8. Radicals and photons properties in the follicle. a) Densities of O, N and OH at the end of the voltage pulse at 160 ns. Images are plotted on a 2-decade log-scale with the maximum value noted in each frame. b) Reference locations for photon fluences. c) VUV photon fluences to the inside surfaces of the follicle at 160 ns (end of voltage pulse) and 1 μs. The locations along the surface of the follicle are indicated by the boxed letters. 147

Figure 6.9. Time evolution of electron density inside hair follicles having different widths of pockets for t = 75-120 ns. a) 85 μm, b) 115 μm, and c) 150 μm. The images are plotted on a 2-decade log-scale having maximum value 5×10^{13} cm^{-3}. 149

Figure 6.10. Electron density in the follicle for different angles with respect to the skin at the times of the plasma reaching the bottom of the follicle. a) 0 degrees at 115 ns, b) 30 degrees at 125 ns, c) 45 degrees at 120 ns, d) 60 degrees at 135 ns and e) -45 degrees at 135 ns. The densities are plotted on a 3-decade log scale having maximum value 6×10^{13} cm^{-3}. 151

Figure 6.11. Electron density for different locations and angles of follicles at 150 ns. a) Base case vertical follicle and a follicle shifted by 1.5 mm. b) Follicle slanted at – 45 degrees and slanted follicle shifted by 1.5 mm. follicle with the same geometry. The densities are plotted on a 3-decade log scale having maximum value 6×10^{13} cm^{-3}. 153

Figure 6.12. Fluence of H_2O_2 and O_3 at 1 ms in the afterglow inside a follicle. The schematic at the right indicates the locations along the inside surface of the follicle. 155

Figure 6.13. Time evolution of the densities of ROS in the afterglow following a pulse inside the hair follicle and above the skin. a) O_3 and b) Concentration of H_2O_2. The densities are plotted on a 3-decade log-scale with the maximum value (cm^{-3}) noted in each frame. 156

Figure 6.14. Electron densities in the nozzle-skin gap and inside the follicle at different times during and following the voltage pulse for different thickness of the fat layer. a) 0.5 mm, b) 2.5 mm and c) 5.5 mm. The densities are plotted on a 3-decade log scale with the maximum value and time indicated in each frame. 158

Figure 6.15. Election density at 150 ns (logarithmic scale) for three skin conductive and dielectric properties corresponding to dielectric relaxation times of infinite, 50 ns and 20 ns. The densities are plotted on a 2-decade log scale having maximum value 2×10^{14} cm^{-3}. 160

Figure 6.16. Conductivity of target substrate determines plasma flow properties. A helium plasma jet with a gas flow of 4 slm is shown. a) Image of plasma with the target being a grounded metal plate. The top image is a side view. The bottom image is a view from approximately 45 degrees. b) The grounded metal plate is covered by a 3 mm silicon pad with the same distance between the plasma tube and surface. The propagation of surface ionization waves are noted. 161

Figure 7.1. Scheme of a computational domain. a) Full domain, b) enlarged half-right APPJ scheme, c) enlarged scheme of step barrier. 172

Figure 7.2. Helium fluid flow diagram demonstrated with colored helium concentration and fluid flow stream lines with local speeds. 174

Figure 7.3. Photograph of the experimental chamber. 176

Figure 7.4. Comparison of the results of simulations for plasma produced with +8 kV voltage to ICCD camera imaging on the experiment for IW striking a dielectric interface. The time scale on the experiment is chosen to match the evolution of plasma in the calculations. 177

Figure 7.5. Plasma propagation generated by +8 kV pulse on up and down barriers of identical 2.6 mm heights. a) SIW on down barriers presented with electron impact ionization source S_e (top row) and electron density [e] (bottom row) from 70 to 125 ns. b) SIW on up barriers demonstrated with electron impact ionization source S_e (top row) and electron density (bottom row) from 65 to 570 ns..... 179

Figure 7.6. Experimental images taken from the bottom of the transparent substrate for SIW propagation over up and down barriers. The images are obtained from the ICCD camera. a) SIW climbing up barrier. The barrier is placed in left side of the image and identified with the bright vertical line. b) SIW moving down barrier. The barrier is placed in the right side of the image and is identified with bright vertical line. 181

Figure 7.7. Plasma propagation over up barrier of 2.6 mm height generated by positive and negative polarity pulses of +/-8 kV. a) negative polarity driven SIW presented by electron impact ionization source S_e (top row) and electron density [e] (bottom row) at 40-90 ns time frame, b) positive polarity driven SIW shown with electron impact ionization source S_e (top row) and electron density [e] (bottom row) at 65-570 ns time frame. 182

Figure 7.8. Negative polarity -8 kV driven plasma interacting with up barrier of different heights 1.6 – 3.6 mm at 85 ns when the SIW is developed on top barriers at all heights. a) data presented for all heights with electron density [e] (top row), b) data shown for all heights with electron impact ionization source S_e (bottom row). 184

Figure 7.9. Positive polarity +8 kV driven SIWs moving across barriers of 1.6 – 3.6 mm heights at times of reaching the top of the barriers (230-485 ns). a) Electron density for all heights [e] (top row), b) electron impact ionization source S_e for all heights (bottom row). 185

Figure 7.10. Positive polarity-driven plasma (+8kV) climbing the barriers of 2.6 mm height with different relative dielectric permittivities $\varepsilon = 4 – 40$ at different time frames addressing the moment of climbing. a) Data presented with electron density [e] (top row), b) data presented with electron impact ionization source S_e (bottom row)..... 186

Figure 7.11. Positive polarity-driven +8 kV SIWs over the barriers of 2.6 mm height with different shapes curved in 45 – 135 degrees range at times of climbing the barrier. a) Data presented with electron density [e] (top row), b) data presented with electron impact ionization source S_e (bottom row). 187

Figure 7.12. Fluence of photons (hv), positive ions (M^+), and O and OH radicals over 550 ns to the interface containing 2.6 height barrier for a) negative polarity, b) positive polarity. 188

Figure 7.13. Schematic of the computational geometry. a) Full computational domain, b) computational mesh, c) enlargement showing chain of microchannels (dotted domain in previous images), and d) enlargement of individual channels. 189

Figure 7.14. Surface site density as a function of length across the material. a) Negative polarity, b) positive polarity. 191

Abstract

Technologies that use atmospheric pressure plasmas play a critical role in modern life and the economy. Advances in the field of atmospheric pressure plasmas help to invent and revolutionize these technologies. As new technology devices have become more complex and operated more selectively, research in the field of atmospheric pressure plasmas has concomitantly increased the complexity of the systems. One of the directions for increasing this complexity is surface morphology. Common laws and patterns of interaction of plasmas with surfaces, particularly those with complex interface configurations of different materials, have not been formulated. To approach this problem, a set of common standard surface types have been computationally studied for this dissertation using nonPDPSIM, a 2-D plasma hydrodynamics model.

Through the application of surface dielectric barrier discharges to arrays of micropores in dielectrics that can represent catalyst supports or combustion filters, common patterns in uniformity of treatment are identified. The inhomogeneous treatment is identified to be caused by the electric field enhancement at a crest of non-planar regions of the interface. Further, principles of plasma propagation to pores with the extremely small opening of a few microns are determined to be guided by the photoionization source. Within a similar setup configuration, another interface, wet microchannels, is modeled. The formation of reverse ionization waves on the channels interface when being treated by the negative polarity pulse are first identified. When channels are extended in horizontal direction having as a result a higher surface-to-volume ratio, the treatment

does not necessarily lead to more efficient coverage by fluxes due to non-uniform plasma propagation along such interface. The validation of the research on microchannels is continued with another setup in which microchannels are treated with an atmospheric pressure plasma jet. Modeling results of plasma propagation are compared with collaborative experimental research. The formation of reverse ionization waves on periodic microchannel structures is again observed, modeled, and explained. Extreme cases of rectangular microchannels that are extended in vertical directions up to several millimeters, which represent hair follicles on human skin, are modeled in contact with atmospheric pressure plasma. The propagation of plasma into the reservoir of hair-follicle-like structures is then demonstrated within the model and supported with a literature search. An atmospheric pressure plasma jet is also used in contact with another interface modeling abrupt change in the height of the surface, known as step barriers. The modeling and collaborative experimental research indicate the existence of a critical height above which plasma propagation is limited. Surface kinetics on a simplified polypropylene model is implemented on a step surface. The non-uniform formation of the resulting chemicals is demonstrated on the surface following the propagation and stopping of plasma with the sensitivity of the electric field at the apexes of steps.

The aim of this dissertation is to contribute to the field of atmospheric pressure plasmas with a particular focus on interaction with solid and liquid interfaces of a complex morphology. Fundamental research in this field has an impact on the development of plasma sources that can be used in medicine, catalysis or microfluidic devices. Identifying shared principles governing plasma interaction with common interfaces like micropores, microchannels, microcapillaries, and step barriers can significantly advance the field's progress.

Chapter 1 Introduction

Plasma as a phenomenon is widely researched. While there is a strict definition for the term plasma (defined in paragraph 1.1), physics and chemistry can deviate from one specific type of plasma to another. The type of plasma discussed in this dissertation is atmospheric pressure plasma, a type of low-temperature plasma. While low-temperature plasma is a general term for broad-pressure ionized gas systems with electron temperature significantly exceeding the overall gas and ion temperatures, atmospheric pressure plasma is a narrow definition for plasmas sustained at ambient pressure. As discussed in detail in the body of the dissertation, atmospheric pressure plasmas have a wide range of existing and potential applications, from medicine to catalysis. However, the rapid development of new technologies and the undiscovered effects of existing ones require studies of more complex systems with many synergistic effects. An example of such systems is atmospheric pressure plasma interacting with the complex interface (any interface that is not planar and/or uniform). This new field of study is gaining attention in the scientific community due to the potential benefits in a number of upcoming technologies. This dissertation aims to study computationally the interaction between atmospheric pressure plasmas and some of the materials with typical interface patterns such as micropores, dry/wet microchannels, microcapillaries and step barriers. The discovered common laws in such interactions can directly impact the development of methods to treat different skin problems, including cancer, modification of microfluidic devices and treatment of their liquid content, and modification of microporous plastics and porous supports. This chapter presents a short description of fundamental atmospheric

pressure plasma knowledge. The description is continued with a discussion of commonly used sources of such plasmas and typical applications.

1.1 Basic Phenomena in Plasmas

Plasma is an essential part of nature, commonly referred to as the fourth state of matter. However, Francis Chen provides a more accurate definition, stating: “A plasma is a quasineutral gas of charged and neutral particles which exhibits collective behavior” [1]. To clarify this definition, three typical plasma characteristics are required: Debye length (λ_D), Debye sphere, and plasma frequency (ω_p) [2–7]. The Debye length (λ_D) can be expressed as

$$\lambda_D = \sqrt{\frac{\varepsilon_0 k T_e}{n_e e^2}} \tag{1.1}$$

where ε_0 is the dielectric permittivity constant, k is Boltzmann’s constant, e is an elementary charge, T_e is the temperature of electrons, and n_e is the density of electrons. It refers to the consideration of a single charged particle in the ionized gas. Every such charged particle that is surrounded by other charged particles is screened from the rest of the plasma, starting from a certain distance. The screening effect is called Debye shielding, and the characteristic distance is called the Debye length. Quasineutrality is satisfied if the scale size of the considered matter (L) is overwhelmingly larger than the Debye length.

An area constrained by a sphere with a radius equal to the Debye length is called a Debye sphere. The number of particles inside a Debye sphere is another important parameter for plasma, expressed by the following formula:

$$N_D = \frac{4}{3}\pi n_e \lambda_D^3 \tag{1.2}$$

To satisfy for collective behavior, the number of particles in a Debye sphere should significantly exceed 1.

Finally, the plasma frequency is a fundamental characteristic that determines the timescale of processes in plasma. The plasma frequency can be expressed as:

$$\omega_p = \sqrt{\frac{n_e e^2}{\varepsilon_0 m_e}} \tag{1.3}$$

This characteristic, expressed as $1/\omega_p$, can be compared with the typical collisional time in neutral gas, denoted as τ. To differentiate motion in plasma from that in neutral gas, the frequency of collisions with neutrals should be lower than the plasma frequency.

The above theory can be summarized with a simple set of criteria for plasma:

1. $\lambda_D << L$ (The size of the system is much larger than the Debye radius of plasma.)
2. $N_D >> 1$ (The number of particles in the Debye sphere is large.)
3. $\omega_p\tau > 1$ (The plasma frequency is larger than the characteristic frequency collisional frequency in the gas.).

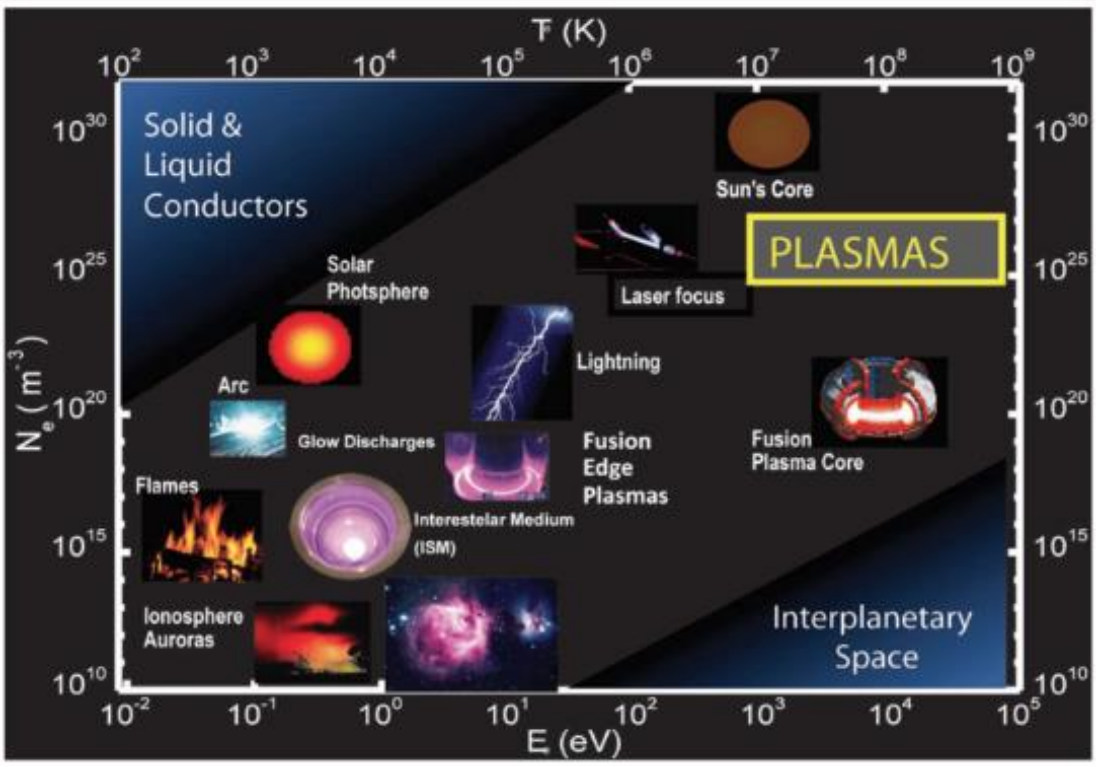

Figure 1.1. Classification of different plasmas by electron temperatures and densities [8].

Such a general definition implies that many physical systems meet the criteria for being classified as plasma. Different types of plasmas are summarized in Fig. 1.1 based on electron

temperature and electron density. There are different classifications of plasmas. In this dissertation, the classification of plasmas is of interest for the following groups: thermal plasmas and non-thermal plasmas (also called low-temperature plasmas (LTPs)). In plasmas, local thermodynamic equilibrium results from equality or quasi-equality between species' mean energies (in other words, temperatures). Deviation of electron temperature from heavy species temperature results in a local thermodynamic non-equilibrium [4], [9]. Electron temperature, different from heavy species temperature, results in deviation of other temperatures such as vibrational or rotational [10,11]. In such plasmas, the relation between species temperatures generally follows $T_e > T_v > T_r \approx T_i \approx T_n$, where T_e is the electron temperature, T_v is the vibrational temperature (for molecules), T_r is the rotational temperature (for molecules), T_i is the ion temperature, and T_n is the temperature of neutrals [4,12,13]. In different gas environments, such a relation can lead to an occurrence of complex chemistry [4,14,15]. The range of conditions for non-thermal plasmas typically spans from mTorrs to atmospheric pressure and from room temperature to a few 10s K elevation from ambient [16]. Chemical components and a range of conditions make such types of plasmas potentially applicable for many industrial needs, such as biomedicine and catalysis. Typical operating systems for such types of plasmas are usually low/atmospheric pressure systems, low-power systems, or pulsed discharges. In this thesis, the major focus is on pulsed discharge systems such as atmospheric pressure plasma jets (APPJs) and surface dielectric barrier discharges (SDBDs). These discharge systems are discussed in detail in the next sections.

The above-described properties of atmospheric pressure plasmas are attractive for various applications in surface treatments. Development of atmospheric pressure plasma technologies is essential because such technologies are potentially low-cost due to not requiring pressure chambers, which are typically expensive. Important chemical components of atmospheric pressure plasmas (APPs) can be particularly attractive for plastic modifications, water purification, and skin treatment [17–19].

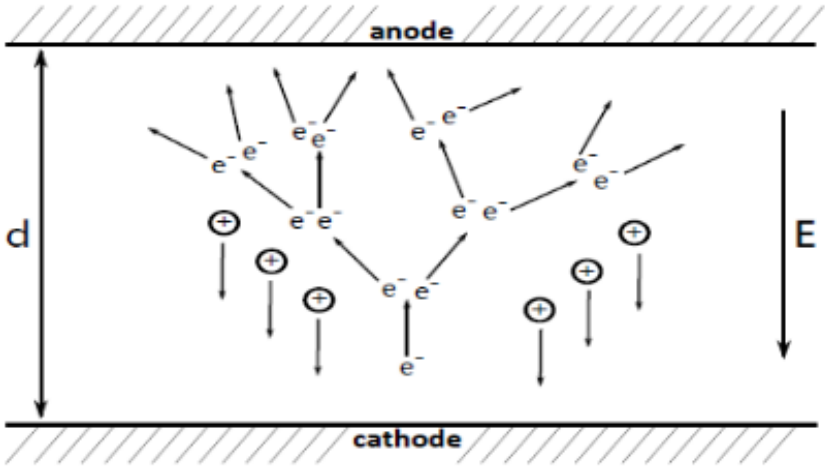

Figure 1.2. Avalanche initiation process in a discharge system [20].

1.2 Phenomenon of Breakdown in Gases

Classical studies of LTPs begin by discussing the gas breakdown phenomenon [21,22]. Gas breakdown occurs when ionization under external action is produced and sustained. The effect of a sudden increase in ionization in gas in an applied electric field is called an electron avalanche [23–25]. The breakdown formation mechanism following an avalanche is described under Townsend's theory [26]. In this theory, free electrons are typically present in the gas, formed due

to the action of cosmic rays. When placed in an electric field, they accelerate, collide with neutral atoms/molecules, ionize these species, and create new electrons that continue undergoing the same process as the initial electrons. The schematic image of the avalanche process is demonstrated in Fig. 1.2. The discharge is considered self-sustained when the ionization rate is high enough to maintain the concentration of electrons. The voltage that provides the conditions to break down the gas gap is given by Paschen's[27]:

$$V_{breakdown} = \frac{Bpd}{\ln(Apd - \ln[\ln[1+\frac{1}{\gamma}]])} \tag{1.4}$$

where $V_{breakdown}$ is the breakdown voltage, *A/B* are the gas specific constants, *pd* is the major parameter in Paschen's law, a product of gas pressure (*p*) and gap distance (*d*), and γ is the secondary emission coefficient. The classical Paschen's curve is demonstrated in Fig. 1.3. Typical

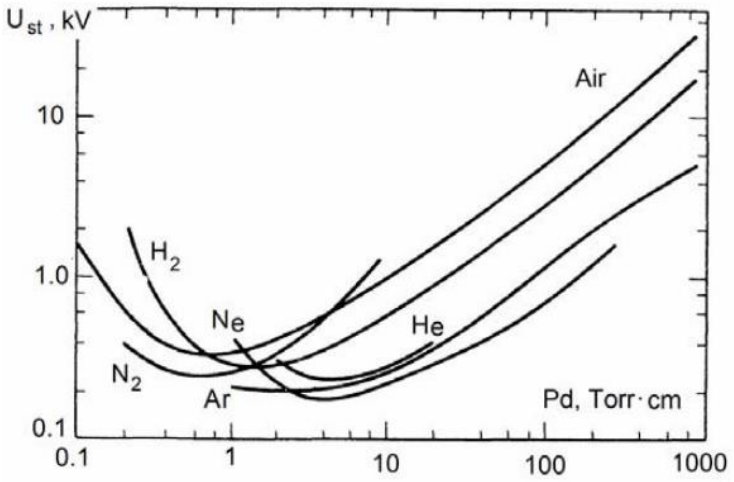

Figure 1.3. Classical Paschen's curves for different gases [28].

values for the pd parameter are within 0.1 – 1000 Torr·cm. Voltage required for gas breakdown has a distinguishing minimum of 100s V.

1.3 Electron Energy Distribution Functions and Electron Temperature

A typical characteristic that is used to describe LTPs is the electron energy distribution function (EEDF). Since the regimes of plasmas operation strongly depend on the energy that electrons can gain in the system (typically from an applied electric field) and deliver into the gas, EEDF is used in descriptions of most LTP systems. This EEDF characteristic is especially important for computational works since it is used to identify rates of chemical reactions. It is a probabilistic function that defines the fraction of electrons having a certain energy. The equilibrium distribution function is called Maxwellian [4,29,30] and has the following expression:

$$f(\varepsilon) = \sqrt{\frac{4\varepsilon}{\pi (kT_e)^3}} \exp(-\frac{\varepsilon}{kT_e}) \tag{1.5}$$

where ε is the energy of the electrons, k is Boltzmann's constant, and T_e is the electron temperature.

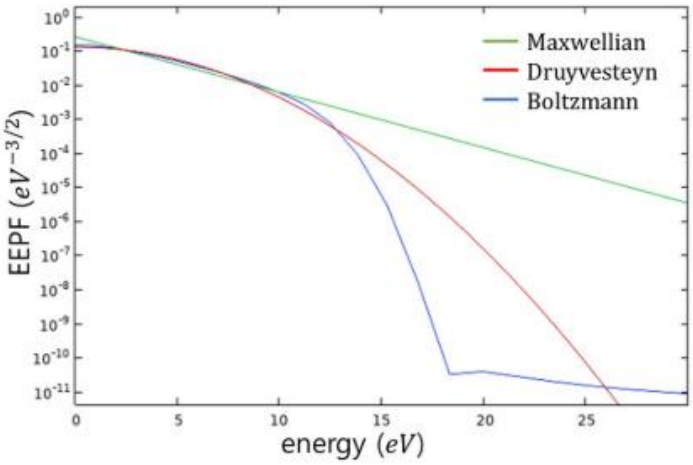

Figure 1.4. Maxwellian, Druyvesteyn, and Boltzmann distribution functions [31].

The classic LTP scenario is when the EEDF deviates from the Maxwellian distribution function. A famous example of the models of non-equilibrium functions is, for example, Druyvesteyn [32].

A more real EEDF can be obtained from the solution of Boltzmann's equation (described in detail in the next chapter). These distribution functions are demonstrated in Fig. 1.4. Further, EEDFs are critical to identifying another important characteristic: mean electron temperature (T_e) is a critical characteristic for studying LTPs. Typical values of T_e in most LTPs are 1–10 eV [4,21].

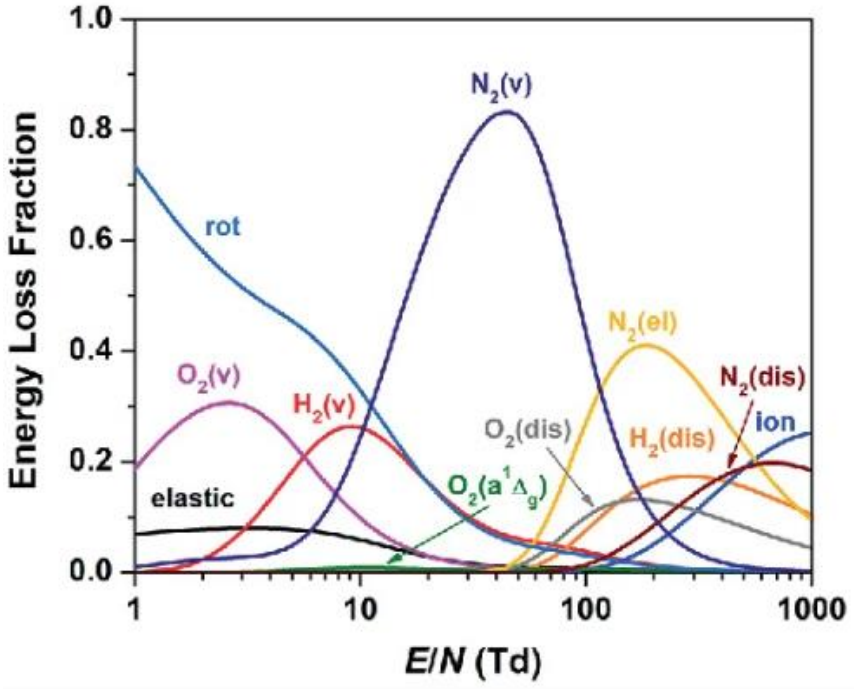

Figure 1.5. Energy loss fraction for different processes in air-hydrogen plasma as a function of reduced electric field [33].

1.4 Reduced Electric Field

Reduced electric field or E/N, where E is the electric field and N is the gas density, is a characteristic scaling parameter for LTPs [4,21,34,35]. It is measured in Td, where 1 Td = 10^{-17} V×cm^2. E/N can represent the physical meaning of energy input per gas molecule. This relation

can serve as a basic scaling law to determine electron temperature (1.7) from the electron balance equation (1.6). See

$$\frac{d}{dt}\left(\frac{3}{2}n_e k_b T_e\right) = \frac{n_e q^2 E^2}{m k_m N} - \frac{2m_e}{M} k_m n_e N \frac{3}{2} k_b (T_e - T_g) - n_e N \sum_i k_i \Delta\varepsilon_i \text{ , and} \tag{1.6}$$

$$T_e = T_g + \left(\frac{3k_b m_e}{M}\right)^{-1} \left(\frac{q^2}{m_e k_m^2} \left(\frac{E}{N}\right)^2 - \frac{\sum_i k_i \Delta\varepsilon_i}{k_m} \right) \tag{1.7}$$

where n_e is the electron density, T_e is the electron temperature, k_b is Boltzmann's constant, q is the elementary charge, E is the electric field, N is the gas density, k_m is the total momentum transfer rate constant, m_e is the mass of the electron, M is the mass of the molecule of the gas, T_g is the gas temperature, i is the counting number for the elementary process in the gas, k_i is the rate coefficient for the elementary process in the gas, and $\Delta\varepsilon_i$ is the energy gap in the process. An example of energy fraction channeling depending on E/N is demonstrated in Fig. 1.5.

1.5 Streamer Phenomenon and Bulk Ionization Waves

Ionization waves (IWs) [21,36,37] are critical phenomena in many gas-electrical processes, such as gas breakdowns. The shape of the ionization wave can be different, but at atmospheric pressure it typically has a spherical shape and propagates, leaving a conductive channel behind. Such a channel is typically named a streamer in the literature [38–40]. The typical speed of such IWs is 10^5–10^8 m/s [38–40]. The usual width of a channel ranges from 100s μm to a few mm [38–40]. The lifetime of the streamer is 100s ns depending on the voltage pulse [38–40]. The limitations are associated with heat losses and gas density. Streamers are typically classified as positive polarity driven and negative polarity driven. The classification is typically associated with the applied electric field and the resulting direction of electric field lines (usually produced by

discharge electric setup). Positive and negative polarity streamers are demonstrated in Fig. 1.6. The mechanism of formation of streamers relies on one of two sources: either electron impact

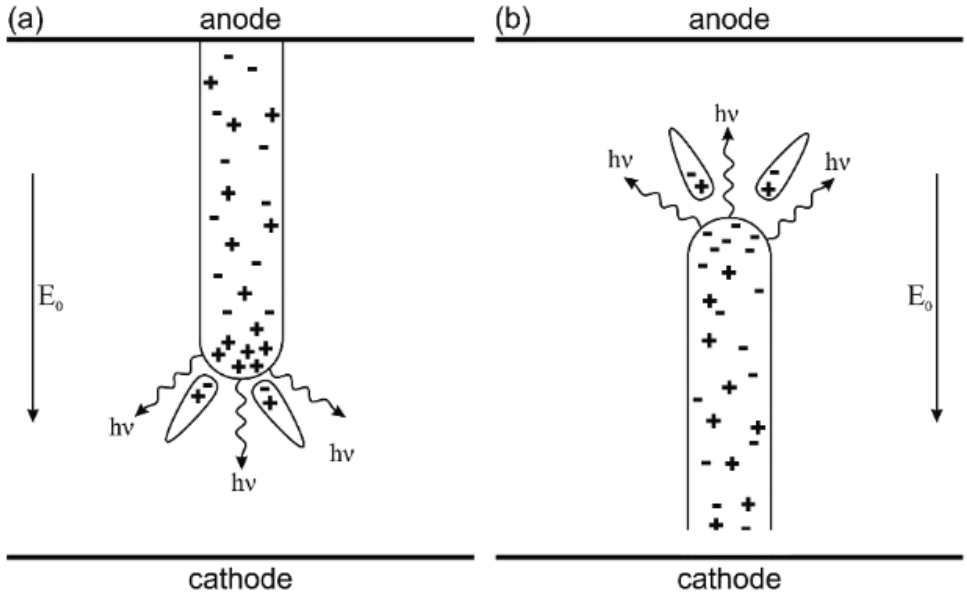

Figure 1.6. Mechanism of propagation of streamers that are a) cathode directed, b) anode directed [41].

ionization or photoionization. In positive-polarity-driven streamers, electrons are forced in the direction against the propagation of the channel, while ions are moving along the axis of propagation of the IW. Since ions are heavy and electrons are much lighter, such a streamer relies mainly on photoionization sources. Conversely, in negative-polarity-driven streamers, electrons are forced away from the plasma channel; thus, the electron impact ionization source dominates in streamer propagation.

1.6 Surface Ionization Waves

The above-described streamer phenomenon is when the IW propagates in the gas phase without encountering any other substances or materials. When the IW interacts with non-gaseous

substances, there are several scenarios. Such scenarios can be roughly sorted by two features: interaction with solids and liquids and interaction with dielectrics and conductors. Interactions with liquid are discussed in more detail in the following sections. The key similarity between solids and liquids is the density of the media. At atmospheric pressure, gas density is in the order of 10^{19} cm^{-3}, while solids and liquids are 10^{22} cm^{-3}. Propagation of steamers through such high-density materials is restricted. In the case of conductive materials, the electric charge continues propagation through the conductor. In the case of dielectrics, the current is limited, and the interface collects the charge; the surface charge then produces an electric field that has a component parallel to the interface that maintains the propagation of the IW along the surface, called a *surface ionization wave* (SIW) [42–45]. This phenomenon is critical in this dissertation and will be discussed in more detail in the following sections.

1.7 Atmospheric Pressure Plasma Jets (APPJs)

To produce LTPs, different sources are invented, investigated, and widely used. One of the sources that has been actively used for a variety of applications is the APPJ [46–49]. The critical feature of this source is that it typically utilizes a noble gas. It consists of an injector of feeding gas that contains a powered electrode. The typical environment surrounding an APPJ is humid air. The electrical operating conditions of APPJs are in the range of 100s V or several kV and kHz frequencies. The typical gas flow speed of the feeding gas is several standard liter per minute slm. When applied to a material, an APPJ is normally placed a few mm to a few cm away from the surface. The ground is typically placed below the material, or the material acquires floating potential. APPJs typically exhibit multibullet behavior [50,51]. This means that a series of IWs are launched with a specific interval. The distinguishing feature of this source is the high flux of

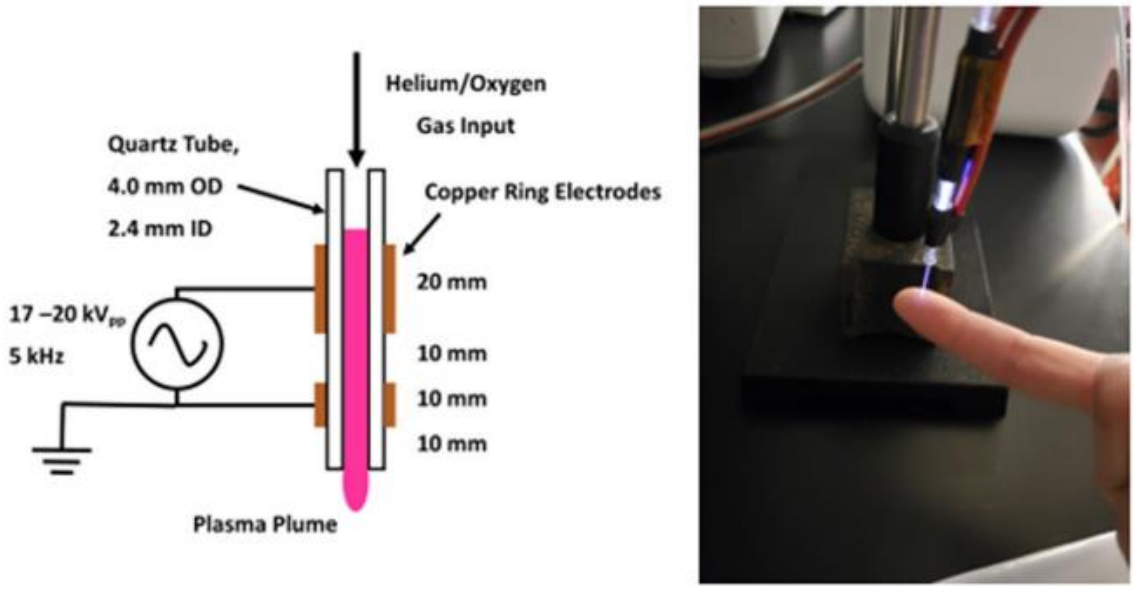

Figure 1.7. Schematic image of an atmospheric pressure plasma helium jet with two powered ring electrodes (left); experimental photograph of this device applied to human tissue [60].

vacuum ultraviolet (VUV) photons and ions to the surfaces on which the APPJ is applied [52,53]. This results from an operating noble gas as a major feeding environment and multibullet behavior. The schematic image of an APPJ is demonstrated in Fig. 1.7. APPJs find applications in plasma medicine [54,55], liquid treatment [56,57], and ozone production [58,59].

1.8 Surface Dielectric Barrier Discharges (SDBDs)

Another popular atmospheric pressure plasma source is an SDBD [61–63]. This type of discharge is a form of dielectric barrier discharge (DBD) [64–66]. In DBDs, the discharge system consists of parallel metal plates (one or both of which are covered with dielectric materials) powered by electrical systems. The dielectrics are placed to limit the current. The discharge in the form of a streamer is typically produced in such systems near one of the electrodes and propagates to the opposite one with the applied electric field. Unlike a classical DBD, which operates with

formation of a streamer in the gas phase, an SDBD generates a streamer near the surface that directly propagates as an SIW, discussed above, when both electrodes are in direct contact with the dielectric material. In this discharge system, plasma propagates as distinct filaments or having a uniform front across the surface. The ionization is mainly sustained by the enhanced electric field produced near the interface from the charged dielectric surface. Typical charge density in SDBDs is 10^9–10^{13} cm^{-3} generated by pulses of several kV with a frequency of several kHz to several 10s of kHz, while the speed of SIW propagation is 10^7–10^8 cm/s [67]. Directly generating the discharge on a dielectric surface saves energy and maximizes fluxes of photons, ions, and reactive species delivered to the interface. One of the classical applications of this discharge is flow control [68]. Due to direct contact with the interface, this discharge system is promising for different surface

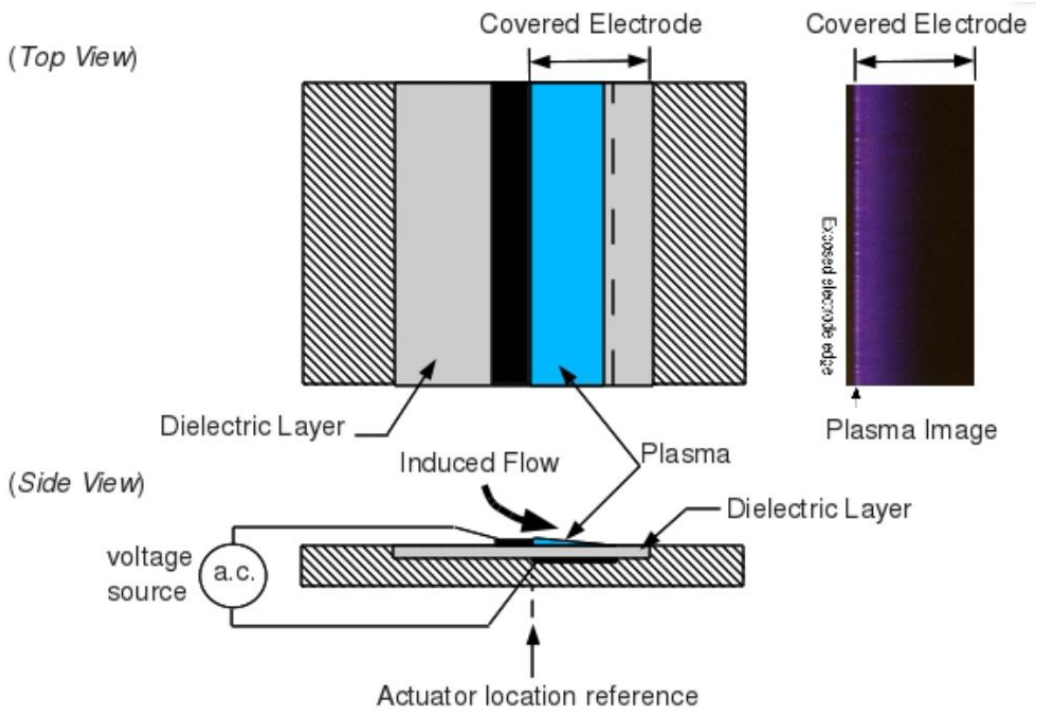

Figure 1.8. Schematic image of the surface dielectric barrier discharge in top view (top-left); experimental photograph of top view (top-right); side view of surface dielectric barrier discharge (bottom view) [71].

treatments that exhibit dielectric properties. For example, this type of discharge can be used in the food industry [69] and in polymer treatment [70]. The schematic image of this discharge system is demonstrated in Fig. 1.8.

1.9 Gas Phase Plasma-Chemistry

As discussed above, APPs exhibit non-equilibrium behavior. This means that the description of such systems strongly relies on an understanding of chemical processes [4,72]. Electrons that gain energy from an applied electric field transfer this energy to the gas by heating it, ionizing it, and shifting its chemical composition. The new chemicals subsequently alter the balance and interact to form new products. Plasma chemistry is complex due to the high number of degrees of freedom in the system; these are due to the presence of electrons, ions (in the ground and in excited state), radicals, excited molecules and atoms (in higher excited energy states),

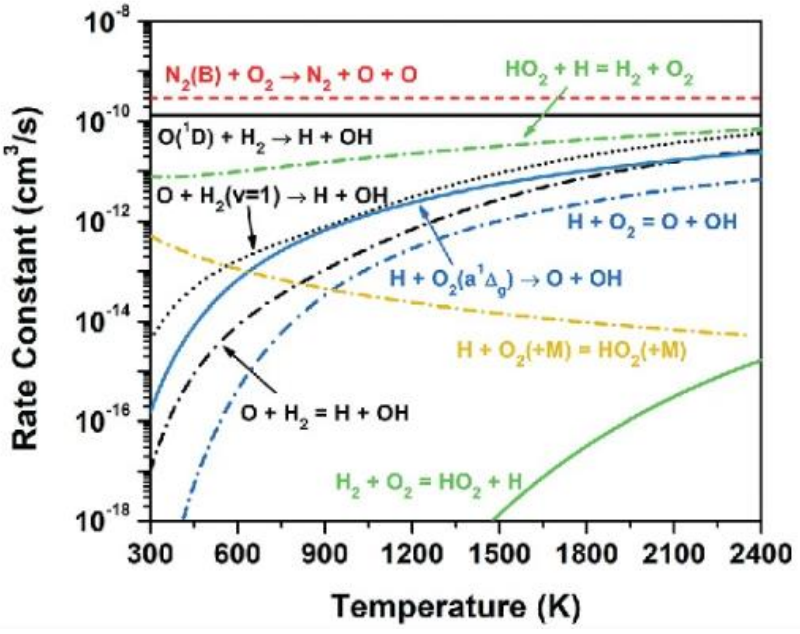

Figure 1.9. Rate coefficients for elementary processes in hydrogen-air plasma presented as a function of gas temperature [33].

photons, and electric fields (which define the speed of some reactions). Typical plasma chemical processes, examples, and characteristic values are summarized in Table 1.

Table 1.1. Characteristic values for the elementary processes in plasmas.

Process Name	**Example of the Process**
Electron impact ionization	$e + Ar \rightarrow e + Ar^+ + e$
Electron impact electronic excitation	$e + He \rightarrow e + He^*$
Electron impact rotational excitation	$e + O_2 \rightarrow e + O_2(rot)$
Electron impact vibrational excitation	$e + N_2 \rightarrow e + N_2(v=1)$
Electron impact dissociation	$e + H_2 \rightarrow e + H + H$
Electron impact momentum transfer	$e + Ne \rightarrow e + Ne$
Electron impact superelastic collision	$e + He^* \rightarrow e + He$
Electron attachment	$e + O + H_2 \rightarrow O^- + H_2$
Energy relaxation	$He^{**} + N_2 \rightarrow He^* + N_2$
Penning ionization	$He^* + H_2O \rightarrow He + H_2O^+ + e$
Chemical reaction with excited state	$O^* + N_2 + N_2 \rightarrow N_2O + N_2$
Electron–ion recombination	$e + Ar^+ \rightarrow Ar^*$
Charge exchange	$He^+ + H_2O \rightarrow He + H_2O^+$
Ion–ion recombination	$Ar^+ + O^- \rightarrow Ar^* + O$
Spontaneous radiation	$Ar^* \rightarrow Ar + hv$
Photoionization	$hv + N_2 \rightarrow N_2^+$
Photodissociation	$hv + O_2 \rightarrow O + O$

The probability of a reaction occurring depends on multiple parameters, such as gas temperature, pressure, electron temperature, and some molecular or atomic parameters. The speed of a bi- or tri-molecular reaction is defined with a rate coefficient. In the general case, such a rate coefficient has an Arrhenius form measured in cm^3/s or cm^6/s, accordingly [73]:

$$k_r = AT^n e^{-\left(\frac{E_A}{kT}\right)} \tag{1.8}$$

where k_r is the rate coefficient, A is a preexponent factor, T is the gas temperature, k is Boltzmann's constant, and E_A is the activation energy needed for a reaction. Classical values for a bimolecular reaction rate coefficient are 10^{-10}–10^{-14} cm^3/s (for charge recombination, this rate is elevated due to Coulomb attraction and is 10^{-7} cm^3/s). Examples of the rate coefficient as functions of gas temperature are demonstrated in Fig. 1.9.

For trimolecular reactions, the typical rates are 10^{-29}–10^{-33} cm^6/s. Electron impact processes are typically defined by cross-sections that are measured in cm^2. Electron impact processes are mainly a function of electron energy. Typical dependence of the cross-section on electron energy is demonstrated in Fig. 1.10. Classical values of electron impact cross-sections are 10^{-20}–10^{-16} cm^2. Cross-sections also characterize photon–atom/molecule interactions. These cross-sections are functions of photon energy or wavelength and have typical values of 10^{-18}–10^{-16} cm^2 at the VUV energy range. The source of photons is the spontaneous emission from the higher excited states characterized by the frequency of range 10^5–10^9 s^{-1} [74].

1.10 Plasma Liquid Interactions

APPs can be applied in various environments. Real applications extend to complex systems

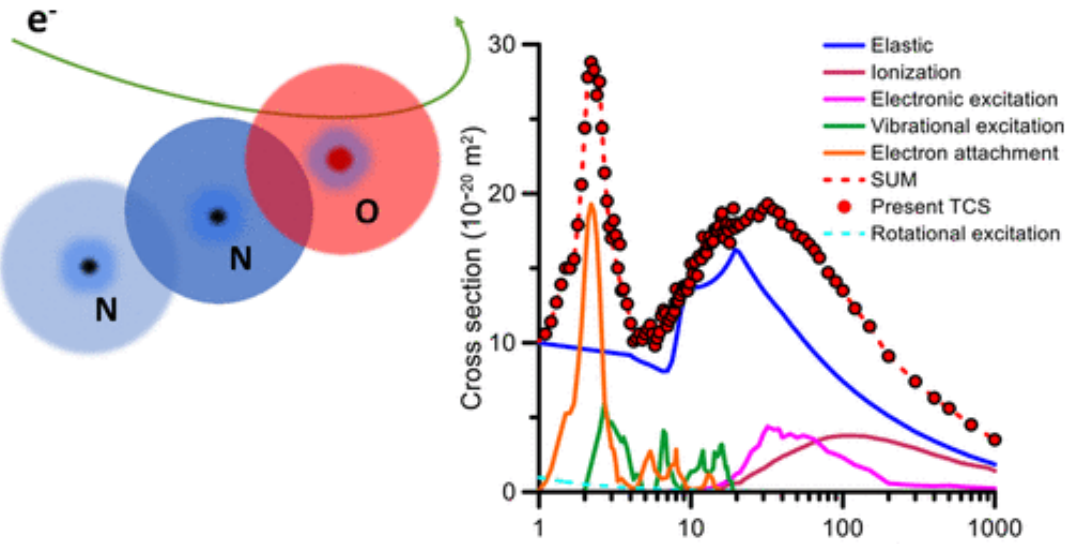

Figure 1.10. Cross-section graphical data presented for electron impact of N_2O molecule as a function electron energy [75].

that have liquids or vapors. Many actual industrial systems can benefit from using plasmas at

atmospheric pressure. Such applications include biomedicine, water purification, and ecology. Applications of plasmas to liquids have three major forms [19,76]: 1) direct discharge in liquids, 2) discharge in a gas phase that contacts a liquid interface, and 3) multiphase discharges such as in bubbles sustained in liquids. In this thesis, the focus is on the plasmas generated in the gas phase that propagates encountering liquids.

When plasma is generated under atmospheric pressure and propagates as a form of streamer, it typically strikes the liquid surface as a surface of solid material and continues propagation based on the dielectric or conductive properties of the liquid. The difference between solid and liquid cases is typically in the ability of different gas phase species to solvate in the liquid. Solvation is a process of reorganizing the molecules' orientation inside the liquid by another molecule (that is being solvated) that penetrates the liquid. Such processes depend on intermolecular forces of attraction and forces that attract the solvent. This process occurs if the balance of such forces shifts to benefit solvation. As a result of the solvation process, many processes of the liquids can be changed. For example, the color, the viscosity, and the pH of the liquid can be altered. Plasma interaction is known to produce hydronium ions H_3O^+. These ions are proven to shift the pH of liquids [76]. Since the lifetime of streamers on the liquid interfaces is limited with 100s of ns or a few μs, the concentration of possible solvents is limited.

Additionally, the limitation extends to the volumes of liquids that can benefit from interactions with APPs. Typical liquids that are attractive for plasma treatment have a high surface-to-volume ratio. Examples of such liquids include water droplets, liquids in microfluidic reactors, and bioliquids that cover wounds. Some of these examples are used to demonstrate their interactions with APPs in this thesis. Liquids can additionally benefit from plasmas by solvating charged species. Many liquids, such as water, exhibit both dielectric and conductive properties.

The electromechanical role of liquid that an IW encounters during propagation defines plasma behavior on the interface. A more detailed analysis is presented in the body of the thesis. Additionally, closely propagating plasmas influences the liquid interface with the photon fluxes. VUV photons can dissociate or ionize molecules in the topical layer of the liquid. The products

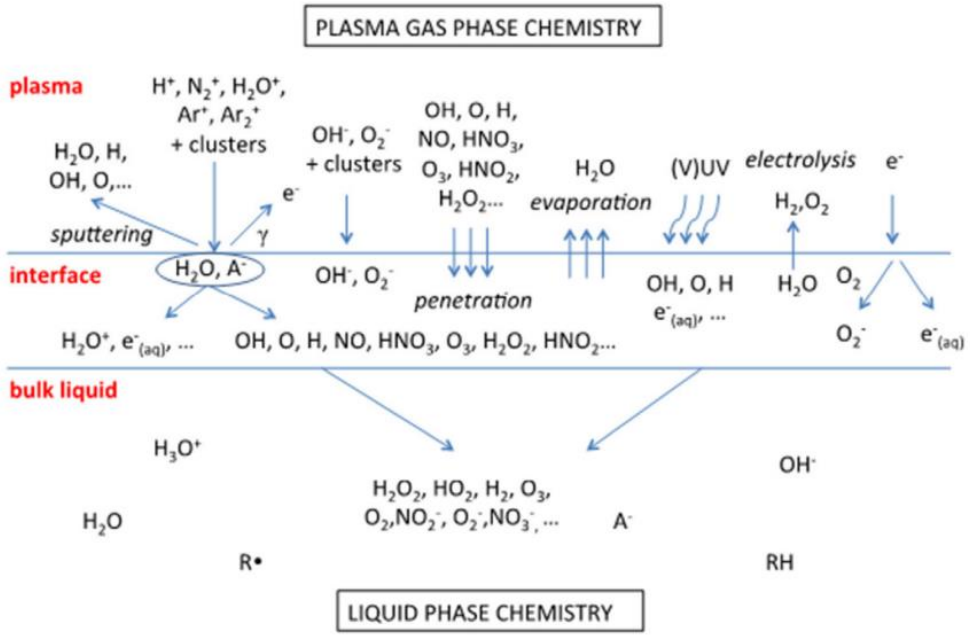

Figure 1.11. Mechanism of species in plasma influencing a simple flat liquid interface [76].

subsequently penetrate liquid depth. The mechanism of the reactive species interacting with the liquid is demonstrated in the Fig. 1.11.

1.11 Chemical Interaction of Plasmas with Interfaces

Interfaces exposed to plasmas can exhibit a behavior that alters surface chemical composition. Plasma interactions with surfaces attract interest due to the high degree of freedom of the system and the high number of high-energy species involved in the interaction. Such features

allow surface modifications that can replace high-temperature processes if controlled or unique. Examples of plasma surface interactions that involve kinetic components are plasma catalysis [76] and plasma plastic modifications [77].

The principles that determine how plasmas interact with interfaces can be broken down into the physics of interaction described in previous sections, surface chemistry, photon–surface interaction, and ion–surface interaction. Chemical interactions of plasmas with the interface are a part of the focus of this dissertation. In this dissertation, surface chemistry is demonstrated in the process of polymer treatment. Polymers have been treated by plasma in many industries. Various polymers are used for applications such as packaging [78] and human implants [79]. However, polymers are typically hydrophobic. Hydrophobicity restricts the applications mentioned above, limiting dying and biocompatibility. APPs are demonstrated to have a sufficient effect on at least temporal alteration of surface properties, making polymers hydrophilic [80]. The mechanism behind this effect is hidden under the chain of reactions that allows the fixation of oxygen atoms on a surface. The schematic image of these processes is demonstrated in Fig. 1.12. Typically, in plasmas, radicals and excited species interacting with polymers initiate surface chemistry mechanisms by abstracting hydrogen atoms from the surface, initiating a chain of reactions. The major importance of the chain of reactions is the attachment of oxygen atoms and molecules to the vacant bonds. Termination of the chain happens when stable forms of connections are occurring.

Oxygen atoms change the surface energy of the interface. Polar water molecules interacting with such a surface begin, instead of repelling, to attract. The material becomes hydrophilic.

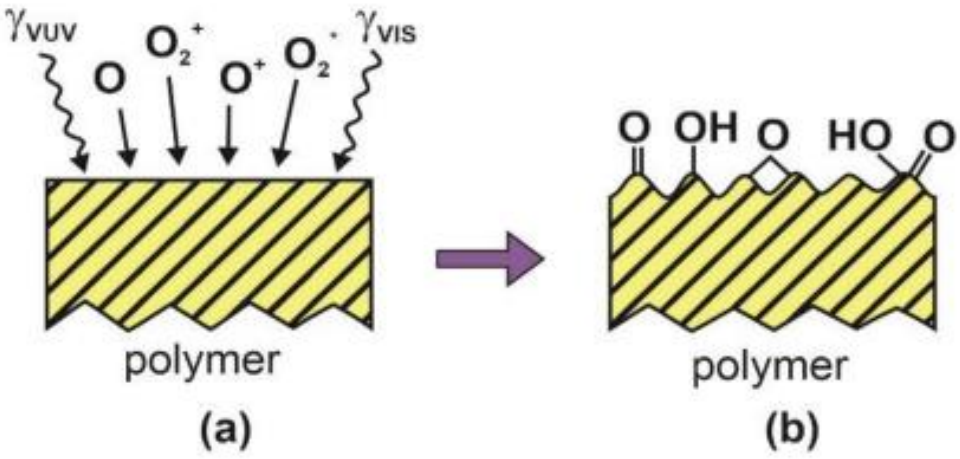

Figure 1.12. Schematic image of atmospheric pressure plasma interacting with a polymer surface: a) prior to surface modification, b) after surface modification [81].

1.12 Atmospheric Pressure Plasmas and Complex Surfaces

Recently, advances in studies of how APPs interact with various interfaces have allowed a detailed description of the underlying mechanisms of interaction of plasmas with different phases of matter. The interaction between different types of APPs and flat, homogeneous interfaces is relatively well understood [82,83]. However, most topical areas of materials are rather non-smooth and/or non-homogeneous in real materials. Such surfaces are united under the term *complex surfaces*. Examples of such interfaces include porous support of catalysts [84], skin with wrinkles or hair follicles [85], microfluidic reactors [86], and microdroplets [87]. All these materials have known benefits from interactions with APPs [88–90]. However, to control the effects of APPs on such materials, one must understand the principles underlying how plasmas interact with complex interfaces or simplified examples of such surfaces. A standard primitive prototype of a complex

interface can be an array of microchannels (dry or water-filled), vertically extended microchannels, an array of micropores, or step barriers. An array of microchannels can represent dry or wet wrinkled skin, vertically extended microchannels can represent hair follicles, an array of micropores can demonstrate combustion filters or catalyst supports, and step barriers can represent any abrupt change in the height of an interface. Principles determining how plasmas interact with such structures are investigated in some research work [91–93]. However, there is a lack of research that determines the main laws or patterns governing such interactions and groups them into categories.

1.13 Role of Modeling in Studying Atmospheric Pressure Plasmas

Studying physical and chemical systems usually requires a combined approach utilizing theoretical, modeling, and experimental work together. The complexity of modern technologies requires profound expertise in all the aforementioned approaches. Typically, researchers have expertise in one of the approaches and collaboratively work to tackle complex problems, sharing knowledge. Similar approaches are common in the field of APPs. The role of modeling in APPs is critical. This is the central approach used in this dissertation.

Unlike theory, the modeling perspective can incorporate many physical and chemical phenomena in one model. Experiment, the only valid method to prove any idea, is typically expensive and time-consuming. Modeling is usually required to validate some experimental theories or provide guidance for experimental research in complex physical and chemical systems with limited theoretical research opportunities. Modeling thus plays one of the most significant roles in the field of APP research. This is a consequence of APP research involving such complex multiphysics and chemistry problems that have so many degrees of freedom.

Multiple different computer modeling methods have been developed for APPs at the time of writing this dissertation. Since chemistry is critical, some modeling work uses 0-dimensional (0-D) or global models [94]. These models typically include the simple discharge model adapted for average characteristics, the solution of Boltzmann's equation, the electron energy balance equation, and a set of kinetic equations. Global models are effective for studying gas and liquid chemistry due to their low time and computer costs. However, to understand space-specific plasma propagation, higher-dimensional models are required. Most popular approaches to modeling APPs are typically 2- or 3-D due to their ability to address inhomogeneous propagation in space. These models usually contain equations to address fluid flows, streamer propagation, and gas and liquid phase chemistries.

There are two general approaches to modeling plasmas: fluid and kinetic. Multifluid models are typical approaches to address the streamer phenomena at atmospheric pressure [95]. This is mainly due to the mean free path in such plasmas being much smaller than the considered dimensions of the phenomena. For most studies in this dissertation, a 2-D plasma-hydrodynamic model was used.

1.14 Motivation

As discussed in the previous paragraph, a lack of consistent knowledge about the application of APPs to complex interfaces leads to limited control of the desired effects and lower yield of new technologies. Common patterns frequently appear in the surface morphologies of both nature and technologies, which are attractive. Propagation of APPs in the form of SIWs can be largely affected by the composition of the interface: surface roughness, inhomogeneous parts, and phase change. When an IW encounters a change on an interface, the propagation can be affected

by the formation of local electric fields, by the shadowing of IWs, or by charge losses on conductive elements. For these reasons, the residence time of plasmas and the uniformity of treatment can differ depending on the interface type. It is of interest to investigate the standard surface patterns that emerge when existing or upcoming technologies come into contact with APPs. Surface patterns that can represent real substrate configuration (microporous dielectrics, arrays of microchannels, microcapillars, and step barriers) are mentioned in the previous section. Different APP sources can be used as a basis for new technologies that enhance surface properties. Ambient conditions of operation for APPs mean that new technologies are potentially inexpensive. The range of applications also extends to treating human tissue, allowing biomedical technologies to be developed. These facts motivated the work that has been done for this dissertation.

1.15 Scope of the Dissertation

This dissertation contains several chapters. Chapter 2 discusses modeling of APPs. This dissertation is written mainly based on the computer simulations performed using nonDPDSIM, a 2-D plasma-hydrodynamic model executed on an unstructured mesh. In this section, critical principles of the work of this code are discussed along with the description of core equations that are solved and methods of their solution.

In Chapter 3, the results of modeling an SDBD setup applied on a microporous dielectric interface are presented and discussed. This chapter outlines the principles of interaction between SIWs and a porous structure; identifies the key features of interaction, depending on the shape of the pores; and points out an important benefit of plasma penetration into pores with critically small openings.

The computational investigation of similar SDBD configurations on a different type of interface is continued in Chapter 4. In this piece of research, the dielectric substrate contains wet microchannels. In this study, the critical difference between the uniformity of treatment and the behavior of SIWs for both negative- and positive-polarity-driven plasmas is demonstrated. The patterns of water-surface layer modifications resulting from plasma treatment are outlined.

Chapter 5 presents a continuation of the research on microchannels. In this study, the computer 2-D study in nonPDPSIM on APPJ applied for treating dry and wet microchannels is demonstrated. This chapter validates the results of the computations with the experimental data. It also presents the mechanism of propagation of negative SIWs across structures; and uncovers and explains the formation of reverse IWs.

A critical example of microchannels are capillaries extended in vertical directions that can represent hair follicles. Chapter 6 describes a 2-D computational study of the APPJ applied on a simulated human skin with resolved hair follicles. It demonstrates that plasma generated in ambient conditions can penetrate human hair follicle-like structures and treat the interior. This finding is supported by the literature search also presented in Chapter 6.

Chapter 7 is dedicated to a 2-D computational study of an APPJ on a surface that contains step barriers. This study identifies that there is a critical height of up-barriers above which SIWs are not propagating. The results of this research are validated with the experimental data performed by the collaborating experimental group. Surface chemistry is studied computationally on such interfaces that simulate polypropylene. Critical patterns of the formation of chemicals on such interfaces are identified based on knowledge of the behavior of SIWs on step barriers.

Chapter 8 presents a summary and concluding remarks. It also outlines the perspectives that future research might take.

1.16 References

[1] F. F. Chen, Physical Review **33,** *Introduction to Plasma Physics and Controlled Fusion*, 33: Springer International Publishing (2016).

[2] L. Tonks and I. Langmuir, Phys. Rev. **33,** 195 (1929).

[3] D. A. Frank-Kamenetskii, *Plasma: The Fourth State of Matter*, Springer US (1972).

[4] A. Fridman, *Plasma Chemistry*, Cambridge University Press (2008).

[5] P. M. Bellan, *Fundamentals of Plasma Physics*, Cambridge University Press (2006).

[6] E. E. Salpeter, Phys. Rev. **120,** 1528 (1960).

[7] D. Pines and D. Bohm, Phys. Rev. **85,** 338 (1952).

[8] F. L. Tabares and I. Junkar, Molecules **26,** 1903 (2021).

[9] D. Schriver, M. Ashour-Abdalla and R. L. Richard, J. Geophys. Res. Sp. Phys. **103,** 14879 (1998).

[10] J. G. Parker, Phys. Fluids **2,** 449 (1959).

[11] E. Weitz and G. Flynn, Annu. Rev. Phys. Chem. **25,** 275 (1974).

[12] S. Park, W. Choe, S. Y. Moon and S. J. Yoo, Adv. Phys. X **4,** 1526114 (2019).

[13] F. Taccogna and G. Dilecce, Eur. Phys. J. D **70,** 251 (2016).

[14] M. Capitelli, R. Celiberto, G. Colonna, F. Esposito, C. Gorse, K. Hassouni, A. Laricchiuta and S. Longo, **85,** *Fundamental Aspects of Plasma Chemical Physics*, 85: Springer New York (2016).

[15] B. Eliasson and U. Kogelschatz, IEEE Trans. Plasma Sci. **19,** 1063 (1991).

[16] H. Gundel, E. Hantzsche and H. Hess, Eur. J. Phys. **12,** 39 (1991).

[17] I. Adamovich, S. D. Baalrud, A. Bogaerts, P. J. Bruggeman, M. Cappelli, V. Colombo, U. Czarnetzki, U. Ebert, J. G. Eden, P. Favia, D. B. Graves, S. Hamaguchi, G. Hieftje, M.

Hori, I. D. Kaganovich, U. Kortshagen, M. J. Kushner, N. J. Mason, S. Mazouffre, S. M. Thagard, H.-R. Metelmann, A. Mizuno, E. Moreau, A. B. Murphy, B. A. Niemira, G. S. Oehrlein, Z. L. Petrovic, L. C. Pitchford, Y.-K. Pu, S. Rauf, O. Sakai, S. Samukawa, S. Starikovskaia, J. Tennyson, K. Terashima, M. M. Turner, M. C. M. van de Sanden and A. Vardelle, J. Phys. D. Appl. Phys. **50,** 323001 (2017).

[18] I. Adamovich, S. Agarwal, E. Ahedo, L. L. Alves, S. Baalrud, N. Babaeva, A. Bogaerts, A. Bourdon, P. J. Bruggeman, C. Canal, E. H. Choi, S. Coulombe, Z. Donkó, D. B. Graves, S. Hamaguchi, D. Hegemann, M. Hori, H.-H. Kim, G. M. W. Kroesen, M. J. Kushner, A. Laricchiuta, X. Li, T. E. Magin, S. Mededovic Thagard, V. Miller, A. B. Murphy, G. S. Oehrlein, N. Puac, R. M. Sankaran, S. Samukawa, M. Shiratani, M. Šimek, N. Tarasenko, K. Terashima, E. Thomas Jr, J. Trieschmann, S. Tsikata, M. M. Turner, I. J. van der Walt, M. C. M. van de Sanden and T. von Woedtke, J. Phys. D. Appl. Phys. **55,** 373001 (2022).

[19] P. J. Bruggeman, M. J. Kushner, B. R. Locke, J. G. E. Gardeniers, W. G. Graham, D. B. Graves, R. C. H. M. Hofman-Caris, D. Maric, J. P. Reid, E. Ceriani, D. Fernandez Rivas, J. E. Foster, S. C. Garrick, Y. Gorbanev, S. Hamaguchi, F. Iza, H. Jablonowski, E. Klimova, J. Kolb, F. Krcma, P. Lukes, Z. Machala, I. Marinov, D. Mariotti, S. Mededovic Thagard, D. Minakata, E. C. Neyts, J. Pawlat, Z. L. Petrovic, R. Pflieger, S. Reuter, D. C. Schram, S. Schröter, M. Shiraiwa, B. Tarabová, P. A. Tsai, J. R. R. Verlet, T. von Woedtke, K. R. Wilson, K. Yasui and G. Zvereva, Plasma Sources Sci. Technol. **25,** 053002 (2016).

[20] R. W. Crowe, J. K. Bragg and V. G. Thomas, Phys. Rev. **96,** 10 (1954).

[21] Y. P. Raizer, *Gas Discharge Physics*, Springer Berlin Heidelberg (1991).

[22] E. E. Kunhardt, IEEE Trans. Plasma Sci. **8,** 130 (1980).

[23] H. Haether, Appl. Sci. Res. Sect. B **5,** 23 (1956).

[24] L. E. Kline and J. G. Siambis, Phys. Rev. A **5,** 794 (1972).

[25] H. Tagashira, Y. Sakai and S. Sakamoto, J. Phys. D. Appl. Phys. **10,** 1051 (1977).

[26] J. Townsend, *The theory of ionization of gases by collision*, Constable, Limited (1910).

[27] F. Paschen, Wiedemann Ann. der Phys. und Chemie **37,** 69 (1889).

[28] L. Babich and T. V. Loiko, IEEE Trans. Plasma Sci. **44,** 3243 (2016).

[29] A. B. Blagoev and T. K. Popov, Phys. Lett. A **66,** 210 (1978).

[30] O. Angelov, A. B. Blagoev and T. Popov, Le J. Phys. Colloq. **40,** C7 (1979).

[31] S. Lee, Y. Shon, D. Kim, D.-C. Kwon and H. Choe, Appl. Sci. Converg. Technol. **29,** 157 (2020).

[32] M. J. Druyvesteyn and F. M. Penning, Rev. Mod. Phys. **12,** 87 (1940).

[33] Y. Ju, X. Mao, J. K. Lefkowitz and H. Zhong, in (ed. Tingas, E.-A.) 429 (Springer International Publishing, 2023).

[34] R. B. Patel, C. Oommen and M. J. Thomas, J. Propuls. Power **36,** 235 (2020).

[35] K. Liu, J. Zuo, C. Ran, M. Yang, W. Geng, S. Liu and K. (Ken) Ostrikov, Phys. Chem. Chem. Phys. **24,** 8940 (2022).

[36] P. S. Landa, N. A. Miskinova and Y. V. Ponomarev, Sov. Phys. - Uspekhi **23,** 813 (1980).

[37] X. Lu, G. V. Naidis, M. Laroussi and K. Ostrikov, Phys. Rep. **540,** 123 (2014).

[38] X. Lu, M. Laroussi and V. Puech, Plasma Sources Sci. Technol. **21,** 034005 (2012).

[39] S. Nijdam, J. Teunissen and U. Ebert, Plasma Sources Sci. Technol. **29,** 103001 (2020).

[40] P. Bruggeman and R. Brandenburg, J. Phys. D. Appl. Phys. **46,** 464001 (2013).

[41] K. Ollegott, P. Wirth, C. Oberste-Beulmann, P. Awakowicz and M. Muhler, Chemie Ing.

Tech. **92,** 1542 (2020).

[42] V. Yordanov, A. Blagoev, I. Ivanova-Stanik, E. M. van Veldhuizen, S. Nijdam, J. van Dijk and J. J. A. M. van der Mullen, J. Phys. D. Appl. Phys. **41,** 215208 (2008).

[43] B. Huang, C. Zhang, I. Adamovich, Y. Akishev and T. Shao, Plasma Sources Sci. Technol. **29,** 044001 (2020).

[44] B. M. Goldberg, P. S. Böhm, U. Czarnetzki, I. V. Adamovich and W. R. Lempert, Plasma Sources Sci. Technol. **24,** 055017 (2015).

[45] P. Viegas, E. Slikboer, Z. Bonaventura, O. Guaitella, A. Sobota and A. Bourdon, Plasma Sources Sci. Technol. **31,** 053001 (2022).

[46] S. Matsusaka, Adv. Powder Technol. **30,** 2851 (2019).

[47] O. V. Penkov, M. Khadem, W.-S. Lim and D.-E. Kim, J. Coatings Technol. Res. **12,** 225 (2015).

[48] J. Winter, R. Brandenburg and K.-D. Weltmann, Plasma Sources Sci. Technol. **24,** 064001 (2015).

[49] J. Laimer and H. Störi, Plasma Process. Polym. **4,** 266 (2007).

[50] M. Teschke, J. Kedzierski, E. G. Finantu-Dinu, D. Korzec and J. Engemann, IEEE Trans. Plasma Sci. **33,** 310 (2005).

[51] X.-J. Shao, G.-J. Zhang, Y.-X. Li and G.-M. Xu, IEEE Trans. Plasma Sci. **39,** 2336 (2011).

[52] Z. Donkó, Plasma Sources Sci. Technol. **31,** (2022).

[53] S. Lerouge, A. C. Fozza, M. R. Wertheimer, R. Marchand and L. Yahia, Plasmas Polym. **5,** 31 (2000).

[54] K.-D. Weltmann and T. von Woedtke, Eur. Phys. J. Appl. Phys. **55,** 13807 (2011).

[55] D. Mance, R. Wiese, T. Kewitz and H. Kersten, Eur. Phys. J. D **72,** 1 (2018).

[56] G. T. Bae, H. J. Jang, E. Y. Jung, Y. R. Lee, C.-S. Park, J. Y. Kim and H.-S. Tae, Polymers (Basel). **14,** 4917 (2022).

[57] S. Mitić, J. Philipps and D. Hofmann, J. Phys. D. Appl. Phys. **49,** 205202 (2016).

[58] S. Zhang, W. van Gaens, B. van Gessel, S. Hofmann, E. van Veldhuizen, A. Bogaerts and P. Bruggeman, J. Phys. D. Appl. Phys. **46,** 205202 (2013).

[59] P. Jia, M. Chen, H. Jia, X. Tan, J. Ran, K. Wu, J. Wu, J. Chen, X. Pang, X. Li and N. Zhao, IEEE Trans. Radiat. Plasma Med. Sci. **7,** 203 (2023).

[60] M. J. Nicol, T. R. Brubaker, B. J. Honish, A. N. Simmons, A. Kazemi, M. A. Geissel, C. T. Whalen, C. A. Siedlecki, S. G. Bilén, S. D. Knecht and G. S. Kirimanjeswara, Sci. Rep. **10,** 3066 (2020).

[61] Y. Lagmich, T. Callegari, L. C. Pitchford and J. P. Boeuf, J. Phys. D. Appl. Phys. **41,** 095205 (2008).

[62] S. Pekárek, J. Phys. D. Appl. Phys. **45,** 075201 (2012).

[63] J. M. Williamson, D. D. Trump, P. Bletzinger and B. N. Ganguly, J. Phys. D. Appl. Phys. **39,** 4400 (2006).

[64] U. Kogelschatz, Plasma Chem. plasma Process. **23,** 1 (2003).

[65] X. Xu, Thin Solid Films **390,** 237 (2001).

[66] R. Brandenburg, Plasma Sources Sci. Technol. **27,** 079501 (2018).

[67] E. Moreau, J. Phys. D. Appl. Phys. **40,** 605 (2007).

[68] J. S. Shang, S. T. Surzhikov, R. Kimmel, D. Gaitonde, J. Menart and J. Hayes, Prog. Aerosp. Sci. **41,** 642 (2005).

[69] Y. Zhao, Y. Xia, T. Xi, D. Zhu, Q. Zhang, Z. Qi, D. Liu and W. Wang, J. Phys. D. Appl.

Phys. **53,** 164005 (2020).

[70] S. J. Kim, I. T. Lee and Y. H. Kim, Smart Mater. Struct. **16,** N6 (2007).

[71] T. J. Williams, A. Jemcov and T. C. Corke, 52nd Aerospace Sciences Meeting, (2014).

[72] J. Perrin, O. Leroy and M. C. Bordage, Contrib. to Plasma Phys. **36,** 3 (1996).

[73] K. J. Laidler, J. Chem. Educ. **61,** 494 (1984).

[74] R. C. Hilborn, Am. J. Phys. **50,** 982 (1982).

[75] A. I. Lozano, J. Rosado, F. Blanco, P. Limão-Vieira and G. García, J. Phys. Chem. A **128,** 699 (2024).

[76] P. J. Bruggeman, M. J. Kushner, B. R. Locke, J. G. E. Gardeniers, W. G. Graham, D. B. Graves, R. C. H. M. Hofman-Caris, D. Maric, J. P. Reid, E. Ceriani, D. Fernandez Rivas, J. E. Foster, S. C. Garrick, Y. Gorbanev, S. Hamaguchi, F. Iza, H. Jablonowski, E. Klimova, J. Kolb, F. Krcma, P. Lukes, Z. Machala, I. Marinov, D. Mariotti, S. Mededovic Thagard, D. Minakata, E. C. Neyts, J. Pawlat, Z. L. Petrovic, R. Pflieger, S. Reuter, D. C. Schram, S. Schröter, M. Shiraiwa, B. Tarabová, P. A. Tsai, J. R. R. Verlet, T. von Woedtke, K. R. Wilson, K. Yasui and G. Zvereva, Plasma Sources Sci. Technol. **25,** 053002 (2016).

[77] E. M. Liston, L. Martinu and M. R. Wertheimer, J. Adhes. Sci. Technol. **7,** 1091 (1993).

[78] M. Ozdemir, C. U. Yurteri and H. Sadikoglu, Crit. Rev. Food Sci. Nutr. **39,** 457 (1999).

[79] N. Recek, Materials (Basel). **12,** 240 (2019).

[80] S. H. Tan, N.-T. Nguyen, Y. C. Chua and T. G. Kang, Biomicrofluidics **4,** (2010).

[81] M. Mozetič, Polymers (Basel). **12,** 2498 (2020).

[82] P. Viegas, E. Slikboer, Z. Bonaventura, O. Guaitella, A. Sobota and A. Bourdon, Plasma Sources Sci. Technol. **31,** 053001 (2022).

[83] N. Benard and E. Moreau, Exp. Fluids **55,** 1846 (2014).

[84] P. S. Shinde, P. S. Suryawanshi, K. K. Patil, V. M. Belekar, S. A. Sankpal, S. D. Delekar and S. A. Jadhav, J. Compos. Sci. **5,** 1 (2021).

[85] H. Choi, Y. Lee, S. Shin, J. Nam, W.-S. Park, B. Park and B. Kim, Biomed. Reports **16,** 16 (2022).

[86] H. Shi, K. Nie, B. Dong, M. Long, H. Xu and Z. Liu, Chem. Eng. J. **361,** 635 (2019).

[87] A. B. Theberge, F. Courtois, Y. Schaerli, M. Fischlechner, C. Abell, F. Hollfelder and W. T. S. Huck, Angew. Chemie Int. Ed. **49,** 5846 (2010).

[88] L. Patinglag, D. Sawtell, A. Iles, L. M. Melling and K. J. Shaw, Plasma Chem. Plasma Process. **39,** 561 (2019).

[89] O. Lademann, A. Kramer, H. Richter, A. Patzelt, M. C. Meinke, J. Roewert-Huber, V. Czaika, K.-D. Weltmann, B. Hartmann and S. Koch, Laser Phys. Lett. **8,** 313 (2011).

[90] F. Gorky, A. Best, J. Jasinski, B. J. Allen, A. C. Alba-Rubio and M. L. Carreon, J. Catal. **393,** 369 (2021).

[91] S. I. Khankina, V. M. Yakovenko and I. V Yakovenko, Radiophys. quantum Electron. **45,** 813 (2002).

[92] J. Morsell, N. Bhatt, C. Dechant and S. Shannon, J. Phys. D. Appl. Phys. **56,** 145201 (2023).

[93] P. Starič, K. Vogel-Mikuš, M. Mozetič and I. Junkar, Plants **9,** 1736 (2020).

[94] A. Hurlbatt, A. R. Gibson, S. Schröter, J. Bredin, A. P. S. Foote, P. Grondein, D. O'Connell and T. Gans, Plasma Process. Polym. **14,** (2017).

[95] J. P. Trelles, Plasma Sources Sci. Technol. **27,** 093001 (2018).

Chapter 2 Model Description

The model that was used in this dissertation is *nonPDPSIM* [1]. This is a 2D plasma hydrodynamics code that is enabled to solve a set of equations on an unstructured mesh. A brief discussion of the equation sets and code architecture is discussed below. However, major modules and equations are described separately in detail in subsections of this chapter. The schematic image of the code operation is presented in Fig. 2.1.

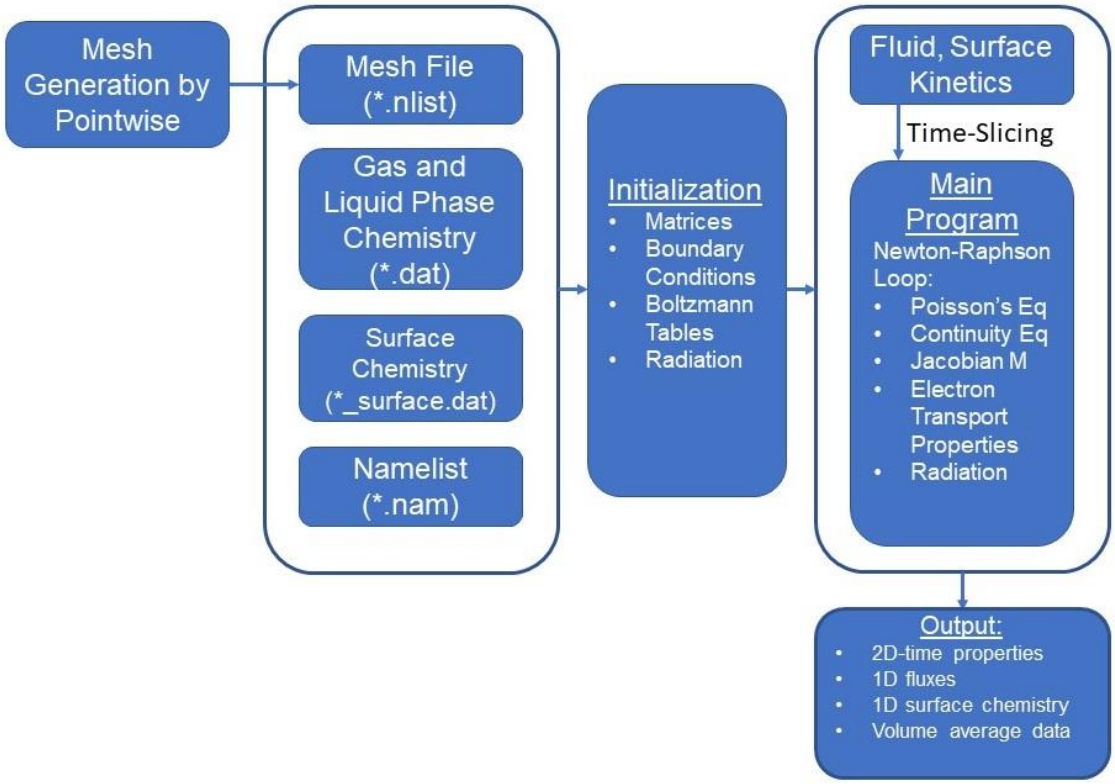

Figure 2.1. Scheme of work of nonPDPSIM.

In the nonPDPSIM, fluid dynamics and plasma evolution are both addressed. Events in plasmas occur on a timescale of pico-nanoseconds, while in fluid dynamics the timescales are shifted to micro-milliseconds. To address the difference in timescales, an algorithm of time-slicing is implemented. This method allows separate time integration schemes for different modules (fluid and plasma), assuming that calculations of time evolution in one module are performed while in other module functions are kept constant. The demonstration of time evolution of the ionization wave onto the modeled human skin produced by an atmospheric pressure plasma jet (APPJ) is demonstrated in Fig. 2.2 [2]. In this dissertation the color schemes have a standard form and values of parameters in the left top corners identify maximal values of the plotted parameters.

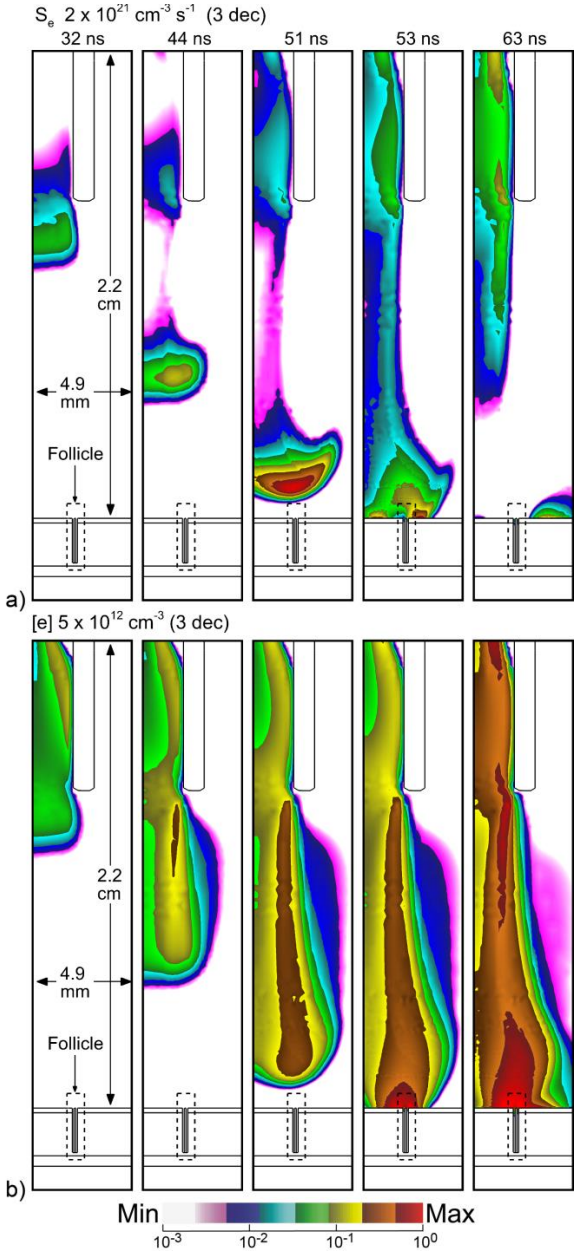

Figure 2.2. Time evolution of plasma computed in nonPDPSIM for an APPJ incident onto modeled human skin: a) electron impact ionization source, b) electron density.

Fluid calculations in nonPDPSIM are addressed with a set of compressible Navier-Stockes equations. A fluid module is typically used to address problems in which gas is not stagnant and

there is an injected gas, as in APPJs. A common fluid field profile is demonstrated for a helium APPJ in Fig. 2.3 [2].

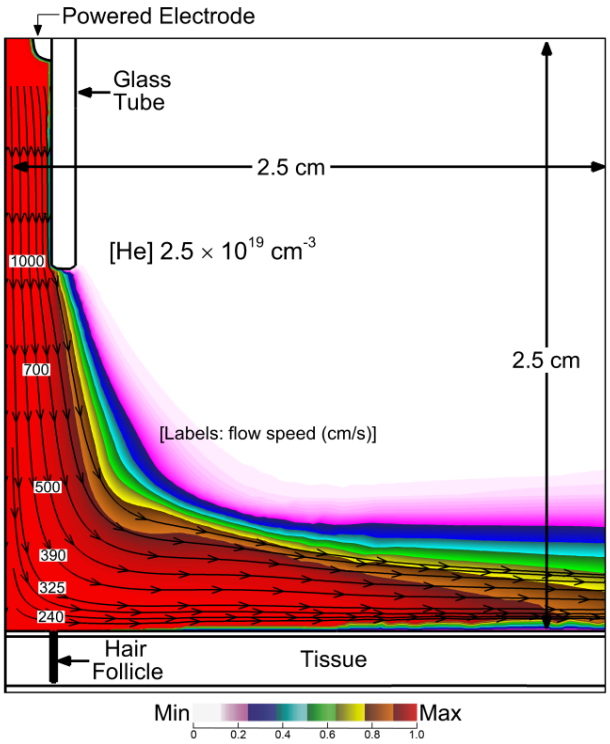

Figure 2.3. Fluid flow of helium produced by APPJ applied on modeled human skin computed in nonPDPSIM.

Plasma calculations are addressed with the following set of equations. The core part of calculations includes a solution of Poisson's equation and continuity equation for charged particles that consider surface charging. Calculations of these equations are performed using a fully implicit numerical scheme. The Newton-Raphson integration algorithm is used. The change of electron temperature is addressed with an electron energy balance equation. Solution of Boltzmann's equation provides rate and transport coefficients that are functions of electron temperature. Photoionization is addressed with Green's function approach. Liquids are treated as a dense plasma-zone with a boundary condition addressed with Henry's law.

The phenomenon of afterglow can be calculated using a different set of equations from the ones used to calculate plasma. To reduce the time of calculation, a neutral plasma module is used to disable the calculations of Poisson's equation and set the electron temperature constant.

The model is written in Fortran and executed in the Linux environment. The typical run time of a case that includes fluid, plasma and afterglow calculations on a 15,000 nodes mesh is

approximately 3 weeks. The program complex includes an option to be compiled enabling parallelization.

The flow chart of input required for the program is demonstrated in Fig. 2.1. The code requires the mesh to be generated by an external software and is provided in a specific internal format *.nlist. All meshes for this thesis were generated using software Pointwise [3]. The list of model parameters that users set is contained in a file *.namelist. Parameters in this file include a description of materials in the system (electrical, thermodynamic and photo parameters), an

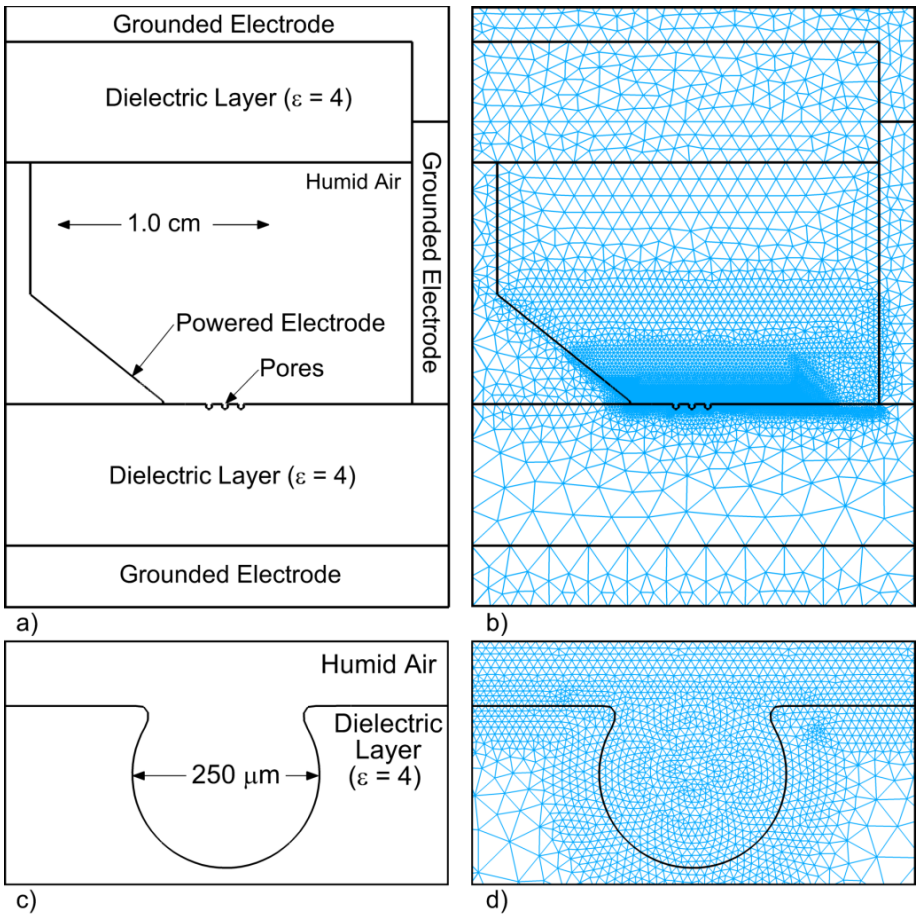

Figure 2.4. Example of the numerical domain corresponding to a setup of SDBD. a) Full numerical domain, b) full map of nodes, c) enlarged geometry microfeature, d) map of nodes in enlarged microfeature.

applied voltage system description (pulse determination or AC periodic voltage), numerical model parameters (type of solver, implicitness fact, list of modules) and a list of subsections for specific physical modules (fluid, surface, afterglow). NonPDPSIM requires a separate file that contains chemistry mechanism *.dat. This file contains a list of chemicals with major parameters (molecular/atomic weight, Lennard-Jones parameters, charge) and a list of reactions with rate coefficients.

2.1 Geometry and Mesh

The program complex nonPDPSIM is developed assuming the implementation of unstructured mesh with an option to build a hybrid mesh with inserted structured zones. Unstructured meshes allow addressing small-scale features in large-scale reactors. At atmospheric pressure conditions, unstructured mesh can also be beneficial for confined plasma propagation zones with steep electric field gradient zones to implement different cell sizes. An example of a computational domain with a map of mesh nodes is demonstrated in Fig. 2.4.

To generate meshes, commercial software Pointwise was used [3]. The program has an implemented solver to allow output of the mesh in format *.nlist to allow a specific structure of the file containing nodes coordinates with assigned zones and material numbers. The typical size of the mesh in this thesis is 10,000–15,000 nodes. The nonPDPSIM reads the file *.nlist with coordinates of nodes and assigned zones and materials. The zones and materials are controlled by the user and are separated for the option of assignment of different properties such as flow rates, conductivity, permittivity, temperature and others. Based on this data, the computational cells are then identified and computed. In utilized finite volume method (FVM) partial differential equations (PDE) for the fluid approach are solved. The method is discussed in detail in the following sections. The finite volume is a computational cell that is computed around every node in the mesh. The computation is performed by applying perpendicular bisectors to the connectors between the nodes. The computational cell is a hexagon (ideally equilateral to conserve fluxes). The example of a computational cell is demonstrated in Fig. 2.5. After the cells are computed, the calculation of the volumes of the cells is performed. The volumes are critical parameters in FVM to convert PDEs and solve them in algebraic form. For the calculation of volumes, the areas of each cell are identified. The volume of the cell then depends on the coordinate system. In

nonPDPSIM, there are options to perform calculations in either cartesian or cylindrical coordinate systems. In the Cartesian coordinate system, the user is required to identify the depth of the domain that is used to compute the volume along with the areas of the cells. When the cylindrical coordinate system is chosen, the volume of the cells depends on the coordinates of the particular cells and is computed using this data instead of the depth.

2.2 Plasma Module

There are three major approaches to describe low temperature plasma: fluid, kinetic and hybrid. In nonPDPSIM, plasma is modeled within the fluid approach where macroscopic parameters such as velocities are solved in order to save computational costs (compared to tracing each individual particle in the kinetic approach, which is unreasonable under atmospheric pressure

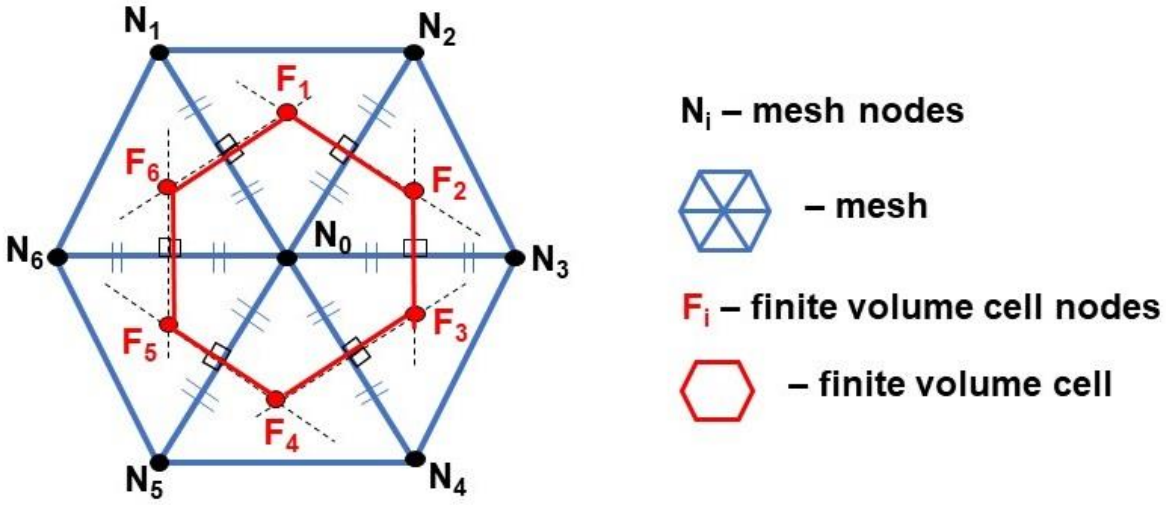

Figure 2.5. Schematic image of a section of the mesh and a constructed finite volume cell.

plasma (APP) number densities). In the plasma module, the critical plasma equations are solved:

Poisson's equation for electrical potential, the continuity equation for charged and neutral species, Boltzman's equation for EEDFs and the electron energy balance equation for electron temperature.

The plasma module is utilized in the majority of problems involving plasmas, unless specific initial conditions are provided. For instance, when dealing with a known gas composition in any 'post-plasma' phase that is solely undergoing decay and recombination, this module is not necessary. Consequently, Poisson's equation remains unsolved in such cases, leading to a significant reduction in computational costs. However, in most other scenarios, the core module is executed.

2.3 Poisson's Equation and Continuity Equation for Charged Species

To account for charge transport in time and space in the nonPDPSIM primary plasma module, a full set of Maxwell's equations is not solved (assuming that magnetic fields produced by moving charges in APPs are low and external magnetic fields are rarely applied). Instead, the solution of only Poisson's equation is coupled with the continuity equation for charged species accounting for surface charging. The Poisson's equation (2.1) is formulated below:

$$\nabla(\varepsilon\nabla\Phi) = -(\sum_i q_i N_i + \rho_m) \tag{2.1}$$

where ε is the material permittivity, Φ is the electrical potential, on the right-hand side of the equation the first term represents summation over gas phase charges with q_i as an elementary charge and ρ_m is the total charge on surfaces and the inside of the materials.

Poisson's equation is simultaneously solved along with the continuity equation for charged species. The time change of densities is represented with the following expression (2.2):

$$\frac{\partial N_i}{\partial t} = -\nabla\vec{\Gamma}_i + S_i + \left(\sum_j -\nabla\vec{\Gamma}_j\gamma_j + \sum_k -\nabla\phi_k\gamma_k\right) \tag{2.2}$$

where N_i is the density of a particular charged particle, t is time, Γ_i is the Shafetter and Gummel (discussed in later subsections) flux given for the flux of charged species, S_i represents the collisional source. The third term represents the total flux of secondary electron emission from the ions and excited states reaching the materials calculated as a sum of the individual particle fluxes Γ_j having secondary emission coefficient γ_j. The fourth term is a sum over the fluxes of secondary electrons sources from photon fluxes φ_k to the materials with secondary emission coefficients γ_k. The fluxes of charged species in (2.2) are formulated with an expression provided by Shafetter and Gummel [4] (2.3):

$$\Gamma_{imn} = \alpha \overline{D_i} \left(\frac{N_{im} - N_{in} e^{\alpha \Delta l_{mn}}}{N_{im} - N_{in} e^{\alpha \Delta l_{mn}}} \right) \tag{2.3}$$

$$\alpha = -\frac{q_i \overline{\mu_i} \Delta \Phi_{mn} + 2 v_{mn}}{\overline{D_i} \Delta l_{mn}},$$

where i is the index counting charged species, m and n are the indexes counting the considered pair of nodes between which the fluxes are computed; $\overline{D_i}$ is the diffusion coefficient for particle i averaged between nodes m and n; N_{in} and N_{im} – are the concentrations of charged species i at nodes m and n; Δl_{mn} is the length between nodes m and n; $\overline{\mu_i}$ is the averaged mobility of species i averaged between nodes m and n; $\Delta \Phi_{mn}$ is the potential difference between nodes m and n; and v_{mn} is the fluid velocity between nodes m and n.

The time evolution of the surface and material charge presented in (2.1) is formulated with the following expression:

$$\frac{\partial \rho_m}{\partial t} = \left(\sum_i q_i (-\nabla \overrightarrow{\Gamma_i} (1 + \gamma_i)) + \sum_j \phi_k \gamma_k \right) - \nabla (\sigma (-\nabla \Phi)) \tag{2.4}$$

where ρ_m is the total material and surface charge. The first term represents the total change in surface charge on materials due to secondary electrons from ions and excited states interacting with interfaces with q_i being a given charged particle, Γ_i being the Shafetter and Gummel flux and γ_i being a secondary emission coefficient. The second term gives the total change of the surface charge caused with the photons fluxes interacting with the surfaces, with φ_k being the given fluxes of photons and γ_i being the secondary emission coefficients. The third term represents the change of the charge in the materials given with Ohm's law.

Some parameters in the above-described equations are updated using the functions executed in other modules.

2.4 Numerical Methods

To perform the solution of the equations systems described above a numerical procedure is used. When the equations are solved, a system of equations is reconstructed using either linearization or analytical technique to build the Jacobian elements and construct a Jacobian matrix *B*. The Jacobian elements are computed based on the perturbation of one of the variables in respect to another. The following equation is then solved:

$$A = \vec{x}B \tag{2.5}$$

where *A* is the solution, *B* is the Jacobian matrix and *x* is the unknown vector.

In nonPDPSIM, a fully implicit technique is used for the solution. The convergence on each iteration is reached using a Newton-Raphson algorithm. The example of the construction of the Jacobian elements is presented below with the change in density perturbing the potential:

$$\frac{\partial N_{ij}}{\partial \Phi_k} = -\frac{\nabla t}{\nabla \Phi}\left(\nabla(\overrightarrow{\Gamma}_j(\Phi_k(t)+\Delta\Phi) - \overrightarrow{\Gamma}_j(\Phi_k(t))\right) \tag{2.6}$$

where the index i counts for species with density N_{ij}, j is their representative node and m counts for the mesh points for the potential Φ_k.

2.5 Neutral Transport

Neutral transport outside of the fluid module when the air is unperturbed is also solved within the plasma module. The neutral species densities change primarily due to the diffusion, chemical reactions in the gas phase and reactions on the interfaces. The expression for the neutral species densities change due these factors is given below:

$$\frac{\partial N_i}{\partial t} = -\nabla(N_i \vec{v}) - \nabla(-D_i \nabla N_i) + S_{gi} + S_s \tag{2.7}$$

where N_i is the neutral species densities, v is velocity, D_i is the diffusion coefficient of species, S_i is the source of neutral species due to chemical reactions, S_s is the source of neutrals due to events on the interfaces and D_i are the estimated coefficients for individual particles diffusing into the specific gas based on the Lennard-Jones parameters [5].

2.6 Boltzmann's Equation

One disadvantage of a fluid approach is that it assumes a Maxwellian distribution function for the particle velocities. This is the source of inaccuracy in the model of LTPs that may lead to a large discrepancy with the actual properties. To reduce the inaccuracy and keep the benefit of the lower computational costs, the electron energy distribution functions (EEDFs) are considered

in modeling LTPs. In nonPDPSIM, the stationary Boltzmann's equation approached with a two-term spherical expansion is solved to obtain the EEDFs:

$$\frac{\partial f}{\partial t} + \vec{v}\nabla_{\vec{r}} f + \frac{\vec{F}}{m}\nabla_{\vec{v}} f = \left(\frac{\partial f}{\partial t}\right)_{coll} \tag{2.8}$$

where f is the electron energy distribution function, the total derivative of which is the entire expression on the left side and the change due to collisions is on the right side, v is velocity, F is the total force, m is the mass of electrons and ∇_r and ∇_v are the space and velocity gradients. The two-term spherical expansion approximation is used to reduce the computational costs. This is a commonly used technique to approach the solution of Boltzmann's equation in gas discharge physics problems [6].

Based on the solution of the equation, the rate and transport coefficients for electron processes are obtained for a wide range of E/N values (up to 1000 Td). The results are grouped in look-up tables that are suitable for having data for different zones if there are areas of mixed gases with steep density gradients.

2.7 Electron Energy Balance Equation

Electron temperature evolution is tracked with the electron energy balance equation. In this equation, the sources of electron energy gains due to external electric fields and chemical processes and losses are accounted for. The equation is formulated below:

$$\frac{\partial}{\partial t}\left(\frac{3}{2} n_e k T_e\right) = S_P(T_e) - L_P(T_e) - \nabla\left(\frac{5}{2}\Gamma_e k T_e - \kappa(T_e)\nabla T_e\right) \tag{2.9}$$

where n_e is the concentration of electrons, T_e is the electron temperature, S_p is the energy source term (Joule heating), L_p is the energy loss/gain collisional term, and the third term represents the convection and conduction of electron energy with κ being thermal conductivity.

This equation is solved using a fully implicit successive-over-relaxation technique.

2.8 Photon Transport Module

The photon transport in nonPDPDIM is addressed with a Green's function approach. The photon transport accounts for the absorption and emission of photons. The balance of these characteristics also affects the ionization source formulated as photoionization and can contribute to the dissociation of diatomic molecules. The photoionization source is presented in the following equation:

$$S_{Pi}(\vec{r}_j) = N_i(\vec{r}_j)\sum_k \sigma_{ik} A_k \int N_k(\vec{r}_l\,')G_{ilk}(\vec{r}_l\,',\vec{r}_j)d^3\vec{r}_l\,' \tag{2.10}$$

where *i* denotes the index of the ionized particle, *k* is the index counting photon emitting species, *l* and *j* are the indexes that represent the counting for the radii vectors r, *N* is the concentration of ionized species, σ is the photoionization cross-section and *A* is the Einstein coefficient.

In this equation, the *G* is the Green's function that is used to address the uniform source of vacuum ultraviolet (VUV) photons:

$$G_{kil}(\vec{r}_i,\vec{r}_l) = \frac{\exp(-\int_{\vec{r}_l}^{\vec{r}_i}\sum_n \sigma_{kn}N_n(\vec{r}_p\,')d\vec{r}_p\,')}{4\pi\left|\vec{r}_i\,'-\vec{r}_l\right|^2} \tag{2.11}$$

Radiation transport plays a crucial role in atmospheric pressure plasmas. However, implementing this module comes with high computational costs. In certain scenarios where the

initial assessment of the system indicates a minimal impact of radiation transport on plasma evolution, it may be justifiable to neglect this module. For instance, when the gas composition predominantly consists of emitting species with low energy to ionize other species.

2.9 Plasma Chemistry Module

Plasma chemical processes not only contribute to the balance of chemicals but also shift the balance for electron energies. Typical plasma chemical processes that are considered in this model are listed in Table 1.1 (Chapter 1). The chemistry data is collected in the single chemistry *.dat file and contains data on molecules, radicals, excited states and ions along with a list of the reactions with characteristic rate coefficients. Typical number of species in the mechanism is 30-50, while number of reactions is up to 1000. The rate coefficients follow the Arrhenius equation (described in Chapter 1). The treatment of the electron impact processes is different from the other processes. Electron impact processes use cross-section data as a critical parameter to compute rates. NonPDPSIM contains data based for the most common electron impact processes with the most used molecules and atoms in the field of APPs. The bi-/tri-molecular processes contain the list of rate coefficients. The photon transport data is also included in this file and requires the photoionization/photodissociation processes' cross-sections and the Einstein coefficients for the emitting or absorbing processes. Chemical interactions with liquid species are also listed in this file with rate coefficients. The surface chemistry is represented in a separate file, which is described in the following sections. The sticking probability of species on certain materials is presented in the chemistry *.dat file and is used by surface kinetic module upon execution. To model the chemical processes with nonPDPSIM, a master chemistry set developed and described by Lietz et al. [7] is used. The master chemistry set contains the most commonly used in APP

molecules, atoms and their excited states and ions such as Ar, He, N_2, O_2, H_2O, O, O_3, N_4^+, $O_2(a^1\Delta)$, $O_2(v)$, Ar_2^* and other species. The file additionally has a list of all major processes corresponding to these chemicals. To reduce the computational costs, an exclude file *_exlude.dat is used. It contains a list of species that are to be eliminated with all processes from consideration in the model.

As outlined in Chapter 1, accounting the chemical aspect becomes essential due to the nonequilibrium characteristic of atmospheric pressure plasmas. This fundamental module is utilized in all scenarios, except fluid calculations when dealing with nonreactive fluid flows.

2.10 Liquid Module

The liquid module is designed to add critical properties to the interactions between plasmas and liquids, addressing realistic physical and chemical phenomena. The liquids are treated as separated dense plasma zones with the following unique characteristics. The interaction between gas/plasma and liquid is defined through the evaporation and solvation processes. The balance between these processes is given with the vapor pressure of the liquid, solvation probabilities and chemistry in the liquid. The fluid mechanics of liquids is not included in the model, and the liquid volume and the interface remain static (defined by the mesh generation). The evaporation of the liquid is limited by the vapor pressure, assuming the liquid density will remain constant. The change of species in the gas phase due to flux from the liquid is given with the following expression:

$$\Gamma_{\mathrm{lg}} = \begin{cases} \dfrac{D_l}{\Delta x}\left(1-\dfrac{n_g}{n_l/h}\right)(n_l-n_g), & n_g \le n_l/h \\ 0, & n_g > n_l/h \end{cases} \tag{2.12}$$

where Γ_{lg} is the flux of liquid species into the gas, D_l is the diffusion coefficient in the liquid, n_g and n_l are the gas and liquid phase species densities, Δx is the distance between the nodes at liquid interface and the considered point in gas, and h is the Henry's law equilibrium constant.

The solvation process depends on the species that interact with the liquid interface. Charge species solvate upon contact with the liquid surface. In the case of water and electrons, the process represents the interaction between polar water molecules and the electrons collected by the water interface. Neutrals are allowed to enter the liquid interface following Henry's law with a flux:

$$\Gamma_{gl} = \begin{cases} \dfrac{D_g}{\Delta x}\left(1 - \dfrac{n_l}{n_g h}\right)(n_g - n_l), & n_l \le n_g h \\ 0, & n_l > n_g h \end{cases} \tag{2.13}$$

where Γ_{lg} is the flux of gas species into the liquid interface, D_l is the diffusion coefficient in the gas, n_g and n_l are the gas and liquid phase species densities, Δx is the distance between the nodes at liquid interface and the considered point in gas, and h is the Henry's law equilibrium constant. Typical values of the Henry's law constants used in modeling in this dissertation are described by Kruszelnicki [8]. The liquid chemicals may undergo chemical reactions that are described within the chemistry file *.dat. Examples of chemical reactions in the liquid phase include chemical conversion, clasterization and charge exchange.

Treating liquids with plasma poses a specific challenge. In many cases, this module is optional. It is executed when the primary research problem involves modifying liquids through plasma treatment.

2.11 Fluid Mechanics Module and Neutral Transport

In APP systems, the rapid gas flows and mixing gases of different properties are common (for example APPJs). It is thus essential to address the proper fluid fields and density gradients for proper electron transport and rates calculation. The fluid module is implemented as a set of modified Navier-Stockes equations. Modifications are primarily addressing the problem of the large ratio between the masses of commonly used gases. The numerical technique is developed for an implicit algorithm for sparse matrices. The communication between fluid and plasma is addressed with a time-slicing algorithm that aims to account for the different timescales of the plasma and fluid phenomena.

The list of the solved equations includes continuity equations, momentum equation, energy conservation equation. The continuity equations are presented in the following form:

$$\frac{\partial N_t}{\partial t} = -\nabla\left(N_t \vec{v} + \sum_{k,i} \frac{f_{ki}}{A_k} \right) \tag{2.14}$$

$$\frac{\partial N_t M_t}{\partial t} = -\nabla\left(\sum_{k,i} m_i \Gamma_i N_i + \sum_{k,i} \frac{m_i f_{ki}}{A_k} \right) \tag{2.15}$$

where N_t is the number density of species, M_t is the average molecular mass of species, v is advective velocity, Γ_i is the flux of species i, m_i is the molecular weight of species i, f_{ki} is the flow rate from the inlet and A_k is the area of the gas inlet.

The momentum equation is presented below:

$$\frac{\partial (N_t M_t \vec{v})}{\partial t} = -\nabla P - \nabla (N_t M_t \vec{v}\vec{v}) - \nabla \bar{\tau} + \sum_i q_i N_i \vec{E} + N_t M_t g \frac{\vec{v}n}{|\vec{v}|} \tag{2.16}$$

where P is pressure, τ is the stress tensor, q_i is the elementary charge, E is the applied electric field and g is the gravitational constant. The sum that contains the electric field accounts for the total momentum transfer between charged and neutral species.

The energy conservation equation has the following form:

$$\frac{\partial(N_t c_v T)}{\partial t} = -\nabla(-\kappa\nabla T + \rho\vec{v}c_v T) + P\nabla\vec{v} - \sum_m R_m \Delta H_m + \sum_i \vec{j}_i \vec{E} \tag{2.17}$$

where c_v is the specific heat, T is the gas temperature, κ is thermal conductivity. The third term represents the chemical reactions contribution with index m, where R is the reaction rate, H is enthalpy. The fourth term representing the Joule's heating, with j being the ion current density and E the applied electric field.

Fluid calculations are unnecessary in many research problems, as gas remains stagnant in numerous real plasma systems. However, they become crucial in systems with gas flows, such as atmospheric pressure plasma jets.

2.12 Surface Kinetic Module

Surface kinetics is implemented and executed upon the request of the user in the model. In general, on any specified interface there is a capability to account for a 1D surface rate of change tracker (adjusted for the depth or radius to obtain 2D surface densities). Surface kinetic data is contained in a separate data file similar to gas phase kinetics. On user-defined materials, surface kinetics can be executed. The module is implemented to obtain fluxes of the gas phase species that reach the interface of the chosen material and with a user-defined time step integrate time rate of change of the species on the interface and the incoming and returning gas phase fluxes as a result of interaction. The processes allowed to be included in a typical surface kinetics mechanism are neutral gas reactions with surface sites, surface sites reacting with each other, ion bombardment of surface sites or bonds, and photon reactions with sites or bonds. The rates of change of surface coverage due to gas surface reaction follow the mechanism of Eley-Rideal [9]. Both absorption

and desorption are allowed. Surface-surface reactions follow the mechanism of Langmuir-Hinshelwood [10]. Ion bombardment and photon-induced reactions are given with probabilities and are allowed after these species reach the interface. The rate of change of the surface species density N_{is} over time is given with the following expression:

$$\frac{\partial N_{is}}{\partial t} = \left[\sum_j \left(a_{ij}^{(2)} \gamma_j v_i \frac{n_{is}}{4} \right)\right] - \left[\sum_j \left(a_{ij}^{(1)} k_j N_{is} \right)\right] + \left[\sum_j \left((a_{ij}^{(2)} - a_{ij}^{(1)}) k_j \prod_l N_{ls}^{a_{ij}^{(1)}} \right)\right], \tag{2.18}$$

where $a_{ij}^{(1)}$ and $a_{ij}^{(2)}$ are the stochiometric coefficients, j is the index counting processes, γ_j is the probability of absorption, v_i is thermal speed of species, n_{is} is the gas phase species density and k_j is the rate coefficient of process j. The first sum in the equation corresponds to the absorption/abstraction reactions. The second term is dedicated to summate desorption reactions. The third term sums over the surface–surface reactions.

The number of surface sites is conserved under the framework of the model. Typical application of the surface kinetic module is to account for time rate of change of sites on the polymeric surface. The module is described in detail by Dorai et al. [11].

Addressing surface kinetics is necessary only in specific cases. Certain surface processes, such as simple interactions of species with the wall (sticking, reflecting), which do not alter the chemical composition of the interface, are handled within the plasma chemistry module. Surface kinetics is taken into account when the focus of the research is on the modification of the chemical composition on the studied substrate by plasma.

2.13 References

[1] S. A. Norberg, E. Johnsen and M. J. Kushner, Plasma Sources Sci. Technol. **24**, 035026 (2015).

[2] K. Konina, T. A. Freeman and M. J. Kushner, Plasma Sources Sci. Technol. **32**, 085020 (2023).

[3] Pointwise Inc. (2021).

[4] D. L. Scharfetter and H. K. Gummel, IEEE Trans. Electron Devices **16**, 64 (1969).

[5] J. O. Hirschfelder, J. O. Hirschfelder and R. B. Bird, *The Molecular Theory of Gases and Liquids*, Wiley (1954).

[6] S. Yachi, Y. Kitamura, K. Kitamori and H. Tagashira, J. Phys. D. Appl. Phys. **21**, 914 (1988).

[7] A. M. Lietz and M. J. Kushner, J. Phys. D. Appl. Phys. **49**, (2016).

[8] J. Kruszelnicki, A. M. Lietz and M. J. Kushner, J. Phys. D. Appl. Phys. **52**, 355207 (2019).

[9] W. H. Weinberg, Acc. Chem. Res. **29**, 479 (1996).

[10] G. W. Roberts and C. N. Satterfield, Ind. Eng. Chem. Fundam. **4**, 288 (1965).

[11] R. Dorai and M. J. Kushner, J. Phys. D. Appl. Phys. **36**, 666 (2003).

Chapter 3 Atmospheric Pressure Plasma Treatment of Porous Dielectrics[1]

Atmospheric pressure plasmas intersecting with dielectric surfaces will often transition into surface ionization waves (SIWs). Several applications of these discharges are purposely configured to be SIWs. During propagation of an SIW over the dielectric surface, the plasma charges the surface while responding to changes in geometrical and electrical material properties. This is particularly important for non-planar surfaces where the polarization of the dielectric results in local electric field enhancement. In this chapter, SIWs interacting with the dielectric surface containing micropores is investigated. SIWs are observed to be sensitive to the electric field enhancement that occurs at the crests of non-planar surfaces. The local increase in ionization rates by the electric field enhancement can result in non-uniform plasma exposure of the surface. Treatment of the interior of the pores, thus, depends on their shapes. Buried pores with small openings to the SIW may be filled by plasma by either flow of plasma into the pore (large opening) or initiated by photo-ionization (small opening), depending on the size of the opening compared to the Debye length. Atmospheric pressure plasma is a unique source that can help treat irregularities on the interfaces of microsizes, especially when some parts of the irregularities are not accessible, for example, for liquid treatments. The results obtained in this dissertation can be useful for developing technologies involving porous dielectrics, ceramic filters, or catalyst supports.

[1] Some parts of the text presented in this chapter along with the research data have been published by Kseniia Konina *et al* 2022 *Plasma Sources Sci. Technol.* **31** 115001.

3.1 Introduction

The interaction of pulsed atmospheric plasmas with dielectric surfaces typically evolves at some point into propagation of a surface ionization wave (SIW) [1,2]. An example of a volumetric plasma streamer transitioning into a SIW occurs in a dielectric barrier discharge (DBD). The detailed description of SIWs and DBDs is contained in Chapter 1. In a DBD, a volumetric plasma streamer oriented perpendicular to the bounding dielectric material evolves into a *surface hugging* ionization wave [3]. This SIW is often referred to as the foot of the streamer in a DBD [4]. SIWs are the intended mode of propagation of atmospheric pressure plasmas in applications including plasma actuators for affecting air flow over surfaces [5], ignition sources for plasma aided combustion [6] and treatment of water contaminated with surfactant-like molecules [7].

The development and propagation of a SIW is a consequence of charging of the surface and electric field enhancement at the interaction of the plasma and the dielectric [8]. In order for the SIW to propagate parallel to the surface, there must be an electric field component parallel to the surface. Again referring to the example of the DBD or a plasma jet striking a surface, the applied electric field is initially perpendicular to the surface. The intersection of the bulk plasma streamer normal to the surface electrically charges the dielectric surface at the site of the intersection [3,9]. The surface charge density generates electric field components parallel to the surface that supports propagation of the SIW [10,11]. Once propagating along the surface, there is charge separation at the head of the SIW analogous to the charge separation in the head of a streamer propagating in a bulk gas. This charge separation produces the electric field that avalanches the gas to propagate the SIW [12]. However, the charging of the underlying dielectric maintains propagation along the surface [13].

At the same time, there is a discontinuity in relative permittivity between the underlying

dielectric and the plasma, with the permittivity of the dielectric being larger. This discontinuity intensifies the electric field at the surface of the dielectric due to polarization of the surface material, which enhances propagation of the SIW [14]. The region near the head of the SIW is constituted of a conductive column of plasma, an insulating surface of the dielectric substrate and the ambient air – therefore, resembling an electrical triple-point [15]. Additional electric field enhancement is therefore produced.

The propagation of the SIW along the surface can also be viewed as the continuous charging of the capacitance of the surface. Charge is removed from the streamer to charge the local surface capacitance, C_s (F/cm^2), of the underlying dielectric. This charging of the dielectric locally transfers voltage to the dielectric. This voltage was previously dropped across the gas phase and partially across the head of the SIW. The locally charged dielectric produces an electric field pointing towards the uncharged dielectric ahead of the SIW, which then supports the propagation of the SIW. However, removal of voltage from the SIW to charge the dielectric also weakens the SIW. There are other subtleties that influence the propagation of SIWs, including secondary electron emission due to ion bombardment, photoelectron emission from the surface, photon induced conductivity and kinetic effects in the intense electric fields near the surface [16]. The latter can produce sheath accelerated secondary electrons.

The propagation of the SIW and charging of the dielectric can be described in terms of approaching the saturation charge [17,18]. The saturation surface charge is that value when the normal component of the electric field in the dielectric is supported by the surface charge, σ_s, while in comparison, the normal electric field in the plasma is zero. That is, $\varepsilon_0 E_{np} + \varepsilon_d E_{nd} = \sigma_s \rightarrow \varepsilon_d E_{nd} = \sigma_s$ where E_{np} is the normal component of electric field in the plasma (pointing away from the surface) and E_{nd} is the normal component of electric field in the dielectric

have permittivity ε_d. After an SIW has propagated across a surface, the surface charge approaches its saturation value.

The charging of the underlying dielectric by the SIW impacts the speed of the discharge across the surface. The SIW requires more time to charge larger C_s and so the speed of the SIW across the dielectric surface decreases with increasing C_s, as Li et al. has shown by modeling [19]. 2-dimensional simulations were performed by Pechereau, et al [20] of a streamer in air intersecting a flat dielectric slab and transitioning to a SIW. The speed of the SIW increased over thicker slabs for the same permittivity, a result of C_s being smaller for thicker dielectrics. For the same thickness dielectric, the SIW speed was lower with larger dielectric constant (larger C_s). Although the speed of the SIW depends on C_s, secondary electron emission processes by ions and photons from the dielectric are less influential [16].

The discussion to this point applies to the propagation of SIWs on planar dielectrics. The propagation of SIWs on non-planar dielectrics has additional complexity due to the electric field enhancement at the convex curvature of the dielectrics. High permittivity dielectric materials expel electric field into bounding materials having a lower permittivity. As a result, electric field enhancement occurs at the apex of convex protrusions of dielectrics in the same manner as electric enhancement occurs at the edges of metal electrodes.

A second complication for SIWs propagating on non-planar dielectrics results from shadowing of ionizing radiation. The propagation of a positive SIW depends on photoionization in front of the head of the SIW in the same way that photoionization supports the propagation of positive streamers in the bulk gas. Non-planar geometries can shadow the photons originating in the head of the SIW from illuminating and photoionizing the region adjacent to the surface in front of the SIW. This lack of preionization due to shadowing of the photon-flux can lead to a distinctive

difference in propagation properties of positive and negative SIWs.

The propagation of SIWs on planar surfaces has been well characterized while there have been limited quantitative investigations of the propagation of SIW on non-planar surfaces. In this context, non-planar refers to surfaces in which the local topology (e.g., roughness or waviness of the surface) has dimensions that are commensurate with that of the SIW. The diameter of atmospheric pressure streamers and thickness of SIWs are up to hundreds of microns [21,22]. This spatial scale is the order of non-planarity that is of concern.

Meyer et al. [18] measured and modeled positive SIWs propagating in atmospheric pressure air across flat and profiled dielectric surfaces ($\varepsilon_r = 3.17$) consisting of shallow troughs (or corrugations) having a period of 1.79 mm and depth of 0.514 mm. For positive streamers produced by a 35 kV pulse having a 420 ns risetime, the positive SIW adhered to the profiled surface, propagating with speed of 1.8×10^8 cm/s, about 15% slower than over the equivalent flat surface. Ning et al. [23] performed 2-dimensional modeling of a plasma jet (see Chapter 1) sustained in atmospheric pressure He/N_2=99.5/0.5 flowing into ambient air onto a wavy dielectric surface consisting of alternating semi-circles with a radius of 0.2 mm and crest-to-crest period of 0.8 mm. The plasma jet strikes the surface as a bulk Ionization Wave (IW) (see Chapter 1), and transitions to a SIW propagating radially outward. Positive SIWs nearly uniformly penetrated into the grooves of the surface, limited by a cathode-fall like sheath at the surface. Negative streamers filled the grooves directly under the plasma jet. However, when transitioning to a surface wave, the negative SIW did not fully adhere to the surface. Fluxes of radicals and ions were then more uniform across the surface for positive SIWs compared to negative SIWs. In simulations of a He/N_2 dielectric barrier discharge with one of the dielectrics being wavy, Wang et al. [24] found differential charging of the surface. The crests of the waves tend to charge negatively while the

grooves tend to charge positively.

One configuration of a non-planar surface is a curved, but smooth, dielectric. Single filament experiments in a DBD having a single or a pair of hemispherical dielectric covered electrodes have shown propagation of SIWs along the smooth, curved surface that are qualitatively similar to those on strictly planar surfaces [12,25]. Optical emission was measured in a DBD by Mujahid in which the dielectric covering the grounded electrode consisted of an array of touching hemispheres [26,27]. Initiating plasma filaments intersected the apex of the hemispheres due to electric enhancement and polarization of the dielectric, followed by SIWs which propagated down the slopes of the hemispheres. Sun et al experimentally and computationally investigated SIWs propagating along a curved polyimide surface sustained with alternating powered and grounded electrodes buried in the dielectric [28]. They found that bending of the thin (100 μm) polymer sheet from being concave to the plasma to convex to the plasma increased electron densities by as much as 30%.

Wang et al. [29] computationally investigated the propagation of positive SIWs in air across profiled dielectrics with concave indentations (what will be called cut-pores in this chapter) and convex protrusions. They found that for indentations 1 mm wide and 0.2 mm or 0.3 mm deep, the SIW conformally propagated into and out of the indentation. However, the photoionization source in front of the streamer, a measure of the ionization rate in the stream head, was modulated as the SIW propagated into and out of the indentations.

In this chapter, a computational investigation of the propagation of SIWs over porous dielectric surfaces sustained in atmospheric pressure humid air is discussed. The non-planar structures in this study are pores berried in dielectric at different heights leaving various openings. The interactions between SIWs and pores are dominated by electric enhancement by curvature of

the surface and charging. Intensified electric field in the regions of pore openings produce hopping of the SIW over the exposed surfaces of the pores. The coverage of the pores by the SIWs depends on the level of cut through the pore. Pores placed deeper into the material are exposed to SIWs with only a part of the interior surface. Plasma leakage into subsurface pores that are connected to the plasma through small openings is largely determined by the size of the opening being larger than or smaller than the local Debye length.

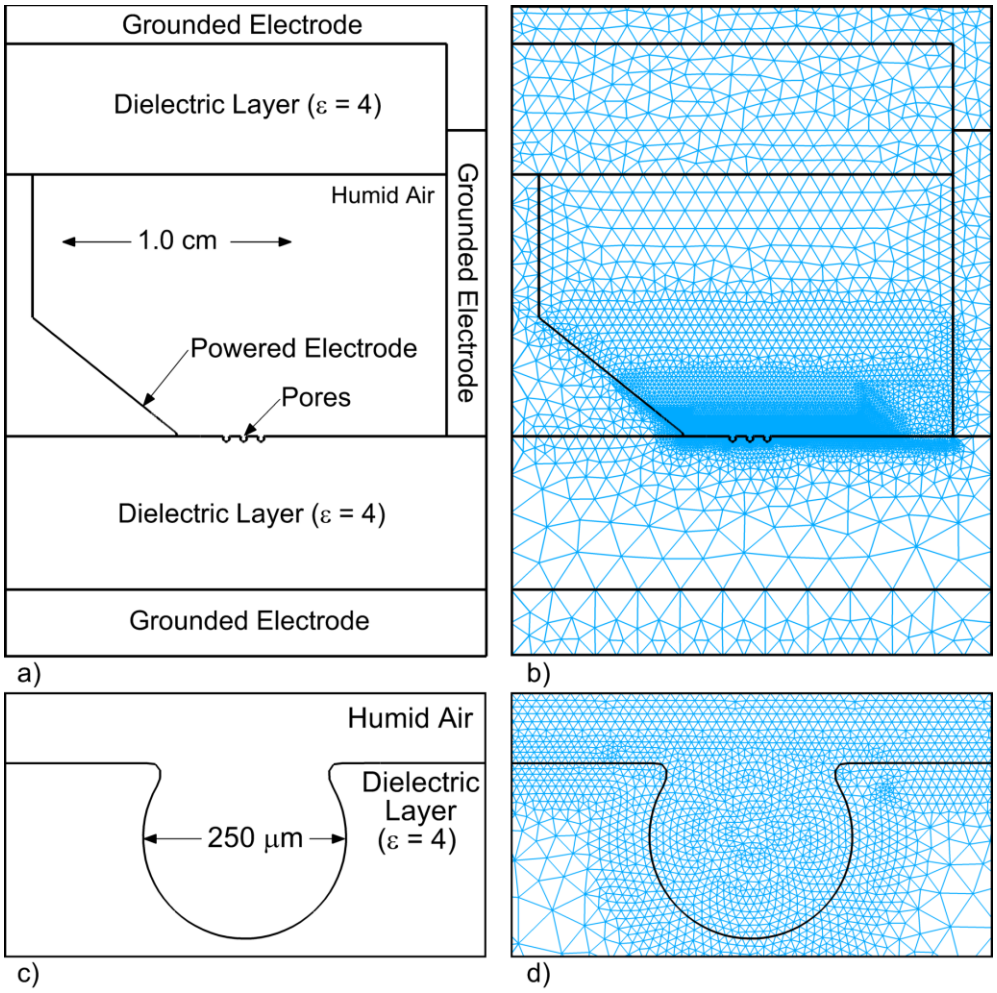

Figure 3.1. The geometry of the model. (a) the entire scheme of the reactor, (b) a full numerical mesh, (c) a zoomed-in image of pore on the top of the dielectric surface, (d) a computational mesh of an enlarged image of the pore.

3.2 Description of the model

A full description of the model nonPDPSIM that was used in this work is contained in Chapter 2. Below is the short description of the specifics of the model used in this chapter. Radiation transport was implemented by using Green's function approximation. A simplified emission-absorption system utilizes one type of photo-ionization process. An emission process from the higher excited state N_2^* to the ground state was used for the subsequent ionization of oxygen molecules O_2. The emission frequency used in all calculations is 2×10^8 s^{-1}. The photo-ionization cross-section was set to be 1.5×10^{-17} cm^2.

This configuration used in this study was motivated by the work of Kettlitz, et al [21]. The 2-dimensional Cartesian model geometry is show in Fig. 3.1. The powered triangular electrode having a tip with radius of curvature of 50 μm is in contact with a dielectric having a relative permittivity of ε_r = 4. The dielectric rests on a grounded electrode which wraps around the computational domain, having a height of 1.5 cm and length of 2.0 cm. There is an insulating break between the ground and powered surfaces. The vertical dielectric section is to prevent SIWs that traverse the computational domain from directly touching ground and arcing. The secondary electron emission coefficient for all positive ions on the dielectric was γ = 0.15. The gas was humid air ($N_2/O_2/H_2O$ = 78/21/1) at 1 atm (760 Torr) and 300 K. Photo-electron emission from the dielectric produced by incident VUV radiation was included with probability γ_{ph} = 0.01.

A spot of neutral plasma having a density of 10^{12} cm^{-3} and 50 μm in diameter was placed at the tip of the powered electrode to seed the discharge. Voltage was applied to the electrode with a linear ramp over 1 ns to a constant voltage to launch the SIW. Porous structure in the surface of the dielectric was imposed starting 2.5 mm from the tip of the electrode at a location where the SIW would propagate on planar surface in a quasi-continuous manner.

3.3 Surface Ionization Waves Propagating across the Flat Interface

The evolution of the SIW over the flat dielectric interface is studied prior to placing the pores on it. The electron density, electron impact ionization source, electron temperature, electric field and photoionization source are shown in Fig. 3.2 adjacent to the surface for a negative SIW launched with a voltage of –30 kV. This particular image is for 20 ns after the voltage is applied, but is representative of the quasi-continuous properties of the propagating SIW. The maximum electron density of 1×10^{13} cm^{-3} with a propagation speed across the surface of 1×10^{7} cm/s. The SIW is sustained by an electron impact ionization source with maximum value of 1×10^{21} cm^{-3}s^{-1}.

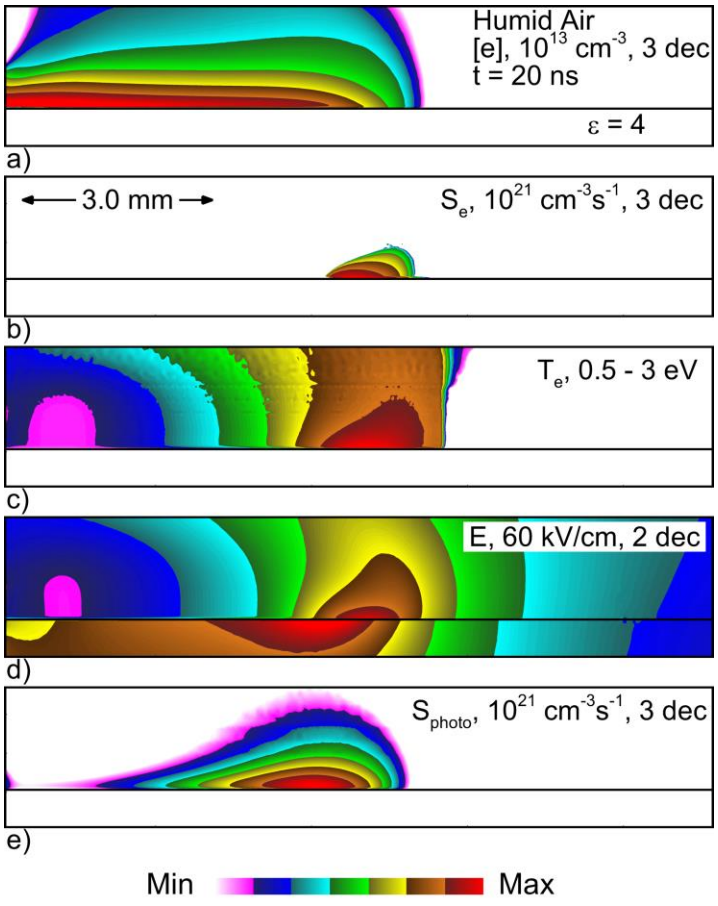

Figure 3.2. Properties of a negative SIW propagating across a flat dielectric surface with relative permittivity $\varepsilon_r = 4$. a) Electron density, b) electron impact ionization source, c) electron temperature, d) electric field and e) photoionization source. The range of values in the image are noted in the frame, with the number of decades for log-plots. Maximal values of the parameters are identified in the figure.

The electric field in the space charge enhanced head of the SIW is 65 kV/cm (or E/N = 240 Td, 1 Td = 10^{-17} V-cm^2), sustaining an electron temperature of 3.0 eV. The plasma is sustained to some degree by photoionization of O_2 and H_2O from the high lying states of N_2.

Reported speeds of SIW vary significantly, with the applied voltage waveform, location of ground planes, permittivity of the dielectric, surface capacitance C_s (F/cm^2) and type of gas. Kettlitz et al. [21] measured speed of propagation of negative SIWs across alumina in synthetic air at 1 atm of 8×10^6 cm/s, albeit for a slow rising voltage pulse (10 μs) of lower peak amplitude (9 kV). At about 80% the applied E/N used here, Stepanyan measured a negative SIW propagation speed (diffusive mode) in high pressure air of 6×10^7 cm/s [6]. Goldberg et al. measured speeds of 1×10^8 cm/s for SIW over alumina sustained in H_2 at 200 Torr [30] with 3 kV, which would correspond to about 11.4 kV at atmospheric pressure. Also at low pressure, 20 Torr N_2, Petrishchev et al. measured initial SIW speeds over quartz of 1×10^8 cm/s for a -12 kV pulse having a 100 ns rise time [31]. Using an actuator, strip-line geometry, Huang et al. [32] measured speeds of SIW in air over epoxy resin ($\varepsilon_r = 4.3$) of 3×10^7 cm/s for an applied voltage of 14 kV with a 200 ns rise time. Li et al., simulating high voltage SIWs in air, predicted speeds of negative waves of up to 3×10^8 cm/s [19].

As the SIW passes over the dielectric, the capacitance of the dielectric is charged, which transfers much of the applied voltage into the dielectric. For example, 1 mm behind the head of the SIW, the potential of the surface of the dielectric is -15 kV, compared to the applied voltage of -30 kV. The electric field inside the dielectric 50 μm below the surface is 60 kV/cm, pointing upwards towards the negative surface charge. The electric field in the gas at the surface of the dielectric has a significant component parallel to the surface at the head of the SIW. As the SIW passes and negatively charges the underlying dielectric, the orientation of the electric field

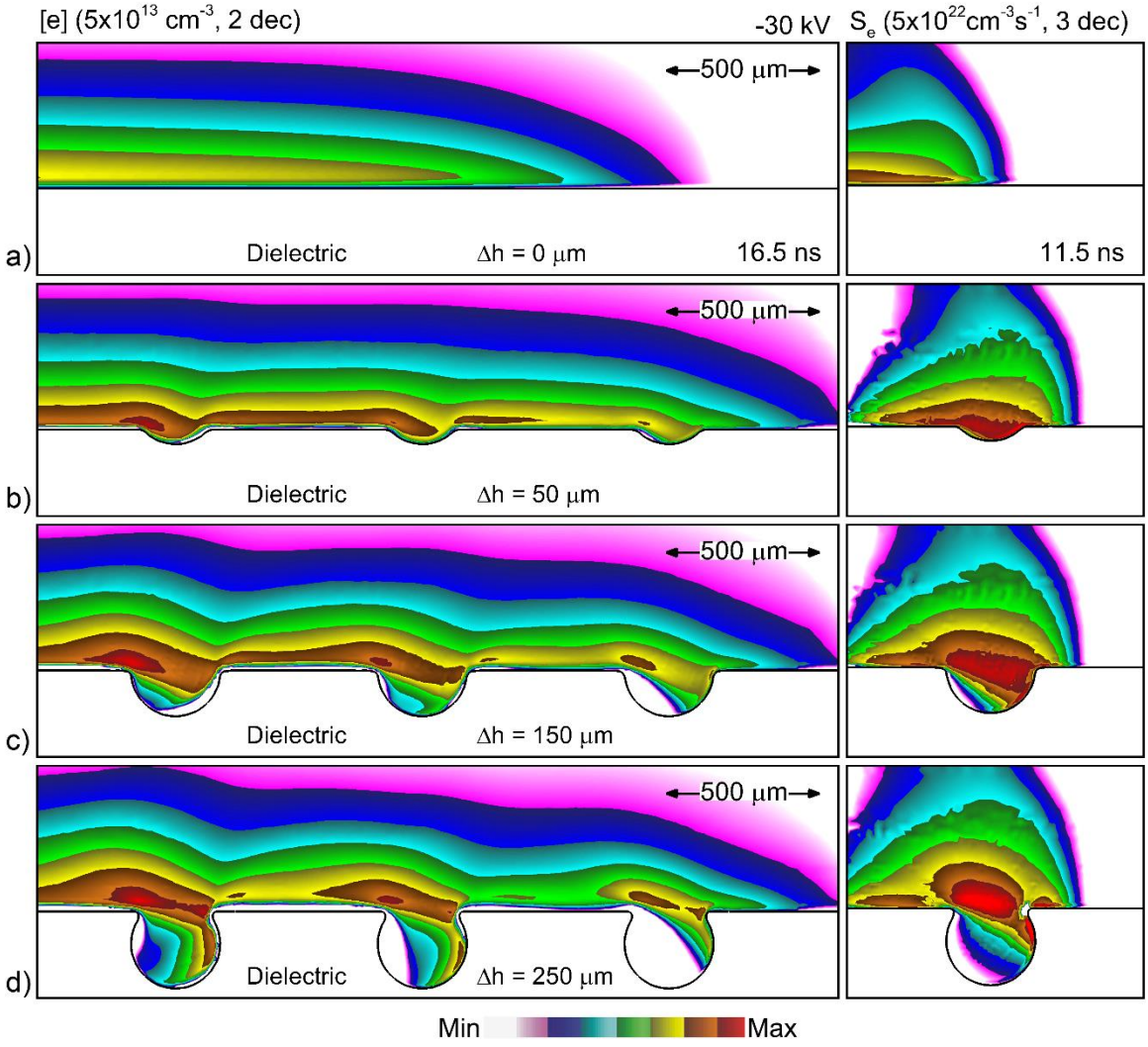

Figure 3.3. Propagation of a negative SIW across a surface with cut pores with diameter 285 having different depths of the pores, Δh. a) Δh = 0 μm (flat), b) 50 μm, c) 150 μm and d) 250 μm. Electron density (maximum 5 $\times 10^{13}$ cm^{-3}, 2-decade log scale) is shown in the left column at 16.5 ns after the SIW crosses the 3 cut pores. Electron impact ionization source (maximum 5 $\times 10^{22}$ $cm^{-3}s^{-1}$, 3 decade log scale) is shown in the right column for the first (left-most) pore when the SIW arrives at 11.5 ns.

becomes vertical. The negative charging of the dielectric is about -1.0 $\times 10^{13}$ q-cm^{-3}, with a positive space charge layer above the surface of (2-3) $\times 10^{11}$ q-cm^{-3}.

Several numerical experiments were conducted to determine contributing factors to the propagation of the SIW. Photoelectron emission from the surface due to VUV produced by the

SIW was included and removed. The secondary electrons from the surface produced by photo-ionization and by ion bombardment were treated using a kinetic Monte Carlo Simulation. Neither of these processes or procedure had a significant effect on the propagation of the SIW due to the surface appearing to be anode-like, electric fields generally oriented in a manner that accelerates secondary electrons back into the surface.

3.4 Surface Ionization Waves Propagating across the Porous Dielectric

The propagation of SIWs over porous dielectrics was investigated for the geometry for two configurations. The first configuration is for pores that are cut by the surface, exposing the inside surface of the pore for pores to have increasing depth. The second configuration is a pore entirely below the surface with a small opening to the surface. Pores are separated by 830 μm with the center of the first pore 2.2 mm from the edge of the electrode.

Pores are generally randomly located in porous materials. When a porous material is cut to create a flat surface, pores are cut-through leaving openings that vary from shallow spherical bowls to spheres with small openings to the ambient. The exposed surfaces that are convex to the plasma polarize and produce electric field enhancement. This electric field enhancement typically occurs at the edges of the cut pores. The surfaces that are concave to the plasma, such as at the bottom of the pore, polarize and produce a decrease in local electric field. Plasma properties shown in Fig. 3.3 for negative SIWs propagating over the dielectric with cut pores having a full pore diameter of 285 μm. Cut pores have depths of Δh = 0 μm (flat surface), 50 μm, 150 μm and 250 μm. The voltage magnitude is -30 kV with a rise time of 10 ns. (The higher voltage, material properties and geometry produce a thicker SIW.) The electron densities are shown at 16.5 ns after crossing over 3 cut-pores. The electron impact ionization source is shown at 11.5 ns,

approximately the time that the ionization wave reaches the edge of the cut pore. The electron density, electron impact ionization source, and E/N are shown in Fig. 3.2 at different times for the first pore, which has a depth of $\Delta h = 250$ μm.

The SIW is able to follow the contours of the surface for moderate depths of the cut-pores, $\Delta h = 50$ - 100 μm, filling the pores with electron density exceeding 10^{13} cm^{-3}. This conformality is consistent with the results of Wang et al. [29]. With increasing depth of the pore, the radius of curvature of the exposed edge decreases, increasing the polarization and producing larger electric field enhancement. The electric field enhancement produces a local maximum ionization rate, launching a bulk IW that crosses the pore's volume. This is a form of SIW hopping, occurring here for $\Delta h > 100$ μm. As shown in the inset for the ionization source in Fig. 3.3, the hopping of the SIW has two components. The first is the electric field enhancement on the leading edge of the pore. The electric enhancement is large enough that a bulk ionization wave is launched, which detaches the SIW from the surface. The second component is the electric field enhancement on the trailing edge of the pore, which attracts the bulk IW into the edge. The end result is that the leading inner surface of the pore (facing to the right) becomes progressively less exposed to the plasma as the cut-pore is located deeper into the dielectric.

The propagation of the SIW in the most deeply cut pore, $\Delta h = 250$ μm, is shown in Fig. 3.4. As the SIW approached the pore (t=11.0 ns), electric field enhancement at the leading and trailing edges of the pore produce ionization sources which launch a bulk IW across the open pore. This transition from an SIW to a bulk ionization wave leaves the leading surface of the pore (facing

to the right) unexposed to the plasma. The bulk IW strikes the trailing edge of the pore, which charges the surface. This surface charge produces two SIWs (t = 11.5 ns). The first, a forward

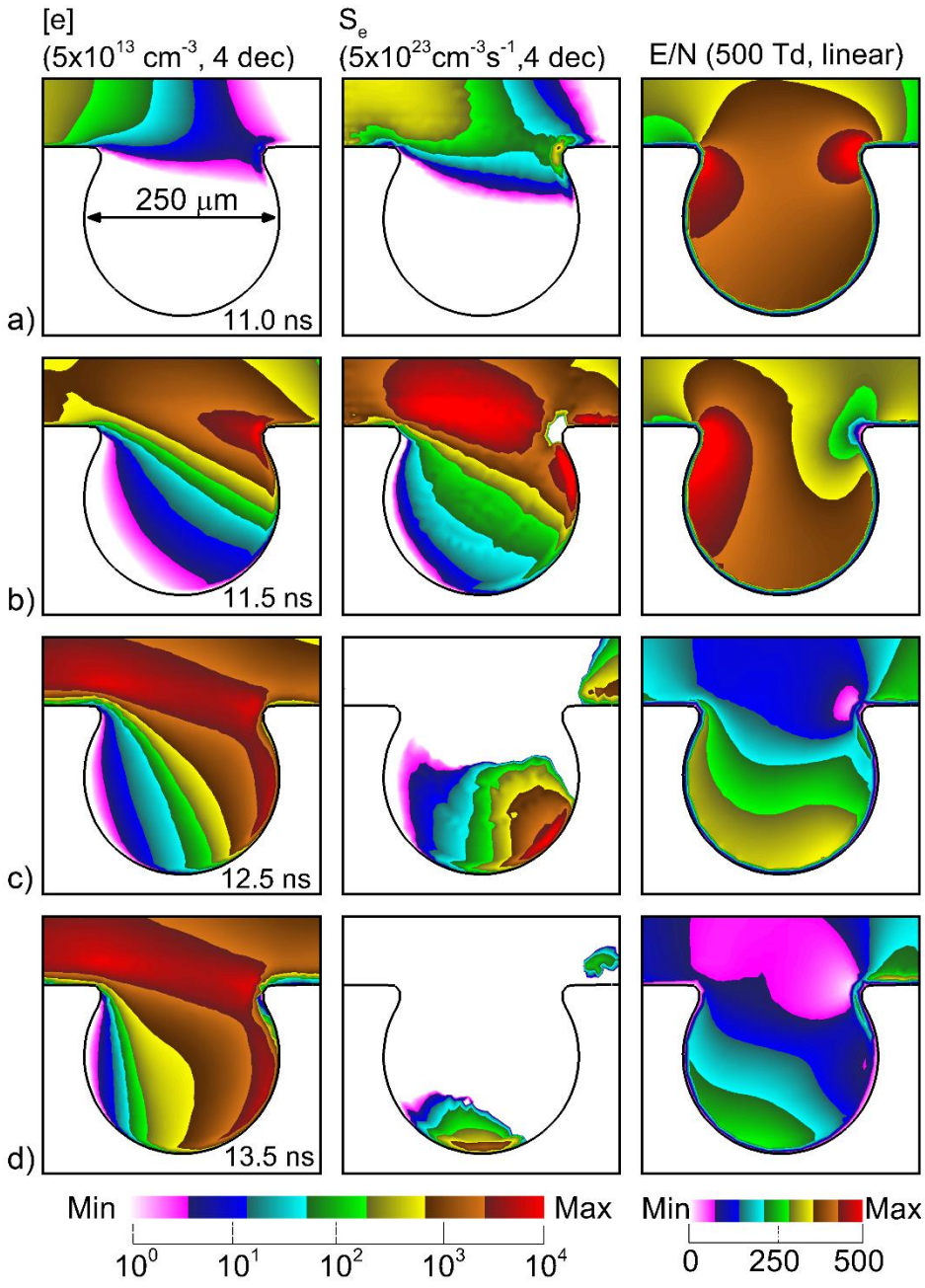

Figure 3.4. Plasma properties for the negative SIW arriving at the first, left-most cut-pore (diameter 285 μm) having depth Δh = 250 μm at times of a) 11.0 ns, b) 11.5 ns, c) 12.5 ns and d) 13.5 ns. The columns (left to right) show electron density, electron impact ionization source and E/N. The range of values for each quantity (and number of decades for log-plots) are shown at the top of each column.

SIW, continues to propagate along the top surface towards the next pore. The second, a reverse SIW, propagates along the inner surface of the pore in a cathode-seeking direction (t = 12.5 ns). The reverse SIW eventually stalls approaching the upward leading surface of the pore (t = 13.5

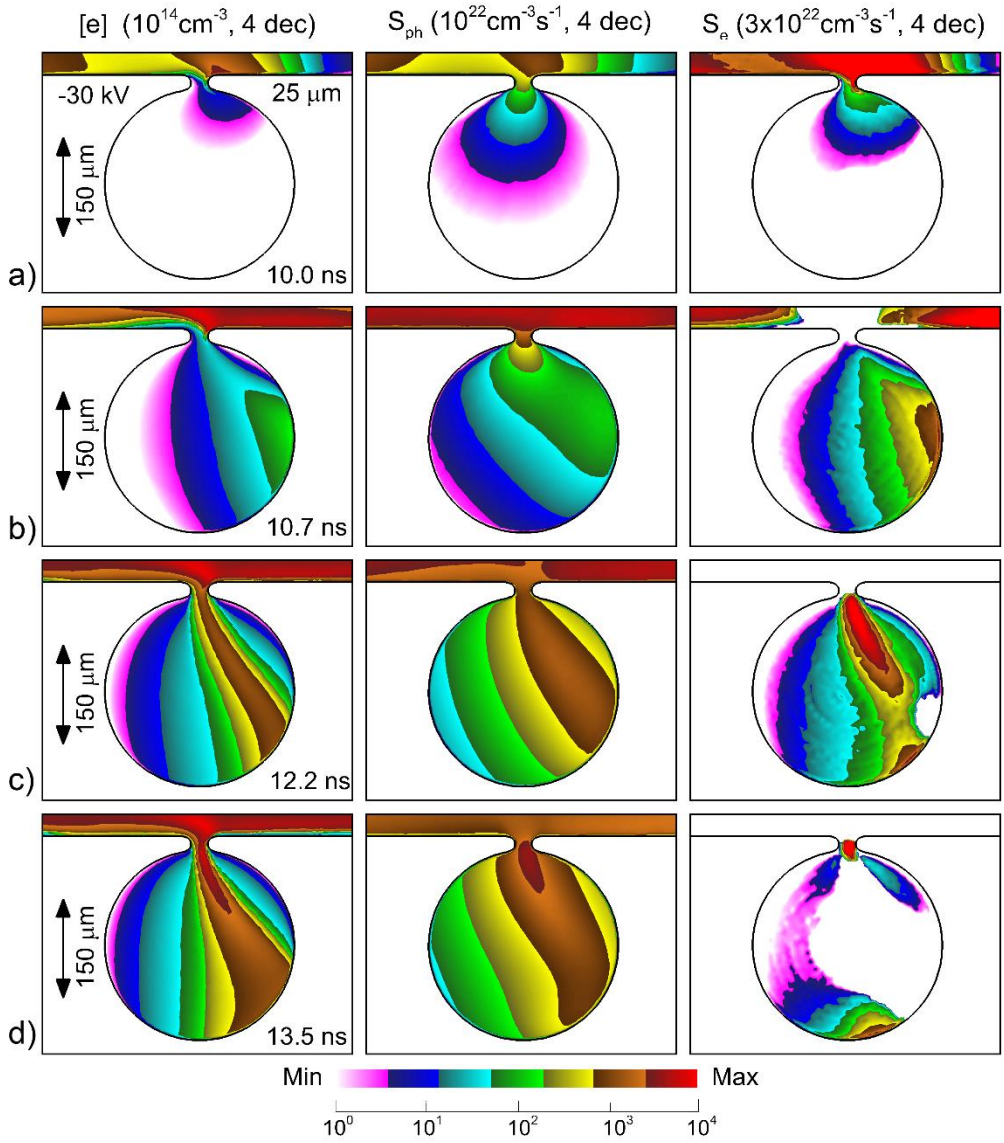

Figure 3.5. Plasma properties for the negative SIW arriving at the first, left-most buried pore (diameter 285 μm) having an opening to the plasma of 25 μm at times of a) 10.0 ns, b) 10.7 ns, c) 12.2 ns and d) 13.5 ns. The columns (left to right) show electron density, photo-ionization source and electron impact ionization source. The range of values for each quantity (4-decade log scale) are shown at the top of each column. Values in the bulk plasma on top of the surface may be saturated for the range of values in the image. The range of values was chosen to emphasize the in-pore properties.

ns). There is insufficient plasma density and insufficient E/N to produce the charge density required to sustain ionization in the leading edge of the reverse SIW.

In taking a cut through a porous material, there is some likelihood of cutting through the opening through two interconnected pores. This cut may leave a small opening of the pore to the plasma, the size of which may be commensurate with the Debye length of the plasma in the SIW passing over the pore. The electron density, photo-ionization source and electron impact ionization source are shown in Fig. 3.5 for a negative SIW (-30 kV, 10 ns risetime) passing over a pore with a 25 μm opening to the plasma. When the SIW on the top surface reaches the opening to the pore, the electron density in the SIW is 5-7 $\times$ 10^{13} cm^{-3} with an electron temperature of 5.7 eV, corresponding to a Debye length of about 2.5 μm. With the opening to the pore being larger than the Debye length, the plasma is able to flow into the pore (t = 10 ns). This propagation of the SIW into the pore is aided by photo-ionization resulting from VUV flux passing through the pore opening from the plasma on the top surface.

With the SIW on the top of the surface intersecting with the trailing edge of the opening of the pore, the surface charges, which launches a SIW along the inner surface of the pore (t = 10.7 ns). As this SIW propagates along the inner surface, differential charging occurs between the inner surface and the opening to the pore, a location where there is natural electric field enhancement due to the curvature of the edges. A bulk IW is then launched across the pore (t = 12.2 ns). With the bulk IW dissipating, the SIW continues along the inner circumference of the pore (t = 13.5 ns). The SIW propagates for another 3 ns before stalling upon approaching the upwards leading surface of the pore (facing to the right). Radiation from high-lying states of N_2 produces photo-ionization that is commensurate with ionization by electron impact processes. This photo-ionization continues after the SIW has dissipated, sustaining the plasma in the pore. Maximum plasma

densities in the pore are $0.5 - 1 \times 10^{14}$ cm^{-3}. To some degree, the plasma in the pore is an extension of the plasma on the top surface. With the opening of the pore being larger than the Debye length,

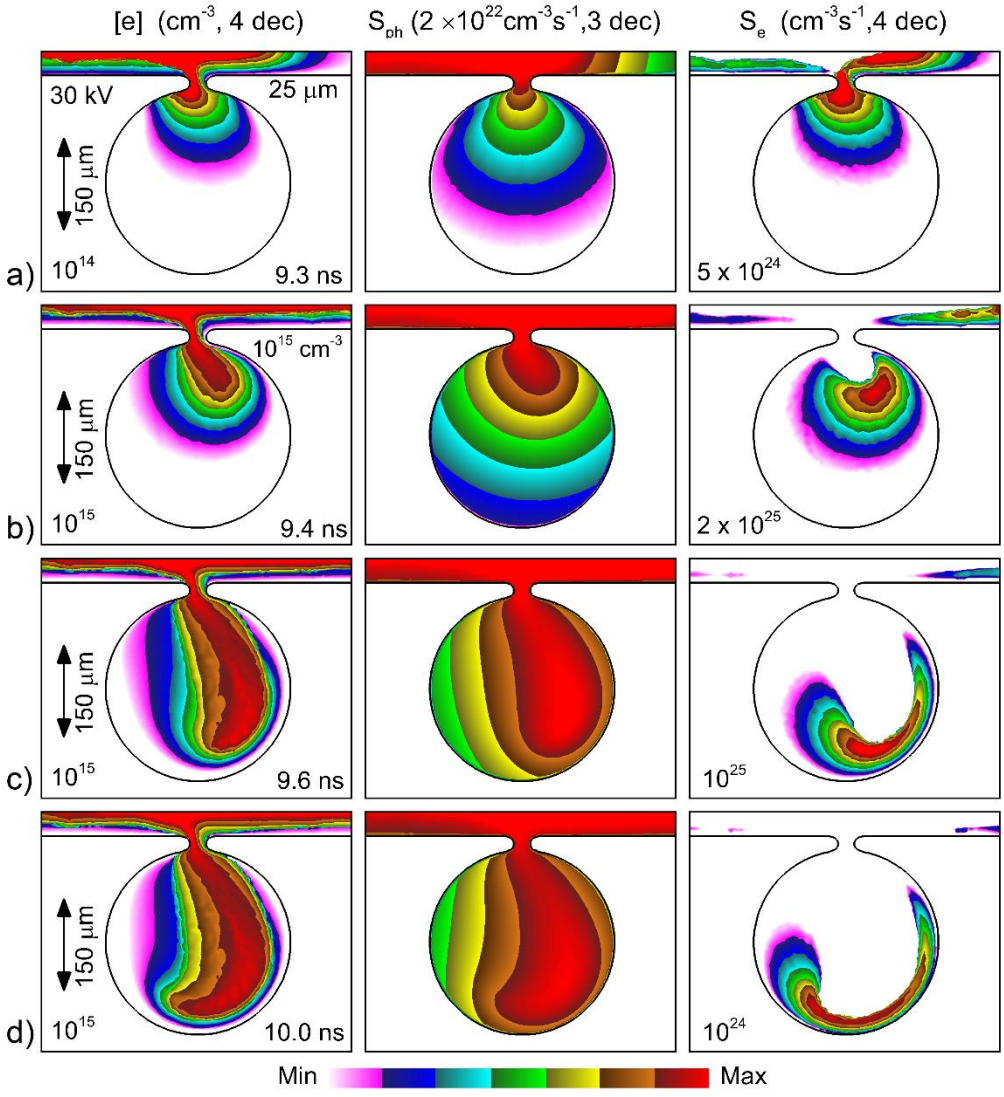

Figure 3.6. Plasma properties for the positive SIW arriving at the first, left-most buried pore (diameter 285 μm) having an opening to the plasma of 25 μm at times of a) 9.3 ns, b) 9.4 ns, c) 9.6 ns and d) 10.0 ns. The columns (left to right) show electron density, photo-ionization source and electron impact ionization source. The range of values for each quantity and number of decades for these log plots are shown at the top of each column. Values in the bulk plasma on top of the surface may be saturated for the range of values in the image. The range of values was chosen to emphasize the in-pore properties.

plasma is able to flow into the pore, a similar observation to Zhang and Bogaerts who investigated plasma penetration into vertically oriented channels [33].

The electron density, photo-ionization source and electron impact ionization source are shown in Fig. 3.6 for a positive SIW (30 kV, 10 ns risetime) passing over the same pore with a 25 μm opening to the plasma. (Note that the properties in the plasma on top of the surface are saturated in color in order to show detail in the pore.) The entry of the positive SIW into the pore occurs from the leading edge of the opening, a consequence of the positive SIW being more conformal to the surface than negative SIW and the plasma density along the top surface being larger (1×10^{15} cm^{-3}). The plasma density that flows into the pore (t = 9.3 ns) is high enough to sustain a bulk IW that is launched across the pore (t = 9.4 – 9.6 ns). A corresponding SIW is not produced due to lack of significant surface charging. The bulk SIW intersects with the bottom of the pore (t = 10.0 ns) and dissipates. The plasma density produced in the pore exceeds 10^{15} cm^{-3}, an extension of the plasma on the top surface.

The electron density, photo-ionization source and electron impact ionization source are shown in Fig. 3.7 for a negative SIW (-30 kV) passing over pore with a 4 μm opening to the plasma. The size of the opening to the pore is about the same as the Debye length. The plasma is not able to readily flow into the pore. Electrons do leak into the pore (t = 10.0 ns) but not as a flowing plasma. The density of the electrons leaking into the pore, 3×10^{7} cm^{-3}, is below the ambipolar limit. As a result, the flow of electrons into the pore is mono-polar and the electron flux is not accompanied by a neutralizing flux of positive ions. With the electron flow being nearly monopolar, the flux into the pore is technically not a flowing plasma.

Initial plasma formation in the pore is dominated by photo-ionization by VUV flux produced in the plasma on the top surface and propagating through the opening. This photo-

ionization resulting from VUV flux passing through the pore opening is indicated by the triangular, shadowed photo-ionization source (t = 10.0 ns). At this time, the electron impact ionization source is essentially zero. This initial seeding of electrons in the pore by photo-ionization then leads to a bulk ionization wave through the volume of the pore that intersects with the inner surface of the

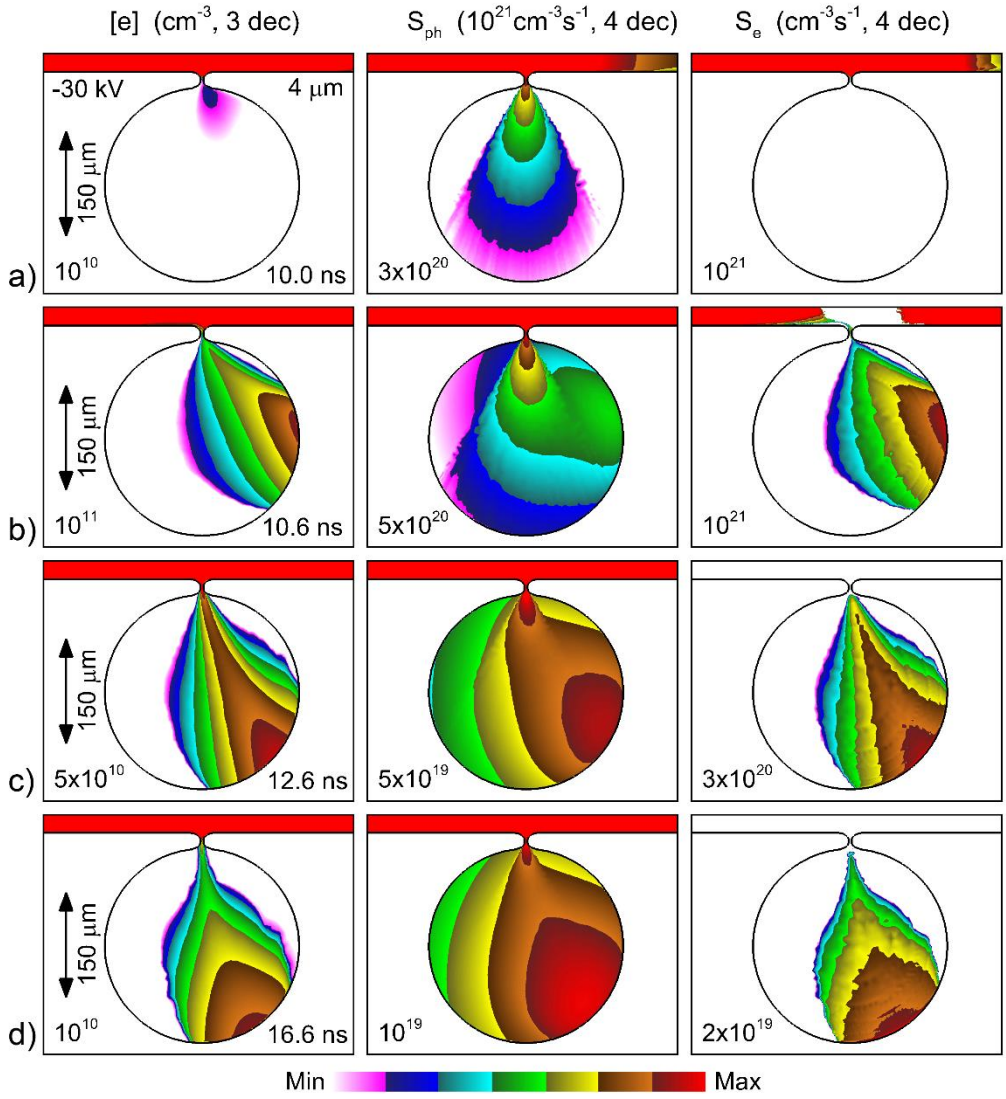

Figure 3.7. Plasma properties for the negative SIW arriving at the first, left-most buried pore (diameter 285 μm) having an opening to the plasma of 4 μm at times of a) 10.0 ns, b) 10.6 ns, c) 12.6 ns and d) 16.6 ns. The columns (left to right) show electron density, photo-ionization source and electron impact ionization source. The number of decades for these log plots are shown at the top of each column. The maximum values for each image are shown in the frame. Values in the bulk plasma on top of the surface may be saturated for the range of values in the image. The range of values was chosen to emphasize the in-pore properties.

pore. Upon charging the surface, there is a transition to a SIW (t = 10.6 ns). Once plasma

penetrates into the pore, there are two components of photo-ionization. The first results from VUV flux that enters through the opening in the pore (shadowed, triangular-shaped ionization source at t = 10.6 ns). The second source of photo-ionization produced by the plasma inside the pore (ionization source that overlaps with the plasma density at t = 10.6 ns). The SIW continues to propagate along the inner surface (t = 12.6 – 16.6 ns) while there is continuous leakage of electrons from the plasma on the top surface into the pore. The electric field enhancement at the opening of the pore then launches these electrons into a weak bulk IW. The plasma density inside the pore does not exceed 5×10^{10} cm^{-3}.

Plasma properties for a positive SIW (30 kV) passing over a pore with a 4 μm opening are shown in Fig. 3.8. The local Debye length in the SIW on the top surface when arriving at the pore is about 1 μm, and so there is some direct flow of plasma into the pore through the 4 μm opening (t=9.3 ns) producing an electron density of (3×10^{12} cm^{-3}). This plasma density is produced in large part by flow into the pore and local electron impact ionization, and secondarily by photo-ionization. Again, there are two components to the photo-ionization – due to photons transmitted through the pore and photons produced inside the pore (t = 9.3 ns). In spite of there being sufficient charge density in the pore to generate a bulk IW, charging of the top surface of the dielectric shields potential from the pore, and reduces E/N near the pore opening where the electron density is large enough to launch an IW (t = 9.5 ns). Due to the low E/N, the ionization source transitions to being negative (t = 10.4 ns). Coupled with onset of free diffusion of electrons in the sub-ambipolar densities, the electron density rapidly decays (t = 13.0 ns).

3.5 Concluding Remarks

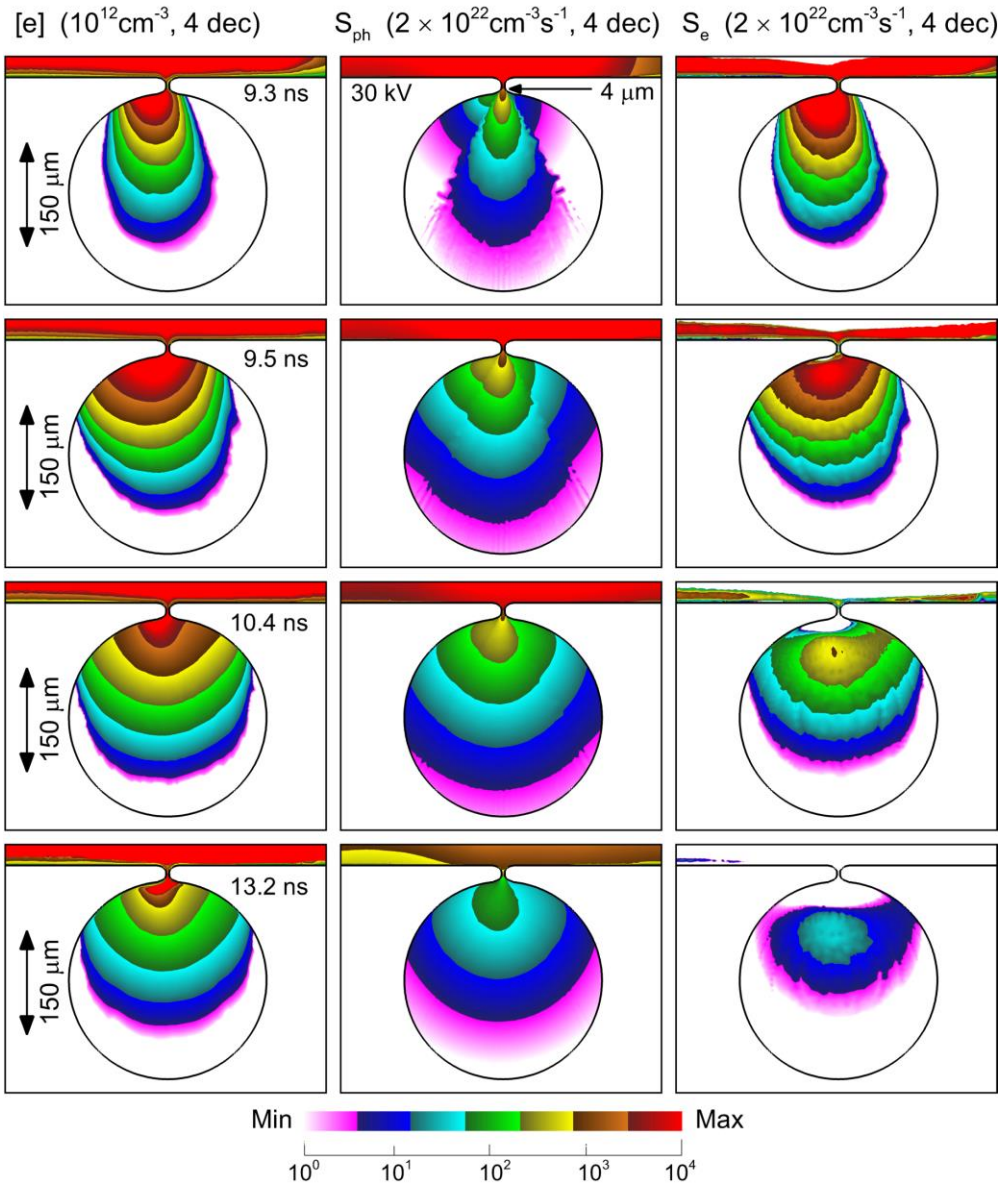

Figure 3.8. Plasma properties for the positive SIW arriving at the first, left-most buried pore (diameter 285 μm) having an opening to the plasma of 4 μm at times of a) 9.3 ns, b) 9.5 ns, c) 10.4 ns and d) 13.0 ns. The columns (left to right) show electron density, photoionization source and electron impact ionization source. The number of decades for these log plots are shown at the top of each column. The maximum values for each image are shown in the frame. Values in the bulk plasma on top of the surface may be saturated for the range of values in the image. The range of values was chosen to emphasize the in-pore properties.

Atmospheric pressure plasmas interacting with dielectric surfaces usually transition into some form of surface ionization wave (SIW). In this chapter, results from a computational investigation of SIWs sustained in humid air propagating over porous dielectrics of different kinds were discussed.

It is found that negative SIWs are able to adhere to the surfaces with shallow open pores. However, the electric field enhancement at the edges of the cuts through deeper pores will launch bulk IWs that hop or skip over the pores. Although there is some backwards propagation of SIWs inside the pore, there are generally surfaces that are left unexposed to the plasma for both negative and positive SIWs.

In the limit of buried pores with small openings to the plasma, the filling of the pores depends on the size of the openings compared to the local Debye length when the SIW arrives at the opening. If the opening is larger than the Debye length, plasma flows into the pore from the SIW. The dynamics of the plasma inside the pore can be complex, resulting in the inside surfaces generally not being uniformly exposed to the plasma. With the opening to the pore being commensurate or smaller than the local Debye length, plasma will not directly flow into the pore. Diffusion of electrons into the pore as a non-neutral current may occur. Photo-ionization by VUV photons generated outside the pore and propagating through the opening also produces electrons in the pore. Neither sources are typically sufficient to sustain a large plasma density in the pores.

3.6 References

[1] V. I. Gibalov and G. J. Pietsch, Plasma Source Sci. Technol. **21**, 024010 (2012).

[2] X. Li, A. Sun, G. Zhang and J. Teunissen, Plasma Source Sci. Technol. **29**, 024010 (2020).

[3] H. Hoft, M. Kettlitz, M. M. Becker, T. Hoder, J. Phys. D **47**, 465206 (2014).

[4] X. Xu, Thin Solid Films **390,** 237 (2001).

[5] A. V. Likhanskii, M. N. Shneider, S. O. Macheret and R. B. Miles, J. Appl. Phys. **103**, 053305 (2008).

[6] S. A. Stepanyan, A. Yu. Starikovskiy, N. A. Popov and S. M. Starikovskaia, Plasma Source Sci. Technol. **23**, 045003 (2014).

[7] C. Nau-Hix, T. M. Holsen and S. Mededovic Thagard, Plasma Proc. Polym. e220036 (2022).

[8] S. A. Shcherbanev, Ch. Ding, S. M. Starikovskaia and N. A. Popov, Plasma Source Sci. Technol. **28**, 065013 (2019).

[9] M. Florkowski, Measurement **186**, 110170 (2021).

[10] F. Pechereau, Z. Bonaventura and A. Bourdon, Plasma Source Sci. Technol. **25**, 044004 (2016).

[11] P. Viegas, E. Slikboer, Z. Bonaventura, E. Garcia-Caurel, O. Guaitella, A. Sobota and A. Bourdon, Sci. Report **12**, 1181 (2022).

[12] B. Huang, C. Zhang, I. Adamovich, Y. Akishev and Tao Shao, Plasma Sources Sci. Technol. **29**, 044001 (2020).

[13] P. Viegas, E. Slikboer, Z. Bonaventura, O. Guaitella, A. Sobota and A. Bourdon, Plasma Sources Sci. Technol. **31**, 053001 (2022).

[14] E. Slikboer, P. Viegas, Z, Bonaventura, E. Garcia-Caurel , A. Sobota , A. Bourdon and O. Guaitella, Plasma Sources Sci. Technol. **28** 095016 (2019).

[15] R. Joshi, J. F. Kolb, S. Xioa and K. H. Schoenbach, Plasma Proc. Polym. **6**, 763 (2009).

[16] X. Li, A. Sun, Guanjun Zhang and J. Teunissen, Plasma Sources Sci. Technol. **29**, 065004 (2020).

[17] H. K. Meyer, F. Mauseth, R. Marskar, A. Pedersen and A. Blaszczyk, Trans. Diel. Elect. Insul. **26**, 1163 (2019).

[18] H. K. H. Meyer, R. Marskar, H. Gjemdal and F. Mauseth, Plasma Source Sci. Technol. **29**, 115015 (2020).

[19] X. Li, A. Sun and J. Teunissen, Trans. Diel. Elect. Ins. **27**, 1178 (2020).

[20] F. Pechereau, J. Jansky and A. Bourdon, Plasma Source Sci. Technol. **21**, 055011 (2012).

[21] M. Kettlitz, R. Klink, H. Hoft and R. Brandenburg, Eur. Phys. J. D **74**, 110 (2020).

[22] T. Hoder, H. Hoft, M. Kettiltz, K-D. Weltmann and R. Brandenburg, Phys. Plasma **19**, 070701 (2012).

[23] W. Ning, D. Dai and L. Li, Plasma Source Sci. Technol. **27**, 08LT01 (2018).

[24] Q. Wang, W. Ning, D. Dai and Y. Zhang, Plasma Proc. Polym. **17**, e1900182 (2020).

[25] S. Jahanbakhsh, V. Bruser and R. Brandenburg, Plasma Sources Sci. Technol. **27**, 115011 (2018).

[26] Z. Mujahid and J. Schulze, AIP Advances **12**, 01528 (2022).

[27] Z. Mujahid, J. Kruszelnicki, A. Hala and M. J. Kushner, Chem. Engr. J. **382**, 123038 (2020).

[28] Y. Sun, B. Zhang, C. Wang and G. Zhang, Adv. Electron. Mater. **7**, 2100369 (2021).

[29] F. Wang, L. Wang, S. Chen, Q. Sun and L. Zhong, Trans. Diel. Elect. Insul. **28**, 2186 (2021).

[30] B. M. Goldberg, P. S. Bohm, W. Czarnetzki, I. V. Adamovich and W. R. Lempert, Plasma Source Sci. **24**, 055017 (2015).

[31] V. Petrishchev, S. Leonov and I. V. Adamovich, Plasma Source Sci. **23**, 065002 (2014).

[32] B. Huang, C. Zhang, I. Adavmovich, Y. Akishev and T. Shao, Plasma Source Sci. Technol. **29**, 044001 (2020).

[33] Q-Z. Zhang and A. Bogaerts, Plasma Source Sci. Technol. **27**, 035009 (2018).

Chapter 4 Atmospheric Pressure Plasma Treatment of Wet Microchannels: Optimal Surface-to-Volume Ratio

Surface dielectric barrier discharge (SDBD) is utilized on a dielectric substrate with implemented wet microchannels in a fully computational study. Wet microchannels are a simplified model suitable for studying of efficient volumetric treatment of liquids by atmospheric pressure plasmas (APPs). It is demonstrated that different plasma parameters, as well as the material of the substrate and the dimensions of the channels, can affect the results of treatment. Positive polarity-driven surface ionization waves (SIWs) are beneficial over negative ones in terms of both higher local plasma density and consistency of treatment along the substrate. The material of the substrate can affect the behavior of the SIW and the shape of the liquid content on it. This study addresses the synergistic effect on plasma propagation of the altered shape of water due to hydrophobicity. It demonstrates that although wet microchannels generally do not produce large obstacles on the interface, minor irregularities can affect the distribution of photoionization and, thus, the photoproducts on the water interface. Extension of the channels in a horizontal direction generally increases the surface-to-volume ratio, potentially enhancing the volumetric treatment of water plasma. This chapter shows that there is a limit for the maximal length of channels, after which the benefits of the treatment reach saturation. Atmospheric pressure plasmas allow for the treatment of large liquid interfaces, resulting in volumetric alteration of the content. The results presented in this chapter can be beneficial for developing technologies in the field of water purification, wound healing, or even cancer treatment.

4.1 Introduction

Rectangular microchannels filled with water can serve as a model for a microfluidic reactor or represent wet skin with wrinkles. Further, APPs exhibit a wide range of effects on both microfluidic reactors and human tissue. By generating fluxes of ions, reactive oxygen and nitrogen species (RONS) [1-3], vacuum ultraviolet (VUV) photons [4,5] and electric fields, APPs may be beneficial for materials functionalization [6,7], bacteria inactivation [8,9], cancer cells illumination [10-11], water purification [12-13] and various other applications. The ability to control specific phenomena enables the development of practical technologies. While there is a wide range of sources for generating APPs, each of them offers distinct advantages suited for various applications. The most common devices include dielectric barrier discharges (DBDs) [14], atmospheric pressure plasma jets (APPJs) [15] and SDBDs [16]. Of these, SDBDs provide the largest fluxes of RONS and photons and the highest electric fields at interface in respect of input energy. This is primarily due to the limited losses of energy in the gas phase, given that the propagation is localized on the surface. In this chapter, an SDBD model is used to perform simulations.

In the existing literature, several studies indicate the effects of APPs on wet and dry microchannel arrays. Microchannels are elementary geometry representing wet or dry wrinkled skin or microfluidic reactors. With developing technologies, microfluidic reactors have gained popularity among scientific communities [17,18]. Recent technologies that are becoming more complex typically require some synergistic approach that combines several fields. Moreover, APPs applied to microfluidic reactors have also been used in several studies [19,20]. The benefits gained from plasma action on such devices extend from modification of materials for substrates (e.g. functionalization of polymers [6,21]) to liquid treatment (e.g. water purification [22,23]). The

morphology of the surface is typically complex. Existing examples of the above-described interfaces are typically a combination of different materials with non-smooth topical coverage consisting of dielectrics or lossy dielectrics. The characteristics of the surface charge guide the interaction of ionization waves (IWs) with such surfaces. Propagation of SIWs across such a material can be altered with irregularities. Generally, the shape of the interface can change the capacitance of the entire domain or a portion of it. Enhanced or decreased capacitance affects local electric fields that drive the SIWs.

Additionally, with the presence of different materials on a single interface, the surface contains so-called *electrical triple-points* [24], the intersection of three dielectric media. Such points in the electric field environment are associated with the enhancement of local electric fields that can promote the propagation of SIWs across such surfaces. Other effects provided with non-smooth interfaces can include shadowing of photoionization source from large obstacles on the ways of SIWs, and some conduction of electrical current by the substrate due to the conductive component in lossy dielectrics. The cumulative effect from the described phenomena can be observed in interactions between SIWs and wet or dry microchannels.

This chapter contains a computational study of SDBD interacting with a dielectric substrate containing wet microchannels. In a 2D model, a triangular-powered electrode, contacting a dielectric substrate, generates SIWs over an array of wet microchannels. We found that negative polarity-driven SIWs generally produce lower plasma density in the researched area than positive ones. This results in an order of magnitude lower photon fluence. In all case scenarios, the SIW starts interacting with an array of channels from the left-most corner of the contact point between the liquid and the substrate in the channels due to the enhanced electric field. The material of the substrate can affect the local geometry of this location of arrival, which subsequently changes the

character of propagation of the SIW across the entire array. For example, varied hydrophilicity of the material and subsequent change in the shape of the water in the channels has an influence on the propagation of SIWs in our study: the most uniform treatment of the liquid interface is reached in the hydrophilic case. Channels are extended horizontally to maximize volumetric treatment. It is identified that such a method has limited benefits for surface coverage by plasma. The issue is that plasma propagation across such a surface is sensitive to electrical triple-points, described above, and SIWs hop between these points. The remaining liquid surface receives limited species fluxes if there is a significant distance between these points. The details of the study are described in the body of the chapter.

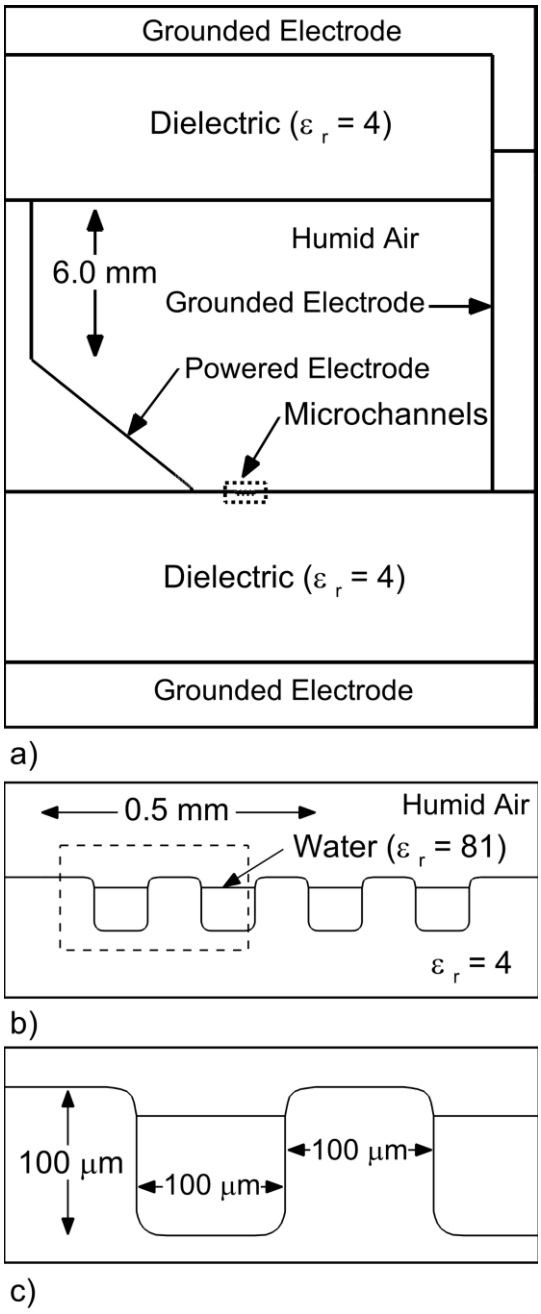

Figure 4.1. Schematic image of the geometry domain. a) Full image of the 2D geometry, b) zoomed-in image of the array of channels, c) zoomed-in periodic channel structure with dimensions.

4.2 Description of the Model

The detailed operations of the code are presented in Chapter 2. The emitting excited state for all photoionization events is considered to be the higher excited state of nitrogen N_2^* and the absorbing species are considered to be O_2, H_2O and H_2O_{aq}. The photoionization cross-section for gaseous and liquid water is considered to be 2.0 ×

10^{-17} cm^2 [25] and the cross-section for oxygen is set to be 3.0×10^{-17} cm^2. Water in the microchannels is addressed with the liquid module. Briefly, the liquid zone is treated as a dense plasma zone (3.0×10^{22} cm^{-3}). The balance for evaporation is addressed with vapor pressure. The diffusion of neutrals across the liquid interface is addressed with Henry's law. The penetration of the charged species and photons through the liquid boundary is given with the unity probability. The chemistry for both gas and liquid phases is considered. The reaction mechanism consists of 62 species and around 1000 reactions. The mechanism is described in detail by Lietz et al. [26].

In this chapter, a standard SDBD (Chapter 1) setup is simulated. The geometry prototype was motivated by Kettlitz et al. [27]. The numerical map of nodes is generated for this work using the commercial software Pointwise (discussed in Chapter 2). Fig. 4.1 demonstrates the geometry domain with details of the model. The setup is similar to the one described in Chapter 3. Briefly, in this model, a triangular-powered electrode is placed on a dielectric surface to generate direct SIWs on a contacting dielectric surface. The ground metal is wrapping the system around. The top area of the system contains another dielectric placed parallel to the one that is used for treatment. Wet channels are placed 1.8 mm away from the powered electrode. Base case microchannels are 100 μm wide and long, placed 100 μm away from each other. The liquid fills the interior of the channels in three forms, assuming that the material of the substrate can be hydrophilic, hydrophobic or neutral (leaving different contact angles between the substrate and the liquid meniscus). The environment of the gas is assumed to be atmospheric pressure 1% humid air. The content of the channels is liquid water with dissolved 8 ppm of $O_{2\,aq}$ [28]. The presence of OH_{aq}^- and $H_3O_{aq}^+$ is set to maintain a neutral pH equal to 7.

4.3 Surface Ionization Wave Interacting With Microchannels

The source that was used in this chapter is direct SDBD. The IW is formed in close contact and propagates from the early stage, interacting with the dielectric material. Unlike more classical remote sources that generate a streamer in a gas phase that can further intersect with a dielectric obstacle, an IW forms in the presence of the dielectric interface in our geometry. The plasma is generated by applying voltage to a triangle electrode. The applied voltage pulse has the following

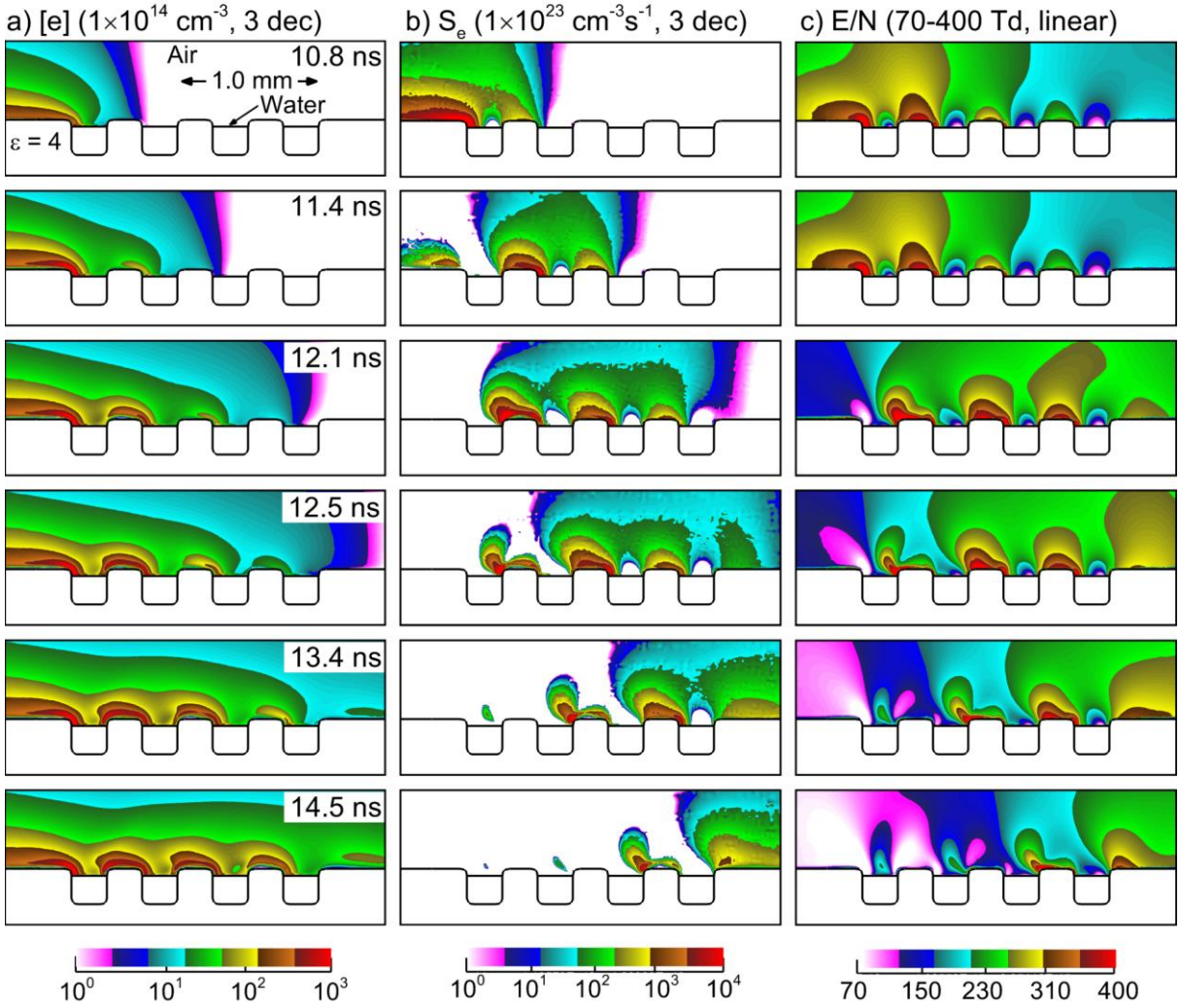

Figure 4.2. Base case: evolution of the SIW on the array of wet microchannels generated by a negative polarity pulse of -30kV. a) Electron density evolution, b) electron impact ionization source, c) reduced electric field.

characteristics: the voltage rise time is 10 ns, the maximum applied voltage is 30 kV and was kept

constant for 240 ns (much longer than the studied period). The initial electron density of 10^{11} cm^{-3} and radius of 150 μm near the tip of the electrode was placed to facilitate the propagation of plasma. In the base case, neutral hydrophobicity of the substrate with a 90-degree contact angle is assumed. Both positive and negative polarities of the source are separately considered. In the negative polarity case, demonstrated in Fig. 4.2, SIW propagates primarily in diffused mode. This means the plasma is not locally contracted near the surface but propagates and diffuses into the ambient air. Such behavior is linked with the nature of negative polarity-driven plasmas. Light electrons are driven by the electric field away from the major plasma plume, causing ionization to be distant from the surface of the dielectric. The interaction of plasma with the surface exhibits a surface-hugging mode, described in detail by Höft et al [29].

When the SIW approaches the array of channels, the further propagation is dominated by the enhanced electric field in so-called triple-points at the intersection between gas, water and solid dielectric. Once closer to the array of channels, the SIW directs to the first triple-point (Fig. 4.2, 10.8 ns). Due to the diffusion of the electrons, ionization occurs ahead of the major plume of plasma reaching the next channel. The precharged space above the ridge of the channel facilitates a so-called backward positive— IW moving from the channel to the previous one. This is a hopping IW that exists in a gas phase on interface with microchannels; it is discussed in detail in Chapter 5. With this mechanism, the SIW continues traveling across the array of channels until it reaches the end of the row. This type of plasma source is sensitive to the distance from the powered electrode. Since the mode of propagation is diffused, the SIW loses energy during propagation on electrons that interact with air in the vertical direction. Thus, the electron density falls in identical regions closer to the end of the array of microchannels.

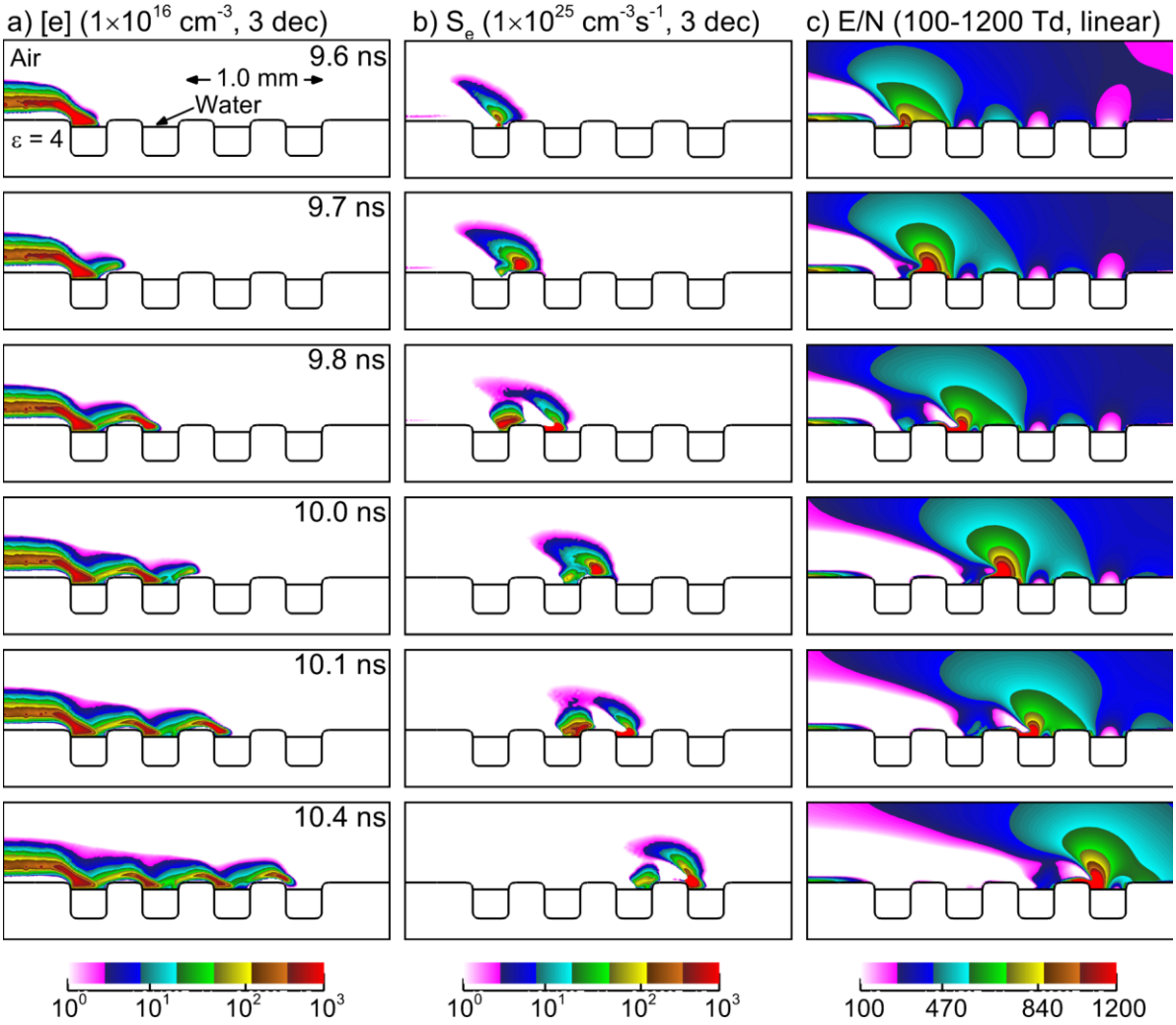

Figure 4.3. Base case: evolution of the SIW on the array of wet microchannels (neutral substrate) generated by a positive polarity pulse of 30kV. a) Electron density evolution, b) electron impact ionization source, c) reduced electric field.

When positive polarity plasma is generated on the above-described substrate, the propagation is different from that of opposite polarity plasma in several ways. Fig. 4.3 demonstrates the SIW generated by a 30 kV pulse. In this case, plasma does not exhibit a surface-hugging mode as with negative polarity. Instead, the dielectric interface acts like a cathode, creating a sheath and distancing the plasma from the substrate. Positive polarity-driven plasmas propagate, attracting electrons toward the major plume of plasma, driving positive ions away from the plume. Heavy ions, unlike electrons, diffuse minimally along the electric field lines due to

having larger mass. For these reasons, plasma is more contracted in space near the surface and propagates more rapidly, losing less energy on vertical propagation. The negative polarity case is similar in that the SIW starts interacting with the array of channels in the left-most microchannel in the dielectric triple-point. The SIW exhibits only forward propagation in this case. Positive polarity-driven plasmas are sensitive to photoionization. The propagation is driven by ionization occurring in front of a plume of plasma by the photoionization source. Positive polarity-driven plasma propagates faster than negative polarity-driven plasma. The maximum density of electrons is higher compared to negative polarity due to there being fewer losses on diffusion in the vertical direction.

The IW that propagates along the liquid interface has several effects on it. Under rapid interaction of plasma with the water surface (a few nanoseconds), it primarily acts as a dielectric. The surface of the water can collect charge by solvating electrons and ions, radicals and molecules, and undergo the influence of the VUV photon environment. Direct sources like SDBD can be beneficial in delivering maximal fluxes of photons to liquid sources. Most photons are trapped by the liquid layer of a thickness of 15 nm. Liquid water in a VUV photons environment dissociates to liquid OH and H radicals or undergoes ionization. Ionized water further converts into hydronium ion. Liquid OH radicals for H_2O_2 molecules contribute to bacterial

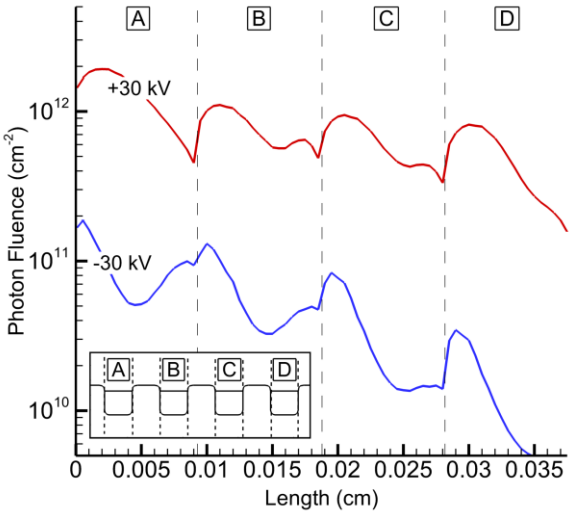

Figure 4.4. Fluence of photons to the water surface over 14 ns.

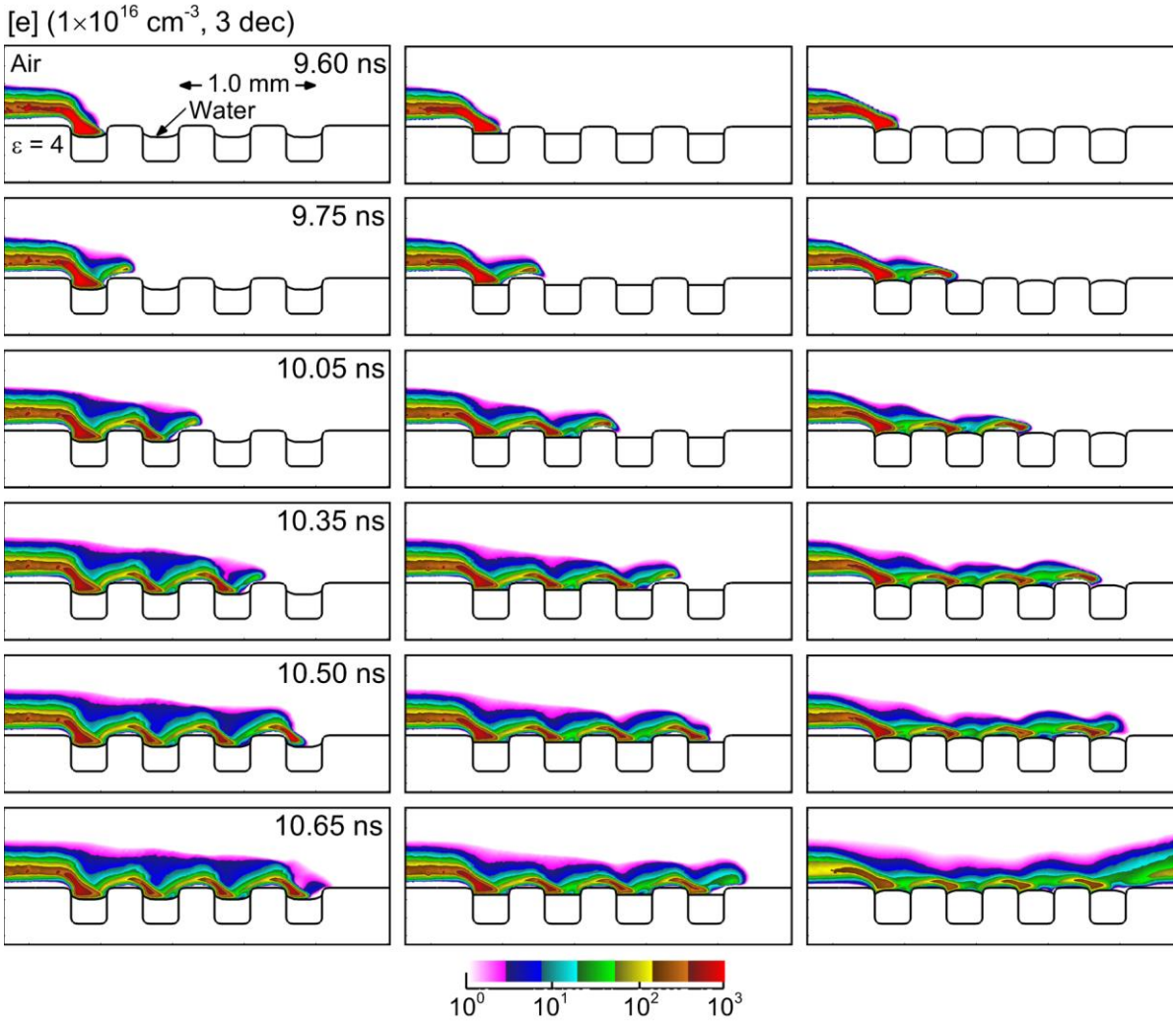

Figure 4.5. Evolution of electron density when the SIW travels across the array of channels with water having different meniscus shapes. a) Hydrophilic substrate, b) neutral substrate, c) hydrophobic substrate.

inactivation. Hydronium ions shift the pH of water from neutral to weakly acidified. The above-described cases with different polarities produce different fluences of the photons on the treated substrate and, thus, on the present water. Fig. 4.4 demonstrates the fluence of photons produced by positive and negative polarity pulses. Two noticeable trends can be distinguished from this calculation. Overall, the fluence of photons produced by positive polarity-driven plasma is higher than that produced by negative ones. This fact is associated with higher electron density production in the first case. Another consequence of plasma propagation across the array of channels is the

difference in average fluence of photons with respect to the distance to the powered electrode. Due to the diffused mode of negative polarity plasma and the resulting decay of electron density along the array of channels, the average fluence of photons also falls in respect to length along the substrate. This is not the case for positive polarity due to its relatively uniform electron density along the plasma propagation.

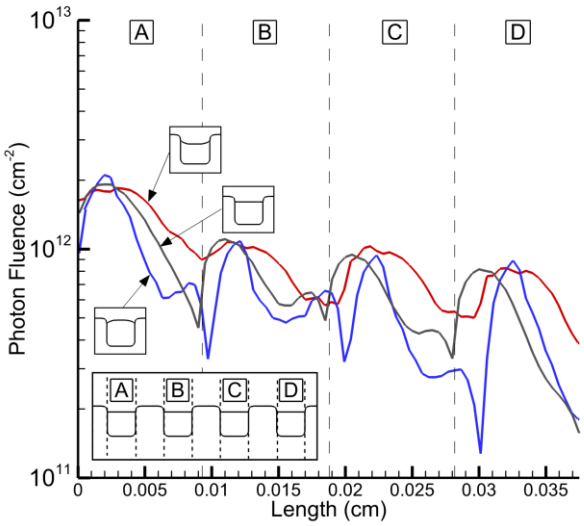

Figure 4.6. Fluence of photons over the water interface for different meniscus shapes.

The maximized effect from increased electron density and the relative uniformity across the array dictated the choice of positive polarity in the subsequent studies. It should be noted that the model is constrained within the 2D computational approach. The model most closely describes the scenario in which the setup is uniform across the third dimension (not addressed in the model). Propagation of plasma in 3D closely describes SIWs that propagate with a smooth, unified front. Positive polarity-driven plasmas are more sensitive to stochastic events and may exhibit filamentary behavior in some conditions. However, some works demonstrate a uniform front of SIWs produced by positive polarity [30]. This case scenario is the most beneficial for treating channels with liquids and is most closely approximated within a 2D model. The speed of propagation of the SIW on a dielectric interface across the array of channels is $1 - 7 \times 10^5$ m/s in negative and positive cases, which is commensurate with the available literature data in the orders of magnitude [31].

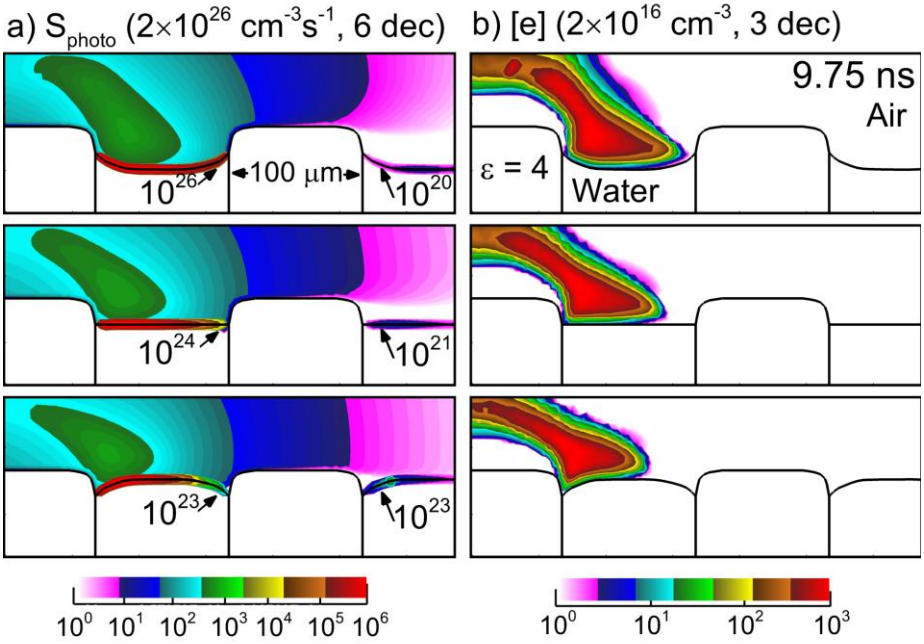

Figure 4.7. Mechanism of precharge of the following channels and the right-most edge of the treated channel for three meniscus shapes. a) Photoionization source, b) electron density.

4.3.1 Hydrophobicity: Shape of Meniscus

Depending on the material of the substrate, liquid can be more or less susceptible to spread across the surface. This effect is known as hydrophilicity. The angle between the liquid and the interface of contact is called the meniscus and can affect the propagation of the SIW across a substrate. Geometrical shapes resulting on the surface may affect local electric fields, cause shadowing of photoionization, or simply change the total length of the treated liquids. In this study, the intend is to demonstrate the influence of substrate material on the potential organization of water inside the microchannels and the resulting propagation of SIWs across such a complex interface.

Fig. 4.5 demonstrates the propagation of SIWs in the form of electron density for three different meniscus cases: hydrophilic, hydrophobic and neutral. When the IW enters the area with channels, in all three cases, the interaction starts in the first channels in the left-most triple-point

between liquid, substrate and air where the electric field is intensified. Further propagation is guided from this point. The shape of the meniscus is responsible for further development. From the results of calculations, it has a minor effect on the speed of propagation of SIWs.

Another more noticeable and more important effect is the distribution of fluence across the interface of liquids. Following the propagation of the SIW, photon fluence is distributed nonuniformly across the liquid interface. Fig. 4.6 demonstrates photon fluence for three different meniscus shapes. The sudden drops in fluence in the right-most corners of the liquid interface in the channels are a consequence of the propagation of SIWs. In more detail, the propagation of SIWs from the entering point relies strongly on the photoionization source (positive polarity). The mechanism of propagation of SIWs from the first channel to the second is demonstrated in Fig. 4.7. The mechanism behind the differences in the propagation of SIWs across the interfaces of altered shapes is in the propagation of photons along this surface. In the case of the hydrophilic surface, the SIW enters the channel in the *valley-shape* location. The depth of this valley is relatively small, in the order of 10 μm. This depth is, however, enough to provide some shadowing effect for photoionization to seed electrons in the

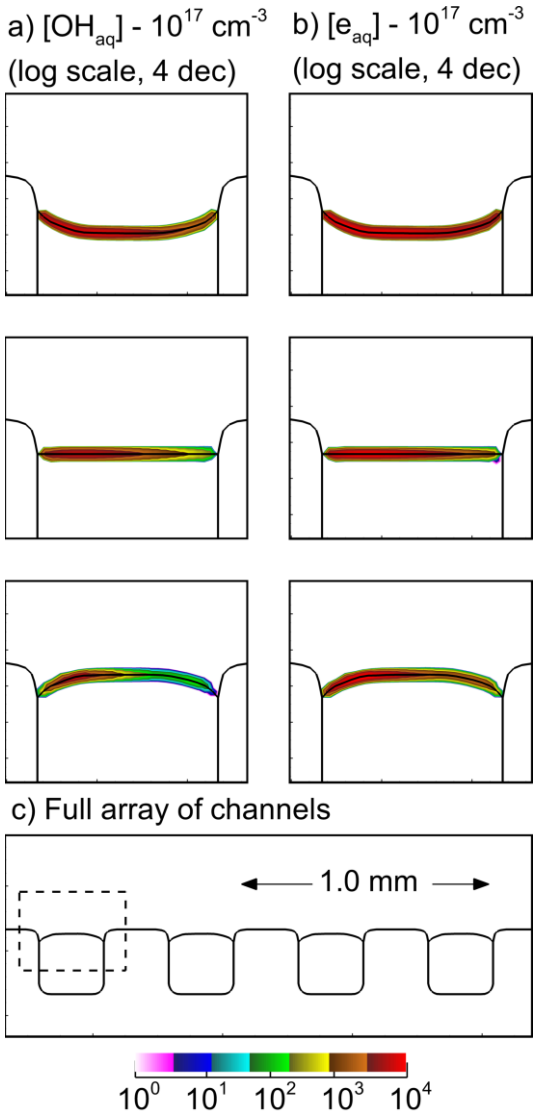

Figure 4.8. OH_{aq} and e_{eq} formed on the water surface at 13 ns.

next channel in the area of another triple-point. This is the reason for the slower propagation of SIW than in other meniscus cases. The concave curvature inside the first channel provides no shadowing inside the channel itself, allowing uniform fluxes of species to the entire surface of the liquid. In the hydrophobic case, the shape of the meniscus is *hill-like*. The elevation is also in the order of 10 μm. This shape makes the entire surface flatter for the photoionization source. For this reason, shadowing is less prominent for the subsequent channels, and the electrons are seeded in the following channels at the time of interaction with the considered channels. This results in some acceleration of movement of the SIW across such an array. However, the hill-like shape of the liquid interface provides shadowing inside of the right-most edge of each channel. This results in reduced fluxes of species to that location of the liquid interface. This fact explains the different influences of species in Fig. 4.6 for varied meniscus shapes.

Nonuniform flux collection by water affects photochemical effects in the top layer. Fig. 4.8 shows the liquid OH_{aq} radicals and the solvated electrons. Within several 10s ns, a layer of 15 nm of H_2O_{aq} is converted into photochemical products. Due to the fact that photon fluxes are collected unevenly, the chemical products are also covering the topical layer following this trend. The smoothness of the topical density falls with growing hydrophobicity. The unevenness is expected to affect the subsequent volumetric treatment. The maximal volumetric effect is anticipated in the case of high density consistent across the interface. For this reason, the following

studies are intended to demonstrate the influence of positive polarity-driven plasma in wet channels containing liquid in hydrophilic material.

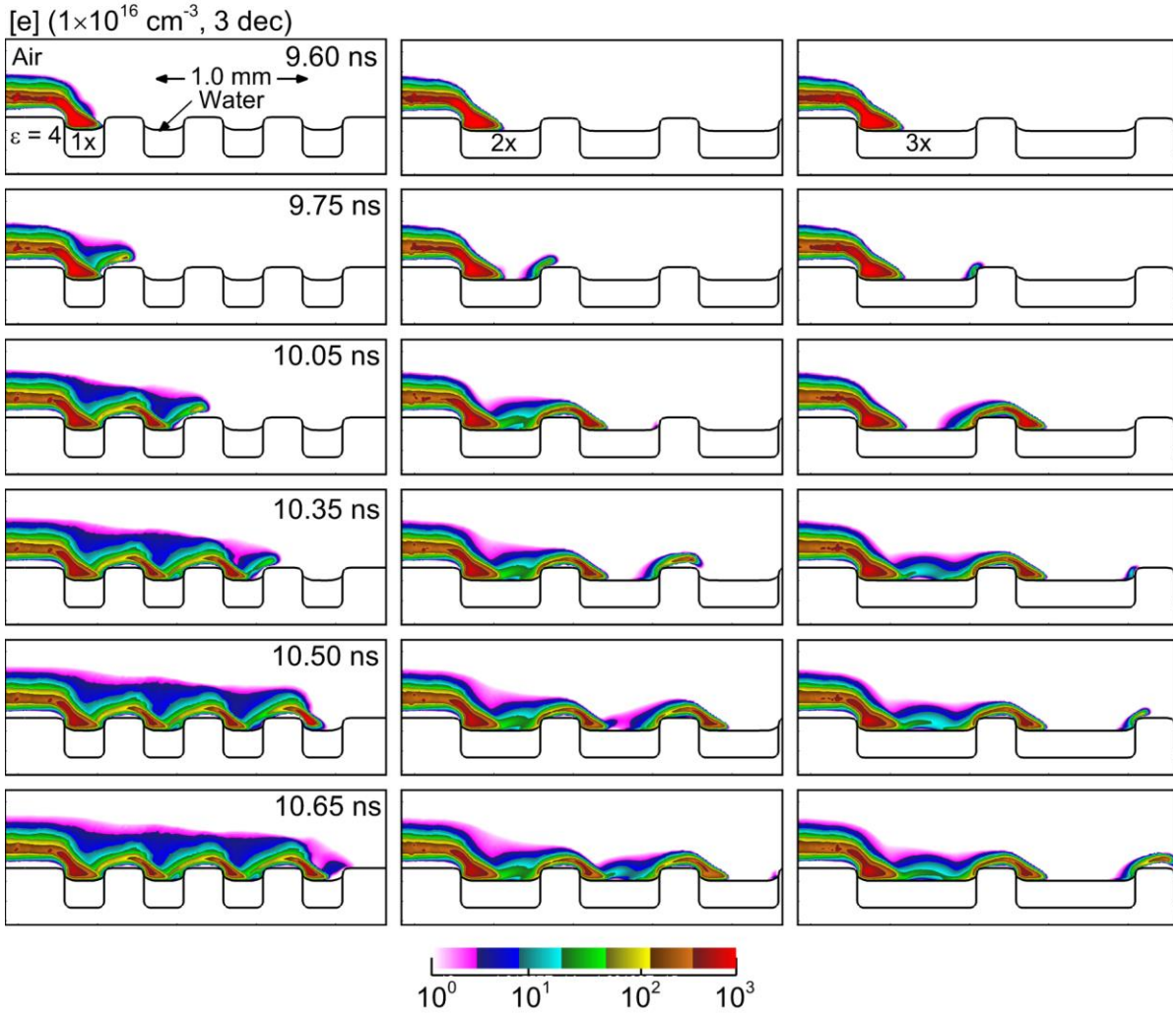

Figure 4.9. Electron density evolution following the propagation of SIWs for three different lengths of channels.

4.3.2 Width of Channels

One of the aims of plasma-water interactions is volumetric treatment. Since most chemical and physical events occur in a thin topical layer at the liquid interface and then diffuse to the depth, the goal is to maximize the surface-to-volume ratio. In this study, the height of channels is fixed,

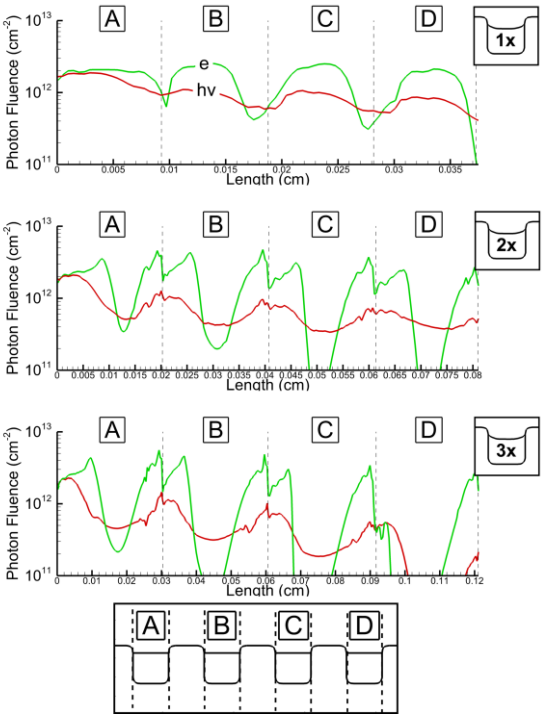

Figure 4.10. Fluences of photons and electrons onto the liquid surface for three widths of channels.

and the length of channels is varied. This is done to enable understanding the trend of interaction with channels with extended surface-to-volume ratio.

In Fig. 4.9, the propagation of positive polarity-driven SIWs across wet channels is shown for three lengths of channels 100 μm–300 μm. The distinguishing feature of the SIW on the shorter channels is continuous propagation. The wavefront and the flowing electron density have no breaks along the array. As channels extend in the horizontal direction, the continuity of the SIW breaks: the SIW hops into the channel area, entering it in the left-most edge, and continues the propagation from the right-most edge, skipping the middle of the channel. This occurs due to the initial space charge in the right-most corner that occurs due to photoionization. Due to the intensified electric field in this corner, ionization proceeds and follows the electric field lines. The IW hops over the ridge of the channel. This trend is replicated in the subsequent channels. The middle region in the first channel is further covered by plasma as well. Due to the minimal electric field above the middle, the propagation of secondary SIWs requires preionization. This preionization occurs due to the photoionization of this space. An ionization wave then travels across this area, covering the middle of the channel.

The fluence of photons and electrons then follows the pattern of propagation of the SIW (Fig. 4.10). The fluence of electrons is more sensitive to the local electric field, which changes the

SIW's behavior. The electron density strictly follows the propagation of the SIW since the electrons are directed toward the plume of the SIW by the applied electric field. Unlike electrons', photons' fluence is smoother across the horizontal axis and less sensitive to local obstacles on the interface. The source of photons is isotropic, with the characteristic trapping distance of a few hundred microns under atmospheric pressure conditions. The roughness on the studied surface is insufficient for shadowing the photon source in this case. As the length of the channels increases, the distance between the breaks in SIW front reaches the characteristic trapping distance of photons, and the fluence of photons drops in the middle of the channel. The strength of photoionization from the secondary SIW that covers the middle of the channel is an order of magnitude lower than from a major one and, thus, does not compensate for the photon source.

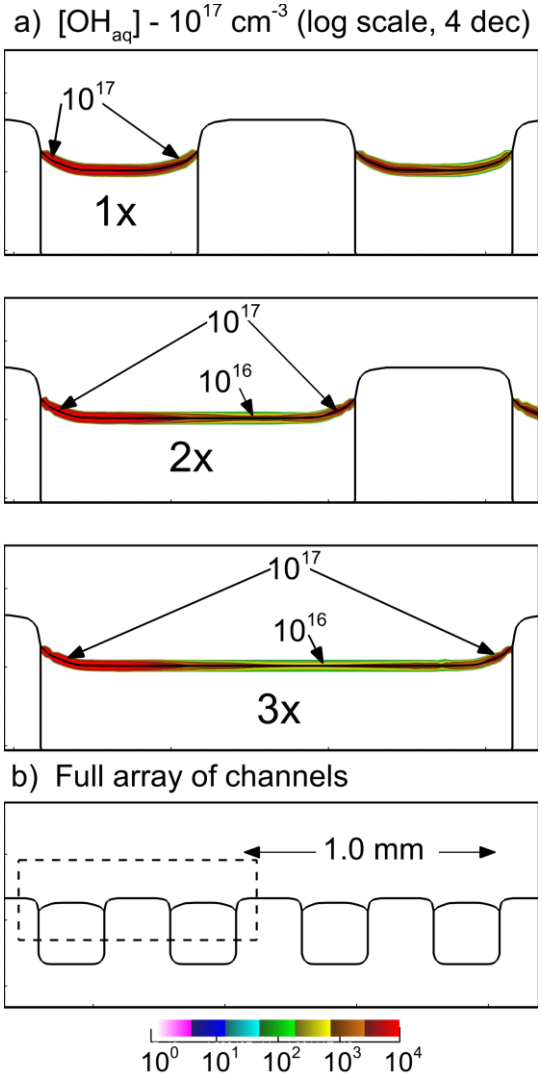

Figure 4.11. OH_{aq} concentration on the interface of liquids in three different widths of channels at 15 ns.

Although the photon fluence is relatively smooth across the water interface, the drops in photon production in the middle of the more extended channels affect the local chemical products such as OH_{aq}. Fig. 4.11 demonstrates the formed densities of OH_{aq}. The spatial distribution of OH_{aq} follows the distribution of the photon fluences. The OH_{aq} fragments are formed by photodissociation of the liquid water. The averaged

density of OH_{aq} across the length of the interface is 1.5×10^{17} cm^{-3} for the shortest case; 1.1×10^{17} cm^{-3} for the middle case; 8.1×10^{16} cm^{-3} for the largest case. The averaged density across the interface is calculated by integrating density across the interface with the following equation $\frac{1}{L}\int_0^L \rho_{local} ds = \frac{1}{L}\sum_0^L \rho_{node} \Delta s$, where $\rho_{node}, \rho_{local}$ are local density at the node or on the surface, respectively; Δs is a unit length for integration; and L is the total length of the interface. The average density has a trend of falling with increased length of the interface. It is nearly doubled for the shortest channels compared with the longest ones. This may indicate that there is a critical length of channels for considered conditions and geometry that will provide the best volumetric treatment.

4.4 Concluding Remarks

This chapter considered SDBD as a source of plasma for the treatment of wet microchannels. Positive and negative polarity-driven SIWs were considered when generating a discharge. It is identified that positive polarity-driven plasma produces benefits in terms of both the total electron density of the plasma near the channels and the consistency of the plasma parameters along the horizontal axis. Liquids can benefit from plasmas in multiple ways. Direct sources of plasmas such as SDBD systems can provide the highest possible local electric fields, photons and charged species fluences. Photons reaching the water interface result in the production of OH_{aq}, H_{aq} radicals and hydronium ions. Their topical density is maximized with the application of positive polarity. The material choice for the substrate can also significantly contribute to the feedback from the plasma to the liquid. The physical properties of the material can dictate the shape of the water in the channels, which itself contributes to the SIW behavior. This chapter

identified that the shape of the meniscus can affect the uniformity of the photon flux collection by the liquid interface and result in different volumetric treatments. Various meniscus shapes were studied. It is demonstrated that the shape of the liquid in the channel influences the behavior of the SIW and, thus, the collection of species in the plasma by the liquid interface. The shape of the liquid has a minor effect on the shadowing of photoionization that contributes to the irregular flux collection by major species in the plasma. The most uniform fluence is presented on the hydrophilic substrate with the concave shape of the liquid interface provided by minimal shadowing effects.

To maximize volumetric treatment, the channels were extended in the horizontal direction with an increased surface-to-volume ratio. In prolonged channels, the uniformity of flux collection of different species across the interface is falling. This is primarily because the SIW relies on an intensified electric field in the edges of the channels at the location of the electrical triple-point. The major propagation occurs over the ridge of the channel. When the length of the water-containing region increases and reaches the absorption distance for photons under atmospheric pressure conditions, the photoionization from the major plumes of the SIW near the edges does not compensate for the region of the middle. Secondary SIWs, which go across the middle of the channel, have lower strength and resulting ionization. As a result, the middle of the longer channels contains fewer products resulting from plasma treatment.

4.5 References

[1] D. B. Graves, Plasma Process. Polym. **11**, 1120 (2014).

[2] S. J. Kim and T. H. Chung, Sci. Rep. **6**, 1 (2016).

[3] A. Privat-Maldonado, A. Schmidt, A. Lin, K.-D. Weltmann, K. Wende, A. Bogaerts and S. Bekeschus, Oxid. Med. Cell. Longev. **2019**, 1 (2019).

[4] F. Liu, L. Nie, X. Lu, J. Stephens and K. Ostrikov, Plasma Sources Sci. Technol. **29**, 065001 (2020).

[5] S. D. McGuire, C. Jacobs, P. B. Mariotto, C. H. C. Grimaldi, A. Tibère-Inglesse and C. O. Laux, J. Thermophys. Heat Transf. **37**, 821 (2023).

[6] A. Vesel and M. Mozetic, J. Phys. D. Appl. Phys. **50**, 293001 (2017).

[7] I. Levchenko, S. Xu, O. Baranov, O. Bazaka, E. Ivanova and K. Bazaka, Molecules **26**, 4091 (2021).

[8] A. Sakudo, Y. Yagyu and T. Onodera, Australas. J. of Dermatology (1995).

[9] A. Soni, J. Choi and G. Brightwell, Foods **10**, 1 (2021).

[10] J. C. Harley, N. Suchowerska and D. R. McKenzie, Biophys. Rev. **12**, 989 (2020).

[11] H. Tanaka, S. Bekeschus, D. Yan, M. Hori, M. Keidar and M. Laroussi, Cancers, **13,** 1737 (2021).

[12] J. E. Foster, Phys. Plasmas, **24**, 055501 (2017).

[13] N. Takeuchi and K. Yasuoka, Jpn. J. Appl. Phys. **60**, SA0801 (2021).

[14] R. Brandenburg, Plasma Sources Sci. Technol. **27**, 079501 (2018).

[15] J. Winter, R. Brandenburg and K.-D. Weltmann, Plasma Sources Sci. Technol. **24**, 064001 (2015).

[16] T. C. Corke, C. L. Enloe and S. P. Wilkinson, Annu. Rev. Fluid Mech. **42**, 505 (2010).

[17] K. S. Elvira, X. C. i Solvas, R. C. R. Wootton and A. J. DeMello, Nat. Chem. **5**, 905 (2013).

[18] H. Shi, K. Nie, B. Dong, M. Long, H. Xu and Z. Liu, Chem. Eng. J. **361**, 635 (2019).

[19] L. Patinglag, D. Sawtell, A. Iles, L. M. Melling and K. J. Shaw, Plasma Chem. Plasma Process. **39**, 561 (2019).

[20] J. Wengler, S. Ognier, M. Zhang, E. Levernier, C. Guyon, C. Ollivier, L. Fensterbank and M. Tatoulian, React. Chem. Eng. **3**, 930 (2018).

[21] J.-P. Booth, M. Mozetič, A. Nikiforov and C. Oehr, Plasma Sources Sci. Technol. **31**, 103001 (2022).

[22] J. E. Foster, Phys. Plasmas **24**, 055501 (2017).

[23] A. Barjasteh, Z. Dehghani, P. Lamichhane, N. Kaushik, E. H. Choi and N. K. Kaushik, Appl. Sci. **11**, 3372 (2021).

[24] R. P. Joshi, J. F. Kolb, S. Xiao and K. H. Schoenbach, Plasma Process. Polym. **6**, 763 (2009).

[25] D. H. Katayama, R. E. Huffman and C. L. O'bryan, J. Chem. Phys. **59**, 4309 (1973).

[26] A. M. Lietz and M. J. Kushner, J. Phys. D. Appl. Phys. **49**, 425204 (2016).

[27] M. Kettlitz, R. Klink, H. Höft and R. Brandenburg, Eur. Phys. J. D **74**, 110 (2020).

[28] NIST Thermophysical Properties of Fluid Systems http://webbook.nist.gov/chemistry/fluid/

[29] H. Höft, M. Kettlitz, M. M. Becker, T. Hoder, D. Loffhagen, R. Brandenburg and K.-D. Weltmann, J. Phys. D. Appl. Phys. **47**, 465206 (2014).

[30] J. Morsell, D. Trosan, K. Stapelmann and S. Shannon, Plasma Sources Sci. Technol. **32**, 095017 (2023).

[31] J. Morsell, N. Bhatt, C. Dechant and S. Shannon, J. Phys. D. Appl. Phys. **56**, 145201 (2023).

Chapter 5 Atmospheric Pressure Plasma Treatment of Microchannels: Formation of Reverse Ionization Waves[2]

Atmospheric pressure plasma jets (APPJs) (see Chapter 1) are increasingly being used to functionalize polymers and dielectric materials for biomedical and biotechnology applications. Once such application is microfluidic labs-on-a-chip consisting of dielectric slabs with microchannel grooves hundreds of microns in width and depth. The periodic channels, an example of a complex surface, present challenges in terms of directly and uniformly exposing the surface to the plasma. In this chapter, the results from computational and experimental investigations of negative APPJs sustained in Ar/N_2 mixtures flowing into ambient air and incident onto a series of microchannels are discussed. Results from 2-D modeling are compared to experimental measurements of electric field and fast-camera imaging. The propagation of the plasma across dry microchannels largely consists of a sequence of surface ionization waves (SIWs) on the top ridges of the channels and bulk ionization waves (IWs) crossing over the channels. The IWs are directed into electric field enhanced vertices of the next ridge. The charging of these ridges produce reverse IWs responsible for the majority of the ionization (also observed in Chapter 4). The propagation of the plasma across water filled microchannels evolve into hopping SIWs between the leading edges of the water channels, regions of electric enhancement due to polarization of the water. Positive, reverse IWs follow the pre-ionized path of the initial negative waves.

[2] Parts of the text presented in this chapter along with the research data have been published by Kseniia Konina *et al* 2022 *Plasma Sources Sci. Technol.* **31** 115001.

5.1 Introduction

Atmospheric pressure plasmas (APPs) are used to treat solid materials to functionalize their surfaces and liquids to produce reactive species on and beneath the liquid surface [1,2]. Technologically relevant solid surfaces treated by APPs typically do not have homogenously smooth surfaces but rather may have complex shapes and/or compositions. Such complexities include metal catalysts embedded in dielectric supports [3], wrinkled or wounded skin [4], and liquid droplets on solid materials [5]. Sources of APPs for surface treatment include dielectric barrier discharges (DBDs) [6], surface dielectric barrier discharges (SDBDs) [7] and atmospheric pressure plasma jets (APPJs) [8] These sources are described in Chapter 1.

APPJs that treat surfaces typically begin as streamers that propagate as bulk ionization waves (IWs) [9]. When a bulk IW strikes a dielectric surface, the interface collects surface charge that produces a local electric field with components parallel to the surface. This local electric field then initiates and sustains the propagation of a surface ionization wave (SIW) [10]. Several recent studies have focused on the propagation of SIWs over non-planar dielectric surfaces [11-13]. The detailed physics of the interaction between SIWs and non-planar dielectric is discussed in Chapter 3. In addition to charge accumulation, non-planar dielectric surfaces polarize when exposed to an electric field, which then produces electric field enhancement at locations with positive curvature and small radii [14]. This electric field enhancement can then alter further propagation of the SIWs [15]. The phenomena of IW and SIW are discussed in Chapter 1.

Microfluidic devices (labs on a chip) consist of rectangular channels typically hundreds of microns wide and fabricated in dielectric substrates, that direct and mix liquids for analysis [16,17]. The surfaces of microfluidic devices channels must often be functionalized to control their hydrophobicity, a process that is often performed using APPs [18,19]. The exposed liquids in open

microfluidic devices may themselves be treated by APPs for activation or chemical conversion of the fluid [20-22]. The APP treatment of these dry- and wet-channels represent another form of complex surface, albeit repetitive structures. In this regard, Patinglag et al produced a filamentary DBD inside a partially liquid filled microfluidic reactor containing a solution of deionized water and methylene blue, demonstrating significant reduction in the concentration of methylene blue [23]. A similar microfluidic reactor was used to demonstrate killing of Pseudomonas aeruginosa and Escherichia coli in solution [24].

APP treatment of human skin [25] also represents a topologically complex surface with channel-like features. Skin may be wrinkled with channels of hundreds of microns to more than 1 mm in depth and width [26]. These non-planar features make it difficult to achieve uniform plasma treatment of the skin for therapeutic purposes.

In this chapter, the results from a computational and experimental investigations of a negative APPJ sustained in Ar/N_2 flowing into ambient humid air incident onto a dielectric surface having square, 250 μm wide microchannels are discussed. The microchannels were dry and filled with water. Comparisons are made of computations to experimental fast-camera imaging of propagation of SIWs across the surface and to electric field measurements. It is found that the incident bulk IW from the APPJ fills the microchannels with plasma directly under the jet while only partially filling more distant channels. The subsequent propagation of SIWs across dry microchannels is dominated by charging of the ridge of a channel which sustains a SIW. Electric enhancement at the next ridge vertex then launches a bulk IW across the channel. The next ridge then charges, launching SIWs across the ridge and into the channel, partially filling the channel with plasma. A reverse positive bulk IW is launched from the vertex following charging. The electric field components in the SIW transition from being dominantly vertical upon initiation of

the SIW to dominantly horizontal. This repetitive sequence results in the channels becoming less filled with plasma as the SIW-IW pairs propagate across the surface. The details of the propagation depend on the conductivity and permittivity of the dielectric, however the pattern does not significantly change.

Propagation of SIWs across water filled channels are dominated by increased electric field enhancement due to polarization of the high permittivity water. The end result is hopping of the SIW-IW from triple point (intersection of gas plasma, water and solid dielectric) to triple point in large part bridging the ridges of the dielectric. The majority of the charged particles in the bridges of plasma are produced by reverse ionization waves.

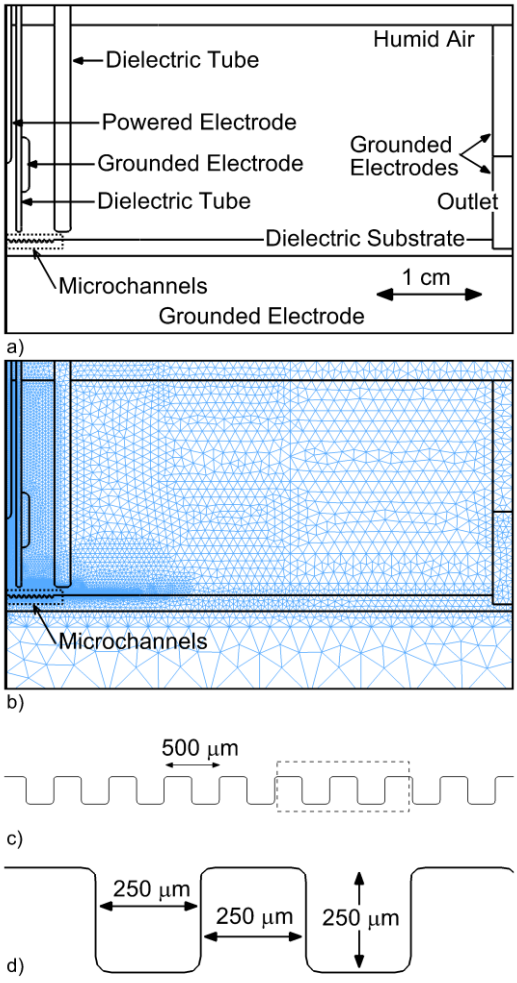

Figure 5.1. Schematic of the computational geometry. a) Full computational domain, b) computational mesh, c) enlargement showing chain of microchannels (dotted domain in previous images), and d) enlargement of individual channels.

5.2 Description of the Model

A full description of the code is written in Chapter 2. Below is the summary of the applied initial conditions and settings.

A schematic of the computational geometry for this study is in Fig. 5.1. The coordinate system is Cartesian with the left edge using reflective boundary conditions. The depth of the domain is 2.35 mm. The jet consists of a powered blade electrode 1 mm wide having a tip

with a 0.5 mm radius of curvature. The electrode is centered in a tube (the central nozzle) having an inner width of 2 mm and wall thickness of 0.5 mm. A grounded electrode surrounds the inner tube at the height of the tip of the electrode. An Ar/N_2 mixture with humid air impurities ($Ar/N_2/O_2/H_2O$ = $0.9/0.1/10^{-5}/10^{-5}$) flows through the central nozzle at 7 lpm. A nitrogen shield gas is flowed at 1.2 lpm through a channel surrounding the central nozzle having a width of 1.4 mm. The relative dielectric permittivity of the inner and outer tubes is $\varepsilon_r = 4$. The gases flow into ambient air with a humidity 0.5%. The humid air is injected at the rate of 10 lpm from the top boundary of the domain to minimize stagnation zones and to mimic entrainment of room air by the jet. Gas is exhausted through pump ports on the right edge of the domain.

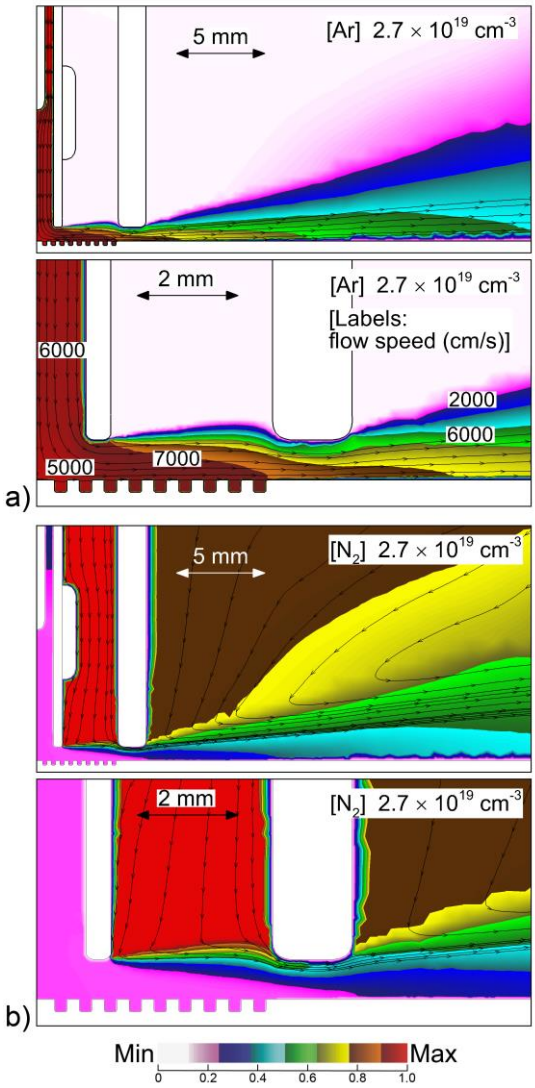

Figure 5.2. The stabilized fluid flow field with flow streamlines prior to application of the voltage pulse. The streamline are labeled with speeds (cm/s). a) Argon and b) N_2 flow with enlargement near the channels.

A detailed description of the plasma-chemistry mechanism for an APPJ sustained in argon flowing into humid air is provided by Lietz et al [27] and Tian at al [28]. The mechanism includes 54 species: e, Ar, $Ar(^3P_2)$, $Ar(^3P_1)$, $Ar(^3P_2)$, $Ar(^1P_1)$, Ar(4p), Ar(4d), Ar^+, Ar_2^*, Ar_2^+, H, H*, H^+, H^-, H_2, H_2(r), H_2(v), H_2*, H_2^+, H_3^+, OH, OH^*, OH^+, OH^-, H_2O, H_2O(v), H_2O^+, HO_2, H_2O_2, H_3O^+, O_2, O_2(v), O_2(r), O_2^*, O_2^{**}, O_2^+, O_2^-, O_4^+, O, O*,

O^+, O_3, N_2, N_2(v), N_2(r), N_2^*, N_2^{**}, N_2^+, N_3^+, N_4^+, N, N*, N^+. The mechanism includes about 1000 reactions. Photoionization of O_2 and H_2O results from resonance radiation from Ar(4p) and Ar(4d).

The substrate is located 0.8 mm beneath the edge of the tube and 7.5 mm below the tip of the electrode. The relative dielectric permittivity of the substrate in the base case is $\varepsilon_r = 6$. A series of 8 microchannels are in the substrate having a spacing, width and depth of 250 μm, as shown in Fig. 5.1. The electrical ground plane is located under the 1.5 mm thick substrate and also wraps around the system. The voltage pulse applied to the powered electrode has an amplitude of -25 kV with a rise time of 5 ns, pulse length of 25 ns and fall time of 5 ns.

The initial neutral gas flow field is shown in Fig. 5.2. The boundary layer of argon over the microchannels is approximately 1 mm thick with there being minimal penetration of the N_2 shield gas. The plasma is largely confined to the argon dominated central flow and boundary layer.

The experiment has 3-dimensional characteristics that will not be captured in 2-dimensional model, and so approximations and scaling need to be applied. The experimental device is a cylindrical plasma jet incident onto a grooved cylinder whose axis is perpendicular to that of the jet. To capture the critical phenomena, the simulations were performed in Cartesian coordinates that best represents the propagation of SIW along the surface of the grooved cylinder. One of the consequences of using Cartesian coordinates is that the powered electrode is a blade in the simulation instead of a pin in the experiment. This difference in geometry results in less geometrical electric field enhancement, both at the physical surface of the electrode and at the leading edge of the bulk ionization waves in the gas phase. To obtain comparable IW characteristics then requires higher voltage magnitudes in a Cartesian geometry compared to cylindrical. Based on past experience, voltage amplitudes should be 1.5 to 2 times as large in Cartesian simulations. This higher voltage then produces higher propagation speeds of the SIW.

5.3 Description of the Experiment

A schematic diagram of the experimental apparatus appears in Fig. 5.3, and is described in detail in the closely related paper [29]. The experimental work was performed by a collaborative experimental group. Briefly, an atmospheric pressure plasma jet (Ar/N_2 = 90/10 with a co-flow of nitrogen), sustained by high-voltage ns duration pulses, is incident on a dielectric target, placed in a Petri dish. The plasma jet is a 1 mm diameter quartz tube with a needle high voltage electrode and a grounded ring electrode, coaxial with a 10 mm diameter polycarbonate plastic tube. The flow rates of the Ar/N_2 mixture (main flow) and N_2 (co-flow) are 7 slm and 5 slm. The jet exit plane is located 0.8 mm above the target surface, a Macor ceramic tube 12.7 mm in diameter, with a series of rectangular cross section channels (0.25 mm x 0.25 mm, spanning 10 mm). A 9 mm diameter tube grounded electrode is inserted into the ceramic tube. The Petri dish, 10 cm diameter and 1 cm deep, is partially filled with distilled deionized water, using a syringe. For these conditions, the channels get filled with water due to the capillary effect. The plasma jet is powered by the repetitive bursts of negative polarity ns duration pulses, 10 pulses/burst, at the pulse repetition rate of 10 kHz and burst repetition rate of 10 Hz. The pulse voltage and current waveforms are shown in Ref. [29].

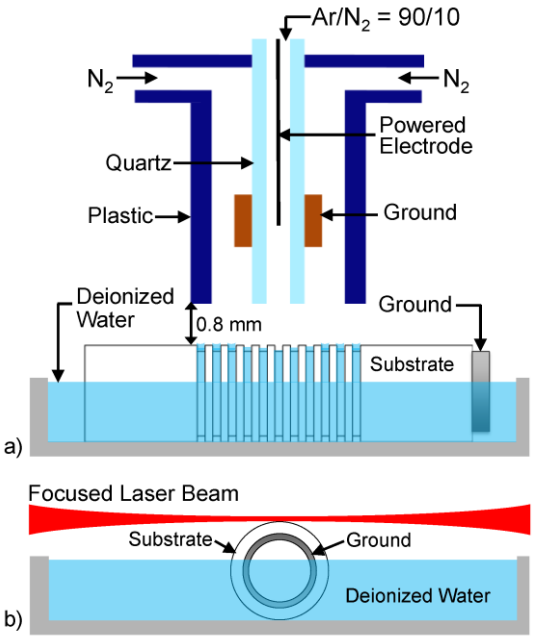

Figure 5.3. Schematic of the experiment. a) APPJ over the grooved substrate sitting in a bath of deionized water. b) Cross section showing the incident laser beam.

The electric field in the jet effluent was measured by ps Electric Field Enhanced Second Harmonic (EFISH) generation, discussed in detail in Ref. [29] and references therein. For the spatially resolved electric field measurements, the jet and Petri dish assembly are moved relative to the laser beam using a translation stage. The time-resolved electric field is measured by changing the delay between the discharge pulse and the laser pulse. Absolute calibration of the EFISH measurements was performed by measuring the Laplacian electric field for the same electrode and dielectric geometry. The calibration data were obtained at every measurement location, both for the vertical and horizontal components of the electric field. The spatial resolution of the diagnostic in the direction of the laser beam is quantified by traversing a pair of biased parallel cylindrical rod electrodes [29]. The calibrated EFISH signal was correlated to the peak Laplacian electric field in the gap. The diameter and position of the laser beam at the focal point are measured by scanning the beam across a knife edge. The surface curvature enables placing the laser beam close to the surface (≈70 μm), without clipping.

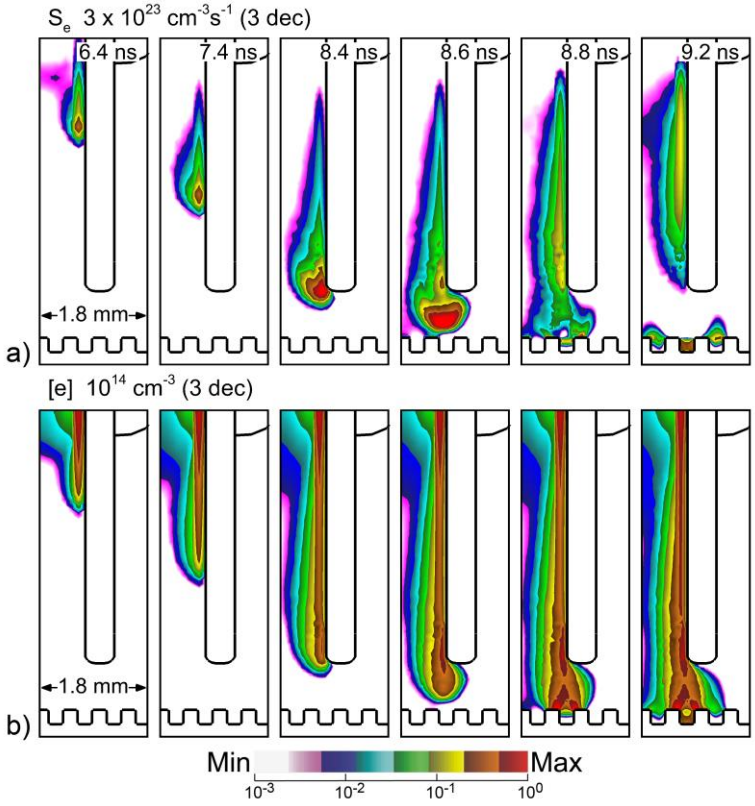

Figure 5.4. Ionization wave propagation through the tube and onto the channeled substrate. a) Electron impact ionization source ($cm^{-3}s^{-1}$) and b) electron density (cm^{-3}). Images are plotted on a 3-decade log scale with maximum values indicated for every characteristic.

5.4 Atmospheric Pressure Plasma Jet Interacting with Dry Microchannels

The propagation of the ionization wave from the tube to the substrate is shown in Fig. 5.4. The simulation begins with a small spot of plasma (1×10^{11} cm^{-3}, 0.3 mm diameter) placed at the tip of the powered electrode. This initial spot of plasma enables launching of an ionization wave (IW) towards the wall of the tube. The IW is directed by the applied electric field between the powered electrode and the grounded electrode surrounding the tube. When the IW strikes and charges the inner surface of the tube, a surface ionization wave (SIW) is produced, which then propagates along the tube in a *surface-hugging* mode [30]. The ionization source in the head of the SIW is maximum at 2-3 $\times$ 10^{23} $cm^{-3}s^{-1}$, with a propagation speed of 1.3 $\times$ 10^{8} cm/s [31,32]. The electron density produced by the SIW is 3-4 $\times$ 10^{13} cm^{-3}, and is 300 – 400 μm thick along the wall.

When the SIW reaches the end of the tube, a bulk IW is launched across the gap. When the IW reaches within a few hundred microns of the surface, polarization of the dielectric and geometrical electric field enhancement directs the IW towards the edges of the ridges of the microchannels. Upon application of full voltage, the electric field at the vertex of the channel under the nozzle is 5.0 kV/cm (E/N = 20.5 Td, 1 Td = 10^{-17} $V\text{-}cm^{2}$). As the IW wave approaches the surface, voltage is compressed in front of the lengthening conductive plasma column, momentarily increasing the electric field at the vertex to 64 kV/cm (260 Td) at 8.4 ns. The IW intersects the dielectric at about 8.7 ns.

The electron impact ionization source, electron density and E/N are shown in Fig. 5.5 upon intersection of the IW with the chain of microchannels and propagation across the channels. When the IW reaches the surface, the applied electric field is largely vertically oriented, which enables penetration of the plasma into the channels (adjacent to location 1). With a fully planar surface, intersection of the IW with the dielectric surface charges the surface, producing an electric field component parallel to the surface which launches a surface ionization wave (SIW). With fully planar surfaces, as the surface charges, the local electric field is reoriented to be more perpendicular to the surface, with the SIW being sustained by space charge in the head of the ionization wave [33]. In the case of the rectangular microchannels, geometrical electric field enhancement occurs at the vertex of the ridges of the channels which directs the incoming IW to

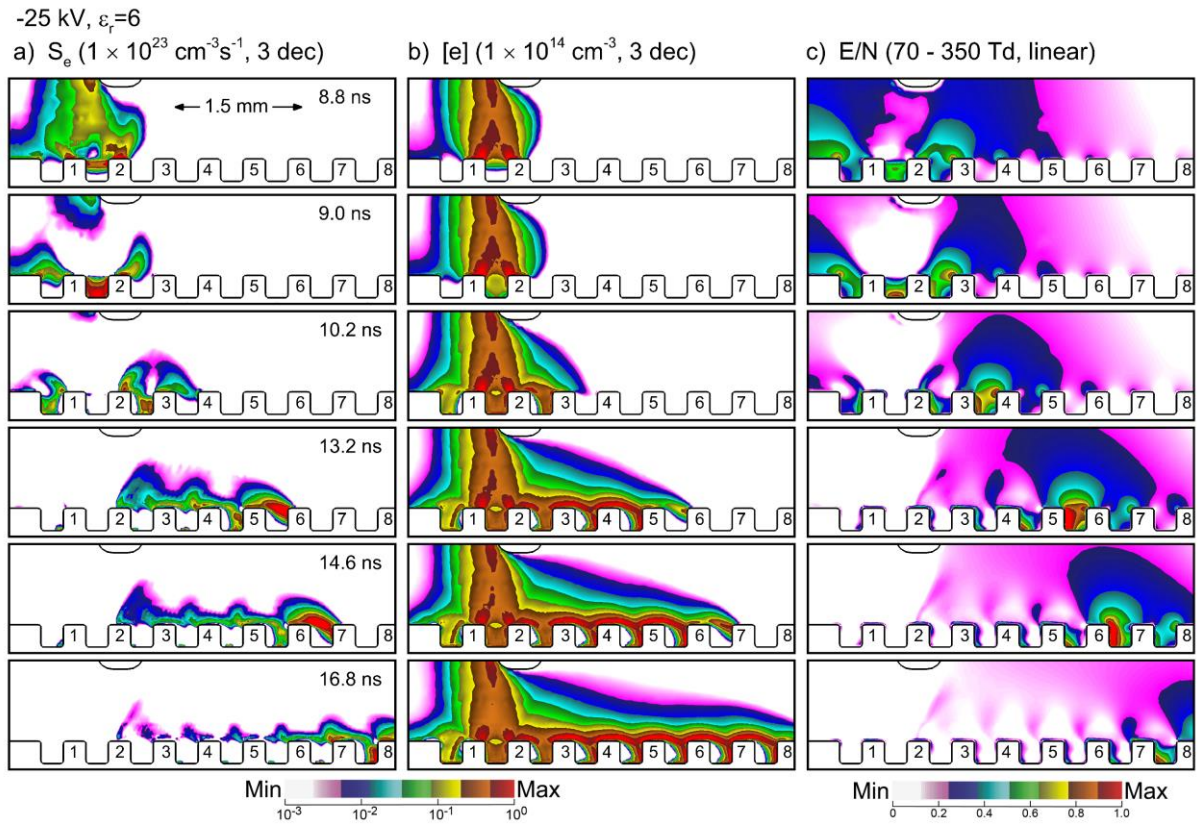

Figure 5.5. Surface ionization wave propagation across a chain of microchannels for the base case. a) S_e – electron impact ionization source ($cm^{-3}s^{-1}$, 3-decade log scale). b) [e] – electron density (cm^{-3}, 3-decade log scale). c) E/N – reduced electric field (Td, linear scale). Maximum values or the range of values are noted in the images.

those locations. Charging of the vertex produces electric components horizontally along the top ridge of the channel and vertically along the inside surface of the channel, for example, at ridge 2. A SIW then propagates along the top of the ridge and down the side of the channel. The latter contributes to filling the channel with plasma. The maximum electron densities across the top of the ridges are 10^{14} cm^{-3}.

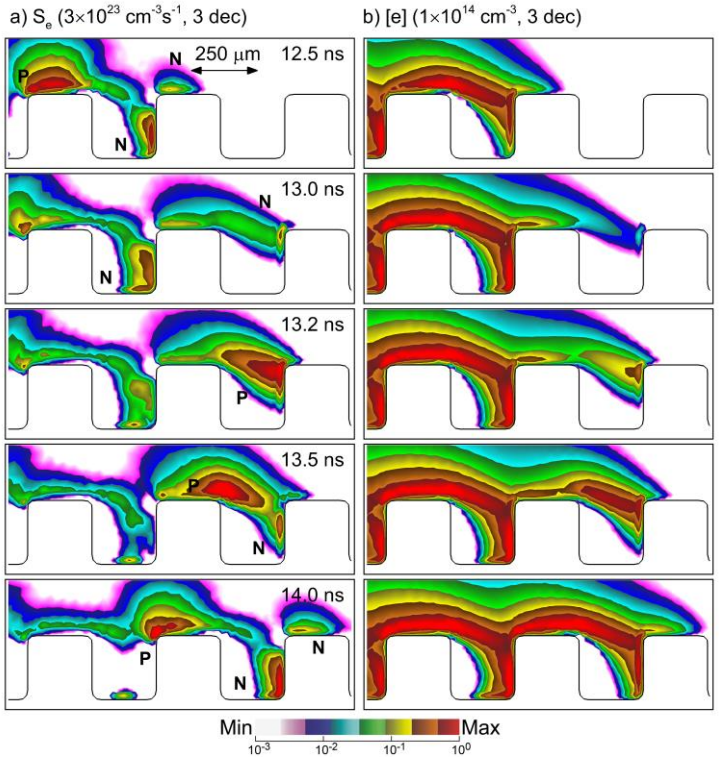

Figure 5.6. Plasma properties demonstrating reverse (positive) ionization wave. a) S_e – electron impact ionization source ($cm^{-3}s^{-1}$) and [e] – electron density ($cm^{-3}s^{-1}$). The "N" and "P" labels indicate a negative or positive ionization wave. Images are plotted on a 3-decade log scale with maximum values indicated.

As the SIW propagates along the ridge of the channel, the surface is charged. This charging reduces the electric field enhancement at the edges. When the SIW reaches the right edge of the ridge, the vertex across the channel is largely uncharged and so retains its geometrical electric field enhancement. This electric field enhancement directs the SIW across the channel, now as a bulk IW, to intersect the opposite vertex. Prior to arrival of the IW, the electric field at the vertex of ridge 4 is 88 kV/cm (300 Td). Upon intersection of the IW with the vertex, the surface of the vertex is charged, launching a SIW along the top of the next ridge and down the adjacent right side wall into the channel. This launching of the IW across the channel leaves the left side of the channel initially without coverage by plasma. This process of propagation of the SIW across the top of the ridge and launching an

IW across the channel into the vertex of the next ridge continues from one microchannel to the next. That portion of the microchannel that is not covered by plasma increases as successive microchannels are encountered.

The electron impact ionization source and electron density during the propagation of the SIW and launching of the IW across the channel are shown enlarged with finer time resolution in Fig. 5.6. The character of the ionization wave, negative or positive, is determined by the space charge at the leading edge of the IW. A negative IW will have negative space charge and generally propagates left-to-right in this geometry. A positive IW will have positive space charge and generally propagates right-to-left. The direction of propagation and character of the IW are indicated by N (negative) and P (positive) labels in Fig. 5.6. At 12.5 ns, the SIWs on the top ridge and inner wall are both negative. With this being a negative ionization wave (for propagation left-to-right in the figure), there is a small diffusion flux ahead of the ionization front. Although photoionization is not required for propagation of the negative IW, there is nevertheless photoionization that occurs ahead of the ionization front. The combination of the electron diffusion flux and photoionization seeds electrons in the high electric field region at the vertex of the next ridge, though the diffusion flux dominates for these conditions. These seed electrons then launch a positive ionization wave propagating from right-to-left across the channel. The reverse positive ionization wave is responsible for the majority of the plasma density across the channel. This reverse wave extends back to the ridge of the prior channel, producing a positive SIW across the ridge. The end results is a curvature in the plasma density that extends from vertex-to-vertex of the ridges of the microchannels.

Marskar and Meyer [11] performed similar simulations for propagation of positive ionization waves in air over square channels having sizes ≥500 μm. They also observed a hopping

of the SIW across channels with the channels under the electrode more filled with plasma. The inner surfaces of more distant channels were less covered by plasma, as seen here. With their simulations addressing initially positive waves, their propagation properties were in general more sensitive to photoionization, and particularly to the transparency of the channels. For the initially negative waves discussed here, the general trends were fairly independent of including or excluding photoionization, as might be expected with negative waves. The exception is that the initially negative SIWs propagated more rapidly when including photoionization.

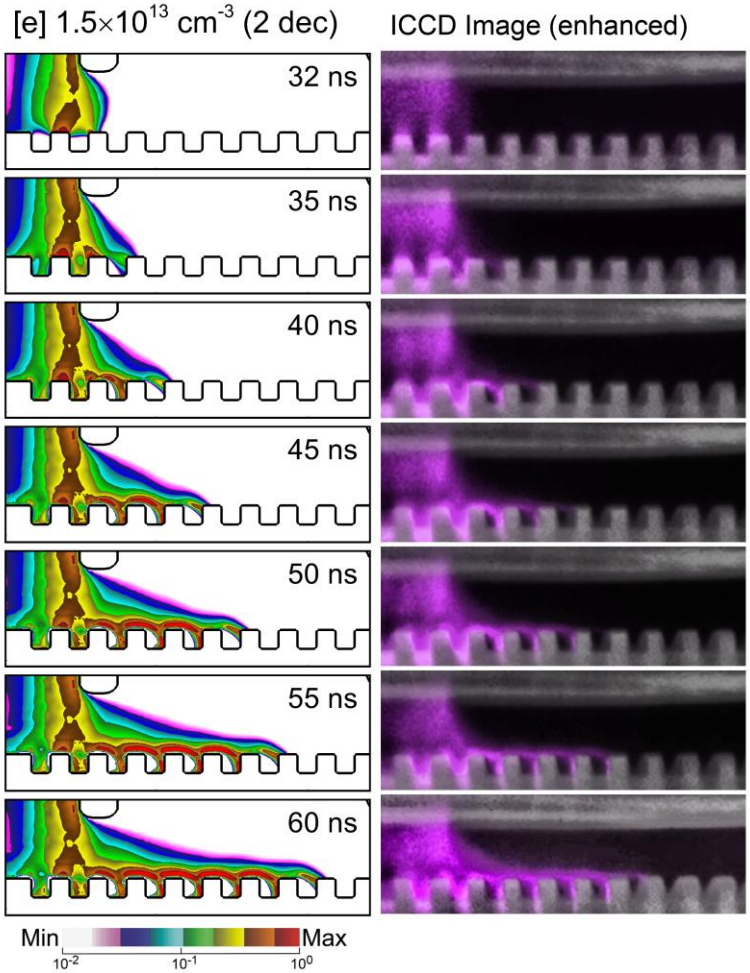

Figure 5.7. Comparison of (left) simulated electron density for applied voltage of -18 kV with (right) ICCD imaging for the plasma jet propagating along dry microchannels. The ICCD imaging frames were chosen for times that showed similar structure as the simulations. These images have been enhanced emphasize regions of weak emission.

Experimental validation of the predicted interaction of the negative plasma jet with microchannels comes from comparison of the electron density obtained from the simulation with imaging of optical emission using a fast ICCD camera, shown in Fig. 5.7. For these comparisons, the applied voltage in the simulation is -18 kV. The plasma density is shown on a 2-decade log-

scale to facilitate better comparison to the estimated dynamic range of the ICCD images. The ICCD images have been artificially enhanced to emphasize regions of weak optical emission. The times shown for the simulation results were chosen to align with the available ICCD images.

In general, the qualitative features of ionization wave propagation across the microchannels revealed by the ICCD imaging are reproduced by the simulation. These features include the filling of the microchannels with plasma directly under the plasma tube; lack of direct plasma exposure of the inner wall of the microchannels which worsens with propagation of the plasma across the microchannels; focusing of the ionization wave into the vertex of following microchannels; and the curvature of the plasma. Although not readily apparent in the images selected here, finer time resolution of the ICCD images confirm the backwards, positive ionization wave that bridges the microchannels.

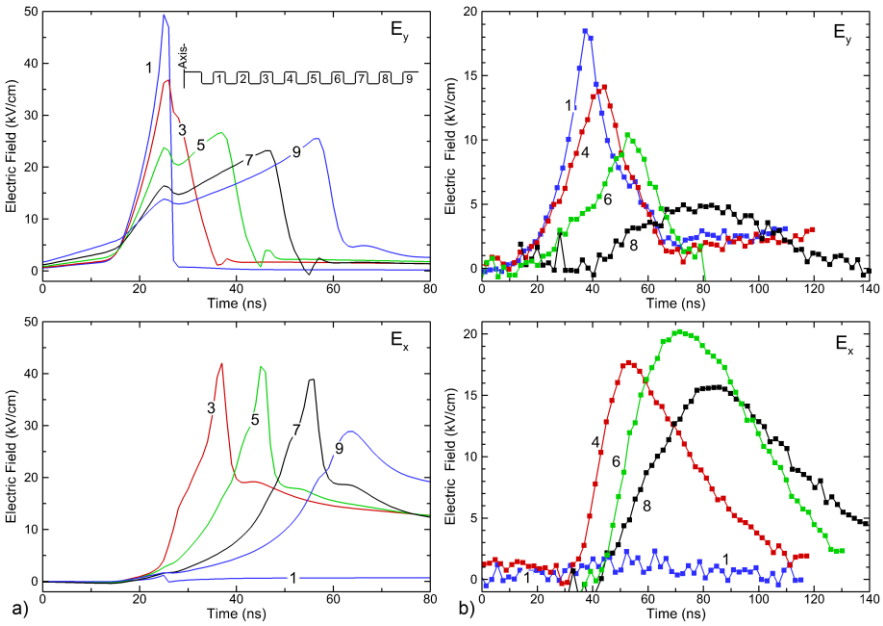

Figure 5.8. Comparison of electric fields on the top of ridges of the channels numbered according to the schematic. a) Simulation and b) EFISH measurements.

Other validation of the ionization wave dynamics comes from comparison of electric field measurements using the EFISH technique. Predicted and measured electric fields are shown in Fig. 5.8 at 75 μm above and centered on the top ridges of the channel. These comparisons should be evaluated on the basis of qualitative agreement with trends and not absolute quantitative

agreement due to differences between the 3-dimensional configuration for the experiments and 2D model. The experimental measurements average the EFISH signal over the spot-size of the laser whereas the simulations are at a single point, which produces a larger value of the electric field. There is general agreement between the trends of the experiments and simulations. The increase in axial electric field (E_y) during 20 ns to 30 ns corresponds to the approach of the bulk IW towards the surface. With the trailing plasma column being highly conductivity and which cannot support a significant electric field, voltage is compressed in front of the IW. This compression produces an increase E_y at the surface. There is little, if any, lateral (E_x) electric field at this time. When the IW arrives at the surface at 30 ns, the E_y collapses from its peak of nearly 50 kV/cm due to charging of the dielectric. Directly under the plasma jet, the lateral E_x component of the electric field remains small. At this time, the axial E_y electric field at the outer microchannels decrease with distance reflecting the larger distance from the electrode. As the ionization wave propagates across the microchannels, the axial electric field E_y increases before collapsing. The increase is due to the approaching IW which has some height above the surface and so produces an axial field. When the IW finally reaches the ridge, the surface is charged and E_y collapses.

The peak of the lateral E_x electric field generally follows in time the peak of the axial electric field E_y. The axial E_y electric field is in large part reduced by charging of the dielectric, which then enables generation of the lateral E_x component. With the plasma column extending from the cathode to the dielectric, a large fraction of the cathode potential is conducted towards the surface. For a cathode potential of -18 kV, the potential immediately above the surface under the jet is as large as -12 kV. This transferred potential then induces a lateral electric field which is intensified in the head of the SIW. The maximum in the lateral components E_x are delayed in time for the more distant channels as that maximum occurs when the SIW arrives.

The electron density during propagation across the microchannels is shown in Fig. 5.9 for voltages of -20 kV, -22.5 kV, and -25 kV with a voltage rise time of 5 ns. The speed of propagation of the ionization wave increases with voltage, from 1.0×10^7 cm/s for -18 kV (shown in Fig. 5.7) to 4.0×10^7 cm/s for -25 kV. There are commensurate increases in electron density, from 1.5×10^{13} cm^{-3} for -18 kV to 1.0×10^{14} cm^{-3} for -25 kV. Although these trends for increasing speed and electron density are expected with increase in voltage, the relative increases are smaller than expected based on analogies for propagation across flat surfaces. Propagation of the SIW across the channels is maintained by electric field enhancement at the vertices of the ridges, and this occurs in a repetitive and periodic manner. Prior to arrival of the SIW at, for example, ridge 5 in

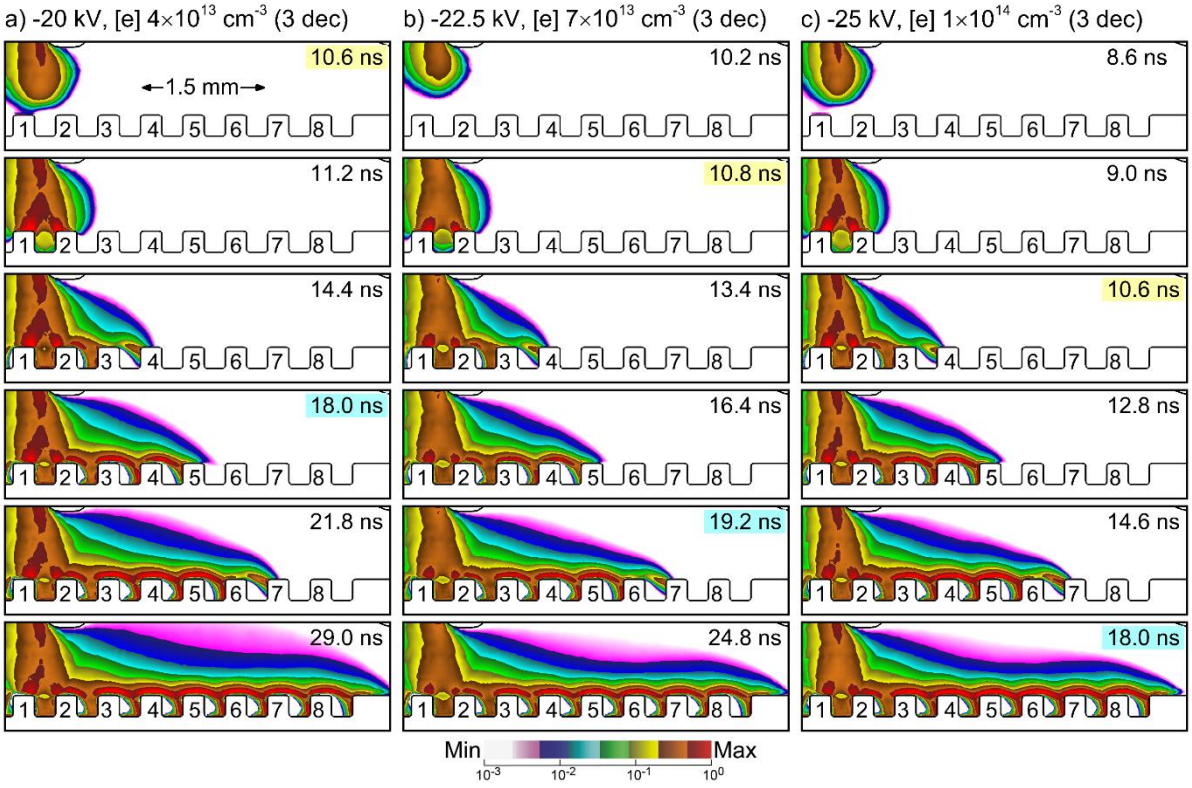

Figure 5.9. Electron density during surface ionization wave propagation across a chain of microchannels for different voltages for otherwise the base case conditions. a) -20 kV, b) -22.5 kV and c) -25 kV. The time for the image is noted in each frame. The horizontally aligned images are for the same propagation distance. The shaded times indicate images at approximately the same time. Densities are plotted on a 3-decade log scale with the maximum value noted.

the center of the array, E/N at the vertex exceeds 150 Td even for the lowest voltage. This value of E/N is well above that found in the head of bulk ionization waves sustained in argon. These vertex enhanced values of E/N results in rapid avalanching both in the forward and reverse ionization waves. This geometrical enhancement, aided by polarization of the dielectric, then negates at least part of the need for higher voltages to sustain the SIW. The end result is that the propagation is not as sensitive to voltage as would be a bulk ionization wave or a SIW over a flat surface.

The permittivity of the dielectric determines, in part, the electrical capacitance of the substrate. The general trends expected for propagation of a SIW across flat substrates is that the speed of the wave will decrease with increasing relative permittivity, ε_r. The increase in ε_r produces an increase in surface capacitance, C_S (F/cm^2). Increasing capacitance requires more net current from the SIW onto the surface to charge that capacitance, thereby lengthening the dwell time of the SIW at any given location. These principles were experimentally quantified by Morsell et al. [34]. With the microchannel geometry, in addition to the bulk value of ε_r, the local value of C_S varies due to the local geometry. Dielectrics that are thicker (surface is a greater distance from the ground plane) will have smaller values of C_S. Surface locations with smaller radius of curvature will have larger values of C_S. With the substrate being 1.5 mm thick and the channel height being 250 μm, the local value of C_S varies from 3.54 pF/cm^2 to 4.25 pF/cm^2 for the base case value of ε_r =6. The effective capacitance at the vertex of the channels is about 20 pF/cm^2. If the SIW followed the contours of the surface into and out of channels, the expectation is that the SIW to speed-up and slow down as regions of smaller and large values of C_S are encountered. With the SIW not being conformal to the ridges and channels, there is some spatial averaging of capacitance of the surface as the SIW passes over these structures.

The electron densities of SIWs passing over the channels for relative permittivity of the substrate of ε_r, = 2, 6 and 20 are shown in Fig. 5.10. The bulk ionization wave arrives onto the substrate earlier for high permittivity materials due to polarization of the substrate. High permittivity materials push potential into bounding materials of lower permittivity, such as the gas above it, which then increases the bulk electric field and accelerates the bulk IW. With the substrate being only 1.5 mm thick and the substrate-to-electrode distance being about 1 cm, the increase in bulk electric field resulting from polarization of the substrate is not large. The arrival of the bulk IW onto the surfaces is shortened by only about 0.5 ns with ε_r, increasing from 2 to 20.

The earlier arrival of the bulk IW for larger ε_r is negated by the slower propagation of the SIW across the microchannels having larger permittivity. For example, the propagation speed from

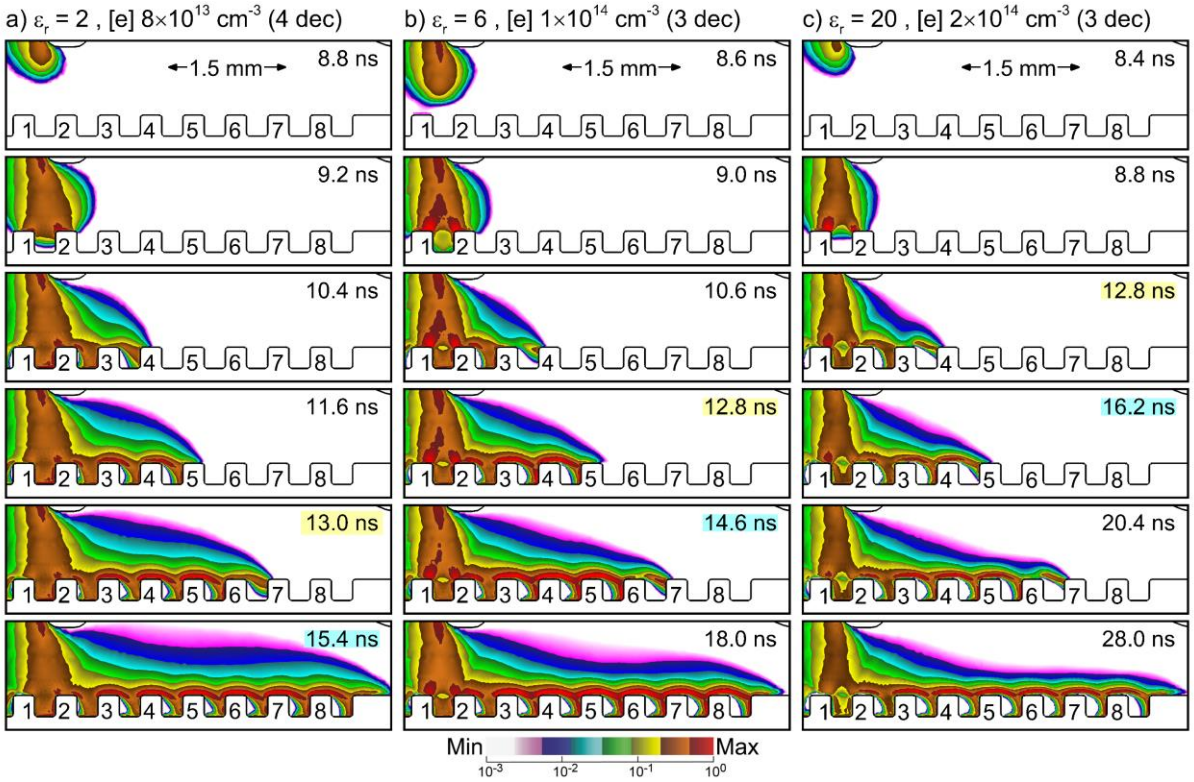

Figure 5.10. Electron density during SIW propagation across a chain of microchannels for different permittivity of the substrate for otherwise the base case conditions. a) ε_r = 2, b) ε_r = 6 and c) ε_r = 20. The time for the image is noted in each frame. The horizontally aligned images are for the approximately the same propagation distance. The shaded times indicate images at approximately the same time. Densities are plotted on a 3-decade log scale with the maximum value noted.

the ridge of channel 3 to the ridge of channel 8 for $\varepsilon_r = 2$ is about 5.7×10^7 cm/s. For $\varepsilon_r = 20$, the speed is 1.9×10^7 cm/s. Due to this increase in dwell time with more current flowing onto the surface to charge a larger capacitance, the maximum electron density increases from 8×10^{13} cm^{-3} for $\varepsilon_r = 2$ to 2×10^{14} cm^{-3} for $\varepsilon_r = 20$. The SIWs across the high permittivity channels are more conformal to the surface with less filling of the channels. Lower permittivity with shorter charging time afford more opportunity for SIWs to propagate along the inside surfaces of the channels.

In the simulations of Marskar and Meyer [11], the speed of propagation of their positive SIW increased with increasing permittivity of the substrate, whereas the results in this study (for

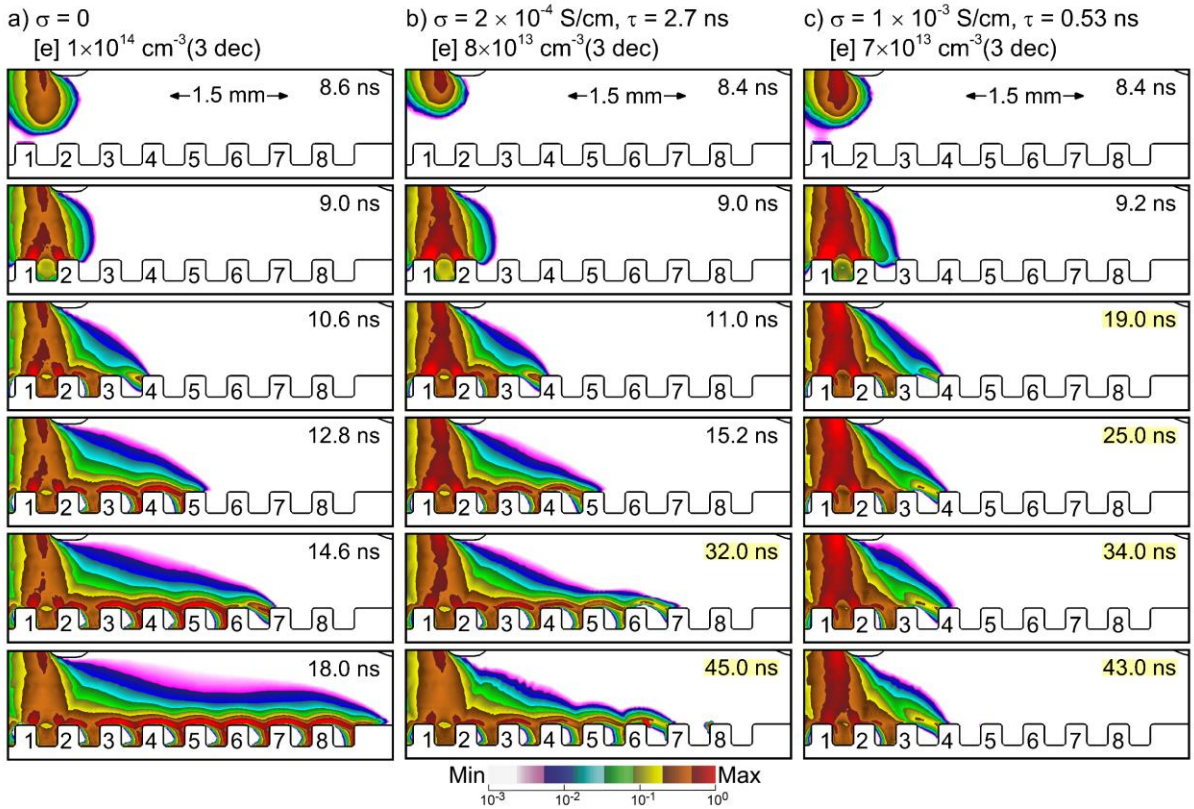

Figure 5.11. Electron density during SIW propagation across a chain of microchannels for different conductivities, σ, and dielectric relaxation times, τ, of the substrate for otherwise the base case conditions. a) $\sigma = 0$, b) $\sigma = 2 \times10^{-4}$ S/cm, $\tau = 2.7$ ns, and c) $\sigma = 1 \times10^{-3}$ S/cm, $\tau = 0.53$ ns. The time for the image is noted in each frame. The horizontally aligned images are for the approximately the same propagation distance of the SIW. The shaded times indicate when the propagation of the SIW stalls. Densities are plotted on a 3-decade log scale with the maximum value noted.

a negative wave) show that the speed of the SIW decreases. These different trends are, in fact,

consistent with the plasma-dielectric synergies, and the polarization of the dielectric. In Marskar and Meyer, the gap between the tip of the electrode and substrate was 2 mm, whereas the thickness of the dielectric was 5 mm. Assuming flat surfaces, increasing permittivity from $\varepsilon_r = 3$ to $\varepsilon_r = 9$ for their dimensions increases the electric field in the gap by a factor of 1.43. This increase in voltage dominates in increasing propagation speed over the increase in capacitance which would otherwise slow the wave speed. For the conditions in this study, the increase in electric field in the gap when increasing permittivity from $\varepsilon_r = 3$ to $\varepsilon_r = 9$ is only 1.04, and so the slowing of the SIW due to the increase capacitance dominates.

The conductivity of the dielectric substrates of interest to biotechnology and chemical conversion will likely be small and support small, if not negligible, current densities through the material. That said, conductivity of the substrate is a possible control parameter for the coverage of the surface and speed of propagation of the SIW. In the absence of significant bulk conductivity of the dielectric, current continuity through the dielectric is maintained by displacement current with charging limited to the surfaces of the dielectric. With increasing conductivity of the dielectric, current continuity is progressively maintained by conduction current through the dielectric which depletes surface charge and decreases the potential drop across the dielectric. The latter trend results in more voltage being dropped across the bulk plasma while decreasing the parallel components of electric field at the surface. In the extreme case of an ideal metal substrate, all of the voltage remains in the gap (or other non-zero impedances in the circuit) and there is no parallel component of the electric field at the surface.

The electron densities during propagation of the SIW across channels having conductivities of $\sigma = 0$ to 10^{-3} S/cm are shown in Fig. 5.11. These values of conductivities were chosen so that the dielectric relaxation times ($\tau = \varepsilon/\sigma$) scale from infinite (no conductivity) to being

commensurate with the time required for the SIW to propagate across several channels (a few ns). Similar to increasing permittivity, the increase in conductivity decreases the speed of propagation of the SIW across the channels. The value of τ is the characteristic time below which current through the material is dominated by displacement current (surface charging) and above which conduction current (charge transport through the material) dominates. For all conductivities, the SIW begins propagating laterally across the channels. However, for the non-zero conductivities, the propagation stalls at some point. This stalling occurs at 32 ns for $\sigma = 2 \times 10^{-4}$ S/cm ($\tau = 2.7$ ns) at the 7^{th} channel, and at 19 ns for $\sigma = 10^{-3}$ S/cm ($\tau = 0.53$ ns) at the 4^{th} channel.

Current continuity from the powered electrode to the ground plane through the substrate is maintained by combination of displacement and conduction current. In the base case having $\sigma = 0$, after the bulk IW reaches the dielectric, current to the surface of the dielectric is largely delivered by conduction. Displacement current through the substrate completes the circuit and maintains current continuity. Upon charging the underlying dielectric to the available voltage, the local impedance of the dielectric increases and the displacement current is greatly diminished. In order to maintain current continuity, the SIW extends to uncharged surfaces of the dielectric that have a lower impedance and which are able to pass displacement current to ground. For zero conductivity, as long as current is flowing through the plasma, the SIW must continue to expand to seek out uncharged surfaces that support displacement current to complete the circuit.

With increasing conductivity of the dielectric, a larger fraction of the current continuity can be maintained by conduction through the dielectric. Unlike displacement current that terminates when the local capacitance is charged, the conduction current, in principle, can continuously flow, particularly if the substrate functions as the anode. When the SIW expands to the point that current

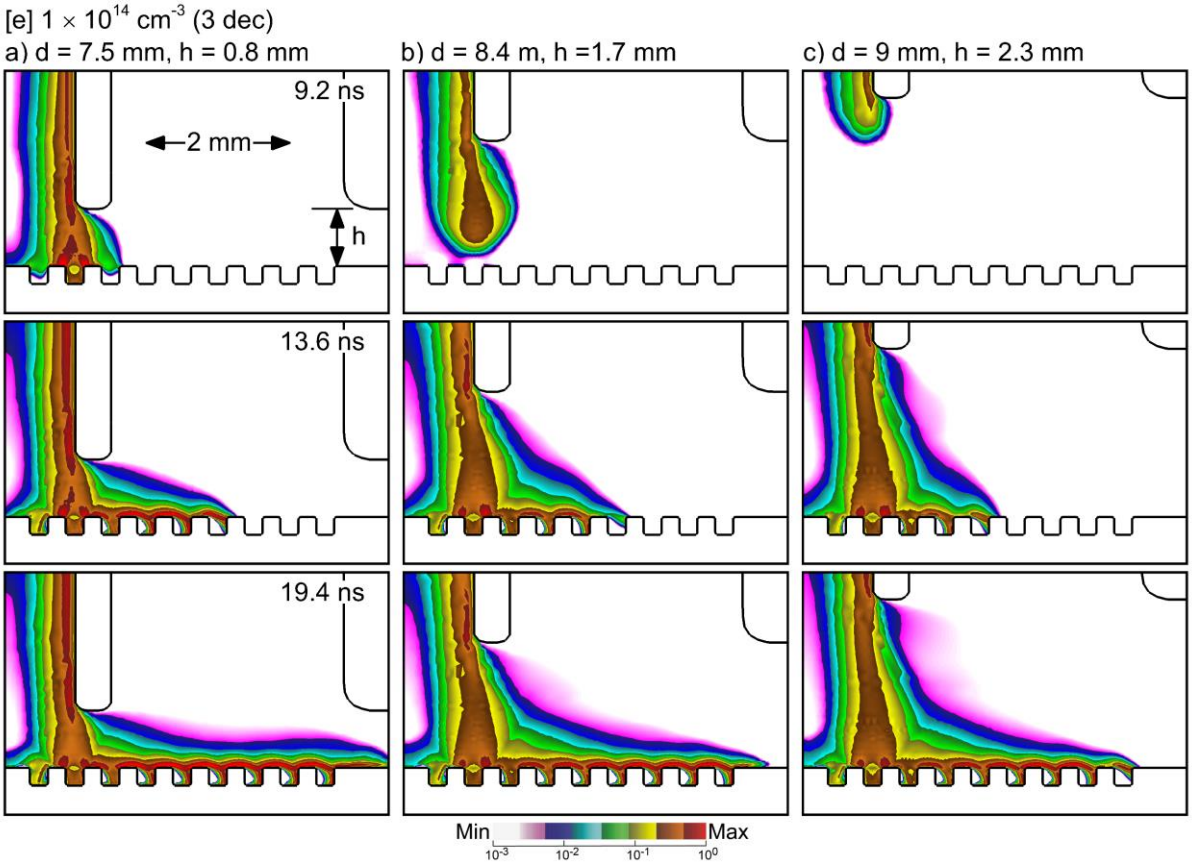

Figure 5.12. Electron density during surface ionization wave propagation across a chain of microchannels for different heights of the powered electrode above the substrate. The electrode position above the electrode is d. The gap between the substrate and bottom of the nozzle is h. a) d = 7.5 mm, h = 0.8 mm, b) d = 8.4 mm, h = 1.7 cm and c) d = 9.0 mm, h = 2.3 mm. Densities are plotted on a 3-decade log scale with the maximum value noted.

continuity is maintained by conduction current, the SIW will stall. At this point, there is no need for further expansion of the SIW to find a lower impedance to pass displacement current. Here, the distance of propagation at which the SIW stalls decreases with increasing conductivity. Again, in the limit that the substrate is an ideal metal, there would be little if any expansion of the SIW. This explanation should also apply to flat surfaces. The nuance with a surface composed of microchannels (or any structured surface) is that geometrical electric field enhancement and polarization focus current into sub-regions of the surface. This focusing of current, which locally charges the dielectric, to some degree limits the total current flow. To maintain current continuity, the plasma launches new bulk ionizations waves. By virtue of their transient nature, these newly

launched waves also add bursts of displacement current connecting the head of the IW to uncharged dielectric ahead of the IW. This need to seek uncharged dielectric to maintain current continuity is manifested in the hopping of the SIW across the surface.

The height of the electrode above the substrate, *d*, and gap between the nozzle and substrate, *h*, affect SIW propagation across the microchannels in at least two modes. The first is gas dynamics, which is a function of h. The purpose of the N_2 shielding gas is to minimize the influence of oxygen and water vapor from the ambient on the propagation of SIW. Smaller gas gaps *h* accomplish this isolation. However, the close proximity of the shield gas to the argon boundary layer also increases the penetration of N_2 into the boundary layer. Larger gaps *h* increase the thickness of the argon dominated boundary layer while decreasing the penetration of N_2 into the boundary layer. The second mode is the applied E/N, which is a function of *d*. Larger heights of the electrode reduce the applied E/N which lowers the speed of propagation of the initial bulk IW wave and which extends to the SIW.

The electron density during propagation of the bulk IW and SIW across the microchannels is shown in Fig. 5.12 for electrode heights and gas gap heights of d = 7.5 to 9 mm, and h = 0.8 to 2.3 mm. The arrival of the bulk IW onto the surface is only moderately delayed by the increase in electrode height. For d = 7.5 mm, the IW arrives at 8.7 ns while for d = 9 mm, the IW arrives at 10.1 ns. Once the SIW is established, this early arrival translates into higher propagation speeds across the microchannels. For d = 7.5 mm, the SIW propagates with a lateral speed of 4.0×10^7 cm/s across the last 4 channels, while for d = 9 mm, the speed is 3.4×10^7 cm/s. The larger gap having less N_2 in the boundary layer produces a SIW that is thicker, penetrating deeper into the argon dominated boundary layer.

5.5 Atmospheric Pressure Plasma Jet Interacting with Wet Microchannels

Plasma interactions with small individual volumes of liquids can be particularly efficient in terms of activating the liquid due to the high surface-to-volume ratio. Large throughputs of plasma activated liquid is then accomplished using parallel processing. The combined use of plasma activation of liquids flowing through microfluidic labs-on-a-chip provides the opportunity to manipulate, mix and utilize the activated liquid in a controllable manner, and provides the opportunity to parallel process. During propagation of plasma jet induced SIWs across dry channels, there are symbiotic interactions between the dielectric and the propagating SIW. Such trend is expected to extend to water filled channels. In this investigation, the focus is on how water

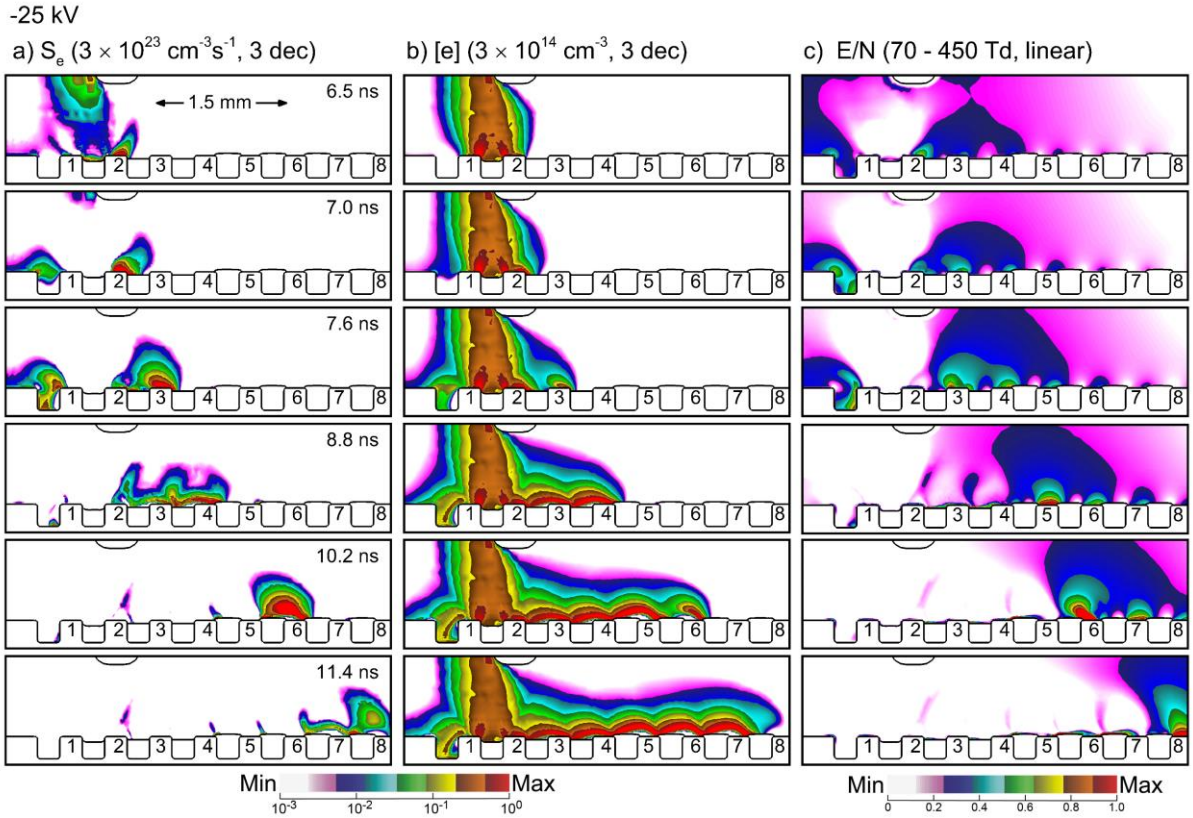

Figure 5.13. Surface ionization wave propagating across a chain of wet microchannels. a) S_e – electron impact ionization source ($cm^{-3}s^{-1}$, 3-decade log scale). b) [e] – electron density (cm^{-3},3-decade log scale). c) E/N – reduced electric field (Td, linear scale). The maximum value or range of values are indicated.

filled channels effects propagation of the SIW, and so the water is modeled as a dielectric having a permittivity of $\varepsilon_r = 80$.

It is intended to compared results of the simulations to companion experiments. The experimental arrangement with gas flow and open channels resulted in the water in channels directly under the jet to be emptied or depleted of water. The levels of and shape of the meniscus of the water in individual channels shown by imaging was approximated in the numerical mesh.

Simulated plasma properties are shown in Fig. 5.13 for the SIW propagating across water filled channels; S_e – electron impact ionization source, n_e – electron density, and E/N – reduced

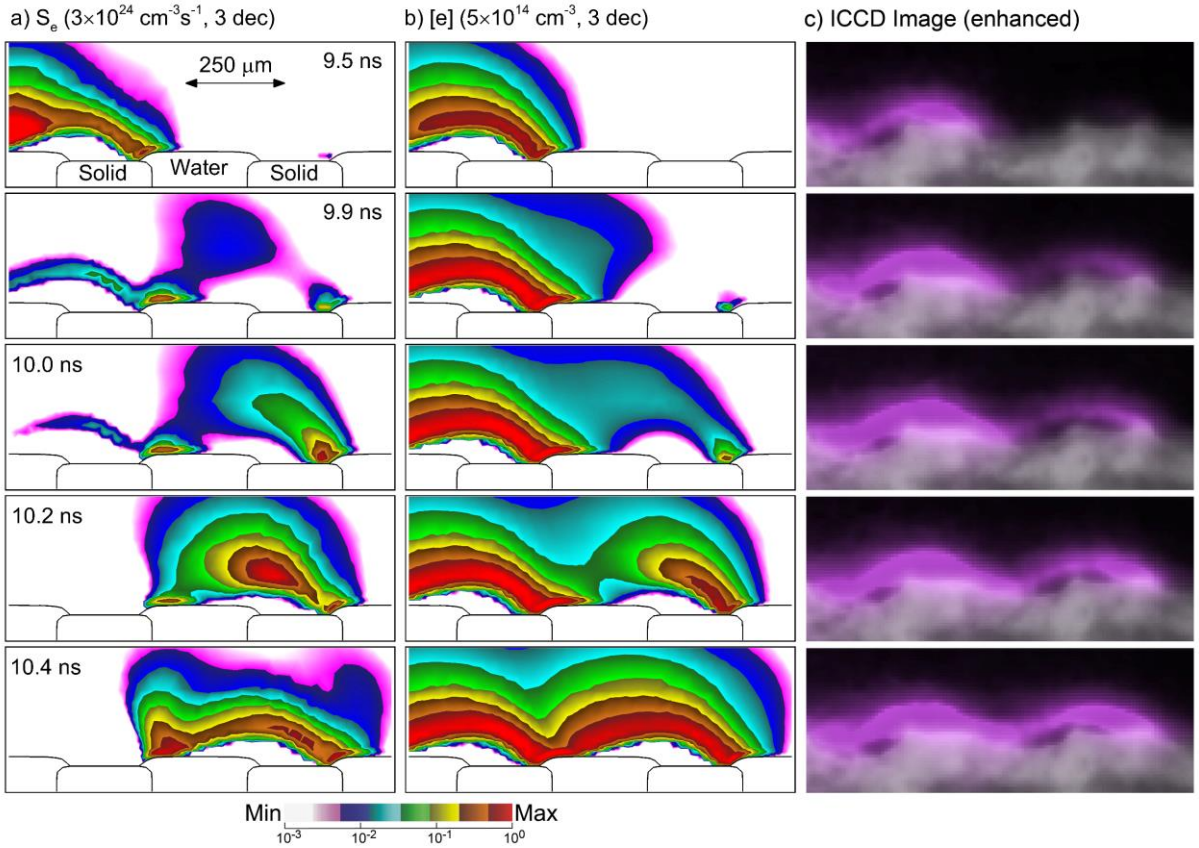

Figure 5.14. Plasma properties centered on water filled channel 6. Simulated a) electron impact ionization source and b) electron density. The time for the horizontally aligned images are indicated in the first column. The properties are shown in a 3-decade log scale with maximum indicated. c) ICCD images chosen at times to align with the simulations. The ICCD images have been enhanced to show dim detail.

electric field. The intersection of the dielectric substrate, water and gas resembles a triple point [35] at which electric field enhancement occurs. Polarization of the water having a meniscus that is concave down would normally locally reduce the electric field in the channels under the nozzle. However, the expulsion of potential out of the wet channels by the high permittivity of the water produces a net increase in electric field at the surface of the water. The transition of the meniscus to convex up in channels further from the nozzle combined with polarization of the water results in locally increasing the electric field, enhanced by the expulsion of potential out of the high permittivity water. The combination of triple point behavior and convex up water produces additional electric field enhancement at the leading edge of the water channels.

As with the dry channels, the bulk IW propagates into the empty channels directly under the jet. As the SIW begins to propagate along the surface, its trajectory is initially onto the surface of the water (channels 2, 3 and 4) due to the locally larger electric field at the surface of the water. Due to the short duration of the plasma-liquid interaction which is less than the dielectric relaxation time, the surface of the liquid charges negatively. This negative charging aids in launching a bulk IW towards the next channel. The IW is directed towards the electric field enhancement at the surface of the water in the next channel. As the water begins to protrude out of the channel to form a positive meniscus (channels 5-8), the electric field enhancement increases. For example, prior to the IW arriving at the water filling channel 3, the electric field at the surface of the water is 115 Td (28 kV/cm). Prior to the IW arriving at the water filling channel 5, the electric field at the leading edge of the water exceeds 250 Td (61 kV/cm). This increasingly large electric field enhancement then directs the IW from leading edge of the water in one channel to the leading of the water in the following channel. There is little contact of the IW wave with the solid dielectric

surfaces of the ridges of the channels. This mode of plasma propagation is probably better described as a hopping bulk ionization wave rather than a SIW.

Enlargements of the ionization source and electron density centered on the water filled channel 6 are shown in Fig. 5.14. The images begin with the IW having terminated on the leading edge of the water in the middle channel where electric field enhancement is the largest (9.5 ns). An electron density of 5×10^{14} cm^{-3} charges the leading edge of the water, which launches a negative IW (indicated by negative space charge in its ionization front) across the remainder of the water. The IW is directed towards the leading edge of the next water filled channel (9.9 ns). The negative IW closes the gap between leading edges with a plasma density of 5×10^{12} cm^{-3} (10.0 ns). With this being a negative IW, there is small density of electrons leading the ionization wave, which seeds electrons in the region of electric field enhancement at the leading edge of the water in the next channel (9.9 ns, 10.0 ns). The seeding of electrons in the large E/N launches a positive IW back towards the prior water channel, indicated by positive space charge at the ionization front of the IW (10.2 ns). The termination of the positive IW on the leading of the water in the prior channel produces an electron density of 5×10^{14} cm^{-3} bridging the two leading edges (10.4 ns). The majority of the ionization is produced by the reverse positive IW. This hopping IW leaves the majority of the both the water and the dielectric ridges not directly covered by plasma with arcs of non-ionized gas between.

Validation of the trends for hopping IWs across the water-filled channels comes from comparison of the results of the simulations with ICCD imaging, shown in Figs. 5.15. The voltage in the simulations is -18 kV. The ICCD imaging shows filling of the dry channels with plasma directly under the jet. As the plasma propagates the bulk IWs first intersect with the ridges of the channels where the channels contain little water. As the channels progressively fill with water, the

IWs first intersect the middle of the water channel. As the IW wave propagates further along the chain, the IW intersects the leading edge of the fully water filled channels. This represents the transition from a SIW to the hopping IW mode from leading edge to leading edge of the water filled channels. These hops then leave regions of at best weakly ionized plasma, indicated by dark regions under the semicircular arcs of hopping IWs.

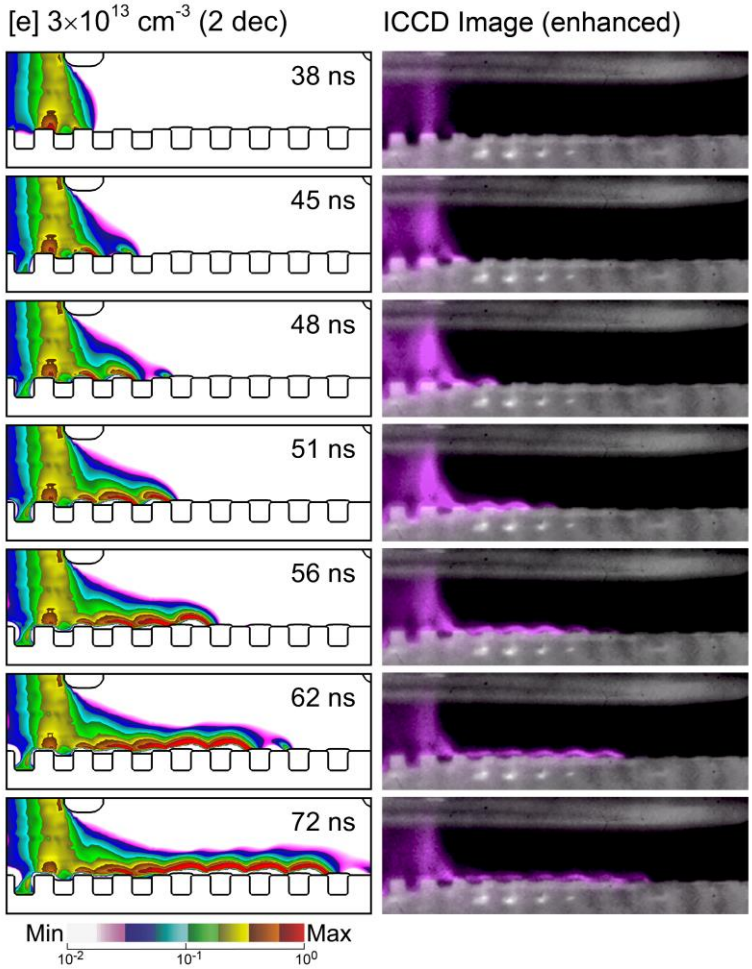

Figure 5.15. Comparison of (left) simulated electron density for applied voltage of -18 kV and (right) ICCD imaging for the Ar plasma jet propagating over water filled microchannels.

The ICCD images also show the propagation of reverse ionization waves, as shown in Fig. 5.14. The sequence of the ICCD images was chosen to coincide with the timings of the simulations. The ICCD images indicate that the leading edge to leading edge gap is first closed by a forward IW. A reverse IW then propagates which produces a brighter image, indicating a higher plasma density. The trends shown by the simulations for the reverse IW closely align with the experimental imaging.

5.6 Concluding Remarks

The use of atmospheric pressure plasmas to treat non-planar, complex surfaces is challenged to uniformly treat those surfaces. For dielectric surfaces these challenges, in part, originate from electric field enhancement, polarization and charging of the surfaces which feed back to the plasma through, for example, higher rates of local ionization. The interaction of APPJs with the dielectric microchannels that might be found in labs-on-a-chip ultimately takes the form of a propagating sequence of surface ionization wave (SIWs) and bulk ionization waves (IWs). Here negative APPJs sustained in Ar/N_2 mixtures propagating into ambient air and onto dry and water filled microchannels are investigated.

Propagation of the plasma across dry channels consists of SIWs across the top ridges followed by launching of bulk IWs across the channels directed towards the electric field enhancement at the vertex of the following ridge. Upon charging of that vertex, SIWs are launched across the ridge and into the interior of the preceding channel. The propagation of the plasma across the channels is then a sequence of bulk IWs which hop from across channels and SIWs which cover ridges and interiors of channels. This process leaves the trailing surfaces of the channel initially uncovered by plasma. The charging of the vertices of the microchannels produce backwards propagating positive ionization waves following the preionized path produced by the forward negative wave. Results from simulations are corroborated by experimental measurements of electric field using the EFISH technique and fast camera ICCD imaging.

The specifics of this pattern of hopping bulk IWs and SIWs depend on the permittivity and conductivity of the dielectric, but the general shape of the pattern remains. Materials with a high permittivity generally increase the total capacitance of the dielectric, which slows propagation of the SIW. However this observation is largely a consequence of the thickness of the dielectric being

small compared to the electrode-surface gap. In cases where the dielectric is of comparable or larger thickness [11], the electric field in the gap increases with increasing permittivity, and the speed of the SIW may increase. Higher conductivity generally slows or stalls the SIW as conduction current is able to provide current continuity and negate the need for the expanding SIW to provide current continuity by displacement current.

The interaction of APPJs with water-filled channels was investigated for the conditions that were accessible in the experiments – empty to partially and fully water filled channels. The high electrical permittivity of water and the formation of a meniscus at the top of water filled channels produce triple point and polarization driven electric field enhancement. The transition between empty to fully filled water channels coincided with surface ionization waves transitioning into hopping ionization waves. The hopping IWs propagate between the electric field enhanced leading edges of the water meniscus of each water filled channel. The majority of the ionization in hemispheres of plasmas formed by the hopping result from backwards propagating, positive ionization waves. The hopping IW left large portions of both the dielectric and the water surfaces not directly exposed to plasma. These computed trends agree well with ICCD imaging.

5.7 References

[1] I. Adamovich, S. Agarwal, E. Ahedo, L. L. Alves, S. Baalrud, N. Babaeva, A. Bogaerts, A. Bourdon, P. J. Bruggeman, C. Canal, E. H. Choi, S. Coulombe, Z. Donkó, D. B. Graves, S. Hamaguchi, D. Hegemann, M. Hori, H. H. Kim, G. M. W. Kroesen, M. J. Kushner, A. Laricchiuta, X. Li, T. E. Magin, S. Mededovic Thagard, V. Miller, A. B. Murphy, G. S. Oehrlein, N. Puac, R. M. Sankaran, S. Samukawa, M. Shiratani, M. Šimek, N. Tarasenko, K. Terashima, E. Thomas, J. Trieschmann, S. Tsikata, M. M. Turner, I. J. Van Der Walt, M. C. M. Van De Sanden and T. Von Woedtke, J. Phys. D. Appl. Phys. **55**, 373001 (2022).

[2] A. Bogaerts, X. Tu, J. C. Whitehead, G. Centi, L. Lefferts, O. Guaitella, F. Azzolina-Jury, H. H. Kim, A. B. Murphy, W. F. Schneider, T. Nozaki, J. C. Hicks, A. Rousseau, F. Thevenet, A. Khacef and M. Carreon, J. Phys. D. Appl. Phys. **53**, 443001 (2020).

[3] Z. Chen, B. E. Koel and S. Sundaresan, J. Phys. D. Appl. Phys. **55**, 055202 (2022).

[4] T. Bolgeo, A. Maconi, M. Gardalini, D. Gatti, R. Di Matteo, M. Lapidari, Y. Longhitano, G. Savioli, A. Piccioni and C. Zanza, J. Pers. Med. **13**, 736 (2023).

[5] P. Hoffer, K. Niedoba, V. Jirásek, V. Prukner and M. Šimek, Plasma Chem. Plasma Process. **43**, 1531 (2023).

[6] R. Brandenburg, Plasma Sources Sci. Technol. **27**, 079501 (2018).

[7] M. Kettlitz, R. Klink, H. Höft and R. Brandenburg, Eur. Phys. J. D **74**, 110 (2020).

[8] J. Winter, R. Brandenburg and K. D. Weltmann, Plasma Sources Sci. Technol. **24**, 064001 (2015).

[9] S. Nijdam, J. Teunissen and U. Ebert, Plasma Sources Sci. Technol. **29**, 103001 (2020).

[10] F. Pechereau, Z. Bonaventura and A. Bourdon, Plasma Sources Sci. Technol. **25**, 044004 (2016).

[11] R. Marskar and H. K. H. Meyer, Plasma Sources Sci. Technol. **32**, 085010 (2023).

[12] A. Hamdan and A. Dorval, J. Phys. D. Appl. Phys. **56**, 215202 (2023).

[13] B. Zhang, Y. Sun, W. Han, L. Fan, W. Guo, W. Li, H. Mu and G. Zhang, Plasma Sources Sci. Technol. **32**, 075020 (2023).

[14] Q. Wang, W. Ning, D. Dai and Y. Zhang, Plasma Process. Polym. **17**, 1900182 (2020).

[15] Z.-I. Mujahid, J. Kruszelnicki, A. Hala and M. J. Kushner, Chem. Eng. J. **382**, 123038 (2020).

[16] G. M. Whitesides, Nature **442**, 368 (2006).

[17] H. Shi, K. Nie, B. Dong, M. Long, H. Xu and Z. Liu, Chem. Eng. J. **361**, 635 (2019).

[18] F. Chen, J. Song, Z. Liu, J. Liu, H. Zheng, S. Huang, J. Sun, W. Xu and X. Liu, ACS Sustain. Chem. Eng. **4**, 6828 (2016).

[19] J. P. Booth, M. Mozetič, A. Nikiforov and C. Oehr, Plasma Sources Sci. Technol. **31**, 103001 (2022).

[20] J. Wengler, S. Ognier, M. Zhang, E. Levernier, C. Guyon, C. Ollivier, L. Fensterbank and M. Tatoulian, React. Chem. Eng. **3**, 930 (2018).

[21] P. Roszkowska, A. Dickenson, J. E. Higham, T. L. Easun, J. L. Walsh and A. G. Slater, Lab Chip **23**, 2720 (2023).

[22] O. Ogunyinka, A. Wright, G. Bolognesi, F. Iza and H. C. H. Bandulasena, Microfluid. Nanofluidics **24**, 13 (2020).

[23] L. Patinglag, D. Sawtell, A. Iles, L. M. Melling and K. J. Shaw, Plasma Chem. Plasma Process. **39**, 561 (2019).

[24] L. Patinglag, L. M. Melling, K. A. Whitehead, D. Sawtell, A. Iles and K. J. Shaw, Water Res. **201**, 117321 (2021).

[25] D. Liu, Y. Zhang, M. Xu, H. Chen, X. Lu and K. Ostrikov, Plasma Process. Polym. **17**, 1 (2020).

[26] J. J. Manríquez, K. Cataldo, C. Vera-Kellet and I. Harz-Fresno, BMJ Clin. Evid. **1711**, (2014).

[27] A. M. Lietz and M. J. Kushner, J. Phys. D. Appl. Phys. **49**, 425204 (2016).

[28] W. Tian, K. Tachibana and M. J. Kushner, J. Phys. D. Appl. Phys. **47**, 055202 (2014).

[29] S. Raskar, I. V. Adamovich, K. Konina and M. J. Kushner, Plasma Sources Sci. Technol. **33,** 025010 (2024).

[30] H. Höft, M. Kettlitz, M. M. Becker, T. Hoder, D. Loffhagen, R. Brandenburg and K.-D. Weltmann, J. Phys. D. Appl. Phys. **47**, 465206 (2014).

[31] X. J. Shao, N. Jiang, G. J. Zhang and Z. X. Cao, Appl. Phys. Lett. **101**, 253509 (2012).

[32] M. Keidar, Plasma Sources Sci. Technol. **24**, 033001 (2015).

[33] S. A. Norberg, E. Johnsen and M. J. Kushner, J. Appl. Phys. **118**, 013301 (2015).

[34] J. Morsell, N. Bhatt, C. Dechant and S. Shannon, J. Phys. D. Appl. Phys. **56**, 145201 (2023).

[35] R. P. Joshi, J. F. Kolb, S. Xiao and K. H. Schoenbach, Plasma Process. Polym. **6**, 763 (2009).

Chapter 6 Atmospheric Pressure Plasma Treatment of Skin: Penetration into Hair Follicles[3]

Sterilization of skin prior to surgery is challenged by the reservoir of bacteria that resides in hair follicles. Hair follilces can serve as a special case of vertically extended microchannels discussed in previous chapters. Atmospheric pressure plasma jets (APPJs) (see Chapter 1) have been proposed as a method to treat and deactivate these bacteria as atmospheric plasmas are able to penetrate into structures and crevices with dimensions similar to those found in hair follicles. In this chapter, the results are presented from a computational investigation of an APPJ sustained in helium flowing into ambient air, and incident onto a layered dielectric similar to human skin, in which there are idealized hair follicles. It is identified that, depending on the location of the follicle, the bulk ionization wave incident onto the skin, or the surface ionization wave on the skin, are able to launch ionization waves into the follicle. The uniformity of treatment of the follicle depends on the location of the *first entry* of the plasma into the follicle on the top of the skin. Typically, only one side of the follicle is treated on for a given plasma pulsed, with uniform treatment resulting from rastering the plasma jet across the follicle. Plasma treatment of the follicle is sensitive to the angle of the follicle with respect to the skin, width of the follicle pocket, conductivity of the dermis and thickness of the underlying subcutaneous fat layer, the latter due to the change in capacitance of the tissue. Utilizing atmospheric pressure plasma presents a distinctive opportunity for treating skin cavities that are inaccessible for liquid-based treatments.

[3] Some parts of the text and the research data presented in this chapter have been previously published by Kseniia Konina *et al* 2023 *Plasma Sources Sci. Technol.* **32** 085020.

The data outlined in this chapter holds promise for the development of treatment modalities addressing various health conditions, including cancer.

6.1 Introduction

Low-temperature, atmospheric pressure plasmas (APPs) are used in biomedical applications [1–3], including cancer treatment [4,5] wound healing[6,7] and sterilization [8,9]. These beneficial interactions with human tissue are produced by a combination of electric fields, UV photons, and short and long-lived reactive species. One of the most common types of short- or long-term infections associated with healthcare are at the surgical site [10]. This complication dramatically increases mortality in high-risk groups [11]. To prevent this, prior to surgery sterilization of the skin in the vicinity of the incision is performed to minimize contamination of the surgical wound [12]. A confounding factor is that the skin surface is covered with pores that open into hair follicles, which can harbor approximately 25% of the pathogens found on skin [13]. In addition to removing hair that may itself contain bacteria, the skin is shaved to better gain access to the interior of the follicles to treat the bacteria they may contain. Current pre-op skin sterilization techniques do not penetrate into these areas as most of the currently used disinfection agents are liquids, and due to the relatively narrow gap between the hair shaft and skin, the penetration of liquid disinfectants by the capillary effect is limited. This motivates alternate means of treating the in-follicle bacteria to eradicate this threat.

APPs have been proposed for sterilizing skin prior to surgery and for treating bacteria in follicles in particular [14]. The surface ionization wave (SIW) that forms when APPs interact with dielectric surfaces, such as skin, can propagate into narrow gaps that are commensurate or larger than the Debye length of the plasma in the SIW. Typical Debye lengths in atmospheric pressure plasma jets (APPJs) are from a few to a few tens of microns [15]. Plasma sterilization of skin and sterilization of follicles by APPJs is especially attractive for their having skin tolerable temperatures while delivering high fluxes of reactive oxygen and nitrogen species (RONS) [14]

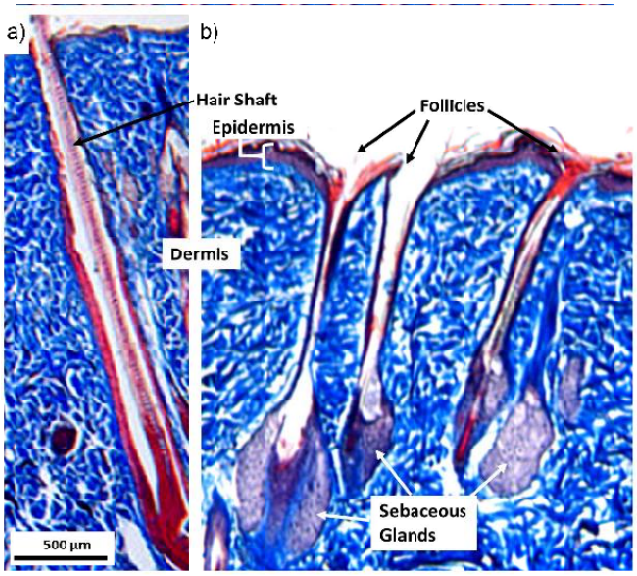

Figure 6.1. Trichrome histology of porcine skin with multiple follicles. a) Typical follicle shows an example of the space that surrounds a prominent central hair shaft. b) Multiple follicles with attached sebaceous glands. Some follicles lack a hair shaft.

[16–19]. For example, it was demonstrated that plasma generated by the kINPen APPJ can be penetrated into hair follicles (on unshaved skin) [20]. The mechanism of plasma penetration into hair follicles is sensitive to many patient and environmental factors.

A typical hair follicle (as shown in Fig. 6.1a) contains a hair shaft or strand (17-110 µm diameter [21–23]) penetrating through the dermis and epidermis (skin) with a spacing between the shaft and surrounding tissue in the range pf 50-140 µm. (This range of values is an estimate based on the total follicle diameter reported as 66-254 µm [22,24].) The gap between the hair shaft and skin varies depending on the individual and location on the body [22,24]. The dimensions of gaps between hair shafts and skin, 50-140 µm, suggest that APPJs may penetrate into the majority of hair follicles, and so have some ability to deactivate bacteria they may harbor. Finding treatment techniques that can penetrate into the follicle can also have added benefit in cancer treatment. Melanoma is one of the more aggressive types of skin cancer. Precursors of melanoma cells are thought to originate in hair follicles which then migrate to skin [25]. Melanoma has a high rate of recurrence [26], with some such risk being associated with “same spot” recurrence, which may be follicles.

In this chapter, a computational investigation of the interaction of APPJ with idealized hair follicles in human skin is discussed. An APPJ sustained in He flowing into room air was directed onto a dielectric surface having the approximate electrical properties of human skin, punctuated with idealized hair follicles (after shaving). It is identified that plasma produced by APPJ can penetrate into typical follicle-like structures. The nature of propagation of plasma into the follicle is typically asymmetric. Given that the model nonPDPSIM (see Chapter 2) is 2-dimensional, the follicle is represented by a pair of capillaries separated by a hair shaft. Asymmetry refers to the plasma preferentially penetrating into one of the capillaries. However, even with asymmetric plasma penetration, photons and long-lived RONS appear to have a more uniform fluence on the inside surfaces of both capillaries. Short-lived RONS, though important to interactions of plasma with human tissue and bacteria, typically follow the patterns of the plasma distribution inside the follicle. The orientation and angle of the follicle with respect to the surface ionization wave (SIW) that the APPJ produced on the surface factor into the penetration and asymmetry of treatment. More uniform treatment of the follicles can be achieved with rastered jets. Patient and site specific factors are also important in determining the uniformity of treatment. For example, the conductivity of the skin (largely determined by oil and moisture content) affects the uniformity of plasma treatment of the follicle, as does the thickness of subcutaneous fat. The thickness of this fat layer varies from patient-to-patient and with location on the body for individuals. In the model, variation of mm to cm in the thickness of the fat layer produced significant variation in the propagation of plasma into follicles.

6.2 Description of the Model

The studies in this chapter are also performed using nonPDPSIM. A short discussion of the settings for this study is contained below.

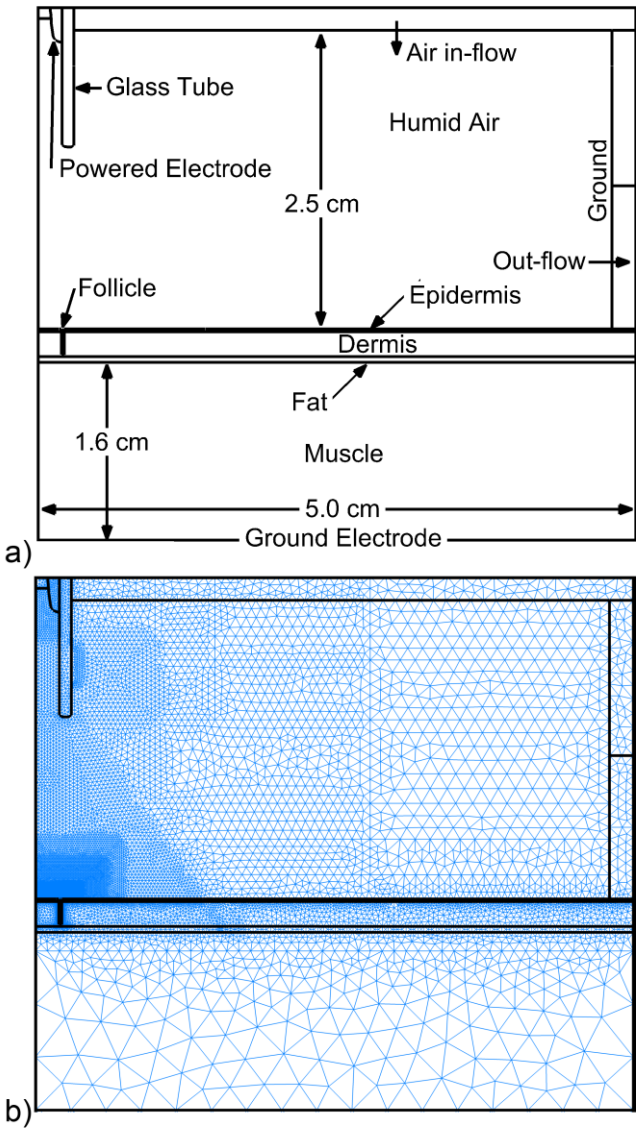

Figure 6.2. Computational domain. a) Schematic of the system which is symmetric across the right boundary. b) Numerical mesh.

In this chapter, the computations include the addressing of the afterglow period. Following the discharge pulse, when there is no applied voltage, and after the plasma begins to dissipate, Poisson's equation is no longer solved. Charge neutrality in the afterglow is enforced, which then enables larger timesteps. During the discharge pulse, timesteps can be on the order of ps. In early afterglow (100 ns), the time step was 2×10^{-11} s. The timestep gradually increases to 10^{-7} s in the late afterglow.

The gas-phase reaction mechanism includes 42 species and 736 reactions. The following species are included in the mechanism: e, H, H^*, H^+, H^-, H_2, H_2(r), H_2(v), H_2^*, H_2^+, H_3^+, OH, OH^*, OH^+, OH^-, H_2O, H_2O(v), H_2O^+, HO_2, H_2O_2, H_3O^+, O_2, O_2(v), O_2(r), O_2^*, O_2^{**}, O_2^*, O_2^-, O_4^+, O, O^*, O^+, O_3, N_2, N_2(v), N_2(r), N_2^*, N_2^{**}, N_2^+, N_3^+, N_4^+, N, N^*, N^+, He, He(2^3S), He(2^1S), He(2^1P), He(2^3P),

He(3P), He(3S), He_2^*, He_2^+, He^+, HeH^+. The photoionization model is based on the emission of VUV radiation by excited states of helium He_2^*, He(^{3}P), He(2^1P) to ionize nitrogen molecules.

A schematic of the cartesian computational domain and numerical mesh are shown in Fig. 6.2. The computational domain is symmetric across the left border. The APPJ is produced by a ring powered electrode inside a glass tube ($\varepsilon_r = 4$) having an 4 mm inside width through which He is flowed at the rate of 1 lpm into an ambient of humid air ($N_2/O_2/H_2O = 0.795/0.2/0.005$) at 1 atm. The He has air and water impurities ($He/O_2/N_2/H_2O = 1/2.4 \times 10^{-6}/4.7 \times 10^{-6}/10^{-4}$) and has a flow speed at the end of the tube of 1100 cm/s. The end of the 1.2 cm long tube is 1.5 cm above the surface of the epidermis of the skin. The APPJ tube is surrounded at the top boundary by a nozzle through which ambient air is injected with an entry speed of 400 cm/s. The purpose of the injected air is to account for entrainment of room air into the flow. All injected gases exit from the domain through the pump port on the right side that is also electrically grounded.

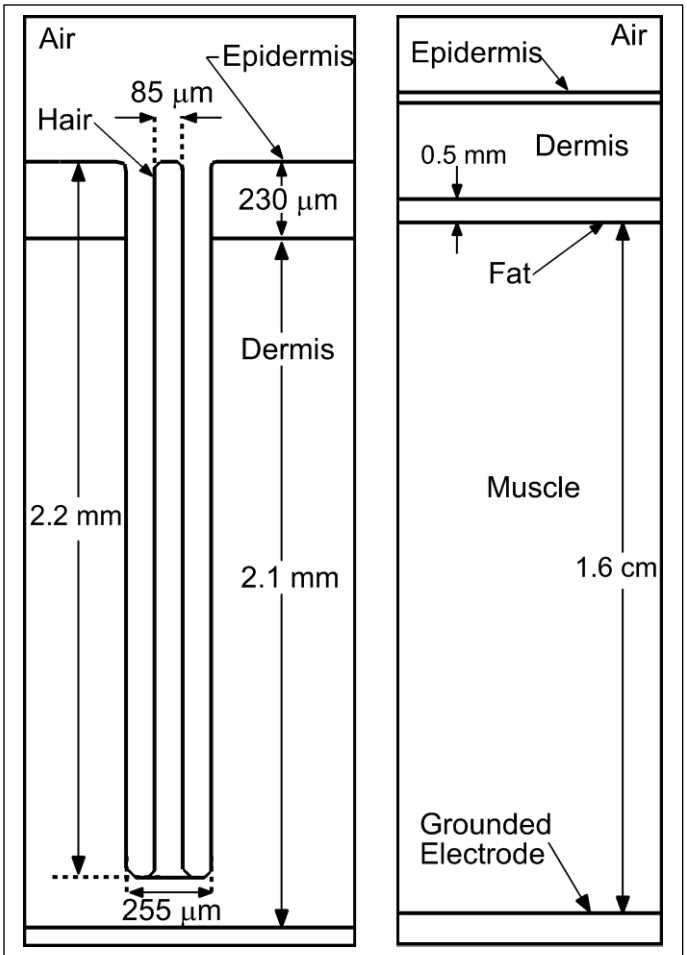

Figure 6.3. Schematic image of the hair follicle and surrounding tissue.

The skin and hair follicle-like structure are represented by a set of dielectric materials, as shown in Figs. 6.2 and 6.3. The intent is to approximate treatment of a follicle on a human wrist

with resolved epidermis, dermis, hair, fat and muscle. The dielectric constants were selected based on the material properties, adjusted so that capacitance of that particular component (e.g., muscle) resembled that of a wrist. The model of skin has no conductivity in the base case and consists of a epidermis layer 230 μm thick (dielectric constant $\varepsilon_r = 10$) over a dermis layer 2.1 mm thick ($\varepsilon_r = 20$). A 0.5 mm fat layer ($\varepsilon_r = 5.3$) sits between the dermis and a 1.5 cm thick muscle layer ($\varepsilon_r = 15$). The bottom of the muscle layer is grounded. The model hair follicle consists of a 255 μm wide, 2.2 mm hole through the dermis and epidermis. A hair shaft ($\varepsilon_r = 4.2$), 85 μm wide, is centered in the follicle hole. The straight edges of the follicle in the model are an approximation as actual follicles have curved edges and more complicated shapes, as shown in Fig. 6.1. The local environment around follicles is more complex due to the presence of blood vessels, glands and fluids or even the absence of a shaft as observed in some glandular follicles (Fig. 6.1b). The simplified geometry used here enables a focus on the fundamental properties of plasma penetration into follicles. On a case specific basis, more detail of the shape of the follicle and of its environment can be included.

The dielectric constants for skin and tissue were selected based on studies discussed in Ref. [27]. The high frequency dielectric constant for the hair shaft is based on its composition being primarily keratin [28].

The base case has a negligible conductivity for the dermis and epidermis. The motivation for this choice was to address short-lived SIWs on dry human skin whose pulse duration is short compared to the dielectric relaxation time. One of the parametric studies is dedicated to the consequences of varying conductivity of the epidermis and dermis. The conductivity of the underlying muscle is not considered as the penetration of electric fields beyond the top few mm of tissue is small.

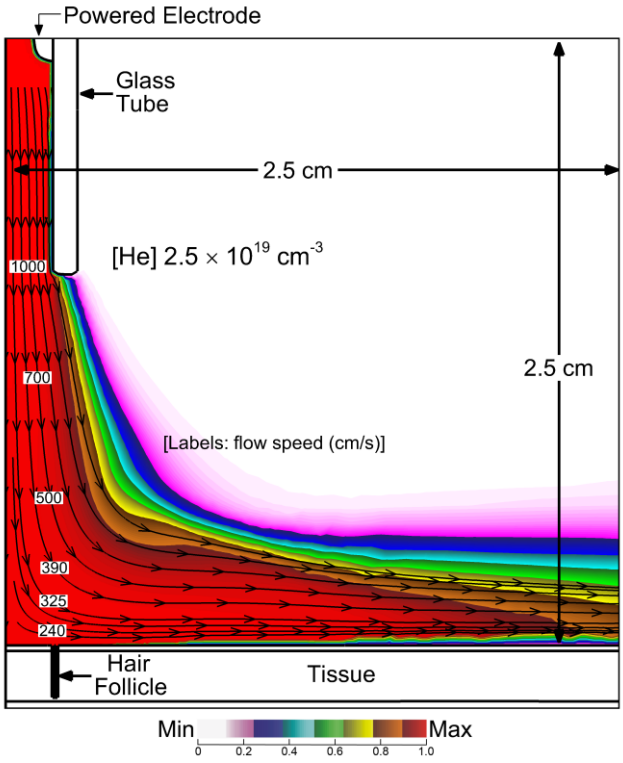

Figure 6.4. The stabilized concentration of helium flow at before the plasma pulse is generated with velocity streamlines. The streamline labels are speeds (cm/s).

The choices of the thickness of the muscle and location of the ground plane were made based on approximating plasma treatment of a human wrist. The electrical representation and effective impedance of the human body, and location of the ground plane, are important considerations in use of any plasma medical device contacting the human body [29]. This sensitivity extends to in vitro studies where series capacitance and ground planes can affect effective dose [30]. For sufficiently short voltage pulses compared to dielectric relaxation times, this sensitivity decreases as the effective capacitance increases. Some aspects of this sensitivity of treatment to the effective capacitance of the treated tissue through varying the thickness of the fat layer are addressed with a parametric study.

It is important to mention that a hair follicle penetrating through skin has many 3-dimensional features, while this model is 2-dimensional. The most glaring difference between a 2-dimensional and 3-dimensional representation is in the isolation of the two sides of the follicle in the 2-dimensional representation. In 2D, plasma inside the follicle gap on the left side is isolated from the gap on the right side. In a 3D representation of a cylindrical hair shaft inside a cylindrical

follicle, plasma could flow around the circumference of the gap from one side to the other. As such, the 2D representation is a worst-case analysis of plasma treatment of the follicle.

6.3 APPJ Interactions with Skin and Follicles

The base case for this investigation is the He APPJ treating the skin surface with a single hair follicle oriented perpendicular to the surface. Before applying voltage, fluid-only calculations are performed for 60 ms to obtain a stable gas flow field, with the results shown in Fig. 6.4. Following establishing the flow field, a voltage pulse of amplitude -25 kV is applied, having a total duration of 160 ns (step function rise, fall time 10 ns). The propagation of the ionization wave and resulting electron density are shown in Fig. 6.5. With the internal ring electrode, the ionization wave (IW) initially propagates as an annulus, producing an

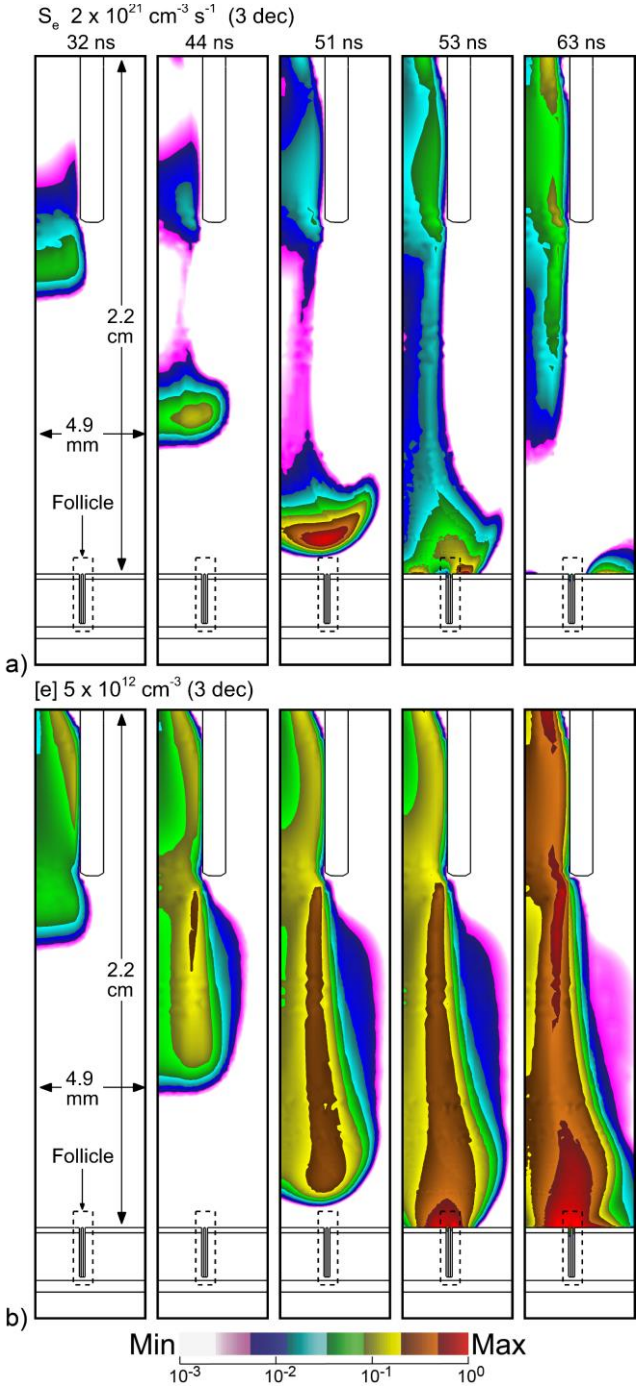

Figure 6.5. Plasma properties during propagation of the ionization wave onto the skin in the vicinity of the follicle. a) Electron impact ionization source and b) electron density. Images are plotted on a 3-decade logscale with the maximum value noted for each frame.

annular distribution of electron density as observed experimentally with similar geometries [31], [32]. The IW crosses the 1.5 cm gap between the bottom of the tube and skin in about 23 ns, producing a streamer speed of 6.5×10^7 cm-s^{-1}, commensurate with propagation speeds for similar conditions [32], [33]. As the ionization wave approaches the skin, the rate of ionization intensifies to a maximum of 2×10^{21} cm^{-3}s^{-1}. The follicle was intentionally placed at approximately the location where the IW strikes the skin. That said, the electric field enhancement that occurs at the edges of the follicle intensifies the rate of ionization in the wave. When the IW strikes the skin, a reverse ionization wave is launched back up the conductive plasma column. Coincidentally to the reverse IW, surface ionization waves (SIWs) are launched in both directions along the skin (53 ns). The inward SIW dissipates while the outward SIW continues to propagate (63 ns). The resulting electron distribution is annular centered over the follicle, with a maximum density 5×10^{12} cm^{-3}.

The electron density, electron impact ionization source and E/N (electric field/gas number density) are shown in Fig. 6.6 at the top of the follicle. The top row of images shows E/N prior to and just as the IW strikes the skin. The following images show the initial development of IWs and plasma in the follicle. Deeper propagation of ionization waves into the follicles (electron impact ionization source and electron density) are shown in Fig. 6.7. Note from Fig. 6.5 that the SIW along the top surface of the skin leaves the vicinity of the follicle by 55 ns.

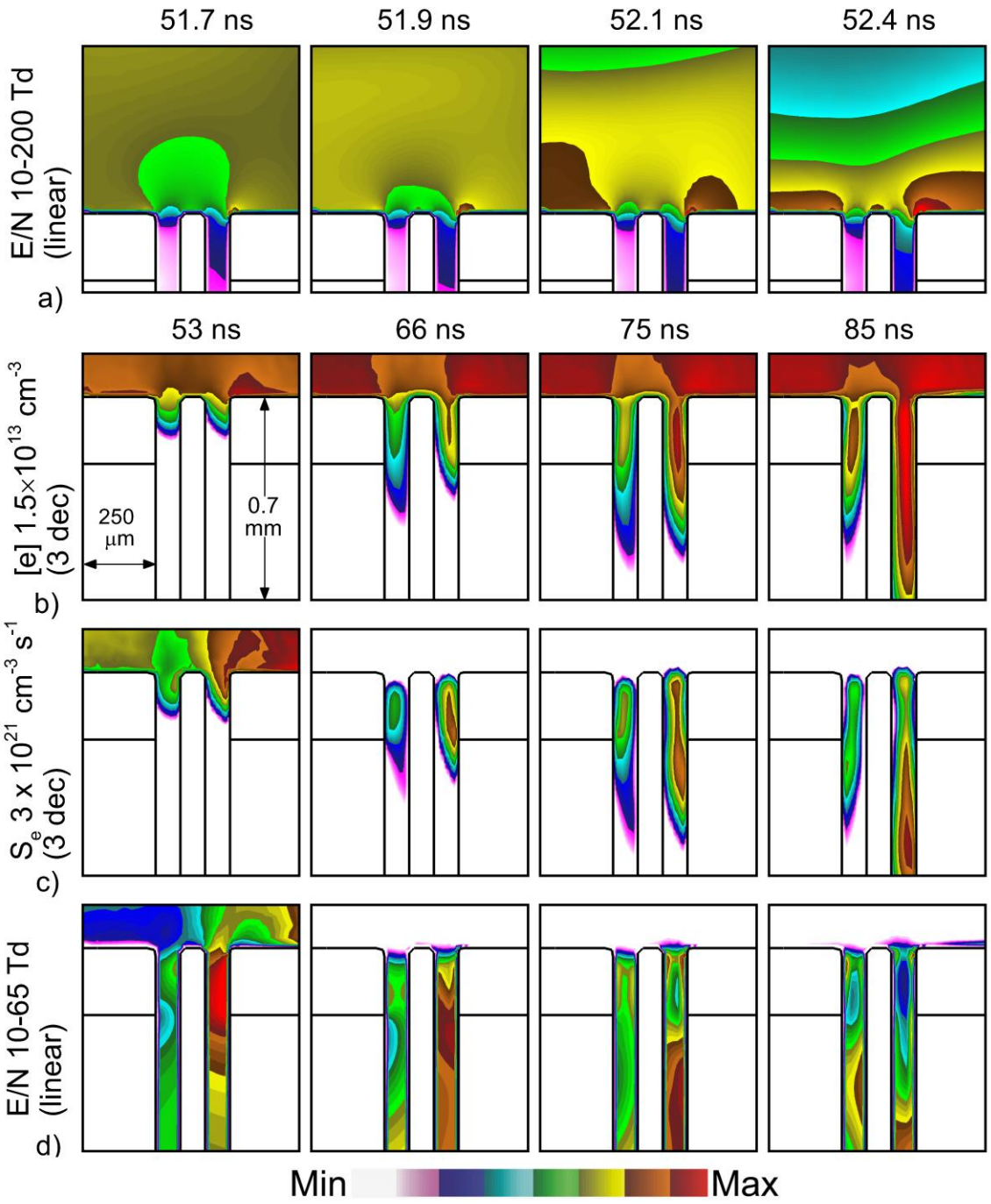

Figure 6.6. Propagation of plasma into hair follicles for the base case for times t = 51.7–52.4 ns. (a) E/N before plasma entry into the follicle (linear), (b) electron density (log-scale), (c) electron density (log-scale) and (d) E/N (linear). The logscale images are plotted over 3 decades. Maximum values are noted for each frame.

As the IW approaches the skin and location of the follicle, the electric potential is

compressed in front of the IW due to the trailing conductive streamer column [34]. Due to the high permittivity of the epidermis (ε_r=10), dermis (ε_r=20) and hair shaft (ε_r=4.2), polarization of these materials produce larger electric fields at the surface of skin than in the gap within the follicle. At 51.7 ns, E/N are 125 Td (1 Td = 10^{-17} V-cm^2) above the skin and 75 Td in the gap. As the IW wave approaches the skin, the curvature of the high permittivity epidermis and hair shaft produce electric field enhancement. E/N is 170 Td and 200 Td on the left and right edges of the follicle, and 150 Td on the hair shaft. This local electric field enhancement then sets the initial conditions for plasma propagation into the follicle.

Due to the particular location of the follicle, the trajectory of the bulk IW and other environmental factors that shape the electric field, the electron impact ionization source, S_e, is marginally larger on the right side of the follicle than the left side. With electric field enhancement occurring at the top of the follicle, SIWs are launched into both sides of the follicle. However, with S_e being marginally larger on the right side, *first-entry* into the structure, and first launching of the SIW occurs in the right pocket. (The term pockets refers to the space between the hair shaft and skin inside the follicle. The outer side of the pocket is skin, while in the inner side is the hair shaft. The larger enhanced electric field on the right side of the epidermis first launches an IW into the right pocket prior to launching the IW into the left pocket. The propagation of the ionization wave in the right pocket is dominantly as a SIW on the outside skin surface, as this surface is charged negatively while the inner surface is not. The SIW is sustained by electron temperatures at the head of the SIW of up to 6.5 eV, with E/N of up to 65 Td. The right pocket fills with electron density of up to 8×10^{13} cm^{-3}. At the end of the voltage pulse the ionization source by Penning ionization of O_2 is about half that by electron impact ionization.

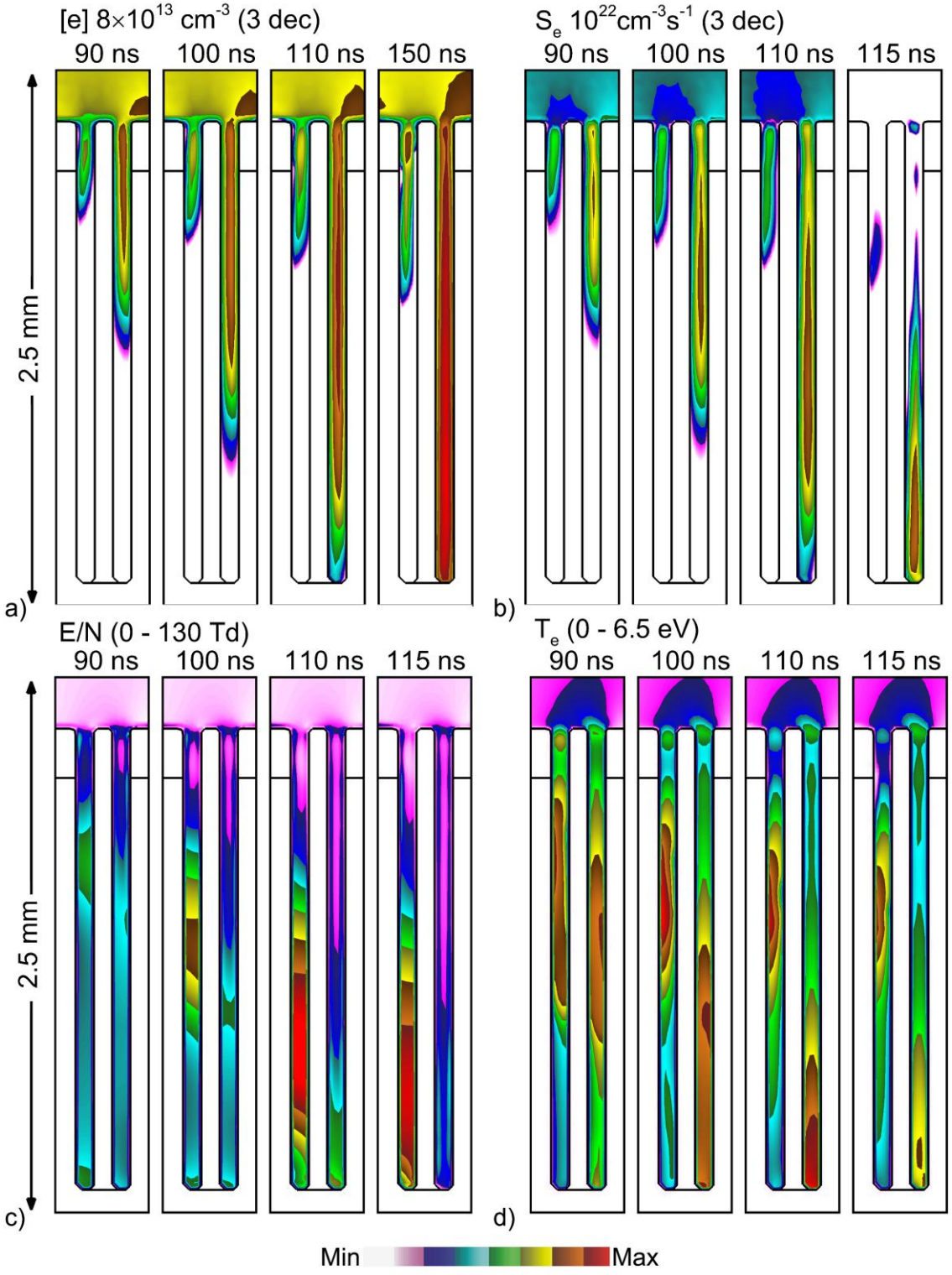

Figure 6.7. Deeper propagation of plasma into hair follicles for the base case for t = 90-115 ns. a) Electron density (logscale), b) electron impact ionization source (log-scale), c) E/N (linear) and d) electron temperature. The log-scale images are plotted over 3 decades. Maximum values are noted for each frame.

The propagation of the *first-entry*, IW in the right pocket occurs from about 55 ns to the

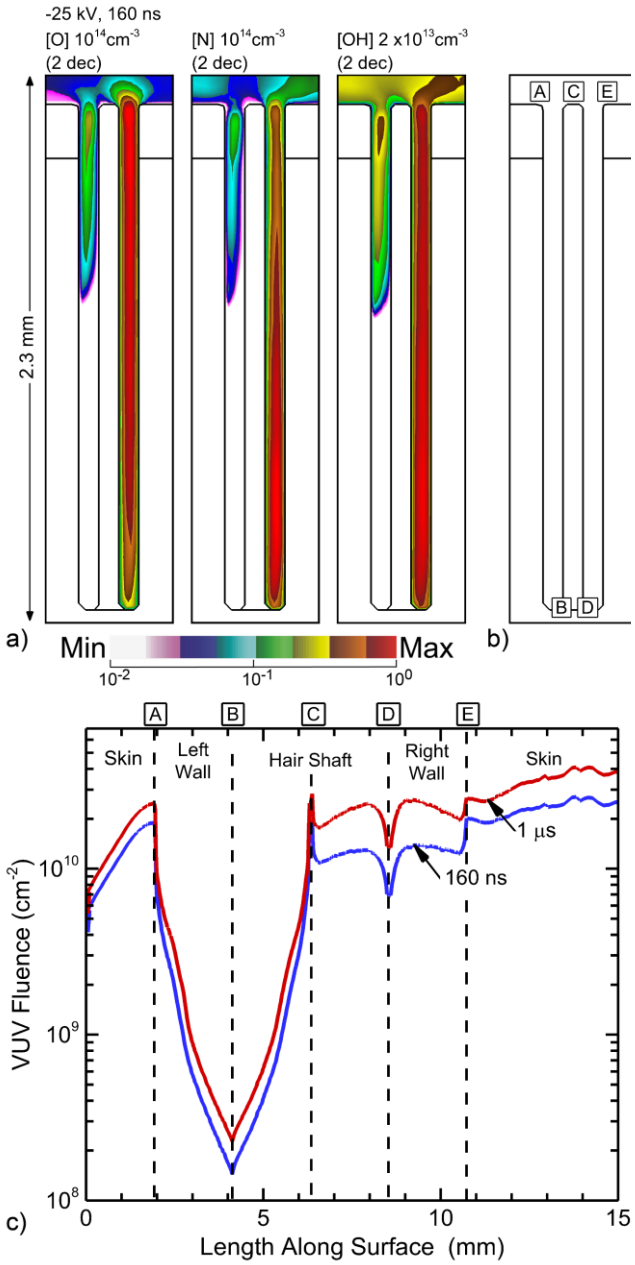

Figure 6.8. Radicals and photons properties in the follicle. a) Densities of O, N and OH at the end of the voltage pulse at 160 ns. Images are plotted on a 2-decade log-scale with the maximum value noted in each frame. b) Reference locations for photon fluences. c) VUV photon fluences to the inside surfaces of the follicle at 160 ns (end of voltage pulse) and 1 μs. The locations along the surface of the follicle are indicated by the boxed letters.

termination of the voltage pulse at 160 ns. During this time, there are no ionization sources in the gas phase above the follicle. The propagation is self-contained within the feature. That said, this propagation is driven in part by the charging of the top surface of the skin which, similar to a dielectric barrier, reaches a significant fraction of the applied voltage, in this case -12.6 kV by the end of the voltage pulse.

During *first-entry* into the right pocket, the high conductivity plasma of the right pocket affects the electric field in the left pocket. First, the high conductivity plasma in the right pocket shorts out the electric potential at that height which reduces E/N in the left pocket. Second, charging of the surfaces of the right pocket orients the electric field horizontally with electron acceleration to the left. The SIW hugs the outer right wall in the right pocket. Propagation of the SIW in the left pocket hugs the left wall. Later during the

voltage pulse (90-150 ns), propagation of the IW stalls in the left pocket in spite of there being plasma in the channel at the top and significant E/N deeper in the channel. The lack of seed electrons deep in the channel and the electric field being oriented in an inopportune direction prevents propagation of the IW in the left pocket.

Ultimately, sterilization of bacteria harbored in the follicle is a function of production of reactive oxygen and nitrogen species (RONS) and UV/VUV radiation. The concentrations of O, N, OH are shown in Fig. 6.8 directly after the voltage pulse. These distributions appear to follow that of the electron density as during this short time, there has been little opportunity for transport of neutral species beyond the location they were produced. The absolute densities of all radicals exceed 10^{12} cm^{-3}. It is unlikely that radicals formed outside follicle will contribute to bacteria inactivation inside the follicle. At atmospheric pressure, the decay rate of radicals is relatively high, providing little time for radicals to transport from the bulk plasma into the follicle. Radicals not produced locally in the channel would need to survive many interactions with the walls in the narrow channel to reach deep into the follicle. Finally, gas flow will advect radicals and longer live species away from the follicles after the discharge pulse, as discussed below. As with the electron density, the treatment of follicles by these short lived RONS is also non-uniform – right pocket compared to left pocket.

One measure of *plasma dose* to the surfaces of the skin and follicles is the VUV fluence (time integral of flux) onto the surfaces. This VUV fluence after 160 ns (end of the voltage pulse) and 1 μs is shown in Fig. 6.8c for points along the surface beginning on the top skin on the left of the follicle and continuing to the top skin on the right side of the follicle. The 50% increase in

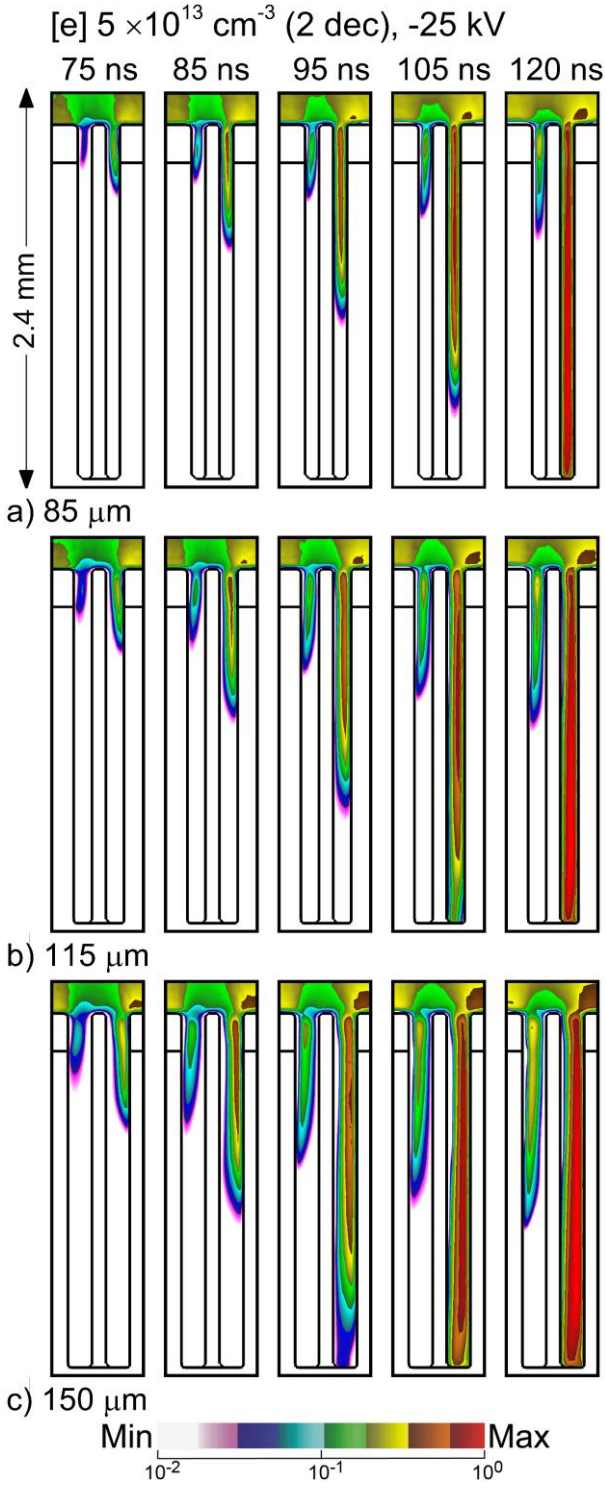

Figure 6.9. Time evolution of electron density inside hair follicles having different widths of pockets for t = 75-120 ns. a) 85 μm, b) 115 μm, and c) 150 μm. The images are plotted on a 2-decade log-scale having maximum value 5×10^{13} cm^{-3}.

fluence between 160 ns and 1 μs is due to dissociative recombination populating high lying atomic states, that then radiate. For some locations the fluence in the left pocket is up to 50 times smaller and far less uniform than in the right pocket. The fluence to the surface in the left pocket largely reflects the view-angle of the surface to the photon source at the top of the channel. The fluence to the surfaces in the right pocket largely are the result of locally emitting species. The small peak in fluence at the top of the hair shaft is due to VUV produced in the bulk plasma.

Asymmetry of plasma exposure is not necessarily the only measure of follicles treatment. Electroporation due to large electric fields also contributes to pathogen treatment [35]. The fill-ing of plasma in one part of the follicle produces, through surface charging, large electric fields in portions of the follicle that are not filled by plasma. These large electric fields could contribute to pathogen treatment.

There is a large range in dimensions of dimensions of hair follicles, based on age and location on the body. The hair shaft itself varies in diameter from 17 μm to 110 μm, and the widths of the pockets can vary from 50 μm to 140 μm. The widths of the pockets in the follicle were varied between 85-150 μm, while keeping the diameter of the hair shaft constant at 85 μm, to determine the consequences on plasma penetration on this variability. Electron densities in the follicle as a function of time and width of the pockets are shown in Fig. 6.9. A general trend is that the speed of propagation of the SIW in the right pocket increases, with perhaps a transition to a bulk IW. With a pocket width of 85 μm, the ionization wave within the pocket propagates with a speed of approximately 5×10^6 cm/s, with the speed being 8×10^6 cm/s for the pocket width of 150 μm. With wider gaps charged particle losses to the walls are lower, which enables a higher propagation speed. For example, with the 85 μm pocket, the ionization wave charges both sides of the pocket (though dominantly the right side. With the 150 μm pocket, the charging is dominantly on the right side, as the width of the pocket is commensurate with the width of the SIW.

In spite of the wider gap and more rapid filling of the right pocket, the left pocket largely remains unfilled with plasma. The penetration of plasma into the left pocket does improve with width of the gap, a consequence of more there being more isolation from the right pocket and more favorable entry of plasma into the pocket at the top of the follicle. At some width (and separation) the left and right pockets will be independent.

6.3.1 Orientation and Location of the Hair Follicle

Although hair follicles are generally oriented perpendicular to the skin surface, hair follicles may have random orientation with respect to the skin surface. The orientation of the

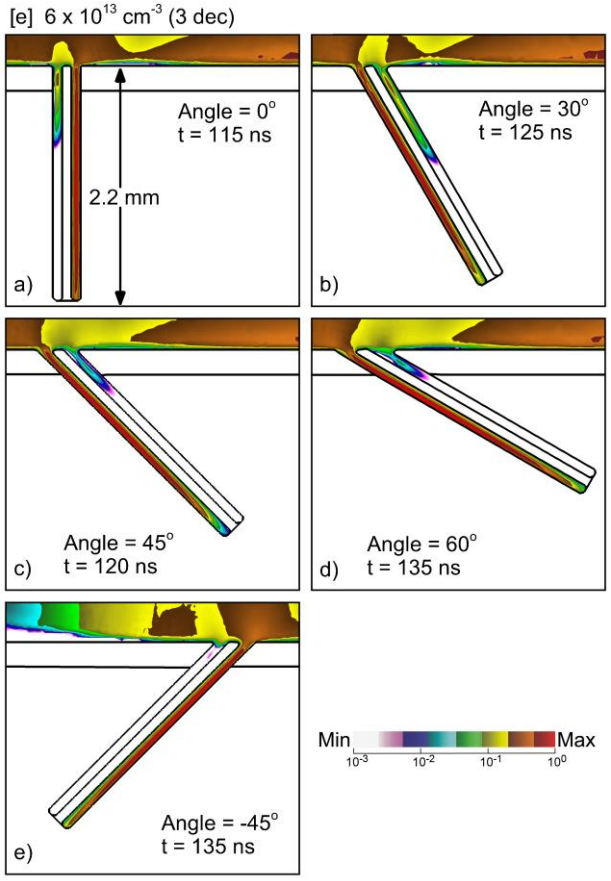

Figure 6.10. Electron density in the follicle for different angles with respect to the skin at the times of the plasma reaching the bottom of the follicle. a) 0 degrees at 115 ns, b) 30 degrees at 125 ns, c) 45 degrees at 120 ns, d) 60 degrees at 135 ns and e) -45 degrees at 135 ns. The densities are plotted on a 3-decade log scale having maximum value 6×10^{13} cm^{-3}.

follicle affects several critical factors for penetration of the plasma: curvature of the surface at the entry to the follicle, open area leading into the follicle and direction of the applied electric field. All factors may affect the *first-entry* of plasma into the follicle. Electron densities are shown in Fig. 6.10 for orientations of the follicle with respect to the skin surface from perpendicular (0°) to 60°, and a reverse direction for 45°. The position of center of the hair shaft at the surface of the skin remains constant as the orientation is changed. All other parameters are kept the same as in the base case, besides the geometry of follicles. The time of each image is when the plasma column reached the bottom of the pocket.

The orientation of the follicle does not have a large effect on their being plasma penetration into one of the pockets. The final plasma density and fill of one of the pockets is nearly the same for all orientations. However, the pocket that has *first-entry* and so fills with plasma is a function of orientation. With increasing slope, the pocket with *first-entry* and which fills with plasma changes from the right pocket to the left pocket. Since the SIW on the top skin surface propagates from left-to-right, the wider opening of the left follicle at the top surface at large angle

enables a less inhibited entry of the plasma into the follicle. The left pocket then fills with plasma while the right pocket does not. With the follicle oriented at -45°, a larger area of the higher permittivity epidermis of the right pocket is exposed to the left-to-right SIW, and so the right pocket has *first-entry*, which then fills with plasma.

Follicles that are oriented away from the perpendicular generally have less uniform of treatment, as measured by the plasma filling of left-and-right pockets. This non-uniformity is in large part a result of the increased likelihood that the SIW has for *first entry* on one side of the follicle as the orientation becomes further from the vertical. For example, a positive angular orientation (tilting to the right in Fig. 6.11) is likely to produce *first entry* on the left side of the follicle, while a negative angular orientation (tilting to the left) is likely to produce *first entry* on the right side. In the cases discussed to this point, the bulk IW striking the skin arrived at nearly the location of the follicle. However, statistically, the IW may strike the skin surface in different locations with respect to the location of the hair follicle, which then influences the *first entry* in the follicle. This will always be the case in treating real skin where hair follicles are generally randomly distributed. Since the permittivity of the epidermis, dermis and hair are large, the surface curvature of the follicle produces local electric field enhancement that can affect the arrival of the bulk IW at the surface of the skin. The location of a follicle with respect to the arrival of the bulk IW and the subsequent SIW is therefore likely to influence the *first-entry* and so the plasma propagation into the follicle.

Electron density is shown in Fig. 6.11 for two follicle locations separated by 1.5 mm and two slopes of the follicle (0° and 45°) with other conditions remaining the same. When transitioning the vertical follicle 1.5 mm to the left, the bulk IW strikes to the right of the follicle. With the subsequent SIW propagating largely to the right, there is not a SIW that propagates across

the opening of the follicle. In this case, the polarization induced electric field enhancement occurring at the curvature at the top of the follicle provides the location ionization that enables *first-entry*. For this particular geometry, *first-entry* favors the left pocket. A similar trend occurs for the slanted follicle when shifted to the left. Polarization induced electric field enhancement produces local ionization above the follicle which then seeds *first-entry* into the left pocket.

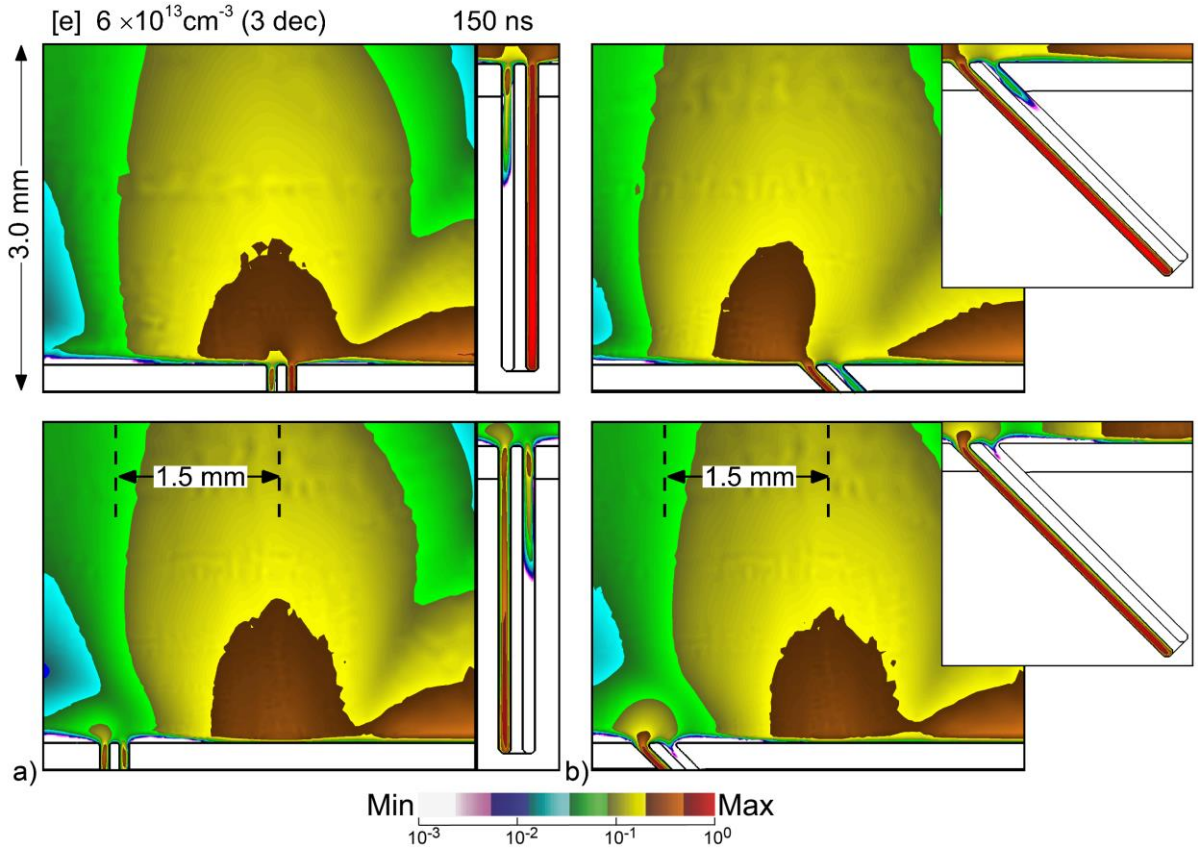

Figure 6.11. Electron density for different locations and angles of follicles at 150 ns. a) Base case vertical follicle and a follicle shifted by 1.5 mm. b) Follicle slanted at – 45 degrees and slanted follicle shifted by 1.5 mm. follicle with the same geometry. The densities are plotted on a 3-decade log scale having maximum value 6×10^{13} cm^{-3}.

The location of the follicle with respect to the bulk IW does feedback to the bulk plasma. Examine in Fig. 6.11 the bulk plasma up to 1 mm above the surface in the vicinity of the sloped follicle. Shifting the follicle has both qualitative and quantitative effects on the distribution of plasma above the surface.

The *first-entry* that determines which pocket fills with plasma is, to some degree, a stochastic process. *First-entry* depends on the location of the follicle with respect to the location where the bulk IW strikes the surface, the direction of propagation of the resulting SIW and the topology of the top of the follicle that determines electric field enhancement. In actual APPJ treatment of skin, the angle of the APPJ is not necessarily perpendicular to the skin. The orientation of the APPJ also likely plays a role. In actual treatment of skin with an APPJ, the jet is repetitively pulsed and rastered across the skin. Any given follicle is either on the right- or left-side of the APPJ and so the location of the follicle is not a critical parameter for uniform treatment. As the relative location of the follicle changes with rastering of the APPJ, it is likely that both pockets fill with plasma during the treatment.

6.3.2 Fluxes and Densities in the Afterglow

Treatment of the follicle, uniformity and magnitude, ultimately depends on the density and fluence (time integrated fluxes) of reactant species to the surfaces inside the follicle. With pulse durations of hundreds of ns and pulse repetition rates of hundreds of Hz to tens of kHz, the duration of the interpulse period (or afterglow) is much longer than the pulse duration. Although the plasma pulse determines the initial location and magnitude of neutral RONS produced by electron impact, the transport and ultimate interaction with the tissue is determined by dynamics during the afterglow.

Short lived species, such as O and OH may have quite different initial distributions within the follicle, as shown in Fig. 6.8. Those short lived species generally have limited fluxes onto the surface as they can be converted to longer-lived species (O to ozone, O_3 and OH to hydrogen peroxide, H_2O_2) prior to reaching a surface. For example, fluences of O_3 and H_2O_2 to the inside

surfaces of the follicle and the adjacent skin are shown in Fig. 6.12 after 1 ms of afterglow for the base case. The fluences to surfaces for the left pocket are focused towards the top of the follicle due to the limited penetration of plasma. The fluences to the surface in the right pocket are focused toward the bottom of the follicle. This trend results from the plasma being somewhat more intense in the bottom of the follicle. The OH density after the voltage pulse (Fig. 6.8) is 1.4×10^{13} cm^{-3} at the bottom of the follicle and 1.1×10^{13} cm^{-3} at the top. However, the majority of the smaller fluence at the top of the follicle is due to transport of O_3 and H_2O_2 out of the follicle during the afterglow.

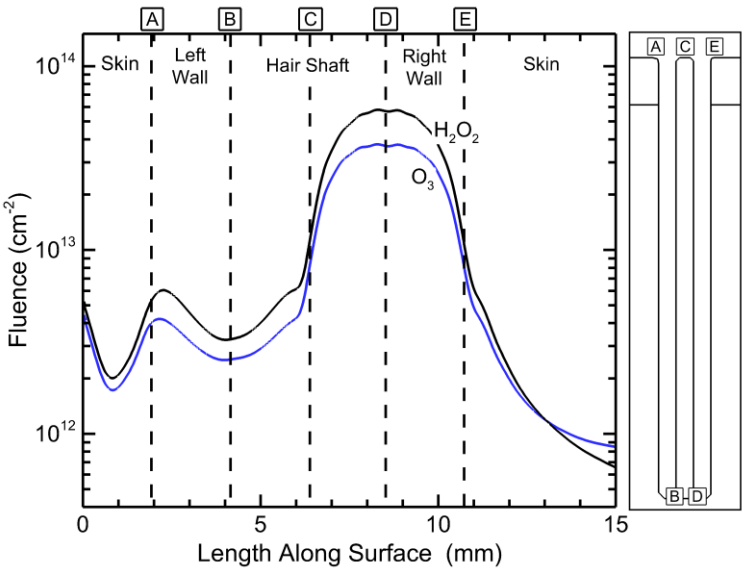

Figure 6.12. Fluence of H_2O_2 and O_3 at 1 ms in the afterglow inside a follicle. The schematic at the right indicates the locations along the inside surface of the follicle.

The APPJ used in this investigation consists of a flow of largely helium initially perpendicular to the skin, which produces a stagnation point at the surface of the skin and flow outwards parallel to the skin. (See Figure 6.4.) The flow is parallel to the surface above the follicle with flow speeds above the follicle in boundary layer of a few hundred cm/s. Inside the follicle, the advective flow is stagnant, with transport being diffusive. The production of O and OH, precursors to O_3 and H_2O_2, occurs during the plasma pulse and immediate afterglow. Little additional O and OH are produced after about 200 ns. Conversion of these radicals to longer lived species (O_3 and H_2O_2) occurs over the tens of microseconds to ms timescales.

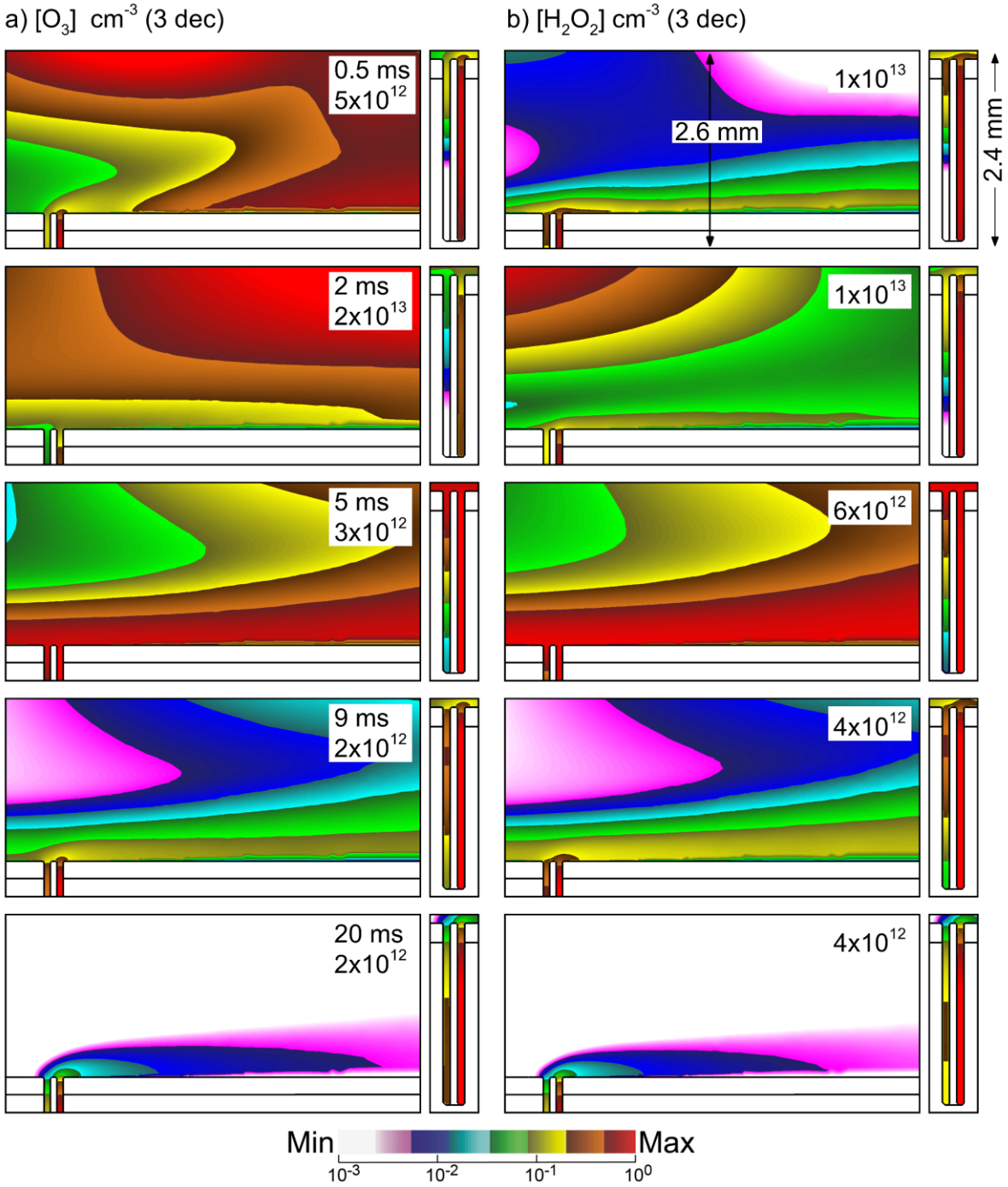

Figure 6.13. Time evolution of the densities of ROS in the afterglow following a pulse inside the hair follicle and above the skin. a) O_3 and b) Concentration of H_2O_2. The densities are plotted on a 3-decade log-scale with the maximum value (cm^{-3}) noted in each frame.

The densities of O_3 and H_2O_2 during the post-plasma afterglow are shown in Fig. 6.13 for times up to 20 ms. With the bulk gas flow parallel to the surface during the afterglow, the O_3 and

H_2O_2 in the bulk plasma is advected away from the vicinity of the follicle until there are negligible densities of O_3 and H_2O_2 above the follicle that originate in the bulk plasma. The O_3 and H_2O_2 in the follicle are largely unaffected by the bulk gas flow. With there being little O_3 and H_2O_2 in the bulk gas, the O_3 and H_2O_2, in the follicle now has the largest density. With the large aspect ratio of the follicle, the O_3 and H_2O_2 slowly diffuse out of the follicle producing a plume that is advected downstream. In practice, the APPJs used for treatment of follicles will be rastered, which at times might produce advective gas flow in a direction that opposes the diffusion of reactants out of the follicle [36]. With typical diffusion times to empty the follicle of reactants being tens of ms, this situation might occur with rapid rastering. That said, these opposing flows would likely redistribute the reactants that diffuse out of the follicle over the adjacent skin as opposed to slowing or preventing the rate of diffusion out of the follicle.

6.3.3 Fat Layer Thickness

The thickness of the subcutaneous fat layer under the skin can significantly vary from person to person and from one part of the body to another. From an electrical perspective, the fat layer is a series capacitance for currents that return to ground through the body. Thin fat layers, corresponding to large capacitance provides a smaller impedance, and less voltage dissipation across the fat layer. Thick fat layers have small capacitance, larger impedance and more voltage dissipation. Since a thicker fat layer increases the distance between the powered electrode and the effective, ground plan the initial voltage available for plasma formation is reduced.

The electron density is shown in Fig. 6.14 in the electrode-skin gap and in the follicles for fat layers of thickness 0.4 – 5.5 mm. With increasing of the thickness of fat layer, the total capacitance in series with the plasma decreases. The decrease in capacitance has several

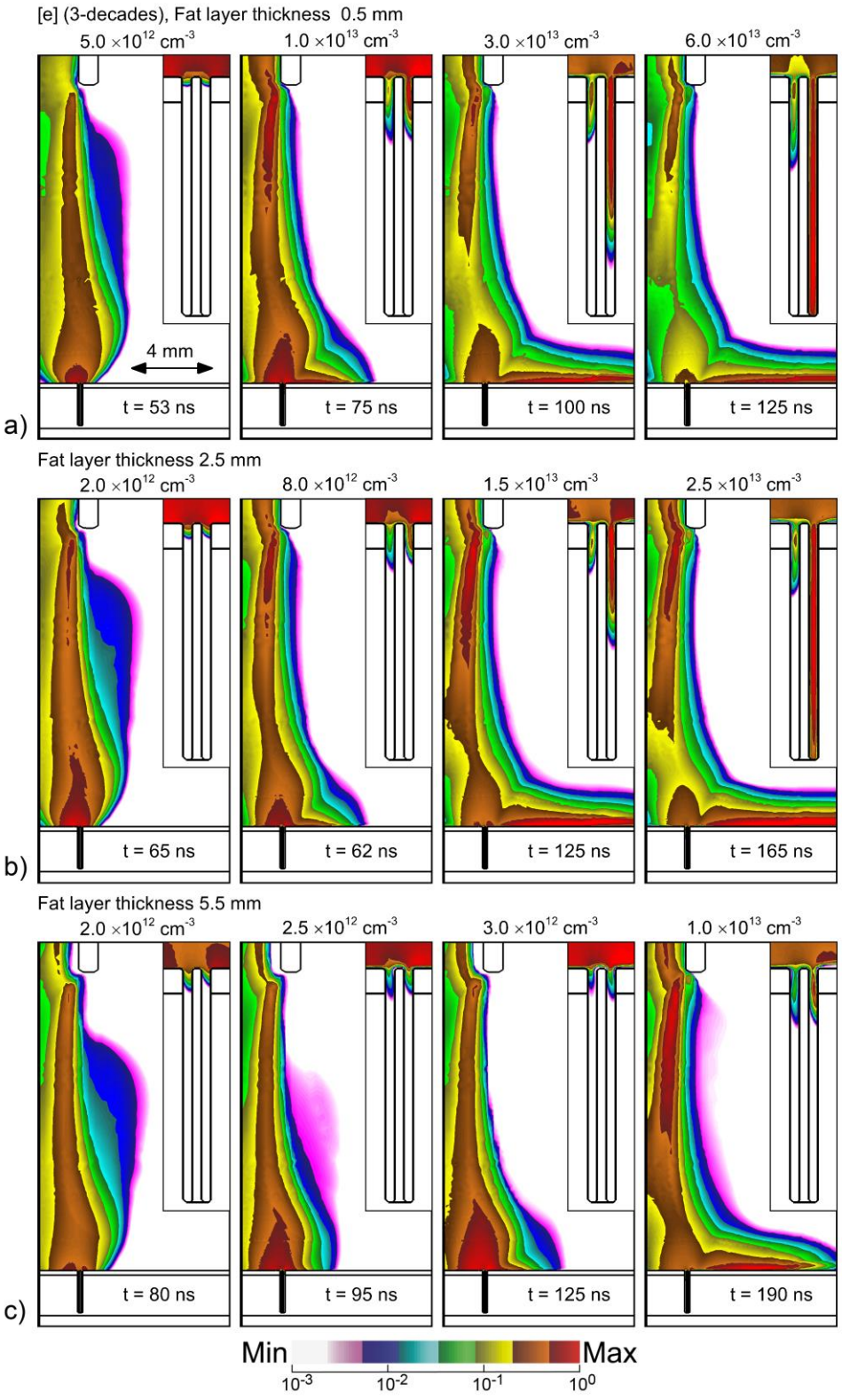

Figure 6.14. Electron densities in the nozzle-skin gap and inside the follicle at different times during and following the voltage pulse for different thickness of the fat layer. a) 0.5 mm, b) 2.5 mm and c) 5.5 mm. The densities are plotted on a 3-decade log scale with the maximum value and time indicated in each frame.

repercussions. The first is that that with the large impedance of the fat layer, there is initially less

voltage available for the gap, which produces a slower bulk ionization wave. The time for first-touching of the bulk ionization wave (first column in Fig. 6.14) increases with increasing fat thickness and decreasing capacitance. The second effect is that the dwell time of the plasma over the follicles is longer with larger capacitance (thinner fat layers), which provides more opportunity for the plasma to enter into the follicle. The third is that the smaller capacitance (thicker fat layer) chargers more rapidly, leaving less voltage available to launch the SIW into the follicle. The end result is that for otherwise the same conditions, there is less plasma penetration into the follicles with thicker, smaller capacitance fat layers.

There are remedies that will produce plasma propagation into the follicles regardless of fat layer thickness– such as smaller gap between the jet and skin, higher voltage, rastering the jet. These results are intended to emphasize the APPJ will respond differently when treating different areas of the patient, and will respond differently patient-to-patient, due to the differences in the equivalent electrical circuit that the APPJ sees.

6.3.4 Skin Properties

Electrical representation of the skin and follicle in the model are as lossy dielectrics – material with a dielectric constant, ε, and conductivity, σ. These values determine the dielectric relaxation time of the tissue, $\tau = \varepsilon/\sigma$. These dielectric properties of skin can significantly vary from person to person, by body location (arm, leg or face), and even depend on respiration or activity level of a given individual. Specific skin structures, like sebaceous glands produce liquids that contain salt, or lipid molecules that will also effect skin conductivity [37]. The treatment of

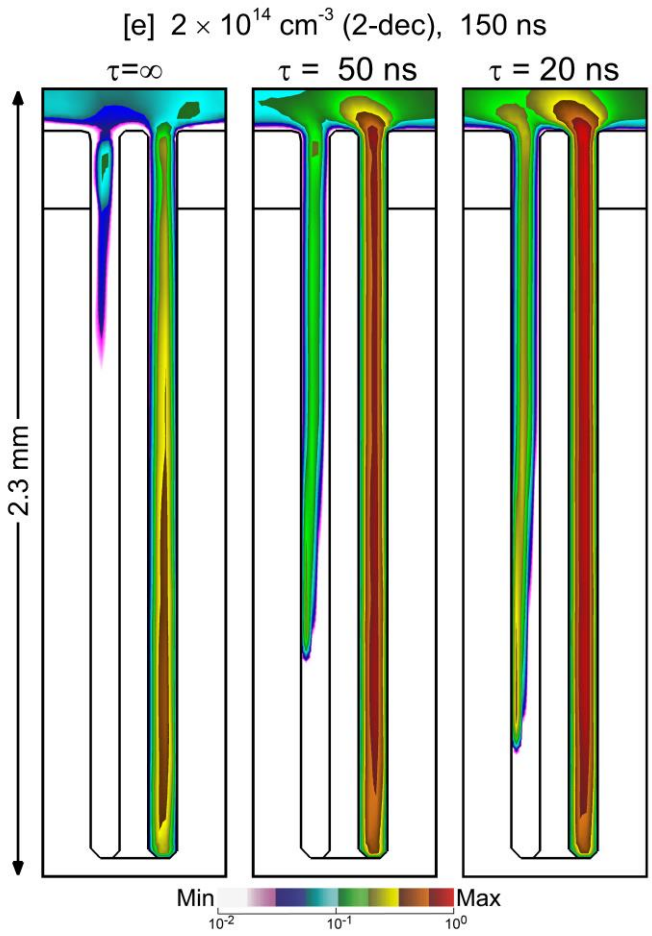

Figure 6.15. Election density at 150 ns (logarithmic scale) for three skin conductive and dielectric properties corresponding to dielectric relaxation times of infinite, 50 ns and 20 ns. The densities are plotted on a 2-decade log scale having maximum value 2×10^{14} cm^{-3}.

follicles in skin having different dielectric relaxation times was examined. While all base case parameters and geometry were kept the same, the conductivity of the epidermis and dermis was varied to yield dielectric relaxation times of infinite (pure dielectric), 50 ns and 20 ns. The resulting electron densities in the follicles at the end of the voltage pulse are shown in Fig. 6.15.

Increasing the conductivity of the skin layer generally improved the uniformity of plasma treatment of the follicles. A purely dielectric, non-conductive skin layer charges as would a capacitor or electrode covering material in a dielectric barrier discharge. As skin has a finite conductivity, some current can continue to flow when there is less surface charging. With less surface charging, electric fields retain a component downwards in the direction of ground and so enhance the propagation of the SIW into the pockets. Physiological limits aside, there is a limit to the improvement to uniformity that can be achieved with increasing conductivity. High aspect ratio channels or vias in conductive materials are nearly equipotential with there being no component of electric field parallel to the surface. Such conditions would not be conducive to sustaining ionization waves into the feature.

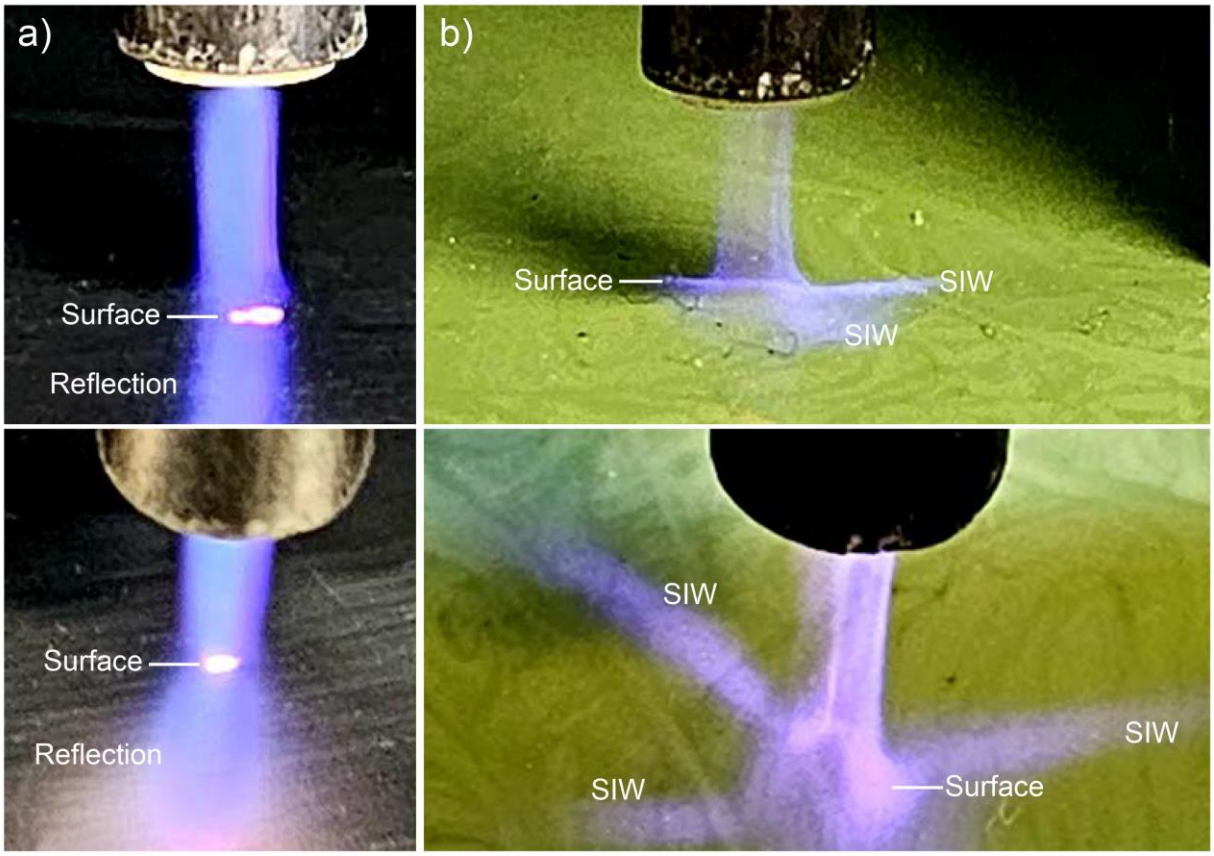

Figure 6.16. Conductivity of target substrate determines plasma flow properties. A helium plasma jet with a gas flow of 4 slm is shown. a) Image of plasma with the target being a grounded metal plate. The top image is a side view. The bottom image is a view from approximately 45 degrees. b) The grounded metal plate is covered by a 3 mm silicon pad with the same distance between the plasma tube and surface. The propagation of surface ionization waves are noted.

The sensitivities to the dielectric properties of the surface of plasma jets striking surfaces are well acknowledged [38], [39], [40]. Given the large variability in skin electrical properties in moisture and oil content, and location on the body, these sensitivities should be a high priority in optimizing plasma treatment of follicles. An example of how combinations of capacitance and conductivity, and the ability of the plasma to contact ground, alters the plasma propagation along a surface is shown in Fig. 6.16 where a silicon pad is placed between an APPJ sustained in helium and the metal ground. While the images integrate over many plasma pulses and do not represent a single pulse, they illustrate the concept. When a conductive surface such as ground is

immediately accessible, the spreading of the jet on the surface is minimal (Fig. 6.16a direct and lateral views). Lack of a lateral component of the electric field along the conductive surface inhibits spreading, and lack of charge accumulation on the surface preserves the voltage across the gap. The plasma jet is significantly less bright and spreads along the surface (Fig. 6.16b) using the same plasma conditions (power and gas flow) while placing a 3 mm silicon pad between the plasma and the ground. The propagation of SIWs are noted in the image. These phenomena, though less dramatic, will occur with significant changes in skin conductivity and affect propagation of the plasma into the follicles.

6.4 Concluding Remarks

Sterilization of skin prior to surgery is challenged by killing of bacteria that is harbored in hair follicles. With a significant fraction of skin resident pathogens residing inside follicles and the limited penetration of liquid disinfectants, other forms of treatment of in-follicle bacteria are needed. From a structural perspective, hair follicles consist of high aspect ratio indentations in a mildly conducting, lossy dielectric – the skin. Atmospheric pressure plasma jets (APPJs) have the ability to penetrate into dielectric structures that have sizes commensurate to or larger than the plasma Debye length. A helium atmospheric pressure plasma jet incident onto skin with idealized follicles was computationally investigated to determine the ability of plasma to penetrate into these structures, and their possible use for sterilization.

It is identified that there is a potential for non-uniform plasma treatment of the interior of hair follicles, at least with a single plasma pulse. The cause of that non-uniformity is that IW waves that are arrive onto the follicle, or SIWs that propagate to the follicle, have a *first-entry* point which establishes a local, high conductivity column having limited coverage within the

follicle. The resulting conductivity of the plasma column reduces the ability of the plasma to propagate into the remainder of the follicle. The in-follicle coverage of plasma is a function of the width of the in-follicle gap between the hair shaft and skin, the angle of the follicle with respect to the top of the skin, the shape of the follicle opening which determines electric field enhancement, the conductivity of the skin and the location of the follicle relative to where the bulk IW wave strikes the skin. To some degree, the point of *first-entry* of any given follicle is likely stochastic. Given that application of APPJs for skin sterilization will use high repetition rate pulses that are rastered across the surface of the skin, it is likely that uniform treatment of the majority of follicles can be achieved.

The precise reactive species that mitigate a given pathogen is an important consideration. Although short lived species may be quite non-uniformly produced in the follicle, diffusion of longer lived species such as O_3 and H_2O_2 can produce significantly more uniform fluences to surfaces in the follicle.

The model that was used in this work is two-dimensional and represents a worst analysis of follicle treatment as there is not direct lateral transport of species between the left-and-right pockets. In actual follicles (cylindrical hair shaft inside a cylindrical cavity), transport around the shaft is possible and so long-lived species have an opportunity to diffuse throughout the follicle during the afterglow between pulses. With that said, our observations are best applied to those situations where short lived species and photons are the dominant biocidal agents.

Although the investigated hair follicles slanted at angles to the skin, hair follicles themselves are generally not straight channels. Typical follicles are narrow near the top and wider near the bottom, and have some curvature. Liquids are also present in the follicles along with gland entries. These structures may produce a non-uniform plasma inside the follicle but generally

should not prevent plasma from penetrating.

Some follicles lack a hair shaft. A condition called alopecia represents a group of diseases resulting in hair loss [41]. It has been recently shown that there may be a benefit from plasma treatment of alopecia patients [42]. Follicles in alopecia patients tend to decrease in size but typically not drop below 130 μm [43]. So the penetration of plasma into follicles likely occurs in alopecia patients, which may explain part of the benefit.

6.5 References

[1] M. G. Kong, G. Kroesen, G. Morfill, T. Nosenko, T. Shimizu, J. van Dijk and J. L. Zimmermann, New J. Phys. **11**, 115012 (2009).

[2] Adamovich, I, J. Phys. D. Appl. Phys. **50**, 323001 (2017).

[3] B. F. Gilmore, P. B. Flynn, S. O'Brien, N. Hickok, T. Freeman and P. Bourke, Trends Biotechnol. **36**, 627 (2018).

[4] J. Schlegel, J. Köritzer and V. Boxhammer, Clin. Plasma Med. **1**, 2 (2013).

[5] C. Hoffmann, C. Berganza and J. Zhang, Med. Gas Res. **3**, 21 (2013).

[6] B. Stratmann, T.C. Costea, C. Nolte, J. Hiller, J. Schmidt, J. Reindel, K. Masur, W. Motz, J. Timm, W. Kerner and D. Tschoepe, JAMA Netw. open **3**, e2010411 (2020).

[7] S. Mirpour, S. Fathollah, P. Mansouri, B. Larijani, M. Ghoranneviss, M. Mohajeri Tehrani and M. R. Amini, Sci. Rep. **10**, 10440 (2020).

[8] S. Lerouge, M. R. Wertheimer and L. Yahia, Plasmas Polym. **6**, 175 (2001).

[9] M. Moisan, J. Barbeau, M.-C. Crevier, J. Pelletier, N. Philip and B. Saoudi, Pure Appl. Chem. **74**, 349 (2002).

[10] M. Abbas, M. E. A. de Kraker, E. Aghayev, P. Astagneau, M. Aupee, M. Behnke, A. Bull, H. J. Choi, S. C. de Greeff, S. Elgohari, P. Gastmeier, W. Harrison, M. B. G. Koek, T. Lamagni, E. Limon, H. L. Løwer, O. Lyytikäinen, K. Marimuthu, J. Marquess, R. McCann, I. Prantner, E. Presterl, M. Pujol, J. Reilly, C. Roberts, L. Segagni Lusignani, D. Si, E. Szilágyi, J. Tanguy, S. Tempone, N. Troillet, L. J. Worth, D. Pittet and S. Harbarth, J. Hosp. Infect. **102**, 267 (2019).

[11] W. J. O'Brien, K. Gupta and K. M. F. Itani, JAMA Surg. **155**, 61 (2020).

[12] J. C. Dumville, E. McFarlane, P. Edwards, A. Lipp and A. Holmes, Cochrane Database Syst. Rev. CD003949 (2013).

[13] B. Lange-Asschenfeldt, D. Marenbach, C. Lang, A. Patzelt, M. Ulrich, A. Maltusch, D. Terhorst, E. Stockfleth, W. Sterry and J. Lademann, Skin Pharmacol. Physiol. **24**, 305 (2011).

[14] M. Ulmer, J. Lademann, A. Patzelt, F. Knorr, A. Kramer, T. Koburger, O. Assadian, G. Daeschlein and B. Lange-Asschenfeldt, Skin Pharmacol. Physiol. **27**, 283 (2014).

[15] C. Tendero, C. Tixier, P. Tristant, J. Desmaison and P. Leprince, Spectrochim. Acta Part B At. Spectrosc. **61**, 2 (2006).

[16] M. Laroussi, X. Lu and M. Keidar, J. Appl. Phys. **122**, 20901 (2017).

[17] J.-H. Hwang, H.-Y. Lee, K. B. Chung, H. J. Lee, J. Kim, K. Song and D.-Y. Kim, Sci. Rep. **11**, 16125 (2021).

[18] R. Laurita, A. Miserocchi, M. Ghetti, M. Gherardi, A. Stancampiano, V. Purpura, D. Melandri, P. Minghetti, E. Bondioli and V. Colombo, IEEE Trans. Radiat. Plasma Med. Sci. **1**, 275 (2017).

[19] O. Lademann, A. Kramer, H. Richter, A. Patzelt, M. C. Meinke, V. Czaika, K.-D. Weltmann, B. Hartmann and S. Koch, Skin Pharmacol. Physiol. **24**, 284 (2011).

[20] O. Lademann, A. Kramer, H. Richter, A. Patzelt, M. C. Meinke, J. Roewert-Huber, V. Czaika, K.-D. Weltmann, B. Hartmann and S. Koch, Laser Phys. Lett. **8**, 313 (2011).

[21] F.-C. Yang, Y. Zhang and M. C. Rheinstädter, PeerJ **2**, e619 (2014).

[22] N. Otberg, H. Richter, H. Schaefer, U. Blume-Peytavi, W. Sterry and J. Lademann, J. Invest. Dermatol. **122**, 14 (2004).

[23] O. de Lacharrière, C. Deloche, C. Misciali, B. M. Piraccini, C. Vincenzi, P. Bastien, I. Tardy, B. A. Bernard and A. Tosti, Arch. Dermatol. **137**, 641 (2001).

[24] F. Jimenez, A. Izeta and E. Poblet, Dermatologic Surg. **37**, (2011).

[25] Q. Sun, W. Lee, Y. Mohri, M. Takeo, C. H. Lim, X. Xu, P. Myung, R. P. Atit, M. M. Taketo, R. S. Moubarak, M. Schober, I. Osman, D. L. Gay, D. Saur, E. K. Nishimura and M. Ito, Nature Comm. **10**, 5023 (2019).

[26] L. A. von Schuckmann, M. C. B. Hughes, R. Ghiasvand, M. Malt, J. C. van der Pols, V. L. Beesley, K. Khosrotehrani, B. M. Smithers and A. C. Green, JAMA Dermatology **155**, 688 (2019).

[27] N. Y. Babaeva and M. J. Kushner, J. Phys. D. Appl. Phys. **43**, (2010).

[28] E. Marzec and L. Kubisz, Int. J. Biological Macromolecules **20**, 161 (1997).

[29] F. Judée and T. Dufour, J. Phys. D. Appl. Phys. **52**, (2019).

[30] A. Stancampiano, T. H. Chung, S. Dozias, J.-M. Pouvesle, L. M. Mir and E. Robert, IEEE Trans. Rad. Plasma Med. Sci. **4**, 335 (2020).

[31] Z-S. Chang, G-J. Zhang, X-J. Shao and Z-H. Zhang, Phys. Plasmas **19**, 073513 (2012).

[32] M. Keidar, A. Shashurin, O. Volotskova, M. A. Stepp, P. Srinivasan, A. Sandler and B. Trink, Phys. Plasmas **20**, (2013).

[33] S. A. Norberg, E. Johnsen and M. J. Kushner, J. Appl. Phys. **118**, 013301 (2015).

[34] T. Darny, J. Pouvesle, V. Puech, C. Douat, S. Dozias and E. Robert, Plasma Sources Sci. Technol. **26**, 14 (2017).

[35] B. F. Gilmore, P. B. Flynn, S. O. Brien, N. Hickok, T. Freeman and P. Bourke, Trends Biotechnol. **36**, 627 (2018).

[36] X. Lu, M. Laroussi and V. Puech, Plasma Sources Sci. Technol. **21**, (2012).

[37] D. P. Lloyd, Nat. Physiol. **294**, 277 (1959).

[38] T. Teschner et al, Plasma **2**, 348 (2019)

[39] E. Slikboer et al, Plasma Sources Sci. Technol. **28**, 095016 (2019).

[40] N. Y. Babaeva, et al, Plasma Sources Sci. Technol. **30**, 115021 (2021).

[41] J. Qi and L. A. Garza, Cold Spring Harb Perspect Med **4**, 3 (2014).

[42] S. Babossalam, F. Abdollahimajd, M. Aghighi, H. Mahdikia and B. S. Dilmaghanian, Aydin, Parviz Toossi, Arch. Dermatol. Res. **312**, 361 (2020).

[43] M. Lee, S. Kossard, B. Wilkinson and J. A. Doyle, Australasian J. Dermatology **36**, 143 (1995).

Chapter 7 Atmospheric Pressure Plasma Jet Treatment of Polypropylene Step Barriers

Atmospheric pressure plasmas in contact with complex interfaces and polymers have been demonstrated to cause a wide range of effects. Used on a dielectric surface, plasma typically strikes an interface and continues traveling across the material in the form of a surface ionization wave (SIW). The application of atmospheric pressure plasma jets (APPJs) in contact with rough polymers has not yet been investigated. To approach this problem, in this chapter, 2D simulations were performed to simulate APPJs applied on dielectric interfaces that contain irregularities in the form of step barriers. It is identified that up and down barriers placed on the way of the SIW interact with it in a different way. Up barriers stop the propagation of SIWs or at least slow them down, while down barriers do not cause such effects. The conclusions from the simulations are supported by collaborative experimental findings. The ability of SIWs to cross the up barrier can be affected by the polarity of the source, the shape of the step barrier, and the dielectric permittivity of the interface. Chemical response to plasma treatment from the surface is studied by implementing a surface kinetic mechanism of polypropylene interacting with helium–air plasma. The fluxes of reactive oxygen species (ROS), photons, and ions to the interfaces in the APPJ environment are distinguished by several phenomena. Fluxes of ROS due to low air content are insignificant during plasma treatment, while fluxes of ions and photons reaching the topical areas are high. The fluxes collected by the interface follow the propagation of SIWs across the interface with the implemented step barrier; thus, after crossing, the up barriers all fluxes drop. The treatment of polypropylene follows the trends of collected fluxes. The high number of photons and

ions contacting the interface induces chain scission, hydrogen abstraction from sites, and subsequent cross-linking. The formation of the chemicals on the interface is not uniform and follows the propagation of SIWs on a step barrier. Atmospheric pressure plasma sources are prevalent in industrial plastic modifications. Progress in investigating these sources interacting with complex interfaces, as detailed in this chapter, can accelerate the development of technologies aimed at creating biocompatible materials, for instance.

7.1 Introduction

Atmospheric pressure plasmas (APPs) represent an important field for fundamental research [1,2] and a source of essential technologies [3,4]. The action of APPs on different existing media is known for all states of matter. Interest in these technologies is usually associated with low costs of device development under ambient conditions. Given the nonequilibrium nature of the phenomena of APPs, interaction of such plasmas with any media typically involves chemical impact. One of the most commonly used technologies involving APPs is polymer functionalization [5]. This is a key technology for the packaging industry that allows for most polymers to be painted. The problem that the technology solves is the reduction of hydrophobicity of the most commonly used polymers. Generation of the oxygen reactive species that connect with the polymer and form functional groups temporarily makes a polymer surface more hydrophilic [6–8].

While reduction of hydrophobicity is the most common application of APPs with polymers, other phenomena in the use of plasmas with polymers also occur. The rapidly developing technologies diversify the desired range of properties for new materials, liquids, and gasses. Thus, application devices such as those that generate APPs need constant adjustment and rethinking. In a recent review [9], the potential applications of plasmas on different polymers can be found in textile, biomedicine, electronics, food processing, and optics industries. Major effects that a typical APP source can cause on a polymer surface are well-known [10] and can be divided into three categories: replacement of polymer topical groups with functional ones [11,12], chain breaks and subsequent cross-linking [13,14], or a combination of these two effects when two added functional groups form a chemical bond. Controlling the desired effects is essential for developing applicable technologies. The selectivity of the system in many cases is defined by the source of the APP.

The number of sources required to generate APPs is researched and applied to polymer surfaces. The most commonly used source is a corona discharge applied in the packaging industry to improve wettability by adding oxygen groups on a surface [15–18]. Other types of discharge systems, although less common, are also used for treating various polymer interfaces. DBD discharge has been also widely used for polymer functionalization, increasing surface roughness, or altering electrical properties [19,20]. APPJ application on polymer surfaces is known for similar purposes [21–23]. All discharge systems are different in the regime of plasma generation, gas environments, photons, ions, and radical fluxes. Complex surface chemical composition and desired modification define the choice of a particular discharge system.

With the development of the research in LTPs and advances in modern technologies, a relatively deep understanding of physics and chemistry of plasmas generated with various discharge systems, plasma chemistry (in gas phase, in contact with polymers and liquids), and mechanisms of interaction of plasma with flat interfaces is reached [2,24]. However, diversification and progress in technologies require simultaneous understanding of the effects of plasma on complex materials and interfaces. Any non-smooth and/or nonhomogeneous interface can be treated as complex. Many irregularities on the surface can be simplified and represented as a sudden elevation of height or simply as a *step*

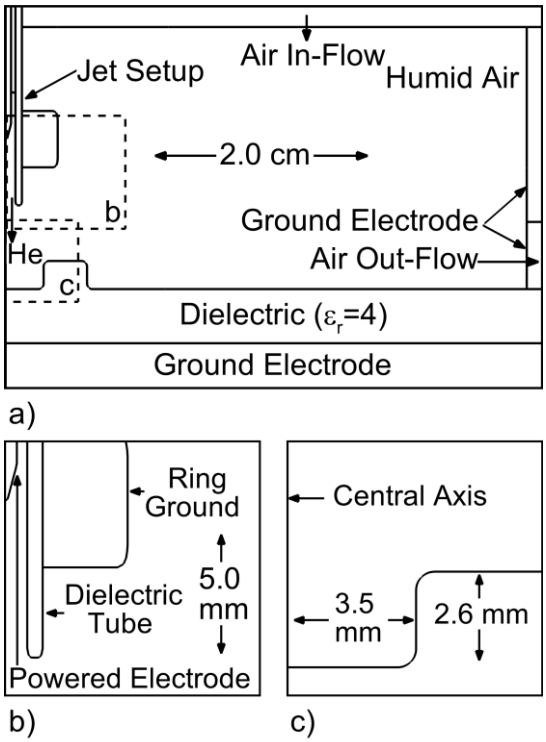

Figure 7.1. Scheme of a computational domain. a) Full domain, b) enlarged half-right APPJ scheme, c) enlarged scheme of step barrier.

barrier. Studying the underlying mechanism of physical and chemical interaction with such structures is critical for invention and enhancement of new technologies. Many practical materials exhibit dielectric properties. Typical interaction of plasma with a dielectric surface involves the charging of a dielectric, intensification of the local electric field, and traveling across the dielectric interface as a surface ionization wave (SIW). Irregularities on the surface alter the local electric field and change the propagation of the SIW. In recent years, a number of scientific papers have been published studying the interaction between APPs and step-like obstacles. A summary of these studies is contained in the introduction of Chapter 3. The purpose of the study in this chapter is to integrate the study of plasma interaction with the irregularities on the dielectric surface with surface kinetics investigation on such obstacles.

In this chapter, the experimental and computational results of the study of the APPJ interacting with dielectric step barriers are presented. The experimental work is conducted by the collaborative experimental group. The findings include the observed existence of the critical height over which plasma is not propagating. Down barriers typically do not slow down SIWs. The shape of the barrier also plays a role in the dynamics of SIWs. Functionalization of barriers is studied by implementing surface kinetics of the polypropylene. It is identified that the chemical feedback on the curved interface is not uniform and follows the propagation of SIWs. The major consequence of the plasma treatment is the effect of photon fluxes on chain scission leading to cross-linking. Ion bombarding and radicals interacting with the substrate result in noticeable hydrogen removal from the surface. Functionalization of the substrate with oxygen is limited during the treatment due to the helium gas environment.

7.2 Description of the Model and Experiment

7.2.1 Description of the Model

Simulations in this chapter are performed using nonPDPSIM. A full description of the code is contained in Chapter 2. The modules that were used in this study are the following: 1) fluid dynamics, 2) plasma, 3) surface kinetics, and 4) multipulse. The modules are utilized to address physical and chemical phenomena occurring in the dynamics of APPJ work and their time scales. The multipulse function is executed to address the effect of the burst of pulses. The equations described in Chapter 2 are used to simulate a single pulse produced by the APPJ. To consider the long-term effects of the APPJ and save the computational costs, the following technique is used. Poisson's equation solution updates are excluded for the period of time in which relaxation of the discharge occurs periodically followed with periods of updated densities originating from the first pulse.

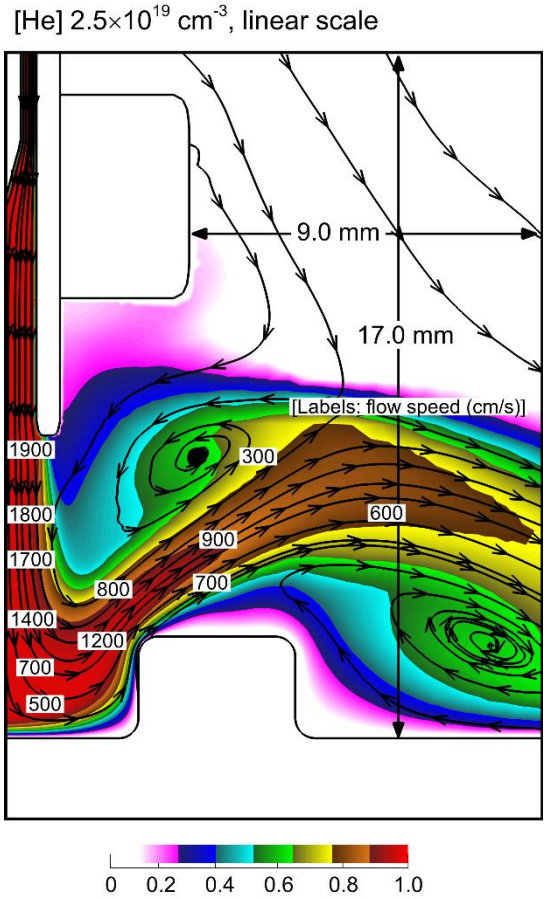

Figure 7.2. Helium fluid flow diagram demonstrated with colored helium concentration and fluid flow stream lines with local speeds.

For this study, the 2D computational domain was developed with the map of nodes for the unstructured mesh. The full domain and the map of nodes are demonstrated in Fig. 7.1. The experimental setups that were simulated are described in detail in the next subsection. The model

includes an atmospheric pressure helium plasma jet presented with the powered central pin electrode, a dielectric surrounding tube with a side grounded electrode. The helium mixture with impurities ($He:N_2:O_2:H_2O = 1 : 9 \times 10^{-6} : 2.4 \times 10^{-7} : 1 \times 10^{-6}$) is injected through the jet at rate 1 lpm reaching 2000 cm/s speed of gas at the exit of the dielectric tube. The fluid flow field calculated prior to plasma calculations is demonstrated in Fig 7.2. The substrate is represented as a dielectric material of thickness 5 mm with a relative permittivity in the range of 4–40 with the implemented step barrier as a small square material (the area of the insert is much smaller than the entire dielectric slot). The height of barriers varied from 1.6–3.6 mm (directed up or down). The grounded electrode is placed under the dielectric substrate and is wrapping the system around (finite size of the domain). The 0.5% humid air is injected from the top boundary surrounding the jet to maintain the atmospheric pressure condition. The gas is exhausted at the bottom-right corner of the geometry to replicate real fluid field conditions within the finite geometry domain.

The gas phase chemistry is modeled using the scheme described in detail by Lietz *et al.* [25]. In this model, the charged species are e, He^+, He_2^+, HeH^+, N_2^+, N_4^+, N^+, O_2^+, O_2^-, O^+, O^-, H_2O^+, OH^+, OH^-. Neutral species are He, He(2^3S), He(2^1S), He(2^1P), He(2^3P), He(3P), He(3S), He_2^*, N_2, N_2(v), N_2^*, N_2^{**}, N, N*, O_2(v), O_2^*, O_2^{**}, O, O*, O_3, H_2O, H_2O(v), HO_2, H_2O_2, OH, H, OH*. Photoionization is implemented on the ionization of nitrogen molecules from higher excited states of helium.

The surface chemistry in this work is developed to simulate polypropylene. The mechanism includes the model of polypropylene backbone sites of three types R_1-H (tertiary), R_2-H (secondary), R_3-H (primary). The initial condition are set for the following proportion between the types of the sites R_1-H : R_2-H : R_3-H = 1 : 2 : 1. The interaction between plasma and polypropele sites result in the formation of new surface chemicals. Within our model the following chemicals

are considered: alkyl radicals R_i-• (i denotes the type of the site), alkoxy radicals R_i-O•, peroxy radicals R_i-OO•, alcohol groups R_i-OH, carbonyl radicals •R_i=O, hydroperoxyl groups R_i-OOH, carbonyl HR_i=O, acid product OH-R=O, chain scission products Ri_s-H, Ri_s-OOH, Ri_s-O, Ri_s-OO, cross-link products R-CH-CH-R. The detailed surface kinetics of polypropylene interacting with helium–air plasmas is described by Dorai *et al*. [26] and Bhoj *et al*. [27].

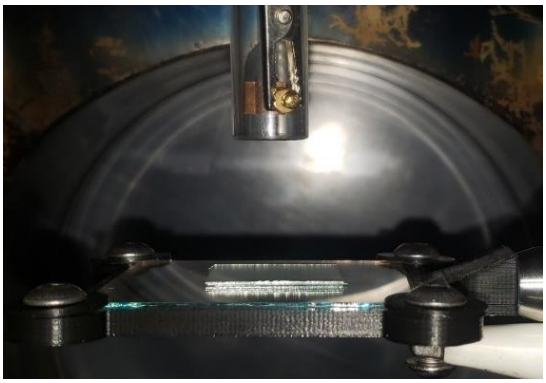

Figure 7.3. Photograph of the experimental chamber.

7.2.2 Description of the Experiment

The experimental setup is developed and implemented to sustain an APP by a collaborating group. A full description of the experimental setup can be obtained in a related publication [28]. The photograph of the experimental chamber is demonstrated in Fig. 7.3. Briefly, an ultrahigh purity helium (up to 10 ppm total of oxygen, nitrogen, water, and carbon dioxide) APPJ sustained at a flow rate of 1 lpm in humid air environment is used to treat dielectric interfaces with and without step barriers. The total thickness of the flat part of the dielectric was varied from a few 100s of μm to a few 10s of mm. A single pin-powered electrode in a quartz tube is surrounded by a ring grounded electrode attached to the tube. The jet is located perpendicular to the dielectric interface. The material of the substrate varied with the relative dielectric permittivity kept in the range between ε_r = 6 - 10. The steps on the interface are implemented distanced from the axis of the jet. The jet setup is covered with a half-sphere metal cover to prevent air perturbation in the

experimental zone. The cover has cylindrical vents in the bottom to exhaust helium and allow air to stagnate in the chamber.

7.3 Propagation of SIWs on Dielectric Interfaces

7.3.1 Propagation of SIWs on Flat Surfaces

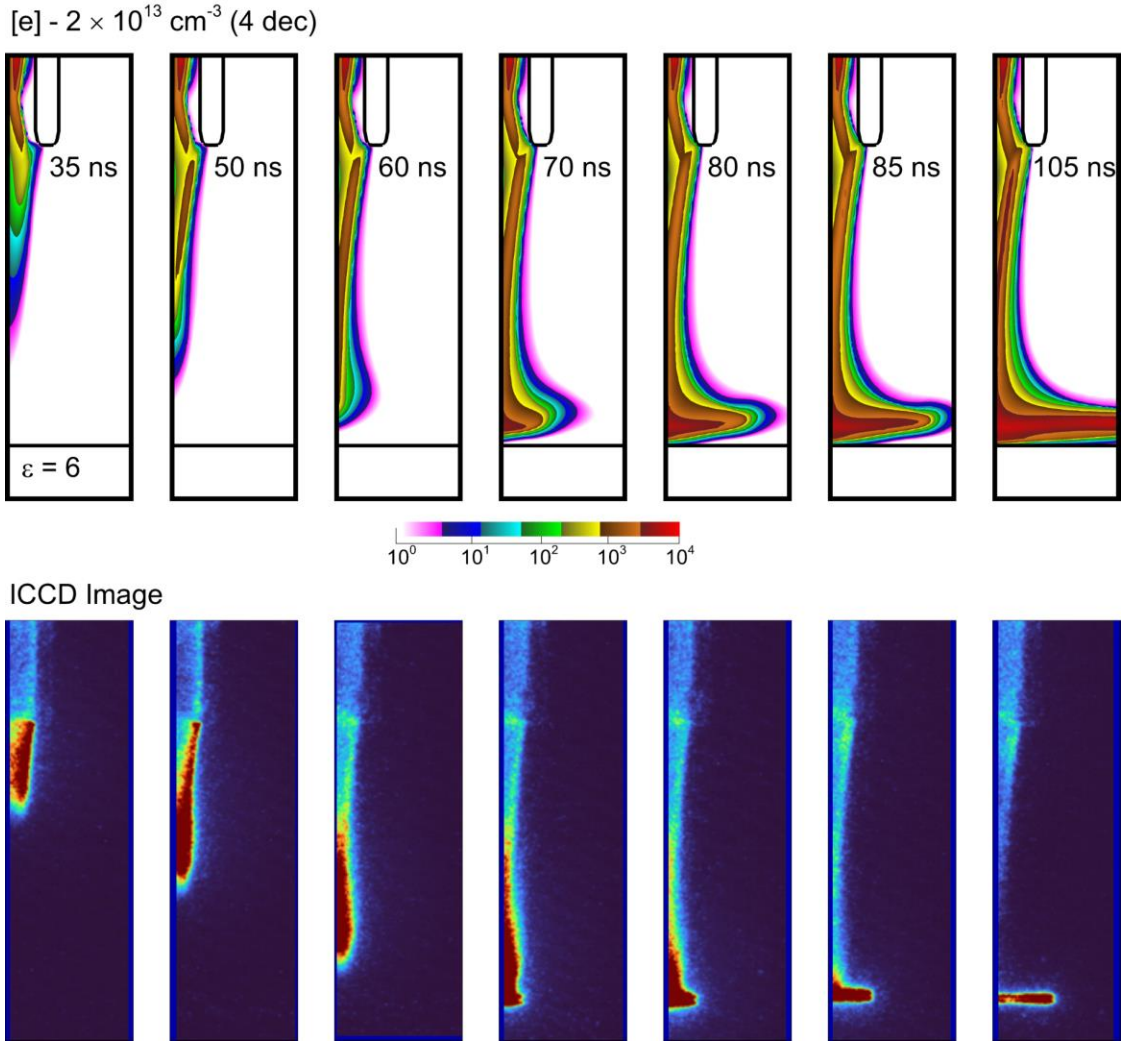

Figure 7.4. Comparison of the results of simulations for plasma produced with +8 kV voltage to ICCD camera imaging on the experiment for IW striking a dielectric interface. The time scale on the experiment is chosen to match the evolution of plasma in the calculations.

Ionization waves interacting with dielectric interfaces typically continue the motion on the interface, forming surface ionization waves. The charge collected by the dielectric interface before

the ionization wave arrival enhances the local electric field, which enhances the ionization wave strength. In Fig. 7.4, the propagation of the ionization wave interacting with the glass interface is demonstrated in the experiment and simulation. The experimental data is obtained from the images taken with an ICCD (intensified charge-coupled device). The discrepancy between the speed of the ionization wave in gas and on an interface is linked to different symmetry types. The implementation of barriers requires the treatment of the system in cartesian coordinates that motivated the fixing of this setup for this study. However, the actual experimental system is powered with a pin electrode. Based on the experience with Cartesian coordinates, the voltage applied to replicate and initiate the plasma propagation of an identical pin electrode experiment should be multiplied by 1.5–2. The overestimation of the voltage also reflects different speeds of propagation of the IW and SIW in simulation compared with the experiment.

Plasma generated in the experiment was powered with a 4 kV magnitude voltage pulse with a total pulse duration of 500 ns. In the simulations, the pulse magnitude was 8 kV with a total duration of up to 600 ns. The substrate thickness was 5 mm in the referred experiment and simulations. The results of the simulations and the experiment have a high qualitative agreement in the development and propagation of IWs and SIWs. The propagating plasma has a single filament shape contracted in space with a 2–4 mm diameter. The total speed of propagation of IWs in gas in the simulations is 8×10^4 m/s for the 5-mm-thick substrate. The experimental data for this characteristic is 1.66×10^5 m/s [28]. The SIW speed of propagation is calculated to be 1×10^5 m/s, while experimental data appears to be 3.68×10^4 m/s. The choice of symmetry can explain the discrepancy in gas and surface propagation. Cartesian coordinates simulate a blade-like

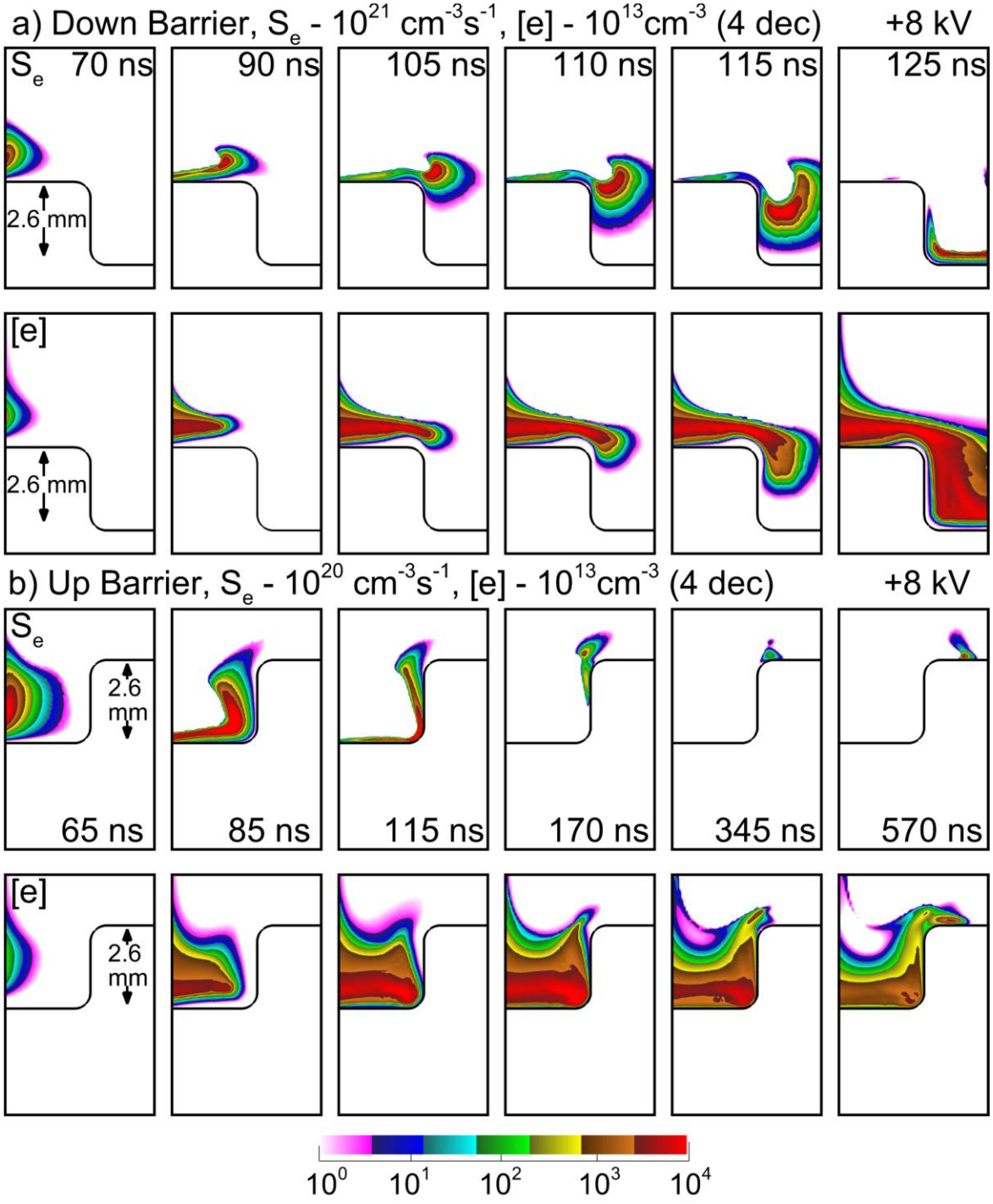

Figure 7.5. Plasma propagation generated by +8 kV pulse on up and down barriers of identical 2.6 mm heights. a) SIW on down barriers presented with electron impact ionization source S_e (top row) and electron density [e] (bottom row) from 70 to 125 ns. b) SIW on up barriers demonstrated with electron impact ionization source S_e (top row) and electron density (bottom row) from 65 to 570 ns.

electrode that generates a lower local (under the electrode) electric field compared with the pin

electrode. This results in a lower speed of propagation of IWs in the gas phase calculated by nonPDPSIM compared with the experiment. However, the speed of SIWs on the interface is higher in simulations. Away from the powered electrode, blade-like electrodes generate an electric field in coherent directions, while pin electrodes produce electric fields pointing in all directions on the planar dissipating energy. This fact contributes to the slower propagation in the experiment compared to simulations due to higher sectoral energy losses. It is also worth mentioning that the simulations are performed in 2D, lacking third-dimensional propagation and dissipation. This fact also contributes to a quantitative difference between the experimental and computational work.

Further investigation of the propagation of the SIWs on the interfaces is continued with step barriers placed on the way of propagation of SIW altering depending on the following scenarios: direction of the barrier (up/down), height of the barrier, shape of the interface, and polarity of the source.

7.3.2 SIWs interaction with Dielectric Steps: Direction of the Barriers

Obstacles on the interface can be roughly divided into barriers that suddenly change the interface direction up or down. The direction of the surface curvature can significantly influence the propagation of the SIW on such an interface. The reason behind such a trend is that the propagation of the SIWs on the dielectric interfaces relies on the charging of the surface. To sustain the propagation of plasma on the up or down barrier, the charge on the walls of the barrier should be organized so that the direction of the electric field is pointing in the direction of propagation (depending on the polarity of the source). When the IW arrives on the interface from the remote source and propagates on the substrate, the fundamental difference between the up and down barriers on the way is in the revert and continuous underlying interface direction. In up barriers,

the direction of the interface suddenly changes and forces the SIW to continue motion in the direction opposite to the applied electric field from the remote source. However, down barriers that align with the direction of the applied electric field do not require the formation of local electric fields that drive SIWs in the opposite direction. The charge reorganization required for the formation of the electric field sufficient to promote the SIW to climb the up barrier can vary based on the height of the barrier. Additionally, the stopping mechanism can be the shadowing of the photoionization by the corners of the barriers. This is particularly important in the case of positive polarity sources that strongly rely on photoionization in propagation.

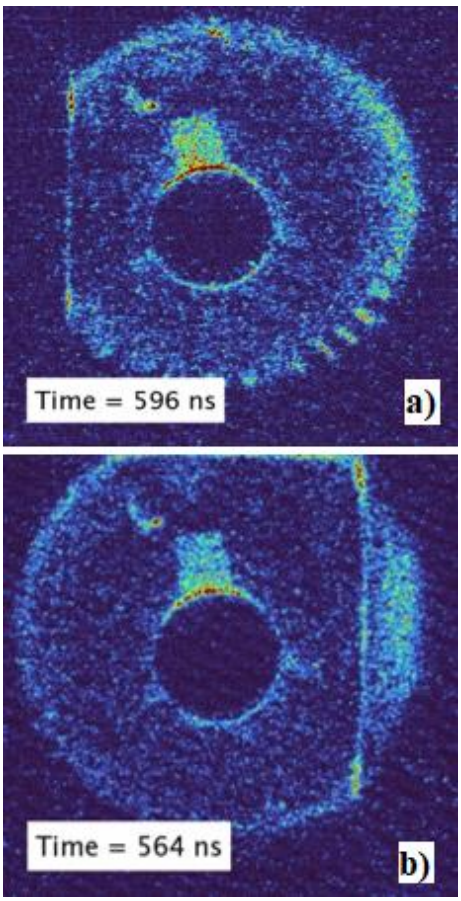

Figure 7.6. Experimental images taken from the bottom of the transparent substrate for SIW propagation over up and down barriers. The images are obtained from the ICCD camera. a) SIW climbing up barrier. The barrier is placed in left side of the image and identified with the bright vertical line. b) SIW moving down barrier. The barrier is placed in the right side of the image and is identified with bright vertical line.

For this reason, the existence of the critical height of the up barriers is expected. Critical height means that SIWs cannot climb over the barrier of this height. The slowing of the SIWs in the case of the down barriers is not anticipated. In Fig. 7.5a, the simulated propagation of SIWs over down barriers is demonstrated with the electron impact ionization source S_e and electron density [e]. It is shown that the strength of the electron impact ionization source is maintained at 10^{21} $cm^{-3}s^{-1}$ throughout the motion over the interface and the barrier is not acting to stop the SIW. The electron

density also remains stable at 10^{13} cm^{-3}. However, in Fig. 7.5b, the propagation of SIWs over the up barrier is presented with different trends. Similar characteristics S_e and [e] have dramatically

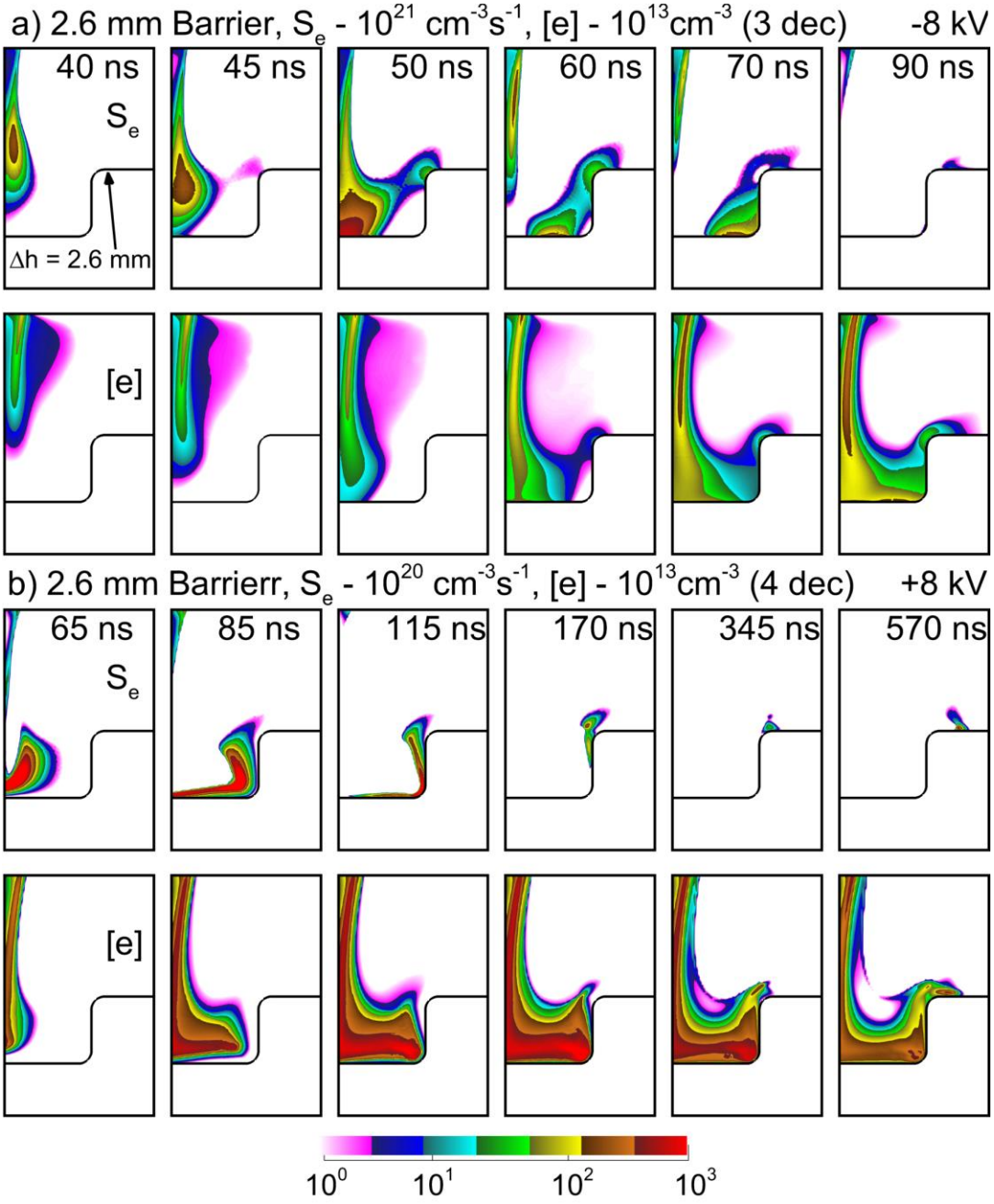

Figure 7.7. Plasma propagation over up barrier of 2.6 mm height generated by positive and negative polarity pulses of +/-8 kV. a) negative polarity driven SIW presented by electron impact ionization source S_e (top row) and electron density [e] (bottom row) at 40-90 ns time frame, b) positive polarity driven SIW shown with electron impact ionization source S_e (top row) and electron density [e] (bottom row) at 65-570 ns time frame.

lower magnitude once the SIW arrives on the top of the barrier. The strength of the electron impact ionization source is weakened to 10^{19} $cm^{-3}s^{-1}$ on the top of the barrier. Electron density is lowered to 10^{12} cm^{-3} at that spot. Additionally, the area that plasma covers has noticeably shrunk. Considering that the time scale of climbing to the top of the barrier is much larger than moving down the barrier (570 ns and 125 ns) and the differences mentioned above, the SIW over up barriers can be concluded as significantly slowed down. This result is supported by the experimental observations. In Fig. 7.6, the top view of SIW propagation is demonstrated with single-frame photographs taken with an ICCD for up (Fig. 7.6a) and down (Fig. 7.6b) barriers. It is demonstrated that for the down barrier the emission from plasma after crossing the barrier is intense. However, there is no noticeable emission beyond the up barrier.

7.3.3 SIWs interaction with Dielectric Steps: Polarity of the Source

The polarity of the source can noticeably influence the formation and evolution of SIWs on the curved interfaces. The propagation of positive IWs relies on the ion drift and diffusion away from the front of the IW. It is less efficient than negative IWs that rely on electron motions. For this reason, positive SIWs propagate depending on the photoionization source. The absorption distance of photons at atmospheric pressure is a few millimeters (in the model, a range of 0.5–1.0 mm is used with no significant difference in the calculations). The barriers are placed 3.3 mm away from the jet axis. Due to the propagation relying on photoionization, positive polarity-driven IWs are not expected to interact with the apexes of the barriers when approaching the substrate (the apex is far enough in a horizontal direction). Positive polarity-driven IWs, thus, first strike the horizontal interface and then move to the barrier and interact with it (Fig. 7.7a). Negative polarity IWs propagate mostly depending on the electron impact ionization source being less sensitive to

photoionization. An up barrier being placed at a relatively short distance away from the axis of the jet can, thus, collect charge prior to the interaction of the IW with the horizontal substrate. Negative polarity-driven plasmas are then expected to be less sensitive toward the height of up barriers. In Fig. 7.7b, this mechanism is demonstrated.

A more quantitative description of the positive and negative polarity-driven plasmas on 2.6 mm height up barriers can be obtained from Fig. 7.7. Negative polarity-driven plasma demonstrated in Fig. 7.7a with the electron density and electron impact ionization source propagating relatively fast (40–70 ns) has a more diffuse mode of propagation and relatively low peak electron density of 10^{12} cm^{-3}. Despite relatively fast propagation and early interaction of plasma with the apex of the barrier due to the diffusion losses in this type of plasma, the SIW weakens dramatically after reaching the top of the barrier (the electron impact ionization source falls to 10^{19} $cm^{-3}s^{-1}$). In comparison, in Fig. 7.7b, positive polarity-driven plasma has a higher peak electron density of 10^{13} cm^{-3}, a much longer time of propagation of 570 ns, and similar decay of the electron impact ionization source. A detailed description of the positive SIW climbing up barrier is presented for explanation in Fig. 7.5.

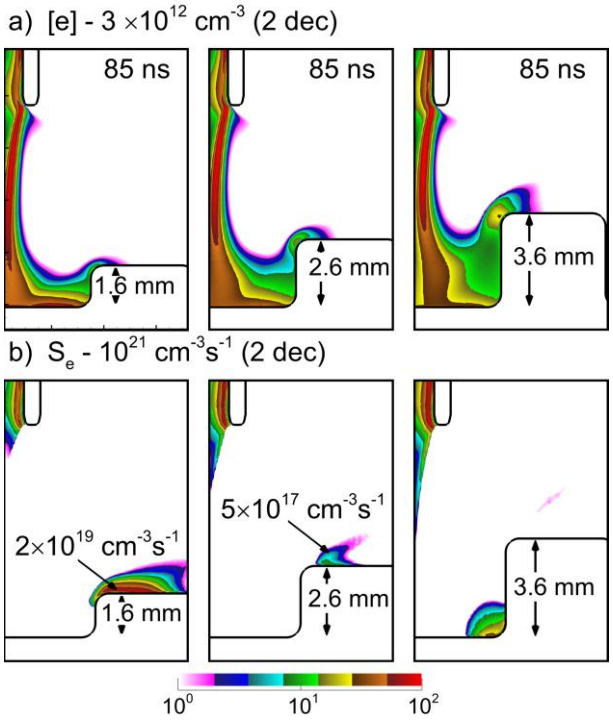

Figure 7.8. Negative polarity -8 kV driven plasma interacting with up barrier of different heights 1.6 – 3.6 mm at 85 ns when the SIW is developed on top barriers at all heights. a) data presented for all heights with electron density [e] (top row), b) data shown for all heights with electron impact ionization source S_e (bottom row).

7.3.4 SIWs interaction with Dielectric Steps: Height of Barriers

As aforementioned, there is a critical height of up barriers across which SIWs cannot propagate. In this parametric study, the height of barriers was altered to demonstrate the existence of critical height in the case of positive and negative polarity.

In Fig. 7.8, the propagation of negative-driven SIWs is demonstrated across barriers of 1.6–3.6 mm. Despite the fact that the apex of the barrier interacts with the plasma early in the propagation and the overall evolution is relatively fast for all heights (the SIW climbs all barriers within 85 ns), the plasma climbing capability over higher barriers is limited. While over 1.6 mm height barriers, the SIW maintains an electron impact ionization source (Fig. 7.8b) of 10^{19} $cm^{-3}s^{-1}$ magnitude and 10^{11} cm^{-3} electron density (Fig. 7.8a), for 2.6 mm height barriers, these characteristics dramatically fall with 10^{17} $cm^{-3}s^{-1}$ for the electron impact ionization source. At the largest height of 3.6 mm, the strength of the electron impact ionization source on the top of the barrier is much weaker than in two other cases. Only the polarized apex attracted an electron cloud, and the SIW is stopped by the barrier.

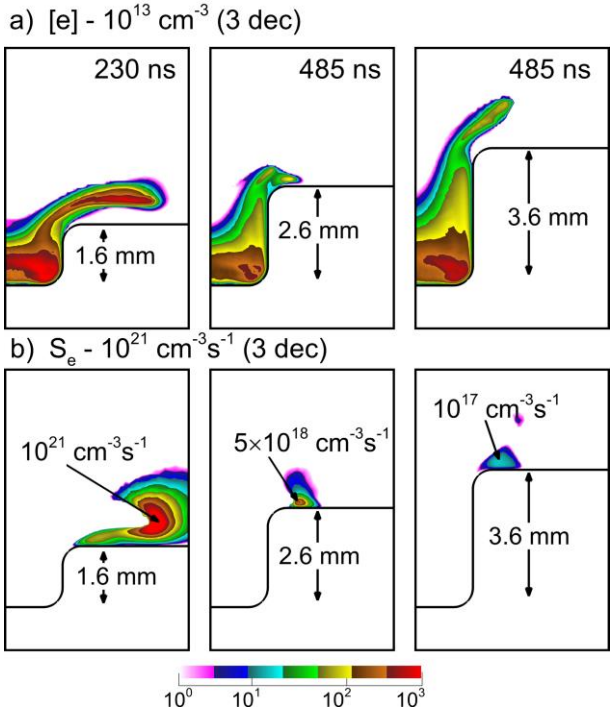

Figure 7.9. Positive polarity +8 kV driven SIWs moving across barriers of 1.6 – 3.6 mm heights at times of reaching the top of the barriers (230-485 ns). a) Electron density for all heights [e] (top row), b) electron impact ionization source S_e for all heights (bottom row).

A similar scenario is simulated for the positive polarity-driven SIWs. In Fig. 7.9, the climbing of positive polarity +8 kV driven SIWs is demonstrated for a similar height of barriers of 1.6–3.6

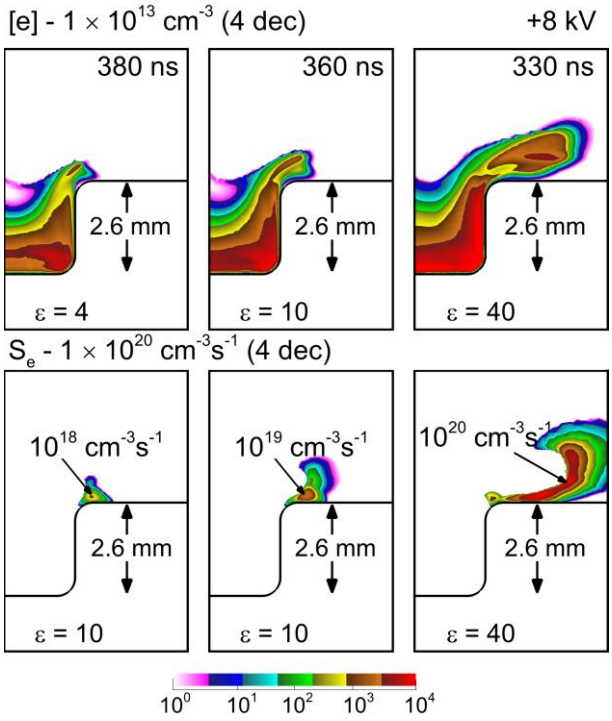

Figure 7.10. Positive polarity-driven plasma (+8kV) climbing the barriers of 2.6 mm height with different relative dielectric permittivities ε = 4 – 40 at different time frames addressing the moment of climbing. a) Data presented with electron density [e] (top row), b) data presented with electron impact ionization source S_e (bottom row).

mm. When the ionization wave climbs the barrier with a small height of 1.6 mm, the strength of the electron impact ionization source is maintained sufficiently for a propagation level of 10^{21} $cm^{-3}s^{-1}$ (Fig. 7.9b), and electron density remains high, reaching 10^{13} cm^{-3} (Fig. 7.9a). Higher barriers have a significantly lower electron density and electron impact ionization source on the top of the barriers. Electron impact ionization peaks at 10^{19} $cm^{-3}s^{-1}$ on the top of the barrier of 2.6 mm height, with electron density covering a few 100s of microns in the space ranging from 10^{11}–10^{12} cm^{-3}. Further increase in the height of the barrier to 3.6 mm results in a more dramatic fall of the strength of the electron impact ionization source by nearly two orders of magnitude.

It is important to note that the propagation of the SIWs along the surface perpendicular to the plane of simulations is not addressed in the 2D model. In the related experiment, a portion of the power used to sustain SIWs is dissipated on the propagation of the SIWs along this direction [29].

7.3.5 SIWs interaction with Dielectric Steps: Dielectric Permittivity of the Barrier

Dielectric permittivity of the barriers can also play a noticeable role in the motion of SIWs and, thus, affect the climbing abilities of SIWs across such. A larger relative dielectric permittivity increases the capacitance of the dielectric material and total charge that the dielectric collects. On the one hand, the collected charge contributes to the intensification of the local electric field. On the other hand, the surface charge originating from the charge in the streamer weakens the strength of ionization in gas. Thus, changing the dielectric permittivity can either enhance or weaken the SIWs and influence the barrier crossing depending on the particular local condition. In Fig. 7.10, the dielectric permittivity of barriers varied in the range of $\varepsilon = 4 – 40$. In this case, the gradual increase in the relative dielectric permittivity leads to increased capacitance of the dielectric material. The effect of this increased capacitance is enough to enhance the propagation of the SIW across the barrier. In Fig. 7.10a, the electron density covers more space for higher dielectric permittivities, taking less time. The electron impact ionization source gradually strengthens in Fig. 7.10b with the increase of dielectric permittivity from 10^{18} $cm^{-3}s^{-1}$ to 10^{20} $cm^{-3}s^{-1}$. In this case, the charge collected by the dielectric interface is insufficient to start weakening the SIW. The relative dielectric permittivity that is required to have a noticeable slowing effect on SIW motion is larger

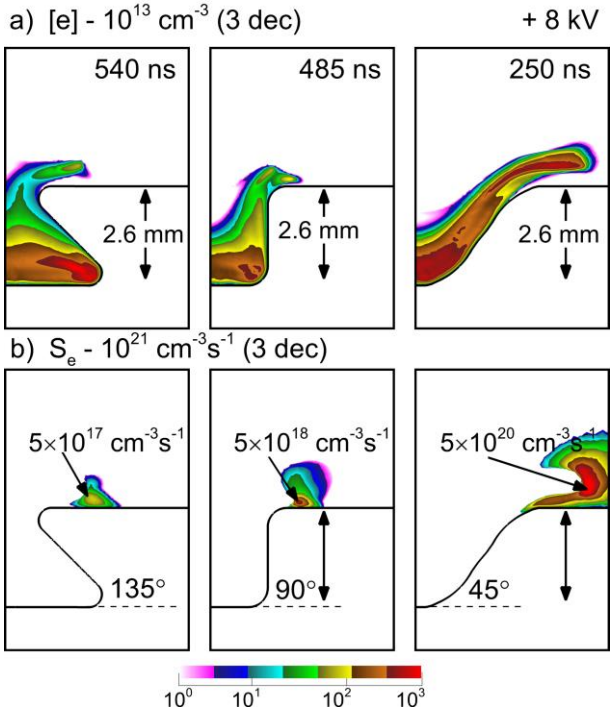

Figure 7.11. Positive polarity-driven +8 kV SIWs over the barriers of 2.6 mm height with different shapes curved in 45 – 135 degrees range at times of climbing the barrier. a) Data presented with electron density [e] (top row), b) data presented with electron impact ionization source S_e (bottom row).

than the one considered. Within the considered range of relative dielectric permittivities, the gradual increase leads to SIW enhancement. Additionally, the arrival time of the SIW due to the increased electric field in higher dielectric permittivity cases is shorter.

7.3.6 SIWs interaction with Dielectric Steps: Shape of the Barriers

The perpendicularly oriented edges of the barriers are a research simplification. Primitive surface patterns help identify common laws. Real interfaces have various abrupt changes of different shapes. The curvature and geometry of the obstacles can affect the propagation of SIW. The radius of curvature of the irregularities results in different total capacitance and polarization of the apexes. The overall geometry and size of the obstacles can additionally shadow the photoionization source. In case of negative polarity, photoionization is an additional electron source that obstacles can partially or fully block. In the case of positive polarity, this is the primary source of ionization. Even partial restriction of this source by corners of the obstacles may significantly weaken the SIW. In Fig. 7.11, the

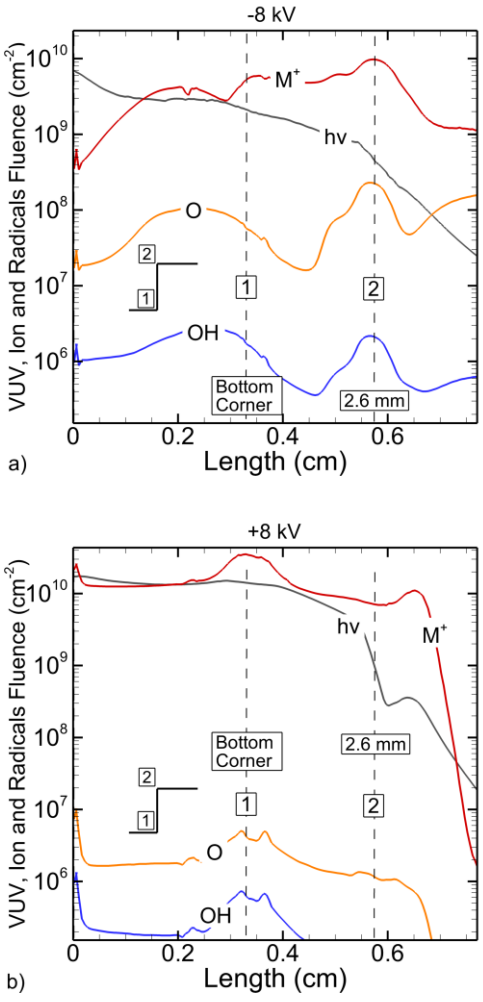

Figure 7.12. Fluence of photons (hv), positive ions (M^+), and O and OH radicals over 550 ns to the interface containing 2.6 height barrier for a) negative polarity, b) positive polarity.

propagation of SIWs in the form of electron density (Fig. 11a) and the electron impact ionization source (Fig. 7.11b) is demonstrated for different curved barriers with a height of 2.6 mm. Sharp corners of the obstacles sufficiently shadow the photoionization source of the climbing SIW, dramatically weakening the ionization strength on the top of barriers up to 10^{17} $cm^{-3}s^{-1}$. Smoother barriers provide less shadowing and, thus, less slowing of SIWs. In the smoothest case, SIW maintains a high enough strength of the electron impact ionization source up to 10^{21} $cm^{-3}s^{-1}$ that is enough to cross the barrier at a relatively short time of 250 ns compared to over 500 ns in two other cases.

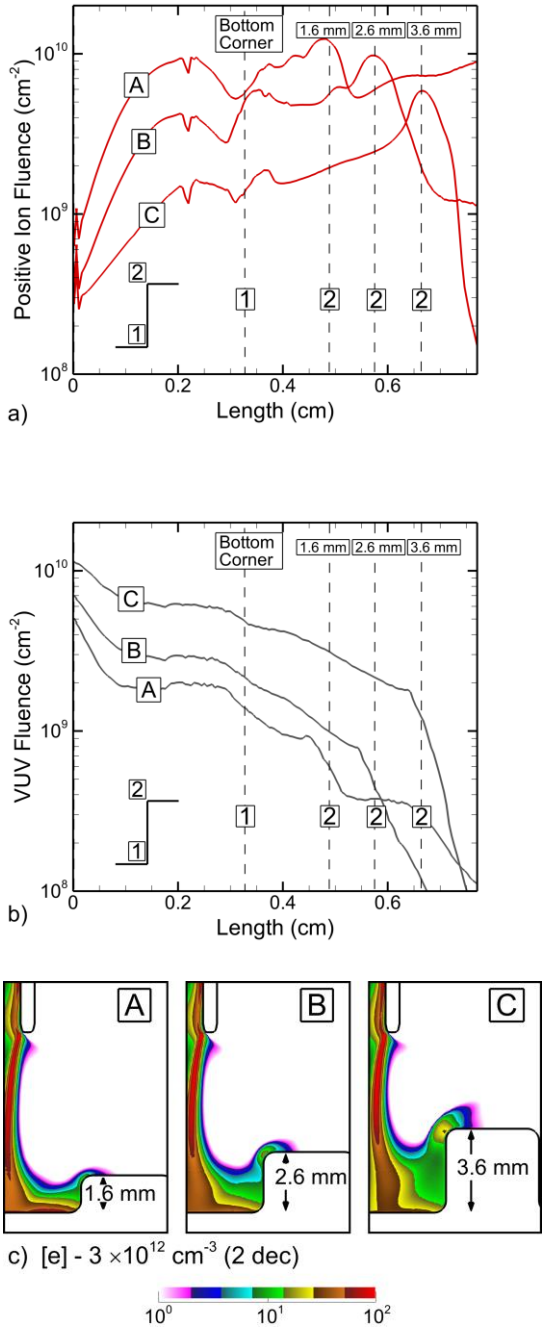

Figure 7.13. Schematic of the computational geometry. a) Full computational domain, b) computational mesh, c) enlargement showing chain of microchannels (dotted domain in previous images), and d) enlargement of individual channels.

7.4 Analysis of Fluxes of Species

The propagation of the SIWs across up barriers can significantly influence the potential chemical response from the chemically active interface (such as polymer surface). The resulting fluxes of radicals, excited states, ions,

and photons are, thus, critical for understanding the potential modification of the interface. In the following subsections, the implemented mechanism of polypropylene on the curved interface is used to demonstrate the example of the chemical response. Under the conditions of the APPJ, the fluxes of ions and photons are critical due to the presence of noble gas. The high reactivity of the polymers with radicals such as O and OH makes these species essential in the analysis. The comparison of the fluences of molecular ions, photons, and radicals over 550 ns for a barrier of 2.6 mm height is demonstrated in Fig. 7.12 for negative and positive polarity-driven plasmas. Several noticeable trends can be identified. In negative polarity-driven plasma (Fig. 7.12a), the fluence of photons and ions to the surface is lower overall compared with these characteristics for positive polarity-driven plasma (Fig. 7.12b). This is the consequence of the higher electron density in positive polarity-driven plasma compared with the negative polarity demonstrated in Fig. 7.7. The fluence of resulting photons and ions depends on the electron density and follows the local propagation of plasma on the interface. For similar reasoning, there is an abrupt drop in the fluence of photons and ions at locations beyond the apex of the step barrier. Following the propagation of the SIW, fluence of these species to the interface is limited by the steeply decreasing ionization rate in positive polarity plasma that has no diffuse electrons that can provide remote ionization away from the plume of the IW. In negative polarity-driven plasmas, such a trend is less noticeable due to more spatially uniform ionization. The top of the step barrier, thus, receives higher fluxes of species. Another noticeable trend considers the fluence of radicals. As demonstrated in Fig. 7.12, fluences of O and OH are insignificant compared with the photons and ions. This is the consequence of the gas composition in APPJs. For this study, the APPJ contained a minimal fraction of 10^{-5} impurities represented with the molecular gases. The concentration of oxygen and other impurities in APPJs may vary depending on the study. However, the major feeding gas is

always an Ar or He noble gas. For this reason, although the fluence may be higher in other APPJ setups, the domination of the photons and ions will still occur for this source. The influence of such chemical composition on the response from the polypropylene surface is discussed in the following section.

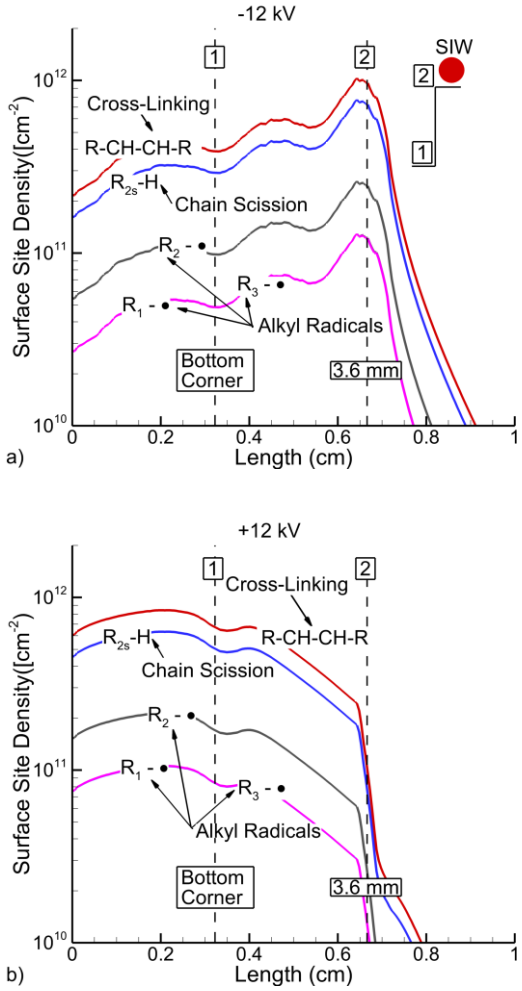

Figure 7.14. Surface site density as a function of length across the material. a) Negative polarity, b) positive polarity.

It is important to note that the height of the barriers influences the propagation of the SIWs across the interface, and also higher obstacles may affect the diffusion of air into the plasma region, shifting electron impact ionization and photoionization rates. In Fig. 7.13, the resulting fluences of ions and photons over 550 ns on the barriers of different heights for negative polarity-driven plasma are demonstrated. In Fig. 7.13c, the height of the barrier leaves a smaller gap for air to diffuse into the plasma zone. The differences in air concentrations in the plasma zone affect electron impact processes and photon production. Higher air concentrations in the plasma zone block photons that can reach the underlying interfaces. For this reason, smaller obstacles result in higher air concentrations in the plasma zone and lower fluences of photons that reach the substrate (Fig. 7.13b). An opposite trend occurs in the production of molecular ions that go up with the higher concentration of air in the plasma region (Fig. 7.13a).

7.5 Polypropylene Modification on the Step Barrier

When the material of the substrate is chemically active, the anticipated effect of APPs on such substrates can be sufficient to modify some properties of such materials. Polymers are a classic example of the type of materials that become chemically active under the action of low-temperature plasmas. The implementation of the model of one of the simplest polymers, polypropylene, on a curved surface is of interest for the development of new technologies. In this study, such a mechanism is implemented on a studied step-like interface. For demonstrational purposes of the effect of the APPJ on a polypropylene material with a step curvature of the surface, as described in the previous sections, the surface kinetic model is executed during the additional study. In this study on the highest barrier, the positive and negative polarity-driven plasma is incident on the step barrier of 3.6 mm height with an elevated voltage magnitude of 12 kV. The duration of every pulse is 210 ns (enough for SIW to reach the top of the barrier under these conditions). The burst of pulses contained 1500 pulses with an interpulse period of 0.2 μs. The result of the calculations is demonstrated in Fig. 7.14. Only the major products formed on the interface as a function of the length along the material are included in this image. The major products for both polarities are the cross-link products (R-CH-CH-R), the sites resulting from chain scission events (R_{2s}-H), and the sites with the alkyl radicals (R_i-•). These products are dominating, being direct products of photon-induced reactions with some contribution of ion bombardment. Due to the gas composition and the operation of the APPJ in the contact area of plasma with the interface, the high fluxes of ions and photons are reaching the interface. The photon processes that typically have high probabilities (1–10 %) to break bonds in polymers upon interaction result in chain scission events in the polymer. Sites resulting from chain scission events

result in cross-link products. Ion bombardment typically also results in some bonds breaking in polymers (in this mechanism, hydrogen abstraction for the creation of alkyl radicals). The dominant product R-CH-CH-R is the result of the photon-induced break of two bonds that results in two H_2 molecules entering the gas phase, while the vacant sites CH form a cross-link. Other dominant photon-induced products in Fig. 14 in our model are demonstrated as unbonded sites R_{2s}-H resulting from direct photon break of secondary sites. Initial backbone sites from which hydrogen atoms are abstracted also play a significant role. Alkyl radicals result from both ion bombardment and photon-surface interaction with initial sites. Other processes in the model include some interaction of radicals, molecules, and excited states formed from the products of an air environment. Given that the presence of these species in the plasma zone is minimal and the production of the O and OH radicals is low, the concentration of surface chemicals resulting from the interaction with this species is also insignificant.

Additionally, the polarity of the source affects the distribution of chemicals across the interface. The product concentration on the surface peaks for negative polarity at the apexes of the barriers with which plasma interacts most, while in positive polarity-driven plasma, chemicals are relatively uniform across the horizontal substrate and dramatically fall after reaching the top of the step barrier.

It is worth mentioning that the alkyl radicals presented in Fig. 7.14 will collect oxygen molecules once exposed to the atmosphere. Thus, the APPJ provides a hybrid effect from photon-induced cross-linking and chain scission effects and photon- and ion-induced alkyl radical formations that further become functionalized.

7.6 Concluding Remarks

APPs in contact with complex interfaces in the form of plain dielectrics containing step barriers are studied. The plasma source, APPJ, is selected to further understand the interaction between intense applied fluxes of VUV and ions on the dielectric in the form of a polymer polypropylene. It is identified that up barriers, in comparison with down barriers, have a characteristic critical height of a few mm (in this study about 2 mm) that stops the propagation of the SIWs. According to simulations, this is expected to be true in plasmas driven by both positive and negative polarities. Although the barriers slow down the SIWs in both cases, the interaction of plasmas with these barriers has different underlying mechanisms. Positive polarity-driven plasmas are sustained mainly with the photoionization source, typically first interacting with the horizontal underlying interface and then climbing the barrier. Negative polarity-driven plasmas affect the charging of the upper apexes of the barrier prior to the arrival of the SIW and interact with the intensified electric field in that region in the first place. This results in the difference in collected fluxes by the interfaces above the barrier. In positive polarity-driven plasmas, when the barrier is high enough to slow down the SIW, the abrupt decrease of photon and ion fluxes above the barrier is computed. The simulated scenario for negative polarity-driven SIWs is different: the computed decline of fluxes is gradual. The effect of stopping the SIWs with up barriers and positive polarity is supported by the experimental findings. It is important to mention that barriers were placed at a fixed distance from the vertical axis of the jet. The polarization of the apexes of the barriers in the negative polarity-driven plasmas is a function of this distance. Further investigations are needed to obtain a clear pattern of the critical horizontal coordinate of the barrier, when the primary polarization of the corners is no longer the case and negative SIW climbs the barrier as demonstrated in the positive polarity case scenario. Additionally, it is identified that the

dielectric permittivity and shape of barriers can play a role for SIWs to cross this obstacle. Higher dielectric permittivities, at least in the range considered in this study, can significantly speed up the SIW and support climbing the barrier due to intensified local electric fields. Smoother shapes of barriers generally result in less shadowing, supporting the propagation of SIWs on curved interfaces.

As discussed, the SIW propagation on the interfaces containing barriers directly influences the fluxes of species that reach and affect the surface. Several key trends are identified in the demonstrated analysis of species fluences. In the dominant helium environment, the fluences of radicals such as O and OH are minimal due to the gas composition. However, due to the presence of noble gas, the fluences of positive ions and VUV photons are dominant. The decrease in the fluences of all species above the higher barriers follows the declining behavior of plasma on such elevations.

The chemical activation of the interfaces that have up barriers is demonstrated in the example of the polypropylene interface. As the fluences of the species follow the propagation of plasmas on the interface, the chemical activation of the substrate is a direct consequence of these fluences. Since the dominant effect is due to the ions and VUV photons, the major products on the interface are the cross-link products, chain scissions, and alkyl radicals. The distribution of chemicals on the interface is uneven. This is a consequence of the plasma interaction with barriers and the decaying motion after climbing them.

7.7 References

[1] M. Keidar, K.-D. Weltmann, and S. Macheret, J. Appl. Phys. **130,** (2021).

[2] I. Adamovich, S. Agarwal, E. Ahedo, L. L. Alves, S. Baalrud, N. Babaeva, A. Bogaerts, A. Bourdon, P. J. Bruggeman, C. Canal, E. H. Choi, S. Coulombe, Z. Donkó, D. B. Graves, S. Hamaguchi, D. Hegemann, M. Hori, H.-H. Kim, G. M. W. Kroesen, M. J. Kushner, A. Laricchiuta, X. Li, T. E. Magin, S. Mededovic Thagard, V. Miller, A. B. Murphy, G. S. Oehrlein, N. Puac, R. M. Sankaran, S. Samukawa, M. Shiratani, M. Šimek, N. Tarasenko, K. Terashima, E. Thomas Jr., J. Trieschmann, S. Tsikata, M. M. Turner, I. J. van der Walt, M. C. M. van de Sanden, and T. von Woedtke, J. Phys. D. Appl. Phys. **55,** 373001 (2022).

[3] K. D. Weltmann, J. F. Kolb, M. Holub, D. Uhrlandt, M. Šimek, K. (Ken) Ostrikov, S. Hamaguchi, U. Cvelbar, M. Černák, B. Locke, A. Fridman, P. Favia, and K. Becker, Plasma Process. Polym. **16,** (2019).

[4] M. Domonkos, P. Tichá, J. Trejbal, and P. Demo, Appl. Sci. **11,** (2021).

[5] C.-M. Chan, T.-M. Ko, and H. Hiraoka, Surf. Sci. Rep. **24,** 1 (1996).

[6] M. Mozetič, Polymers (Basel) **12,** 2498 (2020).

[7] G. Primc and M. Mozetič, Polymers (Basel) **14,** (2022).

[8] C. Ma, L. Wang, A. Nikiforov, Y. Onyshchenko, P. Cools, K. (Ken) Ostrikov, N. De Geyter, and R. Morent, Appl. Surf. Sci. **535,** 147032 (2021).

[9] S. K. Nemani, R. K. Annavarapu, B. Mohammadian, A. Raiyan, J. Heil, M. A. Haque, A. Abdelaal, and H. Sojoudi, Adv. Mater. Interfaces **5,** 1 (2018).

[10] H. Yasuda, J. Macromol. Sci. Part A - Chem. **10,** 383 (1976).

[11] A. Vesel and M. Mozetic, J. Phys. D. Appl. Phys. **50,** 293001 (2017).

[12] D. Hetemi and J. Pinson, Chem. Soc. Rev. **46,** 5701 (2017).

[13] K. Molnar, B. Jozsa, D. Barczikai, E. Krisch, J. E. Puskas, and A. Jedlovszky-Hajdu, J. Mol. Liq. **303,** 112628 (2020).

[14] X. Ge, Y. Guo, J. Zhao, J. Zhao, H. Shen, and W. Yan, Int. J. Biol. Macromol. **215,** 465 (2022).

[15] A. Popelka, P. N. Khanam, and M. A. AlMaadeed, J. Phys. D. Appl. Phys. **51,** 105302 (2018).

[16] L. Ding, X. Zhang, and Y. Wang, Coatings **10,** 1195 (2020).

[17] B. Das, D. Chakrabarty, C. Guha, and S. Bose, Polym. Eng. Sci. **61,** 1449 (2021).

[18] A. Popelka, I. Novák, M. A. S. A. Al-Maadeed, M. Ouederni, and I. Krupa, Surf. Coatings Technol. **335,** 118 (2018).

[19] P. Dimitrakellis, F. Faubert, M. Wartel, E. Gogolides, and S. Pellerin, Processes **10,** 1 (2022).

[20] M. F. Bekkara, L. Dascalescu, Y. Benmimoun, T. Zeghloul, A. Tilmatine, and N. Zouzou, Eur. Phys. J. Appl. Phys. **81,** 10801 (2018).

[21] C. Cheng, Z. Liye, and R. J. Zhan, Surf. Coatings Technol. **200,** 6659 (2006).

[22] M. Noeske, J. Degenhardt, S. Strudthoff, and U. Lommatzsch, Int. J. Adhes. Adhes. **24,** 171 (2004).

[23] T. M. C. Nishime, R. Wagner, and K. G. Kostov, Polymers (Basel) **12,** (2020).

[24] P. J. Bruggeman, M. J. Kushner, B. R. Locke, J. G. E. Gardeniers, W. G. Graham, D. B. Graves, R. C. H. M. Hofman-Caris, D. Maric, J. P. Reid, E. Ceriani, D. Fernandez Rivas, J. E. Foster, S. C. Garrick, Y. Gorbanev, S. Hamaguchi, F. Iza, H. Jablonowski, E. Klimova, J. Kolb, F. Krcma, P. Lukes, Z. Machala, I. Marinov, D. Mariotti, S. Mededovic Thagard, D. Minakata, E. C. Neyts, J. Pawlat, Z. L. Petrovic, R. Pflieger, S. Reuter, D. C. Schram, S. Schröter, M. Shiraiwa,

B. Tarabová, P. A. Tsai, J. R. R. Verlet, T. von Woedtke, K. R. Wilson, K. Yasui, and G. Zvereva, Plasma Sources Sci. Technol. **25,** 053002 (2016).

[25] A. M. Lietz and M. J. Kushner, J. Phys. D. Appl. Phys. **49,** 425204 (2016).

[26] R. Dorai and M. J. Kushner, J. Phys. D. Appl. Phys. **36,** 666 (2003).

[27] A. N. Bhoj and M. J. Kushner, J. Phys. D. Appl. Phys. **40,** 6953 (2007).

[38] J. Morsell, N. Bhatt, C. Dechant, and S. Shannon, J. Phys. D. Appl. Phys. **56,** 145201 (2023).

[39] J. Morsell, D. Trosan, K. Stapelmann, and S. Shannon, Plasma Sources Sci. Technol. **32,** 0 (2023).

Chapter 8 Summary and Future Work

8.1 Summary

In this dissertation, the interaction of atmospheric pressure plasmas with complex interfaces is studied. The patterns, laws, and limitations of plasma propagation on common types of surfaces are identified and classified. The work is predominantly performed using a 2-D plasma hydrodynamic code, relying on experimental data from the closely collaborating groups. The description of the code appears in Chapter 2. The studies that were conducted under the scope of this dissertation are summarized below.

In Chapter 1, the basic phenomena and definitions of plasmas are discussed. The type of plasma used in this work is low-temperature, atmospheric-pressure plasma (APP). The non-equilibrium mode of this plasma requires its physical and chemical phenomena to be studied simultaneously. The discussion in Chapter 1 is extended from the fundamental physics and chemistry of such plasmas to the motivation to study them and the challenges of the modeling methods. Since many atmospheric pressure plasma systems have already been relatively well studied, the research needs lie primarily in building and researching more complex systems relevant to the surface morphology and chemistry of actual systems in nature (such as human skin) or existing/developing technologies (such as lab-on-the-chips). An example of systems that can be attractive for treatment by APPs are surfaces that are not uniform or homogeneous; such interfaces are called complex. Human skin with wrinkles and hair follicles, porous supports for catalysts, and empty or liquid-filled lab-on-the-chip devices may serve as complex interfaces that are known to

benefit from treatment by APPs. The intention of this dissertation is to study the fundamental physics and chemistry of APPs produced by different sources in contact with these systems and identify their potential applications and limitations.

Each subsequent chapter in this dissertation contains a separate study on one of the systems that meets the criteria for this topic. The concluding remarks for every chapter are summarized below.

Chapter 3 is dedicated to a surface dielectric barrier discharge (SDBD) applied on a surface that contains micropores. This source is purposefully chosen to generate surface ionization waves (SIWs) directly on a dielectric interface without generating remote ionization waves (IWs) that further intersect with the substrate. The typical evolution of SIWs is sustained by the charging of the dielectric substrate, which generates a locally intensified electric field. When an SIW encounters porous structures on the way of propagation, local charging alters on the curved structures, producing local minima or maxima of the electric fields that affect the behavior of the SIWs. For this reason, more deeply buried pores with more prominent irregularities receive less uniform treatment. Pores located entirely under the surface with only a narrow neck-like opening (comparable to the Debye length of plasma) can also benefit from plasma treatment. Ionization in such pores can be produced by the photoionization that seeds the initial charge inside of a pore.

A setup similar to that used in Chapter 3 is used to study wet microchannels in Chapter 4. Instead of microporous structures, the SDBD device is used to treat microchannels. It is observed that the locally enhanced electric field produced by the electrical triple points (the intersection of the plasma, water, and substrate) in the edges of the channels is responsible for directing the propagation of SIWs across channels. In the case of negative polarity-generated SIWs, the formation of reverse ionization waves is identified. The phenomenon of reverse IWs is also

captured in a different setup in Chapter 5, supported by the collaborative experimental data. Positive polarity-driven plasma propagates only in the forward direction, is more contracted in space, and has a higher concentration of charged species, photons, and radicals incident on the water interface. The shape of the water, which can alter based on the properties of hydrophobicity, may change the SIW's behavior on such a surface. Providing enough shadowing of prominent parts of the substrate or liquid can slow down the SIW. The smaller an obstacle on the interface is with respect to the size of the plasma, the less the propagation speed is affected. Making channels wide while maintaining the depth increases the surface-to-volume ratio, which can be beneficial for topical plasma treatment. However, in wider channels, the front of the SIWs breaks and leads to the formation of extra IWs that hop across the middle of channels. This leads to lower species fluxes in the liquid interface in the middle of the channels.

The study of microchannels is continued in Chapter 5. The interaction of plasma with the array of microchannels when in contact with an atmospheric pressure plasma jet (APPJ) is studied, in collaboration with the experimental group. The formation of the reverse ionization waves on the chain of microchannels (both dry and wet) in negative polarity-driven plasma described in Chapter 4 is also observed in this study and confirmed by simulations and experiments. A good qualitative agreement in electric field evolution is reached between experimental and modeling data.

In Chapter 6, a special case scenario of vertically extended microchannels is presented in the form of resolved hair follicles in human tissue. Real hair follicles harbor a large number of bacteria, and have narrow openings of 10s to a few 100s microns. Liquid disinfectants are less efficient in treating such zones, while common atmospheric pressure plasmas can flow into follicles with a smaller Debye length than the entering gap. The simulations and their analyses demonstrate the

ability of plasma generated by an APPJ to penetrate the hair-follicle-like structure presented by two rectangular capillaries in the modeled human tissue.

APPJs may provide benefits to the substrates on which the source is applied when compared to other APP sources with a specific gas composition and high fluxes of ions and photons. In Chapter 7, an APPJ is applied on the dielectric substrate with a sizable obstacle on it. The results of the computations demonstrate that up barriers have a critical height that SIWs cannot cross. Down barriers, on the other hand, do not slow down SIWs. These findings are supported by the data obtained in a collaborative experimental group. The modeling results show that fluxes of photons and ions to the substrate in such APPJ systems dominate reactive oxygen and nitrogen species (RONS). The fluxes collected by the interface with step barriers have been demonstrated to follow the behavior of the SIW on the surface. In up barriers, a sudden drop of fluxes of all species is computed at the point of the top edge of the barrier. When the polypropylene mechanism is implemented on the interface, the chemical products on the surface follow the trends of the fluxes of ions and photons. In the APPJ gas environment, these species are dominant and cause the formation of chain scission products, cross-linking, and alkyl radicals.

8.2 Future Work

The research presented in this dissertation may be continued in several ways, in the form of additional computational or experimental studies. New research may include studies of new objects with current or updated states of codes and diagnostic methods. The integration of plasma technologies in new fields of study is another way of extending this research. Finally, because some of the studies in the dissertation had simplifications and limitations, future research might consider more realistic case scenarios for the individual studies. Some specific suggested future research topics are described below.

1) In Chapter 3, porous structures had at least a narrow opening to the atmosphere. However, pores are not always exposed to the atmosphere. Many porous materials have a high level of interconnectivity, in which individual pores are hidden deeply in the material. One direction for future study is to generate plasma directly inside the gaps of pores by injecting gas through the interconnected chains of pores in the material, elevating local gas pressure to cause the breakdown in micro-sized structures, following Paschen's law. Knizhnik et al. [1] suggest a method to facilitate the volumetric treatment of highly porous materials that may yield fruitful results in this area of study. This idea is worth pursuing within 2D model. This is an opportunity for modeling and extending code capabilities for adapting different pd values.

2) Chapter 4 contains a purely computational study. Some findings in this chapter related to reverse ionization waves are confirmed in another computational study supported by the experiment. A similar experiment could be undertaken in future to support computational studies involving alternating polarity of the source, extending dry/wet microchannels in the horizontal direction, and changing the shape of the water by choosing substrates with varying hydrophobicity.

3) All effects described in Chapters 4 and 5 are based on the interaction of a single plasma pulse with arrays of microchannels. Bursts of pulses are typically generated during the operation of the source. Leftover charge in the gas phase and on the surface can significantly affect the dynamics of the subsequent ionization wave. As discussed by Viegas et al. [2], the effect of surface memory charge can also noticeably change, depending on the polarity of the source. Exploring the effect of the leftover charge on the array of microchannels is a future challenge for modeling work, experimental diagnostics, and code development.

4) Additionally, the results of treatment by a burst of pulses as described above would have a noticeable effect not only on a thin topical layer of the liquid interface but also on volumetric treatment. New studies could measure the concentrations of solvents in the water after experimental treatment. Similar research could be performed computationally.

5) In Chapters 3 and 4, positive polarity is used within the framework of a 2-D model. In 3-D, this discharge type relies strongly on photoionization and may exhibit filamentary behavior. The nonPDPSIM has a statistical approach to treating photoionization. Future studies might compare statistical and Green's function approaches in specific positive polarity conditions.

6) In Chapter 6, the work on hair follicles is mainly computational. Performing experimental work on real human tissue or two similar extended channels in a dielectric material could confirm the non-uniformity of treatment documented in the dissertation.

7) In Chapter 7, shadowing of the photoionization source by curved obstacles played a critical role in the propagation of the surface ionization waves. Some materials can be transparent to the photons in plasma. Propagating on such materials, surface ionization waves are less sensitive to the size of the encountered obstacles. For example, in a study by Marskar et al. [3], the effect of a transparent dielectric substrate on the rough surface interacting with atmospheric pressure plasma

is demonstrated. Implementing transparency of the materials constitutes an opportunity for code development.

8) Gas flow calculations in Chapter 7 are performed using symmetric boundary conditions for an atmospheric pressure plasma jet. However, gas flow instabilities and the realistic interaction between the obstacles on the interface and gas are not addressed in such an approach (the gas flow would be more asymmetric in reality if the obstacle is too close to the axis of the jet). Local gas composition can play a noticeable role in the evolution of SIW. Simulations of the full geometry of the jet and obstacle are thus needed.

9) Additionally, studying the electrical properties of human tissue more accurately is essential for a number of reasons. In Chapter 6, the capacitance of the fat layer (which also depends on the dielectric permittivity) played a role in plasma penetration in hair follicles. Computing accurate total capacitance and conductance of the tissue is thus critical. Other applications that also rely on similar data are electroporation [4] and nerve electrical stimulation [5], [6]. Studies of the correct dosing of the applied electric field, which may facilitate the proper growth of pores in living cells or identify activation potential for nerve conduction in the human body, are particularly needed.

10) Electrical triple points and microstructures with sharp edges in a plasma environment result in locally enhanced electric fields. Secondary emission coefficients can, thus, alter in these locations following a different electric field environment [7]. The opportunity for both quantum surface chemistry to obtain the correct coefficients for secondary electron emission and code development for implementing local functions for these coefficients could be beneficial for research in the field of atmospheric pressure plasmas.

8.3 References

[1] A. A. Knizhnik, S. V. Korobtsev, D. D. Medvedev, B. V. Potapkin, N. K. Belov and O. O. Grankina, AIP Adv. **10** (2020).

[2] P. Viegas, E. Slikboer, Z. Bonaventura, E. Garcia-Caurel, O. Guaitella, A. Sobota and A. Bourdon, Sci. Rep. **12**, 1181 (2022).

[3] R. Marskar and H. K. H. Meyer, Plasma Sources Sci. Technol. **32**, 085010 (2023).

[4] M. Deminsky, A. Eletskii, A. Kniznik, A. Odinokov, V. Pentkovskii and B. Potapkin, J. Membr. Biol. **246**, 821 (2013).

[5] M. N. Shneider and M. Pekker, Biomed. Phys. Eng. Express **9**, 035032 (2023).

[6] M. N. Shneider and M. Pekker, Phys. Biol. **19**, 044001 (2022).

[7] E. Husain and R. S. Nema, IEEE Trans. Electr. Insul. **EI-17**, 350 (1982).